UNIVERSIDAD DE GRANADA

INSTITUTO ANDALUZ DE CIENCIAS DE LA TIERRA

CSIC
Consejo Superior de Investigaciones Científicas

Active Components of the Subcontinental Lithospheric Mantle for Crustal Metallogenic Endowment in Off-Craton Regions

Erwin Schettino

Tesis Doctoral

2023

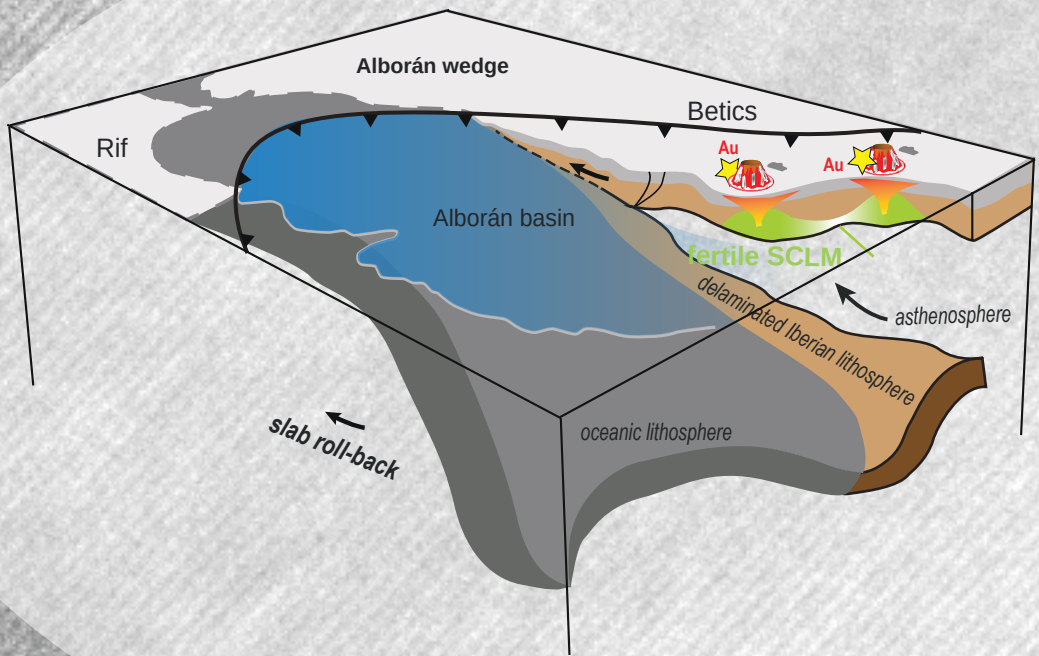

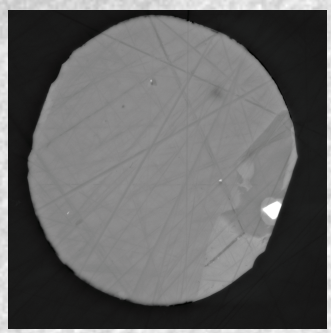

Editor: Universidad de Granada. Tesis Doctorales
Autor: Erwin Schettino
ISBN: 978-84-1117-791-7
URI: https://hdl.handle.net/10481/81248

Active components of the subcontinental lithospheric mantle for crustal metallogenic endowment in off-craton regions

Erwin Schettino

Ph.D. Thesis – Tesis Doctoral

Memoria de Tesis Doctoral presentada por el Licenciado en Geología Erwin Schettino para optar al grado de Doctor por la Universidad de Granada

Granada, febrero de 2023

Esta Tesis Doctoral ha sido dirigida por el Dr. Claudio Marchesi, Profesor Titular de la Universidad de Granada (UGR), y el Dr. José María González-Jiménez, Científico Titular del Consejo Superior de Investigaciones Científicas (CSIC)

El doctorando / The doctoral candidate **Erwin Schettino** y los directores de la tesis / and the thesis supervisors **Claudio Marchesi** and **José María González-Jiménez**

Garantizamos, al firmar esta tesis doctoral, que el trabajo ha sido realizado por el doctorando bajo la dirección de los directores de la tesis y hasta donde nuestro conocimiento alcanza, en la realización del trabajo, se han respetado los derechos de otros autores a ser citados, cuando se han utilizado sus resultados o publicaciones.

/

Guarantee, by signing this doctoral thesis, that the work has been done by the doctoral candidate under the direction of the thesis supervisors and, as far as our knowledge reaches, in the performance of the work, the rights of other authors to be cited (when their results or publications have been used) have been respected.

Granada, 17 de febrero de 2023

Directores de la Tesis / Thesis supervisors;

Claudio Marchesi José María González-Jiménez

Doctorando/Doctoral candidate

Erwin Schettino

Funding: The research presented in this Ph.D thesis has been funded by the BES-2017-079949 “Ayudas para Contratos Predoctorales para la Formación de Doctores” fellowship to Erwin Schettino associated with the project CGL2016-81085-R of the Ministerio de Economía, Industria y Competitividad de España. Additional fundings to research activity were provided by the Spanish projects PID2019-111715GB-I00/AEI/10.13039/501100011033 and RTI2018-099157-A-I00, and by the Junta de Andalucía research group RNM-131 and project FUMESA B-RNM-189-UGR18. Research grants, infrastructures, and human resources leading to this research have benefited from funding by the European Social Fund and the European Regional Development Fund.

a Mamma e Papà

a cui devo tutto

Abstract

Ore deposits are rock volumes with anomalously high concentrations of selected elements that enable their extraction with economic profit. Metallic ore deposits may form in a wide spectrum of geological conditions, although they mostly occur in the magmatic and hydrothermal environments. Despite extensive investigation aimed to clarify the genesis and distribution of magmatic-hydrothermal ores, major controversies still concern the processes that drive the transfer and storage of metals from background levels in their source region to exploitable amounts in the crust. A key unresolved aspect regards whether the ore-productive magmas inherit their metallogenic fertility from pre-enriched domains of the mantle source, or they attain high metal concentrations due to favorable fractionation conditions during magma percolation and ascent. This issue is especially important for targeting mineral camps, as it constrains the specific geological conditions and environments that enhance the metallogenic endowment of the continental crust. To this regard, a better knowledge of the mechanisms and repositories that control the mobility and storage of metals in mantle rocks and magmas is essential.

The general aim of this Ph.D. thesis is to assess the geological factors that govern the mobilization, transport, and concentration of chalcophile metals in the subcontinental lithospheric mantle (SCLM), emphasizing their impacts on the formation and distribution of magmatic-hydrothermal ore deposits in the overlying crust. To achieve this main goal, the thesis investigates the mineralogy, geochemistry and petrology of mantle peridotite xenoliths and associated volcanic rocks from mineralized regions in Central Mexico and Southeast Spain, focusing on base-metal sulfides (BMS), platinum-group minerals (PGM) and nano-to-micrometer-sized metal-rich particles as mineralogical-geochemical tracers of the behavior of precious and semi-metals in the SCLM. For this purpose, this study combines traditional analytical methods (e.g., transmitted/reflected light optical microscopy, scanning electron microscopy, electron microprobe analysis) with advanced techniques for the in-situ characterization of minerals (e.g., laser

ablation-(multicollector) inductively coupled plasma-mass spectrometry, high-resolution transmission electron microscopy).

The structure of the thesis comprises a general introduction to the research topics, followed by the description of aims and methods. Subsequently, the first chapter of the results section (Chapter 4) presents a mineralogical and geochemical study of BMS and silicates in mantle peridotite xenoliths from the Santo Domingo, Ventura-Espíritu Santo and Durango volcanic fields (Central Mexico). The obtained results support that these rocks record low degrees of partial melting in the stability fields of garnet (~ 2%) and spinel peridotites (~ 2-4%), and interaction with hydrous alkaline melts possibly during the Basin and Range extensional tectonism since Late Oligocene. Enclosed and intergranular grains of monosulfide solid solution (mss) in Santo Domingo peridotites are residues after the extraction of 0.1-0.5 fractions of Ni-Cu-rich sulfide melt during mantle melting events. On the other hand, globular sulfides (pentlandite ± chalcopyrite) hosted in glass veinlets in the Ventura-Espíritu Santo and Durango peridotites crystallized from Ni-Cu-rich droplets of sulfide melt, immiscible in the Quaternary silicate magmas that brought the xenoliths to the surface. Rhenium-depletion model ages extrapolated by Re-Os isotope analysis of these sulfide populations indicate that part of the SCLM of the Oaxaquia terrane (beneath Santo Domingo and Ventura-Espíritu Santo) originated in the Archean-Paleoproterozoic as the southernmost extension of the Laurentia craton, and was assembled with the Central terrane (beneath Durango) during the Grenville orogeny (~ 1.0 Ga). Early Paleozoic (~ 500 Ma) model ages common to sulfides from the peridotite xenoliths of the three volcanic fields suggest that the Oaxaquia-Central composite block split away from North America during the Rodinia break-up and experienced the Pan-African-Brasiliano orogeny that led to Gondwana assembly. During the Cenozoic, the reactivation of translithospheric faults bounding this composite old SCLM provided preferential pathways for focusing the ascent of ore-productive magmas/fluids associated with the subduction-related metallogeny of the Pacific active margin of Mexico.

The second chapter of the results section (Chapter 5) examines a suite of spinel peridotite xenoliths (plus one plagioclase-bearing) hosted in alkaline basalts from the Tallante volcanic field (Southeast Spain). Mantle metasomatism in fertile

lherzolites from Tallante caused the crystallization of clinopyroxene + orthopyroxene + spinel clusters due to the percolation of Miocene subalkaline melts during the westward migration of the subduction front in the western Mediterranean. In the Pliocene, heat and volatiles provided by alkaline host-magmas triggered very low melting degrees of metasomatic pyroxene-spinel assemblages, generating melt quenched to silicate glass and reactive spongy coronae around clinopyroxene and spinel. The refertilization event documented by the Tallante peridotites involved the precipitation of abundant base-metal sulfides currently included as spherical droplets within metasomatic clino- and orthopyroxene. These sulfide inclusions consist of pentlandite ± chalcopyrite ± bornite aggregates with homogeneous compositions in terms of major elements (Ni, Fe, Cu) and semi-metals (Se, As, Te, Sb, Bi), but with wide variability of platinum-group elements (PGE) fractionation ($0.14 < Pd_N/Ir_N < 30.74$). Furthermore, several grains of Pt-Pd-Sn-rich platinum-group minerals (PGM) and/or Au-particles were detected as euhedral nano-to-micrometer-sized inclusions within the BMS. The heterogeneous geochemical and mineralogical distribution of precious metals within the Tallante sulfides cannot be explained by conventional models of chalcophile partitioning from sulfide melt. Rather, these characteristics reflect the possible incorporation of distinct populations of BMS, PGM, and metal nanoparticles (especially of Pt, Pd, and Au) during mantle melting and/or melt percolation. Therefore, these results support that Miocene subalkaline melts released by asthenosphere upwelling upon slab tearing of the Iberian continental margin effectively produced metal-rich metasomatized domains within this sector of SCLM. Remarkably high Au concentrations in Tallante BMS (median 1.78 ppm) support that these metasomatized domains provided a fertile source of metals, especially gold, for the ore-productive Miocene magmatism of the westernmost Mediterranean.

The third chapter of the results section (Chapter 6) reports the presence of Pb-rich nanoparticles enclosed in BMS from metasomatized mantle peridotite xenoliths (Tallante volcanic field) and spatially/genetically associated lamproite dykes (Fortuna volcanic field) from the Neogene Volcanic Province of Southeastern Spain. These BMS document the journey of sulfide melt droplets extracted by partial melting of the SCLM and transported in silicate alkaline

magmas through the lithosphere. Nanoinclusions of galena in BMS have microstructural features that are inconsistent with their origin by low-temperature exsolution of PbS previously dissolved within the BMS crystal-lattice. Rather, these minerals likely crystallized from Pb(-Cu)-rich nanomelts originally immiscible within the sulfide liquid. This first mineralogical evidence of immiscibility between metal(Pb)-rich nanomelts and sulfide liquids challenges the traditional models of metal and sulfide transport in silicate magmas based solely on chemical solubility and chalcophile partitioning. Instead, these results require evaluating the role of surface-energy physical relationships between nanophases, sulfide liquids and silicate magmas in the transport and concentration of mantle-derived metals in the crust.

Keywords: *subcontinental lithospheric mantle, peridotite xenoliths, base-metal sulfides, platinum-group minerals, metal nanoparticles, chalcophile elements, Re-Os isotopes, magmatic-hydrothermal ore deposits.*

Resumen

Los depósitos minerales son volúmenes de roca con concentraciones anómalas de elementos que tienen valor económico. Los depósitos de minerales metálicos se pueden formar en un amplio espectro de ambientes geológicos, aunque predominantemente el magmático e hidrotermal. A pesar de la extensa investigación sobre el origen de estos yacimientos, existe aún mucha incertidumbre sobre los procesos que controlan la génesis y distibución de los depósitos magmático-hidrotermales en la corteza continental. En particular, aún queda por resolver si la formación de estos tipos de dépositos minerales está en primera instancia controlada por una fuente enriquecida en metales a partir de la cual se extraen los magmas parentales, o es resultado de la concentración eficiente y localizada a partir de una fuente con metales diseminados en muy baja concentración. A este respecto, una mejor comprensión de los mecanismos y repositorios que controlan la movilidad, el transporte y el almacenamiento de ciertos metales en las rocas del manto y los magmas es clave.

El objetivo general de esta tesis doctoral es evaluar los factores geológicos que gobiernan la movilización, el transporte y la concentración de metales calcófilos en el manto litosférico subcontinental (MLSC), enfatizando sus impactos en la formación y distribución de depósitos minerales de tipo magmático-hidrotermal en la corteza suprayacente. Para lograr este objetivo principal, la tesis investiga la mineralogía, geoquímica y petrología de xenolitos de peridotitas del manto y de rocas volcánicas asociadas procedentes de regiones mineralizadas de México central y del sureste de España. Se presta un énfasis especial al análisis de los sulfuros de metales base (SMB), minerales del grupo del platino (MGP) y partículas metálicas de tamaño nanométrico a micrométrico, usándolos como trazadores mineralógicos y geoquímicos del comportameniento de metales preciosos y semimetales en el MLSC. Para ello, se ha utilizado una combinación de métodos analíticos tradicionales (p. ej., microscopía óptica de luz transmitida/reflejada, microscopía electrónica de barrido, análisis por microsonda electrónica) con técnicas avanzadas para el análisis in situ de minerales (p. ej., espectrometría de masas con fuente de plasma inductivamente acoplado

(multicolector) y ablación láser, microscopía electrónica de transmisión de alta resolución).

La estructura de la tesis incluye una primera introducción general a los temas de investigación (Capítulo 1), seguida de una descripción de los objetivos (Capítulo 2) y métodos utilizados (Capítulo 3). Sucesivamente, el primer capítulo de la sección de resultados (Capítulo 4) presenta un estudio mineralógico y geoquímico de SMB y silicatos de xenolitos de peridotitas del manto procedentes de los campos volcánicos de Santo Domingo, Ventura-Espíritu Santo y Durango (México central). Los resultados obtenidos sugieren que estas rocas registraron bajos grados de fusión parcial en los campos de estabilidad de las peridotitas con granate (~ 2%) y espinela (~ 2-4%), y la interacción con fundidos alcalinos hidratados posiblemente durante la fase tectónica extensional del Basin and Range desde el Oligoceno tardío. Los granos de solución sólida monosulfurada incluidos en los silicatos de las peridotitas de Santo Domingo o intersticiales entre ellos son residuos de la extracción de 0.1-0.5 fracciones de fundido sulfurado rico en Ni-Cu durante eventos de fusión del manto. Por otro lado, los sulfuros globulares (pentlandita ± calcopirita) en venas de vidrio en las peridotitas de Ventura-Espíritu Santo y Durango cristalizaron a partir de gotas de fundido sulfurado rico en Ni-Cu, inmiscibles en los magmas silicatados Cuaternarios que transportaron los xenolitos a la superficie. Las edades modelo obtenidas a partir del análisis de isótopos de Re-Os en estos sulfuros indican que parte del MLSC del terreno Oaxaquia (debajo de Santo Domingo y Ventura-Espíritu Santo) se originó en el Arcaico-Paleoproterozoico como extensión más meridional del cratón de Laurentia, y se ensambló con el terreno Central (debajo de Durango) durante la orogenia Grenville (~ 1.0 Ga). Las edades modelo del Paleozoico temprano (~ 500 Ma) comunes a sulfuros en las peridotitas de los tres campos volcánicos sugieren que el bloque compuesto Oaxaquia-Central se separó de América del Norte durante la ruptura de Rodinia, y experimentó la orogenia Panafricana-Brasiliana que produjo el ensamblaje de Gondwana. Durante el Cenozoico, la reactivación de las fallas translitosféricas que limitan este MLSC antiguo proporcionó los canales preferenciales para el ascenso de magmas/fluidos productores de menas metálicas durante la subducción debajo del margen Pacífico de México.

El segundo capítulo de la sección de resultados (Capítulo 5) examina un conjunto de xenolitos de peridotitas con espinela (más una con plagioclasa) encajados en los basaltos alcalinos del campo volcánico de Tallante (sureste de España). La percolación de fundidos subalcalinos metasomáticos en el Mioceno provocó la cristalización de agregados de clinopiroxeno + ortopiroxeno + espinela en lherzolitas fértiles durante la migración hacia el oeste del frente de subducción en el Mediterráneo occidental. En el Plioceno, el aporte de calor y especies volátiles por los magmas alcalinos encajantes causó tasas muy bajas de fusión de los agregados metasomáticos de piroxeno-espinela, generando fundidos silicatados que se enfriaron dando lugar a vidrio rico en silice y alcalis y coronas de reacción alrededor de clinopiroxeno y espinela. El evento de refertilización registrado en las peridotitas de Tallante conllevó la precipitación de abundantes sulfuros de metales base que ahora se encuentran como inclusiones sólidas en clino- y ortopiroxeno metasomáticos. Estas inclusiones sulfuradas consisten en agregados de pentlandita ± calcopirita ± bornita con una composición homogénea en términos de elementos mayores (Ni, Fe, Cu) y semimetales (Se, As, Te, Sb, Bi), pero con un fraccionamiento muy variable entre los elementos del grupo del platino (EGP) ($0.14 < Pd_N/Ir_N < 30.74$). Asimismo, se identifican abundantes inclusiones euhédricas de minerales del grupo del platino (MGP) ricos en Pt-Pd-Sn y partículas de Au en el interior de los SMB. Dicha distribución geoquímica y mineralógica de los EGP en los sulfuros no puede explicarse mediante modelos convencionales de fraccionamiento de elementos calcófilos en fundidos sulfurados. Más bien, estas características reflejan la posible incorporación mecánica de distintas poblaciones de SMB, MGP y nanopartículas metálicas (especialmente de Pt, Pd y Au) durante la fusión del manto y/o la percolación de fundidos. Por lo tanto, estos resultados respaldan que los fundidos subalcalinos, producidos en el Mioceno por el ascenso de la astenosfera debido a la ruptura del margen continental Ibérico subducido, generaron dominios metasomaticos enriquecidos en metales preciosos dentro de este sector de MLSC. Las altas concentraciones de Au en los SMB de las lherzolitas de Tallante (concentración mediana = 1.78 ppm) sugieren que estos dominios metasomatizados proporcionaron la fuente fértil de metales, especialmente oro, que dió lugar durante el Mioceno tardío a los magmas parentales de los depósitos minerales en el Mediterráneo occidental.

El tercer capítulo de la sección de resultados (Capítulo 6) documenta la presencia de nanopartículas ricas en Pb incluidas en SMB de xenolitos de peridotitas metasomatizadas del manto (campo volcánico de Tallante) y diques de lamproítas asociadas espacial y genéticamente (campo volcánico de Fortuna) de la Provincia Volcánica Neógena del Sureste de España. Estos SMB cristalizaron a partir de gotas de fundido sulfurado extraídas por fusión parcial del MLSC, que luego fueron transportadas fisicamente en magmas alcalinos silicatados a lo largo de toda la sección litosférica. Las nanoinclusiones de galena en SMB poseen características nanoestructurales inconsistentes con un origen por exsolución a baja temperatura de PbS originalmente disuelto en la estructura del SMB. Más bien, éstas cristalizaron a partir de nanofundidos ricos en Pb (y Cu) originalmente inmiscibles en el líquido sulfurado. Esta es quizás la primera evidencia mineralógica de inmiscibilidad entre nanofundidos ricos en metales (Pb) y líquidos sulfurados en la naturaleza, y desafía los modelos tradicionales de transporte de metales y sulfuros en magmas silicatados, basados únicamente en la solubilidad química y la partición de tipo calcófilo. En cambio, estos resultados requieren evaluar el impacto de las relaciones físicas basadas en la energía superficial entre nanofases, líquidos sulfurados y magmas silicatados en el transporte y la concentración de metales derivados del manto en la corteza.

Palabras clave: *manto litosférico subcontinental, xenolitos de peridotitas, sulfuros de metales base, minerales del grupo del platino, nanopartículas de metales, elementos calcófilos, isotopos de Re-Os, depósitos minerales magmático-hidrotermales.*

Acknowledgments

I'll always be grateful and indebted to **Claudio** and **José María**. There is no enough limoncelli to bring you from Italy to prove out my gratitude for letting me have enjoyed my job during these almost five years of PhD. I don't think I could have had better people as for scientific directors and human mentors.

I am very grateful to **Fernando Gervilla** and **Carlos Garrido**. Each conversation with them has been a priceless source of knowledge and stimulating feedback, which strenghted my expertise and largely improved the research presented in this thesis. Moreover, I am indebted to **Edward Saunders**, for his precious willingness and the huge amount of high quality analytical data that he contributed to provide for the elaboration of this study.

Special thanks go to **Károly Hidas**, **José Alberto Padrón Navarta** and **Carmen Rodríguez Ruiz de Almodóvar**, for their unconditional support and comfort during my moments of despair. By the way, I don't really know if I could have achieved such PhD position without **José Alberto**'s (**Claudio**'s as well) unlimited patience in explaining me carefully all that burocratic mess during my application. I also wish to show my gratitude to **Antonio Acosta Vigil**, who was committed to this Ph.D project from the beginning as tutor, especially for his help with official paperwork.

I want to acknowledge **Michel Grégoire**, **Oscar Laurent** and **Mathieu Leisen**, as I really enjoyed spending days on lab analysis and brain storming sessions with you there in Toulouse. You made me feel as part of your group and I really appreciated that.

I am also very grateful to **Stefano Poli**, for the strong expertise he gave to me before to undertake the research career and for being always available for a consult or update on my scientific dilemmas.

I also want to thank all the technicians of the IACT and CIC facilities, in particular **Isa** (how many laughter), **Inma**, **María del Mar**, **Alpiste**, **Miguel Ángel**, as well as **Xavi** from the Universitat de Barcelona, just for made me learn

and enjoy (a lot) at the same time during my lab sessions. **Isa** still owes me a salsa dancing and I don't forget that.

Quiero agradecer enormemente todos mis estupendos compañeros y amigos del IACT y de la Facultad de Ciencias, por todos los buenos momentos que hemos compartido juntos, por saber como transmitir tanta alegría y poder convertir cualquier drama en una risa: **Adri**, **Igor**, **Javi**, **Bob**, **Sarita**, **Álvaro**, **Rubén**, **Manu**, **Ceci**, **Jon**, **Manolis** y **Marievi** y su estupendo hijo, **Claudia**, **Dimitri**. Todos llevais un sol por dentro y os quiero mucho. Desde luego no puedo no agradecer a **Antonio** y **Meri**, por hacerme siempre empezar cada día de trabajo con una sonrisa.

Dedico un agradecimiento especial a **Vanesa**, mi amiga, mi hermana y compañera de piso y de miles de aventuras, por haber vivido conmigo esta experiencia con tanta ilusión y empatía.

Ringrazio su tutto la mia famiglia, in special modo **Mamma**, **Papà**, mia sorella **Maddy**, nonna **Rosetta**, zio **Gae**, per tutto il vostro amore e appoggio che ricevo costantemente.

Por último, quiero agradecer a **Sara**, mi estupenda novia. Esta tesis lleva mucho de ti, del amor que tú me das y del que yo te doy. Ti amo.

Table of contents

Part I – Introduction, aims, thesis structure and methods

Part II – Results

Part III – Conclusions

Part IV – References

"In one aspect the science of mineral deposits is frankly utilitarian, but from the viewpoint of pure knowledge it records the principles governing the cycles of concentrations of the elements and the manifold complexity of the Earth."

(Lindgren, 1933)

Part I

Introduction, aims, thesis structure and methods

1. Introduction

1.1 Conceptual models in metallogeny

An ore deposit is a rock volume with abundances of one or more elements that permit their extraction with economic profit under the prevailing conditions of commodity prices, costs and technology (Misra, 2012). For certain elements of economic interest, average concentrations in the continental crust range from tens parts-per-million (e.g., Ni, Zn, Cu and Pb) to less than one part-per-billion (e.g., platinum-group elements, PGE: Os, Ir, Ru, Rh, Pt and Pd) (Table 1.1; Wedepohl, 1995). Hence, the minimum concentrations required to exploit economically these metals (i.e., their *cut-off grades*) are generally ten to thousands of times higher than their average abundances in the continental crust (Table 1.1).

Table 1.1. Average concentrations of certain elements in the continental crust (Wedepohl, 1995), compared with cut-off grades and approximative concentration factors required for an ore mineralization to be exploited with economic profit (modified after Arndt et al., 2017).

Element	*Average abundance*	*Cut-off grade*	*Concentration factor*
Al - aluminum	7.96 wt.%	30 wt.%	3-4
Fe - iron	4.32 wt.%	50 wt.%	10
Zn – zinc	65 ppm	5 wt.%	800
Ni - nickel	56 ppm	2 wt.%	400
Nd - neodymium	27 ppm	1 wt.%	400
Cu - copper	25 ppm	1 wt.%	400
Pb - lead	14.8 ppm	5 wt.%	3500
U - uranium	1.7 ppm	1 wt.%	5000
Mo - molybdenum	1.1 ppm	0.1 wt.%	1000
Ag - silver	70 ppb	0.1 wt.%	15’000
Au - gold	2.5 ppb	6 ppm	2500
Pt - platinum	0.4 ppb	5 ppm	12’000

Metallic ore deposits have been forming over the Earth’s history in a wide spectrum of sedimentary, magmatic, hydrothermal and metamorphic environments. These deposits have been traditionally classified into genetic types

based on the specific features that characterize the ores themselves and their geotectonic setting (Fig. 1.1; Arndt et al., 2017). The orthomagmatic group encompasses mineralizations originated by the crystallization of magmas, leading for example to the formation of exploitable chromite, PGE reefs, Ni-Cu-PGE sulfide and V-bearing magnetite in mafic-ultramafic layered intrusions, or Ni-rich sulfide in Archean komatiitic extrusions. On the other hand, magmatic-hydrothermal ore deposits precipitate from hydrothermal fluids exsolved from intermediate to felsic subvolcanic intrusions, mainly at convergent margins, such as porphyry Cu-Mo(-Au), epithermal Au-Ag, iron oxide-copper-gold (IOCG), Pb-Zn-Cu-Ag volcanogenic massive sulfides (VMS) and Sn-W pegmatites (Fig. 1.1).

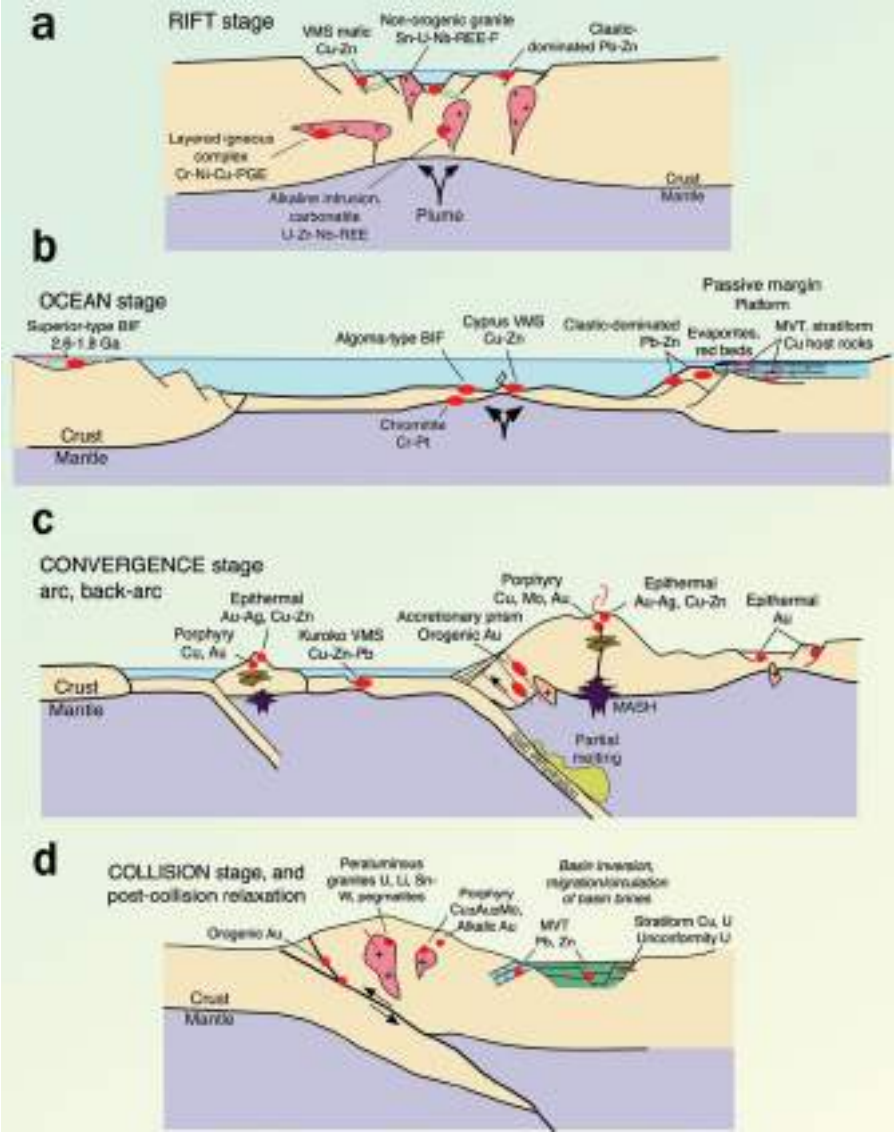

Figure 1.1. Schematic classification of ore deposit types within their plate tectonic settings (after Arndt et al., 2017).

The *deposit model* traditionally applied in mineral exploration mostly seeks to define the geological characteristics that are specific of each deposit, such as the physical (e.g., temperature, pressure) and chemical properties of the host rocks and the mineralizing media responsible for the deposition of the ores. Hence, this approach to regional exploration searches for the structural, geochemical and mineralogical fingerprints that are distinctive of each deposit type. However, these deposit-scale models fail to provide efficient tools for predicting the locations of hidden mineral camps, as they lack holistic conceptual frameworks that link the genesis of mineralizations to the large-scale geological evolution (Groves et al., 2022). In particular, this approach does not explain why ore deposits tend to concentrate in specific areas of the Earth's crust (Fig. 1.2), forming clusters or linear belts during restricted intervals of the geological time (i.e., metallogenic provinces; Kerrich et al., 2005; Sillitoe, 2012).

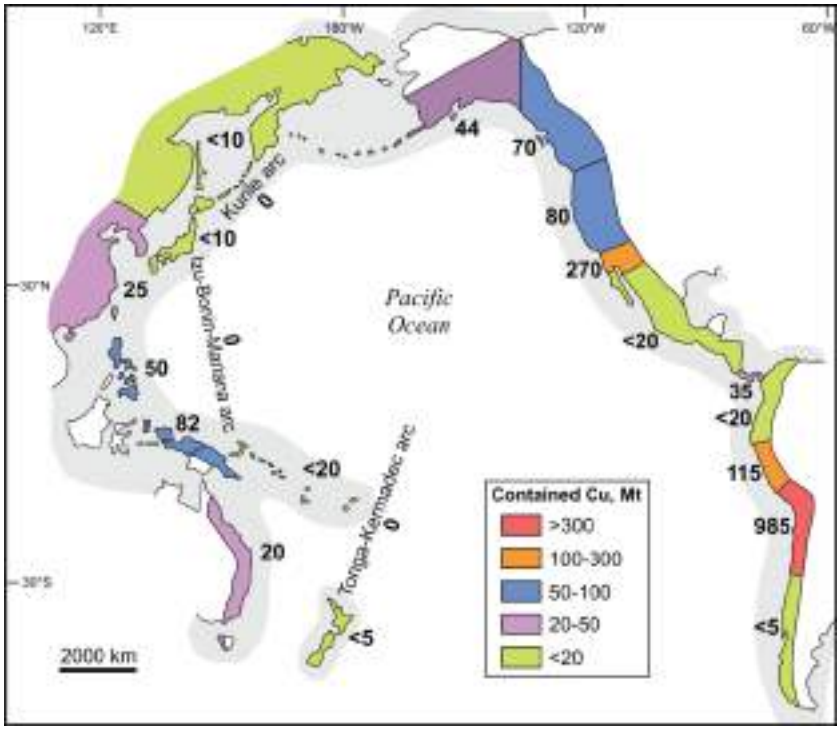

Figure 1.2 . Heterogeneous distribution of total copper endowment of different arc segments of the circum-Pacific Ring of Fire subduction system (after Sillitoe, 2012).

The recognition of this non-uniform space-time distribution, together with the discovery of common geological factors controlling the ore genesis across different deposit types, fostered the development of holistic *mineral system*

models (Wyborn et al., 1994). These models consider the formation of ore deposits as the local expression of ordinary geological processes that operate on a much larger scale and time frame than those considered in traditional deposit-scale models, and which predispose a specific lithospheric region to be endowed with metal resources (McCuaig et al., 2010; Richards, 2013; Wilkinson, 2013; Hagemann et al., 2016). The mineral system analysis has been especially developed for interpreting the genesis of magmatic-hydrothermal ore deposits at convergent margins (e.g., Hronsky et al., 2012), and then has been applied to other types of ore deposits and geodynamic settings (e.g., orthomagmatic ore deposits, Barnes et al., 2016). In fact, the mineral system approach focuses on critical processes that are common to different geological systems, and makes the formation of ore deposits conditional on the following critical factors: 1) a *favorable lithospheric architecture* providing preferential pathways for ore-productive magmas/fluids; 2) a *fertile source* for feeding the cargoes of metals and ligands (e.g., S, Cl, H_2O, CO_2); 3) a *transient remobilization event* triggering the migration of melts/fluids that transfer metals towards a chemical/mechanical trap in the crust. Therefore, the *mineral system analysis* defines *Architecture*, *Fertility* and *Transfer*, together with post-mineralization *Preservation*, as the main geological components dictating the distribution of ore deposits through the space-temporal evolution of the Earth (Fig. 1.3).

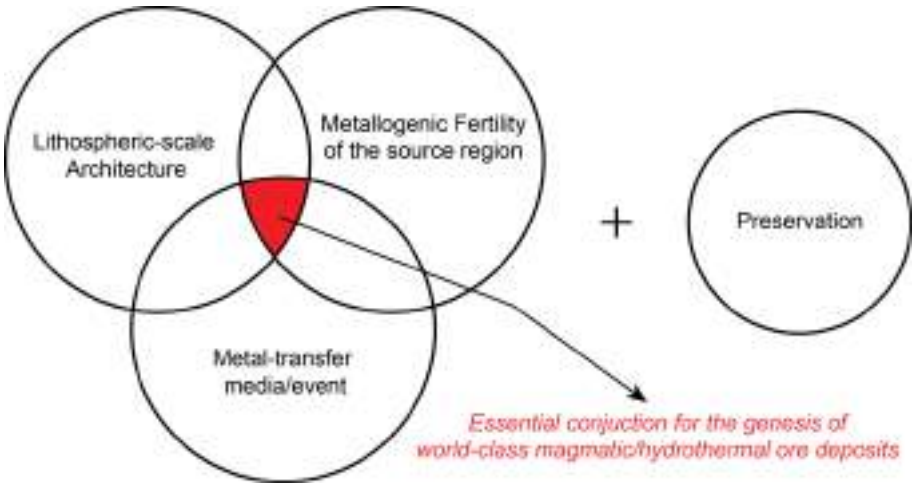

Figure 1.3. Schematic illustration of the conjunction of four independent parameters required to form and preserve world-class hydrothermal and/or magmatic ore deposits. Modified after Hronsky et al. (2012).

In this renewed view of metallogeny, ore deposits are local manifestations of large-scale systems of mass and energy flux whereby extremely efficient geological processes jointly concentrate metals in a small volume of rock (Begg et al., 2010; Hronsky et al., 2012; Hagemann et al., 2016). The ore-forming systems primarily require the dynamic advective transport of magmas and/or fluids that regulate the selective enrichment of economic elements through multiple transient pulses (McCuaig and Hronsky, 2014). A key ingredient of the mineral system model is a localized physical and/or geodynamic permeability barrier that prevents the mass and energy flux associated with such transport from dissipating to the final sink, and that progressively enhances an energy gradient (Fig. 1.4; McCuaig and Hronsky, 2014). These *threshold barriers* act over long periods as lenses magnifying the transport, fractionation and concentration of metals, and once disrupted they transform to *gateways* allowing metal release towards the final depositional zone through short-lived transient episodes (i.e., *avalanches*; McCuaig and Hronsky, 2014).

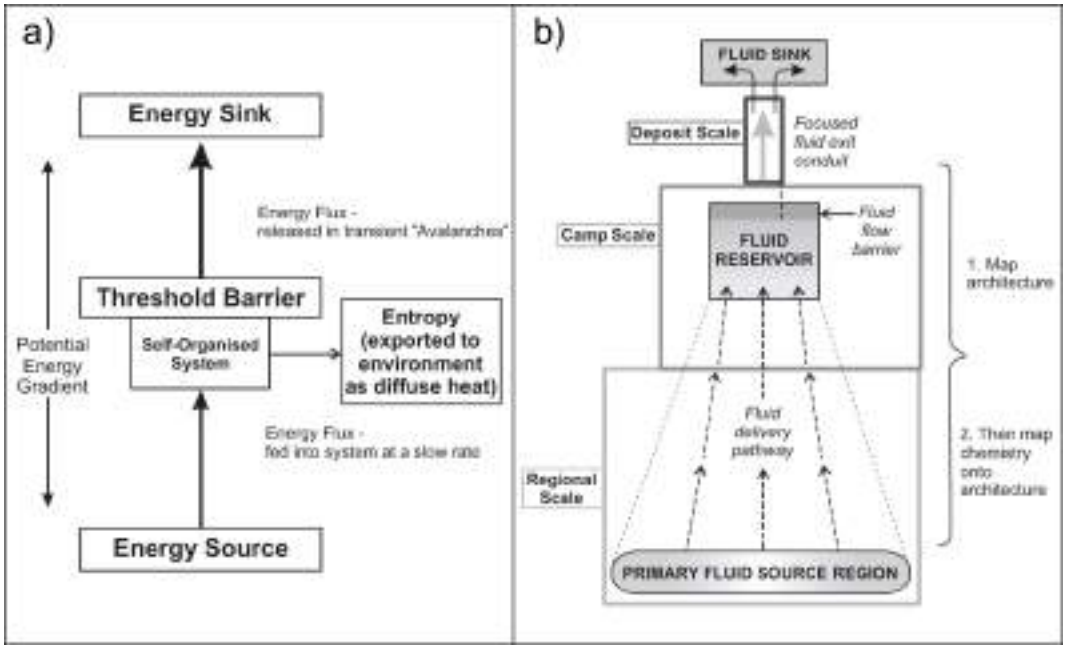

Figure 1.4. Schematic conceptual model for a mineral system applied to ore genesis (after McCuaig and Hronsky, 2014).

Therefore, according to the mineral system model, ores form during episodic events within a long-lived background evolution that predisposes a

specific geologic region to experience focused pulses of ore-forming flux once the physical/geodynamic threshold barrier is overcome (Fig. 1.5).

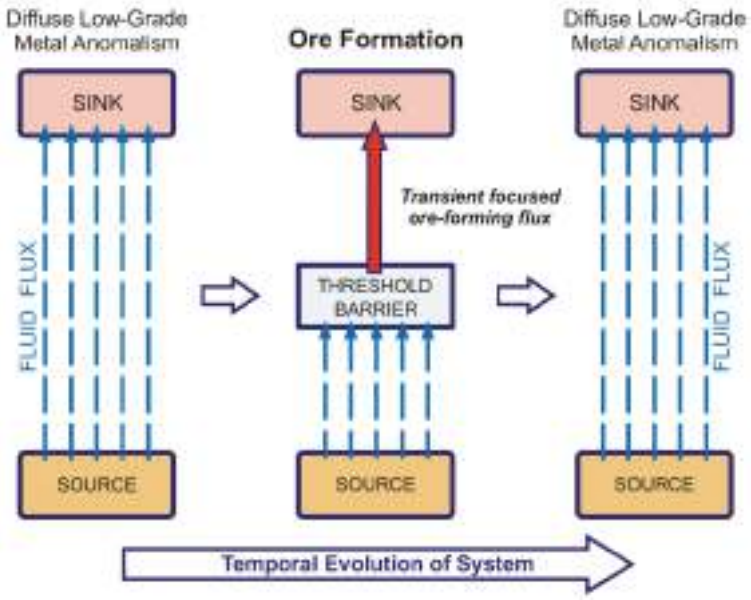

Figure 1.5. Schematic evolution of ore-forming systems whereby ore deposition takes place during brief temporal windows within much longer geologic history (McCuaig and Hronsky, 2014).

1.2 Ingredients of the mineral system model used in exploration targeting

1.2.1 Architecture of the lithosphere

The lithosphere is the outer, highly viscous and cold "skin" of the Earth where heat is transferred by conduction rather than convection as occurs below the *thermal boundary layer* (Fig. 1.6; McKeinze, 1969). The base of the lithosphere approximately coincides with the depth at which a conductive geotherm intersects the mantle isentropic adiabat, typically between 1200-1300 °C (Fig. 1.6), marking the transition from a conductive and rheologically strong lithospheric mantle to a convective and weak asthenosphere capable to flow (Anderson, 1995; Condie, 2022). These thermal properties induce the rigid mechanical behavior of the lithosphere (i.e., *mechanical boundary layer)* such that elastic stresses are

transmitted towards major discontinuities between lithospheric plates that move coherently over the convective mantle (McKenzie et al., 2005; Artemieva, 2009).

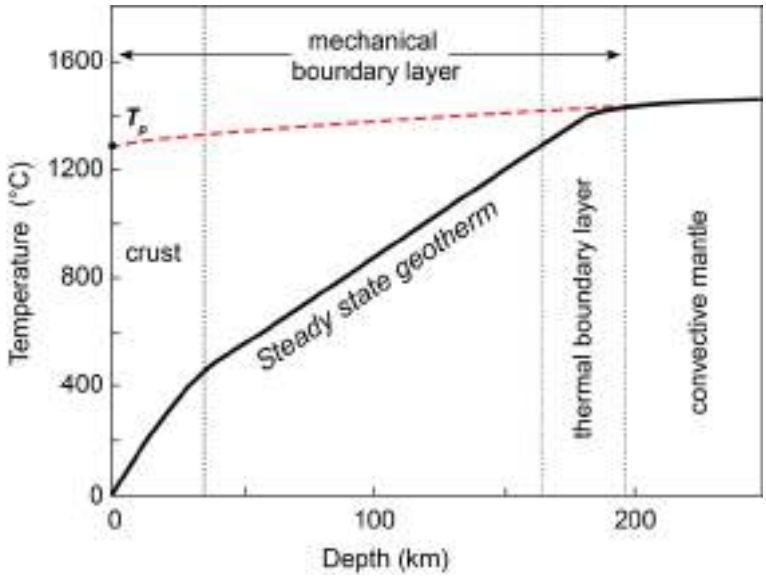

Figure 1.6. Thermal and rheological structure of the lithosphere, showing the mantle potential temperature (T_p) representative of the extrapolation of isentropic adiabat (dashed red line) to the surface. Modified after McKeinze (2005).

The lithosphere includes the crust and the underlying lithospheric mantle that is dominantly made of peridotite, a rock mainly composed of olivine, orthopyroxene, clinopyroxene and an Al-rich mineral, i.e. plagioclase, spinel or garnet with increasing depth (Ringwood, 1962; Pearson et al., 2003). The lithospheric mantle that underlies the continental crust is generally thicker and older than its oceanic counterpart (Fig. 1.7; Jordan, 1975; Carlson et al., 2005), because the latter is continuously created along spreading ridges as the upwelling asthenosphere undergoes decompression partial melting (Johnson et al., 1990). As the oceanic lithosphere ages and migrates away from the spreading ridge, it becomes increasingly cold, thick (up to ~ 100 km) and dense, so that is doomed, before ~ 200 million years, to sink into the convective mantle at convergent plate boundaries. On the other hand, the continents are underlain by a low-density, thick (> 200 km) and old Subcontinental Lithospheric Mantle (SCLM) originally formed during the early-stages of mantle-crust differentiation in the Archean (> 2.5 Ga; Griffin et al., 2009; Capitanio et al., 2020; Pearson et al., 2021).

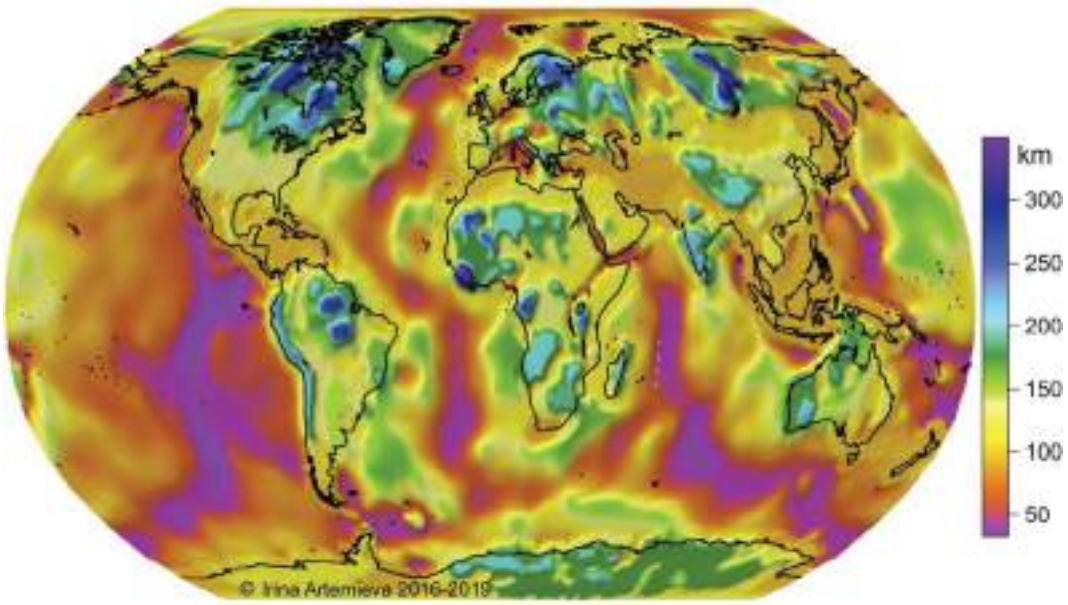

Figure 1.7. Geographic distribution of lithosphere thickness based on S-wave velocity profiles in the upper mantle (Artemieva, 2009).

The low-density composition of the ancient SCLM mainly comes from high melting degrees experienced by the primitive mantle to originate the Archean continental masses (i.e., the cratons), which left a refractory residuum depleted in iron. Importantly, such a buoyant and rigid lithospheric root beneath Archean cratons impedes them to sink into the asthenosphere, favoring the long-term stability of ancient continental crust (Jordan, 1978). Cratonic nuclei of Archean age are commonly bounded by younger, Proterozoic (~ 0.6-2.5 Ga) to Phanerozoic (< 600 Ma), off-craton continental crust underlain by thinner (~ 100-200 km) and less depleted SCLM (Fig. 1.7). In general, the SCLM in off-craton regions is more fertile and thinner with decreasing age of the first major tectono-thermal event in the overlying crust, pointing out a long-term crust-mantle coupling over the Earth's history (Griffin et al., 1999; Pearson et al., 2007; Pearson and Wittig, 2014).

The heterogeneous architecture of the SCLM exerts a first-order control on the distribution of ore mineralizations in the crust, as it determines the locus of trans-lithospheric plumbing systems of mass and energy flux that enhance the concentration of metals in specific crustal domains (Begg et al., 2010; Griffin et

al., 2013). This control is particularly highlighted by the distribution of magmatic-hydrothermal ore deposits in the subduction systems around the Pacific Ocean (Fig. 1.2; Groves et al., 2021). At the tectonic-scale of mineral system analysis, these world-class magmatic-hydrothermal ores are genetically connected as they all formed during the progressive evolution of subduction-related magmatism (Groves et al., 2019). However, at these and other convergent margins, mineralized provinces usually cluster into specific arc segments (Sillitoe, 2012), especially those located close to ancient lithospheric blocks (Pettke et al., 2010; Hou et al., 2017; Groves and Santosh, 2021). This irregular distribution of mineralized provinces stems from the presence of discrete fragments of Archean continental lithosphere separated from younger domains of arc-related lithosphere by major trans-lithospheric faults connecting the crust with their mantle roots (Lee et al., 2001; Griffin et al., 2011; Hronsky et al., 2012; González-Jiménez et al., 2013; Hou et al., 2015; Xu et al., 2021). Therefore, the margins of Archean SCLM represent inherited boundaries of great rheological contrast and structural weakness, which provide the preferential pathways for the upward flux of mineralizing magmas and/or fluids (Fig. 1.8; Hou et al., 2017; Groves et al., 2021; Wiemer et al., 2022).

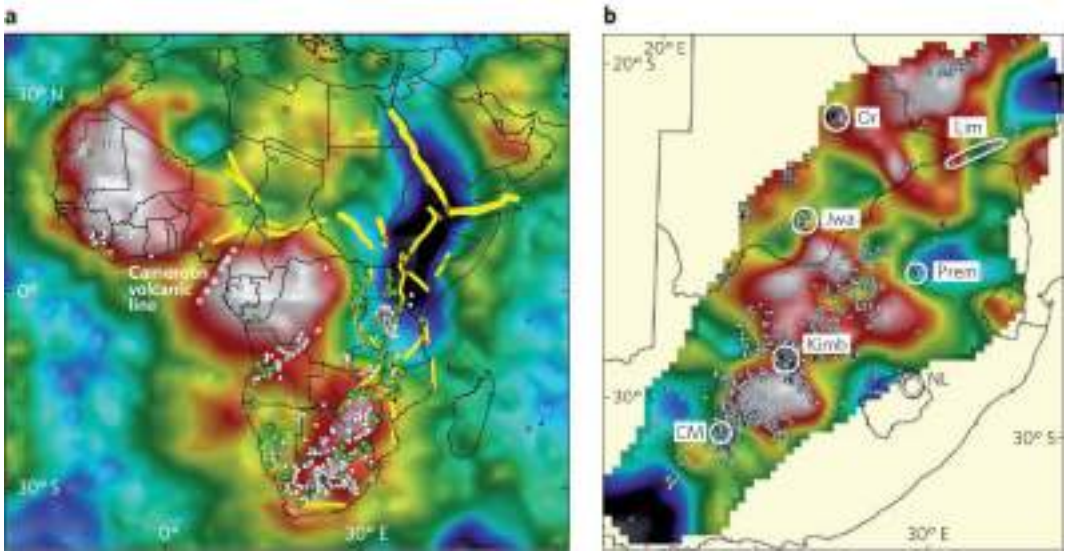

Figure 1.8. a) Distribution of kimberlite (white dots), carbonatite (green circles) magmas and major rift systems (yellow lines) relative to the S-wave velocity structure and cratonic blocks of Africa; b) detailed seismic tomography at 200 km depth of the Kaapval craton, showing the location of volcanic centres around the margins of high velocity regions (Begg et al., 2009; Griffin et al., 2013).

The key-role of the SCLM architecture on governing the spatial patterns of ore mineralizations is further illuminated by the correspondence between the global-scale distributions of major Ni-Cu(PGE-rich) sulfide deposits and the margins of Archean cratons (Fig. 1.9; Kerrich et al., 2005; Begg et al., 2010, 2018; Griffin et al., 2013; Mole et al., 2015).

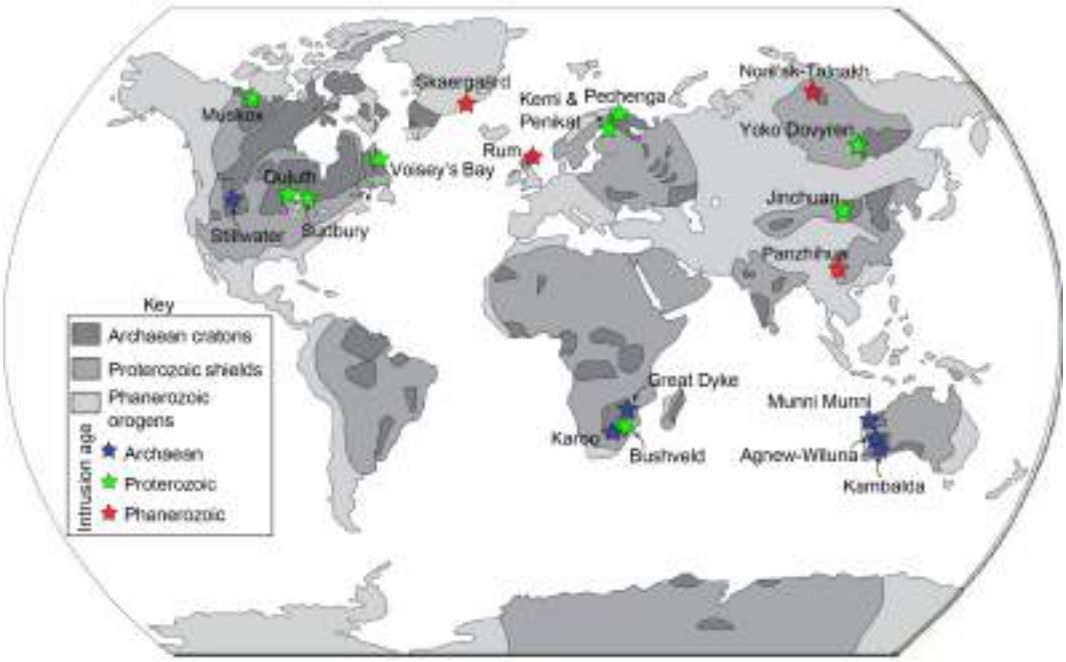

Figure 1.9. a) Global distribution of major Ni-Cu(-PGE) mineral camps associated with large igneous intrusions (LIPs) and/or komatiite extrusions and inferred boundaries of Archean cratons (modified after O'Driscoll & VanTongeren, 2017; Begg et al., 2018; Chistyakova et al., 2019).

These magmatic ore deposits were fed by parental magmas of large igneous provinces (LIPs) and/or komatiitic lavas sourced from asthenospheric plumes (Keays, 1995; Fiorentini et al., 2010; Barnes et al., 2015). As the upwelling plume heads impacted the base of thick (> 200 km) cratonic SCLM, they deviated towards areas of thinnest continental lithosphere (Fig. 1.10; Begg et al., 2010, 2018) promoting higher degrees of mantle melting (Barnes et al., 2016). These tectonic boundaries evolved as trans-lithospheric fault systems that enhanced the focused and rapid rise of large volumes of ore-productive primitive magmas (e.g., komatiites, picrites) towards the crust (Mole et al., 2015).

Importantly, plume-sourced LIPs and continental flood basalts erupted in younger crustal terranes are generally barren of relevant mineralizations (Zhang et al., 2008). Hence, mapping the regional distribution of ancient Archean lithospheric blocks is especially important for targeting the loci of both orthomagmatic and magmatic-hydrothermal ore deposits. However, the global SCLM architecture may be much more puzzling than expected if we assume the long-lasting dichotomy between thick, old and highly depleted cratonic SCLM *vs.* thin, younger and more fertile off-craton SCLM. Several isotopic studies have reported that off-craton regions of Proterozoic/Phanerozoic upper crust are underlain by Archean-age lower crust (e.g., Zheng et al., 2004, 2006) and/or SCLM (e.g., Lee et al., 2001; Begg et al., 2009; Griffin et al., 2009, 2011; McCoy-West et al., 2013; Scott et al., 2021). These findings indicate that many portions of SCLM underlying off-craton continental crust are Archean cratonic SCLM that was pervasively reworked and refertilized during younger tectono-thermal events (Begg et al., 2009; Griffin et al 2009). Therefore, decoding the cryptic presence of Archean SCLM may provide key clues to predict the storage of metal resources throughout the geological evolution of the continents.

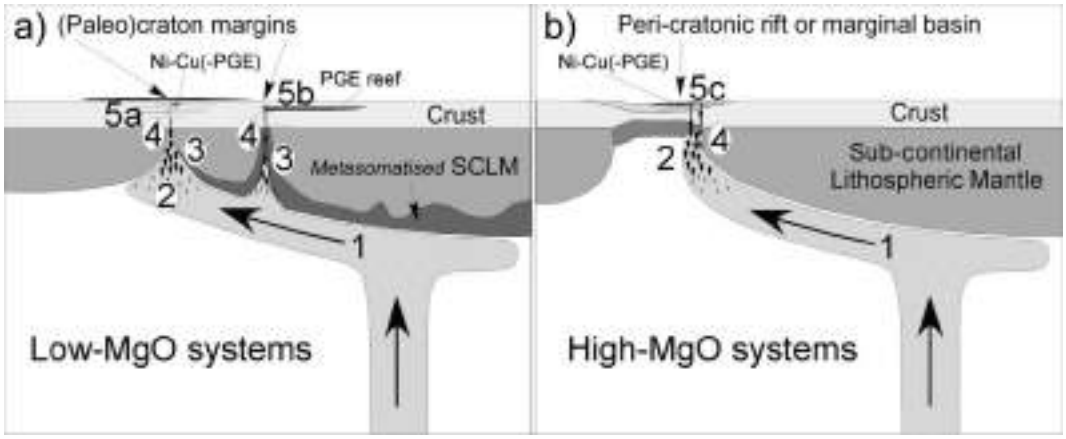

Figure 1.10. Generalized model for the formation of Ni-Cu(-PGE) and PGE reef deposits, involving: 1) mantle plume impact at the base of the SCLM and flow towards areas of thinner lithosphere; 2) decompression melting of asthenospheric mantle at shallow depths; 3) transfer of melts via active trans-lithospheric faults along craton margins; 4) variable interaction of upwelling melts with melt-fertile regions of the continental lithosphere; 5) Nickel sulfide precipitation and accumulation (Begg et al., 2018).

1.2.2 Source and fertility

Metallogenic *fertility* is defined as the stronger endowment with metals of a particular lithospheric region compared to other areas (Hronsky et al., 2012). This concept builds on the idea that ore-forming magmas are enriched in metals compared with "barren" magmas (Connors et al., 1993; Hedenquist and Lowenstern, 1994; Core et al., 2006; Park et al., 2019). In particular, several works pointed out that mineralizing magmas in subduction zones have a distinct geochemical signature compared to normal arc magmas (Hronsky et al., 2012; Loucks, 2014), supporting the hypothesis that mineralized domains in the upper continental crust inherit the metallogenic fertility of the underlying lower crust or lithospheric mantle (Bierlein et al., 2009; Sillitoe, 2012; Holwell et al., 2019). For example, epithermal sulfide ores at convergent margins have osmium isotopic compositions that match with those of the underlying SCLM, fingerprinting a link with a mantle source for the mineralizing fluids (McInnes et al., 1999; Mathur et al., 2000; Tassara et al., 2022). These observations support that metal-rich domains of the SCLM are a key ingredient for the genesis of a wide range of magmatic-hydrothermal ore deposits (Hronsky et al., 2012; Groves et al., 2019, 2021). Following this hypothesis, the ore-productivity of calc-alkaline to alkaline magmas associated with porphyry Cu-Au and epithermal Au mineralizations in subduction settings is generally ascribed to melting of metal-rich volumes of the subarc lithospheric mantle (Richards, 2009; Holwell et al., 2019; Chang and Audétat, 2023). Moreover, igneous rocks in LIPs with world-class orthomagmatic ore deposits, such as the Bushveld complex in South Africa, have Sr-Nd-Os isotope compositions indicative of an underlying metasomatized, cratonic SCLM (Richardson and Shirey, 2008; Zhang et al., 2008). Therefore, plume-related ore-forming melts of Bulshveld could have boosted their metallogenic productivity by interacting with fertile, metal-rich volumes of the cratonic SCLM (Richardson and Shirey, 2008; Zhang et al., 2008; Griffin et al., 2013).

According to these results, the SCLM exerts an active role on determining the metallogenic productivity of mineral systems in a wide range of geological environments. The core of this idea founds from the evidence that depleted SCLM may be replenished in incompatible elements, including ore-forming chemical components, by interaction with magmas/fluids ascending from the asthenosphere

(i.e., metasomatic refertilization, O'Reilly and Griffin, 2013). The metallogenic refertilization of the SCLM is especially efficient when thinned craton margins are bordered by subduction zones (Griffin et al., 2013; Begg et al., 2010, 2018). In fact, ongoing devolatilization of subducting oceanic lithosphere may supply fluids that transfer metals to the shallow continental lithosphere (Hou et al., 2017; Tassara et al., 2017; Fiorentini et al., 2018; Holwell et al., 2019; Chong et al., 2021). However, several works point out that extensive mantle interaction with subduction-related fluids or volatile-rich melts does not produce a metal-enriched SCLM (Saunders et al., 2018; Wang et al., 2019). Moreover, the crystallization of gold-rich minerals within fusible domains of the SCLM beneath auriferous crustal provinces is due to the percolation of asthenospheric melts (Fig. 1.11a; Tassara et al., 2017). These findings support that the metallogenic fertility of the SCLM is mostly controlled by refertilization via asthenosphere-derived melts rather than slab-derived hydrous fluids or volatile-rich melts, which in turn could act in a later stage as efficient media for scavenging metals towards the crust (Fig. 1.11b).

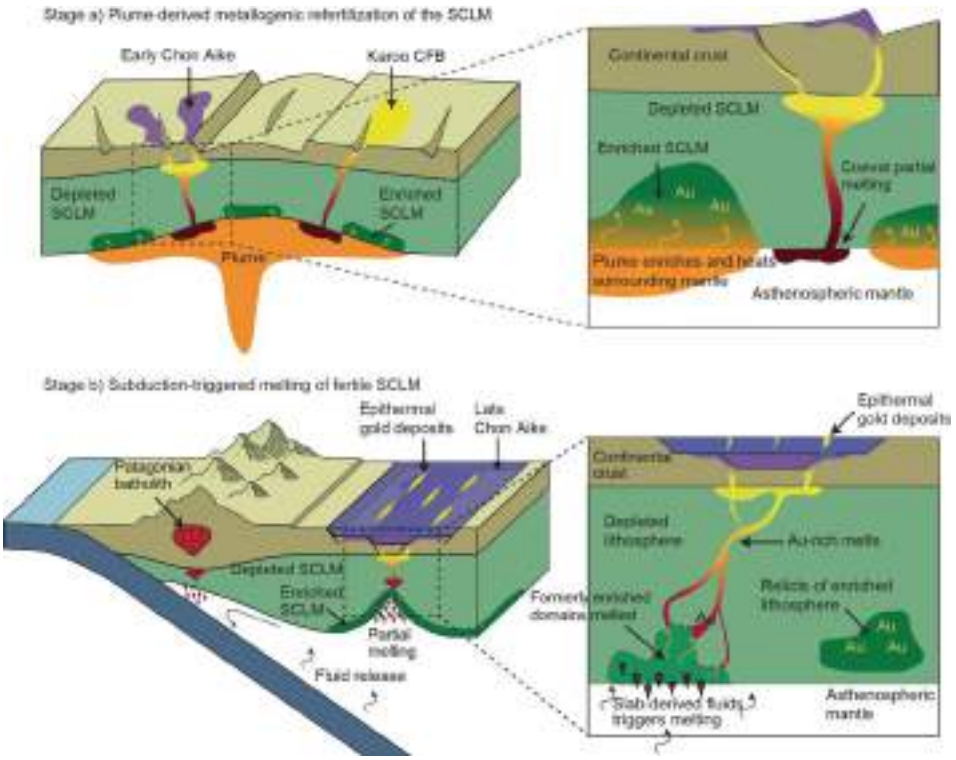

Figure 1.11. Lithospheric-scale processes involved in the generation of large auriferous provinces. Stage a): plume upwelling induces metasomatic Au enrichment in the overlying SCLM. Stage b): onset of the subduction zone provides fluids capable of scavenging Au from pre-enriched domains of the SCLM, generating ore-productive calc-alkaline magmas feeding gold mineralization in the crust (Tassara et al., 2017).

The heterogeneous metallogenic fertility of the SCLM is largely ascribed to the strong chalcophile (sulfide-loving) affinity of several base (Ni, Cu, Zn, Pb), precious (Au, Ag, PGE) and semi-metals (Te, As, Bi, Sb, Se), which causes their preferential partition within accessory (< 0.1 vol.%) base-metal sulfides (BMS, Mitchell and Keays, 1981; Alard et al., 2000; Lorand and Alard, 2001; Luguet et al., 2001; Lorand et al., 2008; Harvey et al., 2011, 2016; Aulbach et al., 2016; Lorand and Luguet, 2016). In particular, mantle peridotites may contain several generations of sulfides with distinct mineralogy, texture, PGE-Au concentrations and Re-Os isotopic signature (Alard et al., 2000, 2002; Lorand and Alard, 2001; Griffin et al., 2002, 2004; Aulbach et al., 2004; Lorand and Grégoire, 2006).

Traditional classification of sulfides in peridotites distinguishes between enclosed *vs*. interstitial BMS. Enclosed sulfides typically form rounded blebs of Ni-poor and Ni-rich monosulfide solid solution (mss) with minor pentlandite and chalcopyrite rims (Fig. 1.12a), which are interpreted as the exsolved products of former high-temperature mss (Alard et al., 2000). If they are included within refractory silicates (e.g., olivine), enclosed BMS normally have negatively-sloped chondrite-normalized PGE patterns enriched in most compatible I-PGE (Os, Ir, Ru), as expected for residual mss left after mantle melting (Fig. 1.12c; Alard et al., 2000; Bockrath et al., 2004; Ballhaus et al., 2006). However, mss with I-PGE-rich patterns may also constitute interstitial grains in glass pockets or within metasomatic minerals, suggesting that mantle sulfides may preserve their original PGE signatures during fluid/melt-mediated metasomatic remobilization (Aulbach et al., 2004; Lorand et al., 2004; González-Jiménez et al., 2014). On the other hand, interstitial BMS are commonly dominated by pentlandite-rich aggregates (Fig. 1.12b) with positively-sloped chondrite-normalized patterns enriched in most-incompatible P-PGE (Pt, Pd) and Au (Fig. 1.12c), interpreted as the cooling products of Cu-Ni-Fe sulfide melt produced by incongruent melting of mss (Alard et al., 2000; Bockrath et al., 2004; Ballhaus et al., 2006; Lorand and Grégoire, 2006). This type of sulfides may also constitute rounded inclusions within metasomatic silicates (Andersen, 1987; Lorand and Alard, 2001; Sen et al., 2010; Delpech et al., 2012). Moreover, interstitial sulfide veinlets enriched in Os, Pd, Au and Re may also precipitate from oxidizing, CO_2- and S-rich hydrous fluids by

sulfidation reactions with mantle peridotites (Alard et al., 2011; Delpech et al., 2012; Tassara et al., 2018).

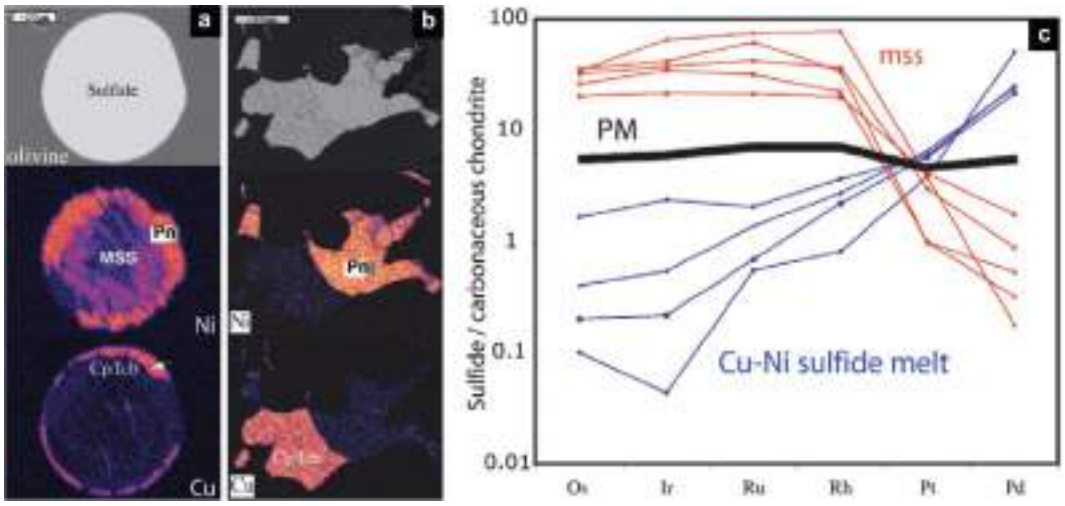

Figure 1.12. Backscatter electron images and elemental (Ni and Cu) X-ray maps of enclosed "residual" (a) and interstitial "metasomatic" (b) base-metal sulfides in mantle rocks, showing their typical chondrite-normalized platinum-group elements distributions (c) as determined by laser ablation in situ analysis (Lorand et al., 2008).

Base-metal sulfides do not always account for the whole budget of precious metals in mantle rocks, as PGE may also form their own platinum-group minerals (PGM) and/or metal alloys of nano-to-micrometer sizes (Keays et al., 1981; Luguet et al., 2007; Lorand et al., 2008, 2010; Ackerman et al., 2009; O'Driscoll and González-Jiménez, 2016; González-Jiménez et al., 2020). In their recent review, González-Jiménez et al. (2020) showed that Pt-Ir-Os alloys, laurite [RuS_2], erlichmanite [$(Os,Ir)S_2$] and cooperite [PtS] may dominate the bulk-rock PGE budget of mantle peridotites, especially in highly depleted volumes of refractory SCLM. Moreover, Pt-(Pd) bismuthotellurides and arsenides, such as moncheite [$PtTe_2$], merenskyite [$PdTe_2$] and sperrylite [$PtAs_2$], are singularly common within pervasively metasomatized peridotite xenoliths from fertile volumes of off-craton SCLM. The origin of these minerals has been traditionally ascribed either to complete consumption of pre-existing mss undergoing desulphurization upon high degrees (F > 25%) of mantle melting (in the case of Pt-Ir-Os alloys and laurite-erlichmanite; Peregoedova et al., 2004; Luguet et al., 2007; Lorand et al., 2010; Fonseca et al., 2012; Mungall and Brenan, 2014), or to

low-temperature exsolution from metasomatic BMS (in the case of Pt-Pd bismuthotellurides and arsenides; Lorand et al., 2008, 2010). However, recent findings reported that PGM and metal alloys may also crystallize from percolating silicate melts prior to or during the attainment of sulfide saturation (Sinyakova et al., 2016, 2019; González-Jiménez et al., 2019, 2020; Kamenetzky and Zelensky, 2020). These observations evidence that magmatic partitioning of precious and semi-metals may not always be ruled by canonical sulfide solubility models and chalcophile affinity, but by early formation of magmatic nano-to-micrometer-sized minerals.

The distribution and storage of precious metals and semi-metals in mantle peridotites are thus largely affected by the behavior of distinct populations of BMS, PGM and metal alloys during melting, melt percolation and mantle metasomatism (Lorand et al., 2013). The modification of the metallogenic budget of the SCLM during melt-rock interaction primarily depends on the composition of percolating melts/fluids and the melt-fluid/rock ratio. For instance, the upward migration of sulfide-undersaturated silicate magmas at increasing melt volumes usually removes interstitial BMS from the shallower portions of the SCLM, leading to a dramatic depletion of the metallogenic inventory of pervasively percolated mantle peridotites (Lorand and Alard, 2001; Ackerman et al., 2009; Wang et al., 2009; Lorand et al., 2013; Saunders et al., 2015). On the other hand, the interaction of mantle peridotites with small fractions of sulfide-saturated silicate melts at decreasing melt volumes typically yields supra-chondritic PGE relative abundances (van Acken et al., 2010), through the crystallization of interstitial Cu-Ni-rich BMS and/or bismuthotellurides/arsenides enriched in Pt, Pd and Au (Lorand and Alard, 2001; Luguet et al., 2003; Wang et al., 2009; van Acken et al., 2010; Alard et al., 2011; Tassara et al., 2018; Burness et al., 2020; González-Jiménez et al., 2020). In general, the extent of metal refertilization in mantle peridotites decreases with increasing proximity to the inferred melt conduit, reflecting the chromatographic fractionation of silicate melts upon reaction with peridotite wall-rocks (Fig. 1.13, Saunders et al., 2015). Finally, metasomatism by oxidizing fluids in supra-subduction mantle generally causes sulfide depletion and crystallization of mineral alloys and refractory PGM that selectively fractionate fluid-mobile PGE (e.g., Os and Pd; Kepezhinskas et al.,

2002, 2022; Siegrist et al., 2021; Chen et al., 2022). In summary, decoding the mineralogical and compositional effects of melting and metasomatism on the distribution and mobility of base, precious and semi-metals in mantle peridotites provides key constraints for assessing the metallogenic fertility of distinct volumes of the SCLM.

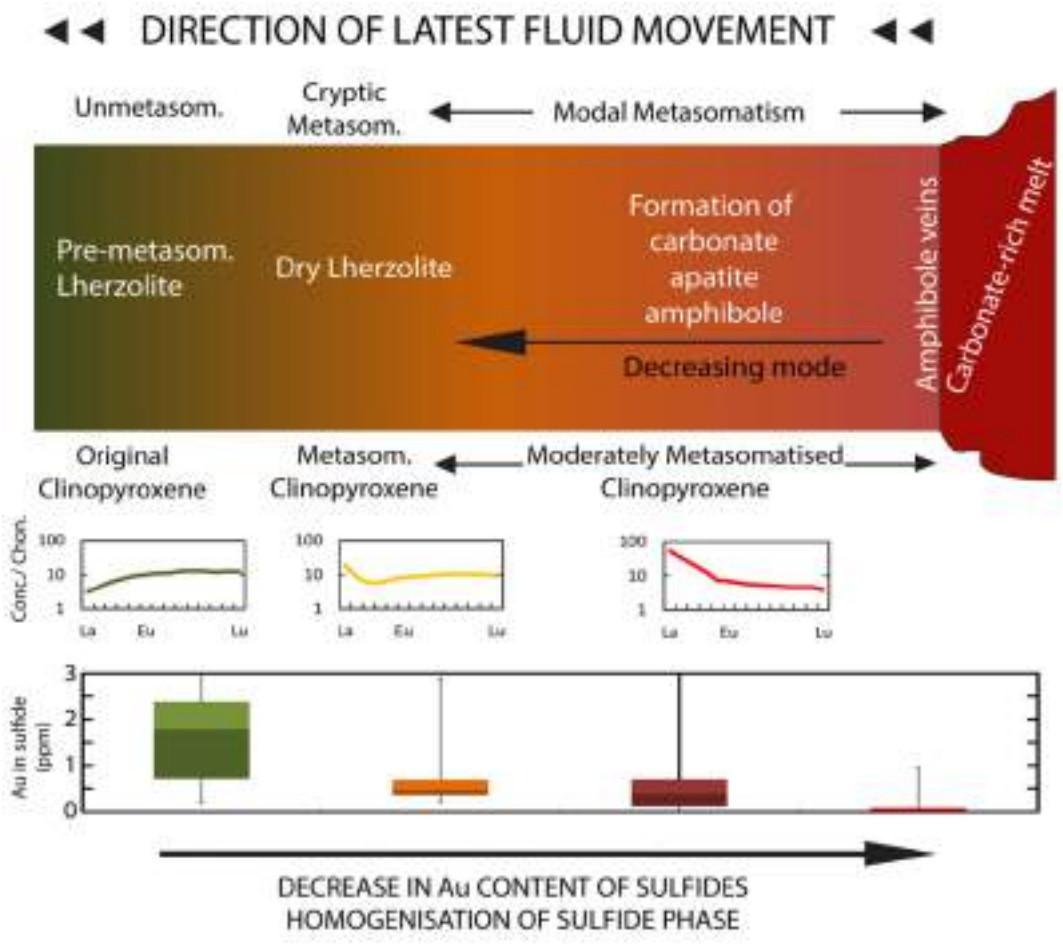

Figure 1.13. Cartoon model of chromatographic fractionation of silicate melts percolating through mantle peridotites. Plots indicate median chondrite-normalized rare earth-element patterns of clinopyroxene and the range of Au abundances through different xenolith lithologies (Saunders et al., 2015).

1.2.3 Metal-transfer media

Deposits of magmatic and hydrothermal sulfides are the most important sources of base (Ni, Cu, Zn, Pb) and precious (Au, Ag, PGE) metals, although the latter also significantly reside in chromitites from igneous layered intrusions (e.g., UG2

and Merensky reefs in the Bushveld complex) (Ballhaus and Sylvester, 2000; Cawthorn, 2010) or ophiolites (Gervilla et al., 2005). The key difference between deposits of magmatic and hydrothermal sulfides relies on the physical nature of the mineralizing medium at the time of deposition, i.e. a sulfide melt immiscible in silicate magmas or a volatile-rich hydrous fluid, respectively (Mungall, 2003). Volatile-rich hydrous fluids usually exsolve from evolved silicate magmas as they ascend to shallow crustal depths, owing to the decreasing solubility of volatile components (e.g., H_2O, CO_2) with decreasing pressure. Conversely, the solubility of sulfur S^{2-} (i.e., sulfide) in silicate melts exponentially decreases with increasing pressure, so that most mantle-derived magmas are initially saturated with sulfide (Mavrogenes and O'Neill, 1999). Therefore, ore-productivity of parental magmas in both magmatic and hydrothermal mineral systems is traditionally modeled based on the equilibrium partitioning of chalcophile metals between silicate and sulfide melts during magma segregation and ascent (Fonseca et al., 2009; Li and Audétat, 2012; Kiseeva and Wood, 2013; Mungall and Brenan, 2014; Zelenski et al., 2018; Chowdury et al., 2021; Li et al., 2021; Holwell et al., 2022).

The metallogenic endowment of mantle-derived magmas is primarily dictated by the conditions of partial melting and the chemical/physical response of mantle sulfides during magma segregation. Considering sulfide solubility of ~ 1000 ppm in basaltic melts at 1-2 GPa (Mavrogenes and O'Neill, 1999) and 250 ppm of S in fertile mantle source (McDonough and Sun, 1995), the exhaustion of mantle sulfides requires melting degrees > 18-25% (Rehkämper et al., 1999; Fischer-Gödde et al., 2011; Luguet and Reisberg, 2016). Similar degrees of partial melting characterized ancient mafic-ultramafic magmatism (LIPs and komatiites), in which the complete exhaustion of mantle sulfides enhanced the transfer of metals into sulfide-undersaturated melts parental of orthomagmatic Ni-Cu-(PGE) ores (Keays, 1995; Barnes et al., 2015). Because of the high content of sulfur required for sulfide saturation at low pressure (Mavrogenes and O'Neill, 1999) and their extremely high temperature, these magmas reached the shallow crust at sulfide-undersaturated conditions (Keays, 1995; Fiorentini et al., 2010; Barnes et al., 2016) and could segregate an immiscible sulfide melt only by assimilation of country rocks or magma mixing (Fig. 1.14; Bekker et al., 2009; Ripley and Li, 2013). The extent of metal upgrading in the sulfide ores was finally determined by

the ratio between the fractions of sulfide melt and silicate magma in which metals were originally dissolved (i.e., the *R-factor*, Campbell and Naldrett, 1979).

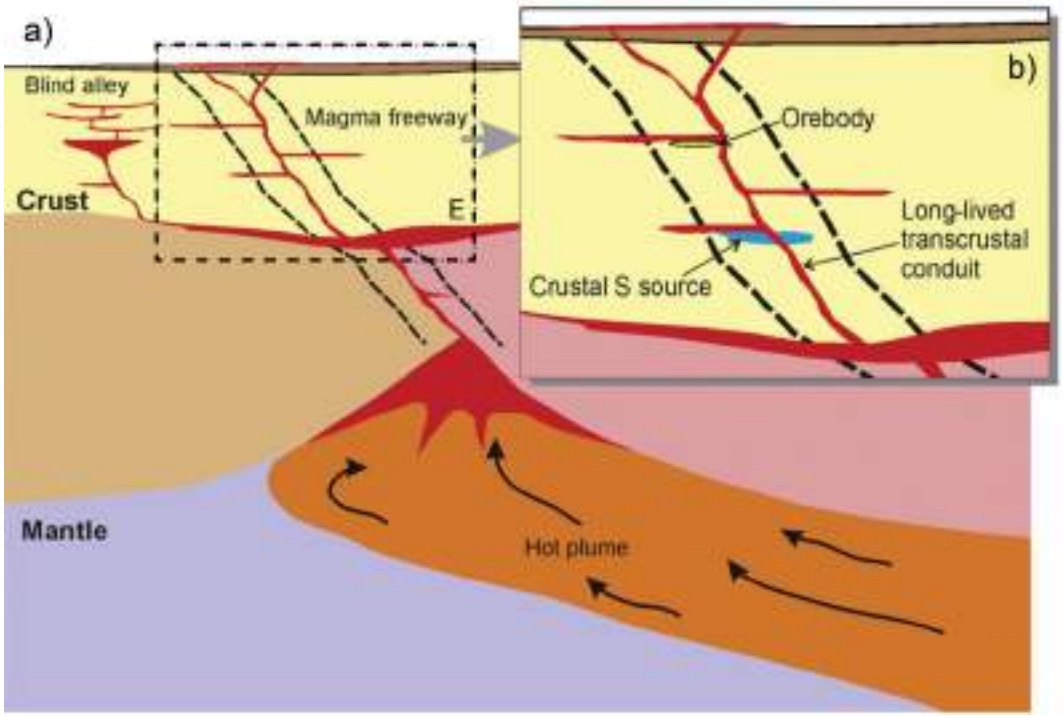

Figure 1.14. Schematic model illustrating the generation of orthomagmatic Ni-Cu-PGE sulfide deposits associated with mafic-ultramafic intrusions during plume events (Barnes et al., 2016).

On the other hand, common basalts from spreading ridges or subduction zones are generated at relatively low melting degrees (F = 10-15%), such that the retention of chalcophile metals into residual mantle sulfides hampers the metallogenic endowment of primitive magmas (Fonseca et al., 2011; Mungall and Brenan, 2014). In subduction zones, this obstacle may be overcome by the influx of slab-derived fluids in the subarc lithospheric mantle, which may drive oxygen fugacity (e.g., FMQ > 1; Evans et al., 2012) that stabilizes more soluble sulfate (S^{6+}) instead of sulfide species (S^{2-}) (Jugo et al., 2010; Bénard et al., 2018; Chowdhury and Dasgupta, 2019; Tassara et al., 2020). Therefore, oxidized arc magmas may be capable to dissolve mantle sulfides and scavenge chalcophile metals as they ascend through the subarc lithospheric mantle (Tassara et al., 2017; Li et al., 2019), reaching the base of the crust at sulfide-undersaturated conditions (Mungall, 2002). Then, upon fractional crystallization and cooling in the lower crust, arc magmas may become saturated with immiscible sulfide melt

(Wilkinson, 2013). Therefore, chalcophile metals, especially the most compatible (e.g., Os, Ir, Ru and Rh), are sequestered into sulfide-bearing cumulates in the lower crust (Chen et al., 2020; Edmonds et al., 2018; Huang et al., 2020), while sulfide melts transport upwards more incompatible metals (e.g., Cu, Au, Pt, Pd, Te) (Jenner et al., 2017; Holwell et al., 2022). This decoupling stems from the existence of a temperature window at ~ 1000-1200 °C (the so-called "Goldilocks zone", Fig. 1.15; Holwell et al., 2022), in which the sulfide phase breaks up into crystalline Fe-Ni mss and Cu-rich sulfide melt (Bockrath et al., 2004; Ballhaus et al., 2006; Li et al., 2021).

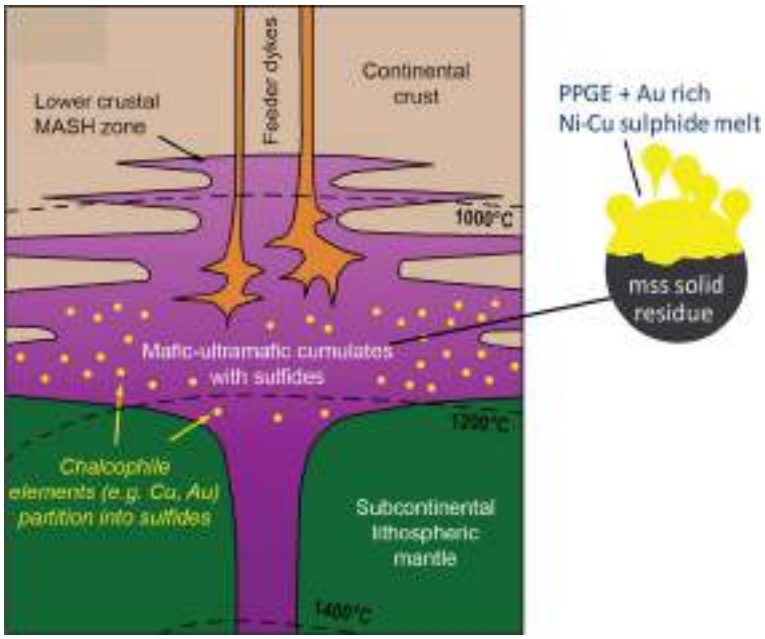

Figure 1.15. Schematic representation of sulfide-saturated cumulates in the lower arc crust (Holwell et al., 2022).

The upward transport of dense sulfide melts is enhanced by volatiles, which favor the buoyancy necessary to overcome the density contrast between sulfide and silicate melts (Mungall, 2015; Blanks et al., 2020; Iacono-Marziano et al., 2022). The last step in the formation of hydrothermal sulfide ores involves the transfer of metals from metal-rich magmas into hydrothermal fluids/brines, either as dissolved sulfide species (Fig. 1.16; Simmons and Brown, 1996; Heinrich et al., 1999; Loucks and Mavrogenes, 1999; Ulrich et al., 1999; Audétat et al., 2008)

or colloidal flocculations of nanoparticles (Petrella et al., 2020, 2022; Hastie et al., 2021; MacLeish et al., 2021).

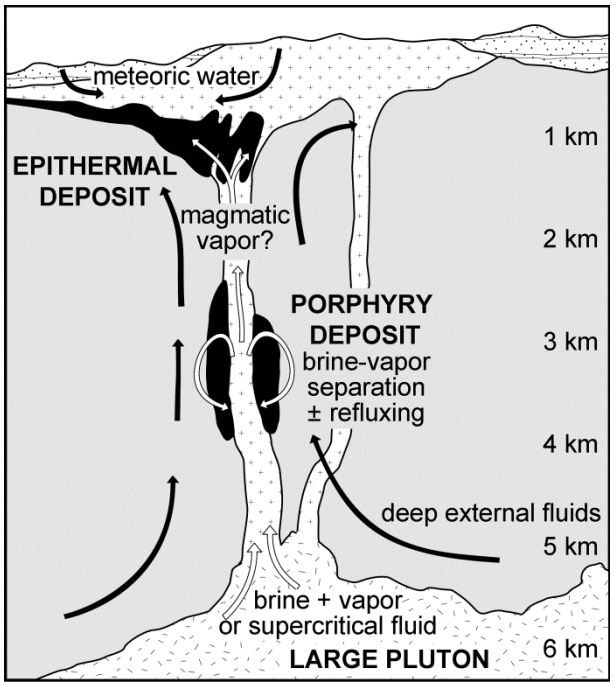

Figure 1.16. Schematic illustration of hydrothermal mineral systems (e.g., Cu-Mo-Au porphyry and Au-Ag epithermal ore deposits) associated with magma emplacement in subduction zones (Heinrich et al., 1999).

The transport models of chalcophile metals in the lithosphere normally assume they dissolve in silicate/sulfide melts or fluids, and then enter in the crystal lattice of their solid products (mainly BMS) that constitute magmatic and hydrothermal ores (Barnes et al., 1997; Mansur et al., 2019). This canonical view is challenged by an increasing number of studies documenting that precious and semi-metals in natural and experimental magmatic sulfides preferentially crystallize as submicrometer-sized particles of PGM and metal alloys (Holwell and McDonald, 2007; Piña et al., 2012; O'Driscoll and González-Jiménez et al., 2016; Sinyakova et al., 2016; 2019; Anenburg and Mavrogenes, 2020). The genesis of these metal-rich, submicrometer-sized minerals has been traditionally ascribed to subsolidus exsolution from pre-existing sulfide at low temperature (Ballhaus and Ulmer, 1995; Prichard et al., 2004; Zelenski et al., 2017). However, sulfide-hosted PGM and alloys generally have textural and compositional characteristics that cannot be reconciled with low temperature exsolution, but

support they crystallized before the solidification of the sulfide melt (Ballhaus and Sylvester, 2000; Godel et al., 2007; Wirth et al., 2013; Zelenski et al., 2017; Kamenetsky and Zelenski, 2020). Moreover, many magmatic sulfide ore deposits have PGE abundances exceeding their concentrations that can be dissolved in the entire magma chamber (Naldrett et al., 2009), requiring huge amounts of sulfur that are not accounted for by realistic volumes of magma (Ballhaus and Sylvester, 2000). All these observations substantiate the pioneering hypothesis of Tredoux and co-workers (1995) that metals may occur in magmas as insoluble, nanosized clusters of atoms connected by metal-metal bonds, which are stabilized by envelopes of semi-metals (e.g., S, Se, As, Sb, Te) (Fig. 1.17). The progressive coalescence of polymetallic complexes, in order to minimize their chemical potential, may finally lead to the early saturation of the silicate melt in PGM and/or metal alloys before sulfide saturation (Tredoux et al., 1995; Ballhaus and Sylvester, 2000; Bockrath et al., 2004).

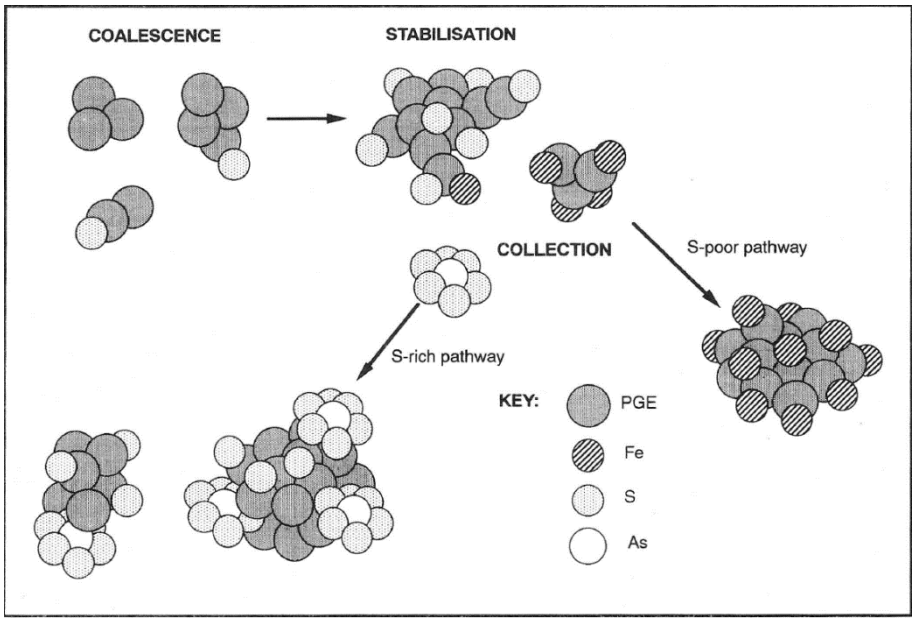

Figure 1.17. Schematic illustration for the formation of PGE-semi-metals clusters in magmas (Tredoux et al., 1995).

This hypothesis finds support in the experimental results by Helmy et al. (2013) and Anenburg and Mavrogenes (2020), who reported that PGE and semi-metals can self-organize as insoluble nanoclusters, or immiscible liquids, even if

the bulk sulfide system is highly undersaturated with respect to discrete PGM. The selective affinity of certain PGE to form specific metal-metal, metal-S, or metal-semi-metal complexes could also drive mechanical fractionation between I-PGE-rich and P-PGE-rich metal-complexes (Helmy and Bragagni, 2017). The early-stage saturation of silicate magmas with metal alloys can be also triggered by local redox gradients promoted by chromite and oxide crystallization (Finnigan et al., 2008; Anenburg and Mavrogenes, 2016), which could explain the common close association of these minerals with PGM and alloys (Kamenetsky et al., 2015; González-Jiménez et al., 2019).

All these new observations challenge the traditional models of transport of precious metals and have fundamental implications for the genesis of sulfide ores. In fact, if PGM and metal alloys routinely crystallize from silicate magmas regardless they are sulfide-saturated or not (e.g., Kamenetsky et al., 2015; González-Jiménez et al., 2019; Kamenetsky and Zelenski, 2020), then the close association of PGM and alloys with magmatic sulfides is due to mechanical entrapment rather than to chemical equilibrium partitioning. This process would imply that: 1) the extent of metal enrichment in ore deposits is primarily controlled by the PGE budget of silicate magmas in form of metal-rich nano-clusters; 2) sulfide melt acts as a mechanical collector, immobilizing and accumulating pre-existing PGE nanoclusters by surface energy properties rather than by chemical chalcophile affinity (Ballhaus and Sylvester, 2000; Helmy et al., 2013; Anenburg and Mavrogenes, 2020). In this scenario, the reliability of conventional models on predicting the behavior of precious metals in the lithosphere based on sulfide solubility and sulfide/silicate partitioning coefficients requires comprehensive re-examination.

2. Aims and Thesis structure

2.1 Aims

The general goal of this thesis is to assess the geological factors that control the mobilization, transport, and concentration of chalcophile metals in the subcontinental lithospheric mantle (SCLM), which may in turn influence the generation of ore-productive, mantle-derived melts and fluids able to produce metallogenic endowment of the continental crust.

For this purpose, I studied mantle-derived rocks, mainly peridotite xenoliths, from ore-productive regions of the continental lithosphere, such as the Mesa Central of Central Mexico (**Chapter 4**) and the Neogene Volcanic Province of Southeast Spain (**Chapters 5** and **6**). Peridotite mantle xenoliths brought to the surface by volcanic activity preserve the "freezed" mineralogical-geochemical fingerprints of the processes controlling the mobility and storage of metals in the SCLM. Therefore, the samples studied in this thesis provide the rare opportunity to constrain these processes in the SCLM beneath economically important metallogenic provinces, and in particular to: 1) define how the evolution and architecture of the SCLM influence the distribution of magmatic-hydrothermal ore deposits in the continental crust (factor n° 1, *lithospheric architecture*, **Chapter 4**); 2) determine the petrological mechanisms and mineral repositories that govern the metallogenic fertility of the SCLM (factor n° 2, *metallogenic fertility*, **Chapter 5**); 3) track the mechanisms controlling the transport of chalcophile metals during the ascent of ore-productive magmas from the mantle source to the overlying crust (factor n° 3, *transfer media*, **Chapter 6**).

Specific targets associated to these main goals include:

- To define the petrogenesis of mantle xenoliths, in order to outline the long-term evolution of the SCLM shaped by partial melting and mantle metasomatism;
- To determine how distinct populations of base-metal sulfides (BMS), platinum-group minerals (PGM) and metal alloys control the budget of

the SCLM in terms of chalcophile elements, and their responses to partial melting and mantle metasomatism;

- To explore the relationships among metallogenic re-fertilization and/or depletion of the SCLM, major geodynamic events, and the formation of magmatic-hydrothermal ore deposits;
- To constrain the nature of "ore-productive stores" and major "plumbing systems" in the SCLM, which may feed the flux of metals to the overlying crust.

2.2 Thesis structure

This Ph.D thesis comprises four main parts. ***Part I*** includes a general conceptual introduction to the state-of-art of the research topic (**Chapter 1**), the aims and overview of the structure of the thesis (**Chapter 2**), and a detailed description of the analytic methods that have been employed in this research (**Chapter 3**).

Part II presents and discusses the results of the thesis. Each chapter of ***Part II*** focuses on one of the three major topics that comprise this work, i.e., *lithospheric architecture* (n°1), *metallogenic fertility* (n°2) and *transfer media* (n°3). In **Chapter 4**, I report a detailed petrographic and compositional study of mantle peridotite xenoliths sampling distinct lithospheric blocks in Central Mexico (from the Santo Domingo, Ventura-Espíritu Santo and Durango volcanic fields). These results have been used to discuss how the large-scale lithospheric architecture may control the locus of trans-lithospheric plumbing systems associated with the formation and evolution of metallogenic belts (goal n°1). These results have been published in the JCR journal *International Geology Review* as a peer-reviewed regular article (Schettino, E., González-Jiménez, J.M., Marchesi, C., Dávalos-Elizondo, M. G., Camprubí, A., Colás, V., Saunders, E., Aranda-Gómez, J. J., & Griffin, W. L. A fragment of inherited Archaean lithospheric mantle rules the metallogeny of central Mexico. *International Geology Review*, 2022, DOI: 10.1080/00206814.2022.2127125).

In **Chapter 5**, I present an extensive petrographic and chemical study of a suite of peridotite xenoliths from the Tallante volcanic field (Southeastern Spain),

in order to define the main processes controlling the metallogenic fertility of the SCLM underlying this ore-productive crustal region (goal n°2). These results have been published in the JCR journal *Geological Society of America Bulletin* as a peer-reviewed, open access regular article (Schettino, E., Marchesi, C., González-Jiménez, J. M., Saunders, E., Hidas, K., Gervilla, F., & Garrido, C. J. Metallogenic fingerprint of a metasomatized lithospheric mantle feeding gold endowment in the western Mediterranean basin. *GSA Bulletin*, v. 134, no. 5/6, p. 1468-1484, 2022, doi.org/10.1130/B36065.1)

In **Chapter 6**, I present a comprehensive mineralogical study of nanosized, metal-rich mineral inclusions hosted in peridotite mantle xenoliths from Tallante and lamproite dykes from the Fortuna volcanic field (Southeast Spain), in order to unravel the mechanisms that control the transfer of chalcophile metals (especially Pb) throughout a trans-lithospheric magmatic path associated with magmatic-hydrothermal ores (goal n° 3). This chapter is a manuscript submitted as a regular article currently under review in the JCR journal *Communications Earth & Environment* (Nature portfolio).

The conceptual introductions in **Chapters 4**, **5** and **6** of the ***Part II*** have been summarized in order to avoid repetitions of concepts already presented in the **Chapter 1** of the thesis.

Part III presents the main conclusions of the three studies and open questions for future investigations (**Chapter 7**), followed by a list of the cited references (***Part IV***).

In addition to the publications cited above, the results of this thesis have been disseminated as oral and poster communications at several international and national conferences and meetings, including *Goldschmidt Conference* (Virtual, 2020; Virtual, 2021), *European Geosciences Union General Assembly* (Virtual, 2021), *II Jornada de Jóvenes Investigadores de la Sociedad Española de Mineralogía* (Virtual, 2021), *European Mineralogical Conference* (Cracow, Polonia, 2021), *MEREMA 2nd Edition International School on Mantle Dynamics* (Sestri Levante, Italy, 2021), and *Earth Mantle Workshop* (Toulouse, France, 2022).

3. Methods

3.1 Optical and scanning electronic microscopy

Preliminary petrographic characterization of peridotite mantle xenoliths and mantle-derived volcanic rocks (lamproites) was carried out under transmitted/reflected light optical microscope in multiple polished thick/thin sections of selected samples. Qualitative identification and textural analysis of minerals were conducted by scanning electron microscopy (SEM) on carbon-coated thin sections, by using a QEMSCAN 650F field emission gun environmental scanning electron microscope (FEG-ESEM) equipped with energy dispersive X-ray spectroscopy (EDS), secondary electrons (SE), and backscattered electrons (BSE) detectors at the Centro de Instrumentación Científica (CIC) of the Universidad de Granada (Spain) (Fig. 3.1). Operating conditions were 20 kV accelerating voltage for a 5 µm spot-size beam, and the intensity of beam current was optimized to a sufficient number of counts during EDS microanalyses.

Figure 3.1. Field emission gun environmental scanning electron microscope (FEG-ESEM) at the Centro de Instrumentación Científica (CIC) of the Universidad de Granada (Spain).

3.2 Electron microprobe analyses

Major element compositions (expressed in wt.% of SiO_2, TiO_2, Al_2O_3, Cr_2O_3, FeO, MnO, MgO, CaO, Na_2O and K_2O) of silicates, oxides and glass were determined by electron microprobe analysis (EMPA) using a JEOL JXA-8230 EMP at the Serveis Cientificotècnics of Universitat de Barcelona (Spain) (Fig. 3.2) or a JEOL JXA- 8900 R instrument equipped with five wavelength-dispersive spectrometers (WDS) at the Laboratorio Nacional de Geoquímica y Mineralogía of the Universidad Nacional Autónoma de México (UNAM). Silicates and spinel were analyzed by employing 20 kV accelerating voltage and 15-20 nA beam current for a 5 µm spot-size beam diameter. Silicate glass was analyzed using defocused 20 µm spot-size beam and 6.5 nA beam current. Counting time for each element was 20 s for peak and 10 s for background, and ZAF correction was applied online. Calibration was performed using natural and synthetic standards.

Figure 3.2. JEOL JXA-8230 electron microprobe analyzer at the Serveis Cientificotècnics of the Universitat de Barcelona (Spain).

The major element compositions (S, Fe, Ni, Co, Cu) of base-metal sulfides were determined by using a CAMECA SX 100 EMP equipped with five wavelength-dispersive spectrometers (WDS) bearing LPET, LLIF and LTAP crystals at the CIC facilities (Universidad de Granada, Spain). Analytical conditions were 20 kV accelerating voltage and 30 nA beam current for a 5 µm spot-size beam. Counting times for S, Fe, and Ni were 30 s for peak and 15 s for background; for Co and Cu were 50 s for peak and 25 s for background. The S Ka was acquired on LPET (channel 1); Fe Ka and Cu Ka were acquired on LLIF (channel 3); Ni Ka and Co Ka on LLIF (channel 4). The following standards were adopted to determine the major element composition of sulfides: FeS_2 for S and Fe; pentlandite for Ni; native Co for Co; Cu_5FeS_4 for Cu. The bulk compositions of polyphase sulfide aggregates were determined by mass-balance calculations between EMP analyses of individual grains and their volumetric abundances. Volumes were retrieved by image analyses performed on BSE maps using a customized routine developed as a Mathematica© notebook.

3.3 Laser ablation-inductively coupled plasma-mass spectrometry

The trace element compositions of clinopyroxene and silicate glass were determined by laser ablation inductively coupled plasma mass spectrometry (LA-ICP-MS) on polished thin sections by coupling a Thermo ICAP-Q ICP-MS with a Resolution M-50 Excimer laser at the Centro de Geociencias-UNAM (Mexico), and an Agilent 8800 QQQ ICP-MS with a Photon Machine Analyte G2 excimer 193 nm laser at the Instituto Andaluz de Ciencias de la Tierra, CSIC-Universidad de Granada (Spain) (Fig. 3.3).

The thin sections were put into a double volume ablation cell, supplied with a He gas flow of 9.7 l/min. Maximum sensibility of analysis was achieved by employing an energy density of 7-8 J/cm^2 for a 60-110 µm spot-size and 5-30 Hz repetition rate. A 40 µm spot-size was applied to ablate clinopyroxene spongy coronae. The ablation mode was static spot and performed as automatic driven positioning. Integration time for all analyses was 50-60 milliseconds for each

mass and the validation standards BHVO-2G (synthetic glass, IAG-USGS) and augite Kakanui 122,142 (Jarosewich, 1980) were included between the unknowns to check the accuracy and precision of the analyses. Data reduction was performed using the Iolite 2.5 software package (Paton et al., 2011) on the IgorPro platform by the careful inspection of time-resolved spectra to check for the homogeneity and stability of signals during ablation time. Elements were calibrated using the synthetic glass NIST611 SRM. Calcium content, determined by EMP, was used as internal standard.

Figure 3.3. Photon Machine Analyte G2 laser ablation system (a) coupled to an Agilent 8800 QQQ inductively coupled-plasma mass spectrometer (b) at the facilities of the Instituto Andaluz de Ciencias de la Tierra (CSIC-Universidad de Granada, Spain).

The concentrations of chalcophile and siderophile elements in base-metal sulfides were determined by LA-ICP-MS at the Geochemical Analysis Unit of CCFS/GEMOC, Macquarie University (Sydney, Australia). The analyses were performed by using a Photon Machines Excite 193 nm excimer laser microprobe coupled with an Agilent 7700 ICP-MS, following the methodological approach of Saunders et al. (2015, 2016). Ablation was performed using He as carrier gas, which was blended with Ar prior to the introduction into the plasma. The laser system was operated at 5 Hz with laser energy of 5.69 J/cm^2 for a spot-size ranging from 25 to 50 µm. Composition of chalcophile and siderophile elements was determined by acquiring the following isotopes: ^{34}S, ^{59}Co, ^{60}Ni, ^{63}Cu, ^{66}Zn, ^{75}As, ^{82}Se, ^{107}Ag, ^{111}Cd, ^{115}In, ^{121}Sb, ^{125}Te, ^{208}Pb, ^{209}Bi, ^{189}Os, ^{193}Ir, ^{101}Ru, ^{103}Rh,

^{105}Pd, ^{108}Pd, ^{195}Pt, ^{197}Au. A quenched NiS bead (PGE-A: Alard et al., 2000, 2002) was employed as external calibration standard with the exception of Sb, which was calibrated against a chalcophile glass (IMER-2), and Zn an In, which were calibrated against a powdered Fe sulfide standard (UQAC-FeS-1) analyzed as unknowns. Two additional sulfide standards (Po-725 and UQAC-FeS-1) were employed to evaluate analytical accuracy. Data were processed using the GLITTER^{TM} software (Griffin et al., 2008), which allowed to select the part of the time-resolved spectrum devoid of inclusions and host silicates. Sulfur content, determined by EMP, was used as internal standard. Argide isobaric interferences (^{63}Cu^{40}Ar = ^{103}Rh, ^{65}Cu^{40}Ar = ^{105}Pd) were corrected by ablating a pure Cu wire during the runs and applying the correction factor on the measured ^{103}Rh. The reliability of correction on Pd was monitored by comparing Pd concentrations based on ^{105}Pd against the ^{108}Pd data, which show similar values within uncertainty of measurements. ^{108}Pd data were finally used to determine the concentration of Pd.

3.4 *In-situ* Re-Os isotopes

Rhenium-osmium isotope analyses of base-metal sulfides were performed at the Geochemical Analysis Unit of CCFS/GEMOC using a New Wave/Merchantek UP 213 laser microprobe with a modified ablation cell, coupled with a Nu Plasma Multicollector ICP-MS. Due to the small size of the BMS, the in situ Re-Os analyses couldn't be performed on BMS grains that were previously obliterated by laser ablation analysis of PGE concentrations, but were performed in equivalent BMS located after repolishing of the same block. During the ablation runs, ion beams were collected using a mix of Faraday cups and ion counters. The laser was fired at a frequency of 5 Hz, with energies of 1–2 mJ/pulse and a spot size of 20–80 μm. The PGE-A standard was analyzed between samples to monitor drift in the Faraday cups and ion counters; these variations typically were less than 0.1% over a long day analytical session. During the analyses, a dry aerosol of Ir was bled into the gas line between the ablation cell and the ICP-MS to provide a mass-bias correction with a precision independent of the abundance of Os in the

unknown. All the analysed grains had $^{187}Re/^{188}Os < 0.5$, and the limited overlap of ^{187}Re on ^{187}Os was corrected by measuring the ^{185}Re peak and using $^{187}Re/^{185}Re = 1.6742$. Data were treated using the Nu Plasma time-resolved software, which allows selection of the most stable intervals of the signal for integration. The selected interval was divided into 40 replicates to provide a measure of the standard error. Under the ablation conditions described above, a typical run lasted 100 s and the signal intensity of Os was between 0.01 and 0.23 V, giving a precision for $^{187}Os/^{188}Os$ from 2.60E- 5 to 8.60E-3.

The Os isotope compositions of mantle minerals and rocks can be recast as model ages (T_{MA} and T_{RD}) to reveal the history of mantle depletion (Shirey and Walker 1998). The T_{MA} model age represents the time of separation from a chondritic mantle reservoir calculated using the measured Re/Os ratio, whereas T_{RD} (Re-depletion model age) assumes complete removal of Re during melting and represents a minimum age for separation from a chondritic reservoir. Both types of model ages are dependent on the model reservoir selected to represent the Os isotopic evolution of the mantle. In this study, I used for this purpose the Enstatite Chondritic Reservoir (ECR) (present-day $^{187}Os/^{188}Os = 0.1281$ and $^{187}Re/^{188}Os = 0.421$; Walker *et al*. 2002). The quoted uncertainties on model ages of BMS include the uncertainties of the measured $^{187}Os/^{188}Os$ and $^{187}Re/^{188}Os$, calculated according to the equation of Sambridge and Lambert (1997).

3.5 Thin-foil sampling by focused ion beam

Electron transparent thin (~ 90 nm) foil samples were prepared and extracted from selected nanoparticle-bearing sulfides by using a focused ion beam scanning electron microscope (FIB-SEM) in the Laboratorio de Microscopías Avanzadas (LMA) at the Instituto de Nanociencia de Aragón (INA), Universidad de Zaragoza (Spain). Thin foil sampling was performed with a Dual Beam FEI-Thermo Fisher Scientific, model Helios 650. The selected regions of interest were firstly covered with a ~ 300 nm carbon strip by focused electron beam induced deposition and, subsequently, with a ~ 1 μm platinum strip in order to protect the thin foils from physical damage during ion milling, polishing and extraction processes. The bulk

material was removed on both sides of the lamellae by a rough Ga^+ ion milling with a 30 kV current at 2.5 nA. The lamellae were then polished with a 30 kV current at 0.23 A and transferred to a TEM grid using an OmniProbe nanomanipulator with a tungsten tip. Ion-beam assisted Pt deposition was performed in order to weld the lamellae to the TEM grid. Electron transparency of the thin foil samples was achieved by milling the lamellae with a 5 kV current at 68 pA, and monitored with an Everhart-Thornley secondary electrons detector.

3.6 High-resolution transmission electron microscopy

The thin foil samples were analysed by using a FEI Titan G2 transmission electron microscope (TEM) equipped with field emission gun cannon XFEG at the CIC facilities of the Universidad de Granada (Spain) (Fig. 3.4).

This microscope was provided with spherical correction for the objective lens, 4 detectors of X-rays energy dispersion (EDX) (FEI microanalysis Super X), and a high angle-annular dark field detector (HAADF). High magnification electron microscopy images (HMEM) and High-Resolution Transmission Electron Images (HRTEM) were acquired using a Gatan CCD Camera. The instrument was operated at 300 kV accelerating voltage. The textural and chemical characterization of selected areas of interest was carried out by a combination of EDX elemental maps, HAADF Z-contrast and bright field scanning transmission electron (STEM) imaging, coupled with HRTEM imaging down to the atomic scale. The obtained images were subsequently processed with Digital Micrograph® Version 1.71.38 and maps with INCA® Microanalysis Suite version 4.09 software packages. Structural data of minerals were obtained by selected area electron diffraction patterns (SAED) and/or by single crystal Fast Fourier transforms (FFT) calculated from HRTEM images.

Figure 3.4. High-resolution transmission electron microscope at the Centro de Instrumententación Científica de la Universidad de Granada (Spain).

Part II

Results

4. A fragment of inherited Archean lithospheric mantle rules the metallogeny of central Mexico*

**This chapter has been published in Schettino, E., González-Jiménez, J. M., Marchesi, C., Dávalos-Elizondo, M. G., Camprubí, A., Colás, V., Saunders, E., and Aranda-Gómez, J. J., 2022, A fragment of inherited Archaean lithospheric mantle rules the metallogeny of central Mexico: International Geology Review, DOI: 10.1080/00206814.2022.2127125.*

4.1 Introduction

Magmatic-hydrothermal ore deposits form clusters distributed in specific regions of the Earth's crust, thus constituting metallogenic belts. The formation of these belts chiefly requires favourable trans-lithospheric plumbing systems (Begg et al., 2009) that facilitate the focused migration of ore-productive melts/fluids from a fertile source of metals to a mechanical/geochemical trap in the crust (McCuaig and Hronsky, 2014). Hence, the architecture of the subcontinental lithospheric mantle (SCLM) exerts a first-order control on determining the regional distribution of metal resources in the continents. In this regard, the characterization of Re-Os isotope signatures of distinct generations of base-metal sulfides (BMS) and platinum-group minerals (PGM) in mantle peridotites yields powerful tools for dating the sequence of petrological events (e.g., partial melting and melt-rock interaction) associated with the construction and transformation of the continental lithosphere (Rudnick and Walker, 2009; González-Jiménez et al., 2013; Luguet and Pearson, 2019). Therefore, the study of BMS and PGM in mantle rocks provides key clues for outlining the architecture of the SCLM and its implications for the genesis of metallogenic belts in the crust.

The architecture of the Mexican lithosphere consists of distinct fault-bounded lithospheric blocks with coherent tectono-magmatic evolution (i.e., terranes, Campa and Coney, 1983), assembled during multiple Wilson cycles (Camprubí, 2017; Centeno-García, 2017). Notably, this lithospheric mosaic includes a highly ore-productive continental crust that provides the world's largest supply of silver and one of the world's leading productions of copper, gold, zinc,

molybdenum, bismuth, and other commodities (Camprubí, 2009, 2013). The mapping of tectono-stratigraphic terranes and their suture zones has highlighted the distribution of mineral resources through the distinct continental blocks of Mexico (Campa and Coney, 1983; Camprubí, 2013; Centeno-García, 2017). However, only few studies have assessed the role of the lithospheric mantle on determining the relationship between the distributions of terranes and ore mineralization in this world-class mining region (Ruíz et al., 1988; González-Jiménez et al., 2017a, b). In this chapter, I report a detailed petrographic and compositional characterization of silicates, glass (major and trace elements) and BMS (major elements, PGE-Au, and Re-Os isotopic ratios) from a set of mantle peridotite xenoliths sampling distinct lithospheric blocks of Central Mexico. I use these data mainly to determine the genesis of different BMS populations, to constrain the petrological evolution of peridotites and its bearing on the SCLM architecture beneath Central Mexico, and to assess how the evolution and architecture of this sector of SCLM influenced the metallogenic productivity of one of the world's largest mineralized provinces.

4.2 Geological background

4.2.1 Architecture of the Mexican continental lithosphere

The present-day architecture of the Mexican continental lithosphere is a mosaic of displaced fragments of the Laurentia craton and allochtonous terranes (i.e., fault-bounded lithospheric blocks) that accreted to North America during the assembly of Pangea in the Late Paleozoic (Gondwana-type), or the subduction-related evolution of the paleo-Pacific margin in the Mesozoic (Cordilleran-type) (Fig. 4.1a) (Campa and Coney, 1983; Sedlock et al., 1993; Dickinson and Lawton, 2001; Keppie, 2004; Ortega-Gutíerrez et al., 2018). The Paleoproterozoic crust of Laurentia craton, exposed in NW Mexico (North America terrane) was split into fragments (Caborca and Cortés terranes) by strike-slip movements related to the opening of the Gulf of Mexico in the Late Jurassic (i.e., Mojave-Sonora megashear) (Fig. 4.1a) (Silver and Anderson, 1974; Anderson and Silver, 2005). Gondwana-derived terranes in central and eastern Mexico (Oaxaquia, Maya and

Mixteca terranes) (Fig. 4.1a) consist of exotic Proterozoic and Paleozoic continental slivers that accreted to North American in the Late Paleozoic (Ruíz et al., 1988; Ortega-Gutiérrez et al., 1995, 2018; Centeno-García, 2005). Since the Permo-Triassic, development of continental arc magmatism along the NW margin of Pangea (Kirsch et al., 2012) marked a shift towards regional tectonic regime dominated by the accretion of Cordilleran-type Mesozoic terranes of magmatic-arc derivation (e.g., Alisitos arc and Guerrero composite terrane) along the Pacific active margin of North America (Fig. 4.1a) (Centeno-García, 2008; González-Jiménez et al., 2017a, b).

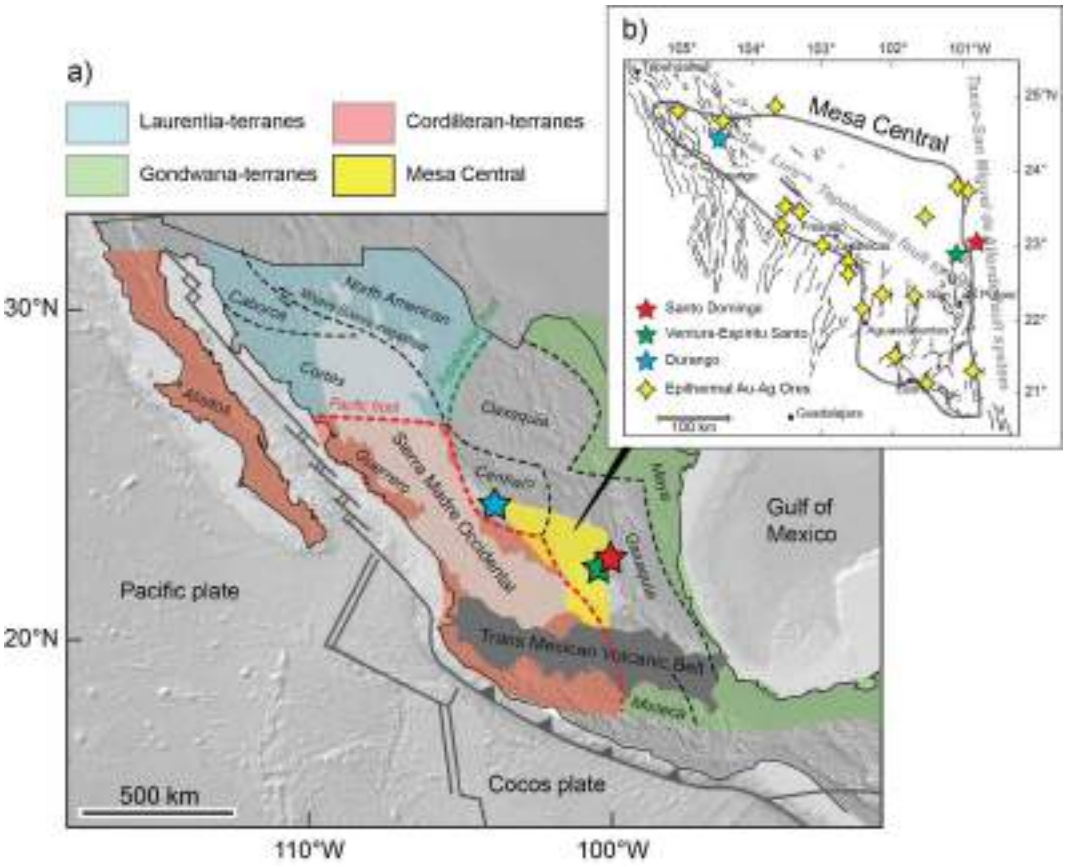

Figure 4.1. Panel a): Map of tectono-stratigraphic terranes of Mexico (Laurentia-terranes: blue; Gondwana-terranes:green; Cordilleran-terranes:red) (modified from Centeno-García, 2005, 2017). Stars indicate the locations of the Quaternary volcanic fields bearing the mantle peridotite xenoliths studied in this work (Santo Domingo: red, Ventura-Espíritu Santo: green, and Durango: blue). Panel b) shows the locations of Au-Ag epithermal ores (yellow diamonds) and fault systems in the physiographic region of Mesa Central (yellow area in the main figure) (edited from Camprubí et al., 2003 and Nieto-Samaniego et al., 2007).

Previous work pointed out the important control of terrane distribution and suture boundaries on the loci of magmatic-hydrothermal ores in Mexico (Campa and Coney, 1983, Nieto-Samaniego et al., 2005, 2007; Camprubí, 2009, 2013, 2017; Centeno-García, 2017). Thus, mantle xenoliths sampling distinct terranes provide an opportunity to assess how the architecture of the Mexican SCLM could have governed the metallogenic productivity of the overlying crust. The mantle xenoliths from Santo Domingo and Ventura-Espíritu Santo, sampled in this study, probably are portions of the Oaxaquia subcontinental block (Fig. 4.1a). This Grenville-age (~ 1.0 Ga) block is commonly regarded as a single lithospheric domain across eastern Mexico, north to south (Ortega-Gutiérrez et al., 1995). It is interpreted to have originally formed as a peri-Gondwana island arc before being accreted to North America during the Appalachian-Ouachita orogeny in the Late Paleozoic (Weber et al., 2010; Ortega-Gutiérrez et al., 2018). On the other hand, the Durango volcanic field is located on the Central terrane (Fig. 4.1a). This virtually unexposed crustal basement is arguably sandwiched by the western Mesozoic Cordilleran terranes (i.e., Guerrero) and the eastern Proterozoic Gondwana-type blocks (Fig. 4.1a). The presence of a subduction-related accretionary wedge along its northeastern boundary (i.e., the Taray formation, Anderson et al., 2005; Centeno-García, 2005) suggests that the Central terrane accreted along the Pacific margin of Oaxaquia during the Late-Triassic-Early Jurassic (Centeno-García et al., 2008). However, the boundaries and provenance of this suspect terrane, as well as its significance in the evolution of the Mexican lithosphere, require further investigation.

4.2.2 Geological setting

The mantle peridotite xenoliths of this study were collected from the Quaternary volcanic fields of Santo Domingo, Ventura-Espíritu Santo (San Luis Potosí state, < 1.4 Ma), and Durango (Durango state, ~ 1 Ma) (Luhr and Aranda-Gómez, 1997; Aranda-Gómez et al., 2005), which are located along the eastern border and at the northwestern corner of the Mesa Central, respectively (Central Mexico, Fig. 4.1b). This physiographic region forms an elevated plateau mainly consisting of Mesozoic sedimentary sequences imbricated during the Laramide orogeny in the

Cretaceous (Fitz-Díaz et al., 2018), and segmented by normal faults due to extensional tectonics of the Basin and Range Province in the Cenozoic (Nieto-Samaniego et al., 2005, 2007). As a result, the continental crust under the Mesa Central is relatively thin compared to nearby provinces (~ 32-35 km) and bounded by major structural lineaments (Nieto-Samaniego et al., 1999, 2005, 2007; Peredo et al., 2021) that mark the loci of extension in the Cenozoic (i.e., San Luís – Tepehuanes to the west, and Taxco – San Miguel de Allende fault systems to the east, Fig. 4.1b, Alaniz-Álvarez and Nieto-Samaniego, 2005, 2007). A significant portion of the Mesa Central is covered by a thick ignimbrite succession that is genetically associated with the Late Eocene-Early Miocene magmatism of the Sierra Madre Occidental, which occurred in response to the eastward subduction of the Farallon plate beneath North America (Ferrari et al., 2005, 2007, 2018). The WNW-ESE trending San Luís – Tepehuanes fault system controlled the regional distribution of this volcanism (i.e., ignimbrite flare-up event, ~ 32 to 27 Ma) and the associated epithermal Au-Ag and polymetallic ores (Camprubí et al., 2003; Camprubí and Albinson, 2007; Nieto-Samaniego et al., 2005, 2007), including the world-class epithermal mining districts of Zacatecas, Fresnillo and Guanajuato (Camprubí, 2013). Since the Late Oligocene-Early Miocene, the northward subduction of the Cocos plate shifted the loci of calc-alkaline volcanism to the southern part of Mesa Central during the early stages of the Trans Mexican Volcanic Belt (Gómez-Tuena et al., 2005, 2007). Because of the southward migration of the subduction front, regional scale N-S trending grabens associated with the Basin and Range tectonism controlled the extrusion of Late Oligocene (~ 24 Ma) to Quaternary intraplate-type alkaline basalts (Luhr et al., 2001; Ferrari et al., 2018). This volcanic activity finally faded into small-volume eruptions of Quaternary alkaline basalts/hawaiites (Santo Domingo and Durango volcanic fields) and olivine-nephelinites/basanites (Ventura-Espíritu Santo volcanic field), which brought to the surface abundant mantle and crustal xenoliths (Heinrich and Besch, 1992; Luhr and Aranda-Gómez, 1997).

4.2.3 Samples

Mantle xenoliths from Santo Domingo, Ventura-Espíritu Santo, and Durango volcanic fields vary in composition from highly depleted to fertile anhydrous peridotites (Liang and Elthon, 1990; Luhr and Aranda-Gómez, 1997). Hydrous phlogopite- and amphibole-bearing peridotites, olivine websterites, and composite xenoliths crosscut by kaersutite-rich pyroxenites are also common in Santo Domingo (Heinrich and Besch, 1992; Dávalos-Elizondo et al., 2016; Levresse et al., 2016). A suite of 13 anhydrous spinel lherzolites with bulk-rock Al_2O_3 = 2.92-4.30 wt.% and CaO = 1.32-2.78 wt.% (Dávalos-Elizondo et al., 2016) was selected based on the presence of BMS. Samples from Santo Domingo were collected from the maars of Santo Domingo (SD10 and SD11), Joya Prieta (JP2 and JP3) and Joya de los Contreras (JC11, J15 and JC21). Mantle xenoliths from Ventura-Espíritu Santo were collected from pyroclastic deposits around the maars of Laguna de los Palau (LP1 and LP2) and Joya Honda (JH6). Samples from Durango were collected from the La Breña-El Jagüey maar complex (LB1, LB3, and LB7) (Aranda-Gómez et al., 1992; Pier et al., 1992).

According to the classification of Mercier and Nicolas (1975), the selected xenoliths display either porphyroclastic (Santo Domingo) or coarse-granular texture (Ventura-Espíritu Santo and Durango) (Dávalos-Elizondo et al., 2016), but they all share the same range of pressure-temperature conditions of equilibration (10-15 kbar and 850-1050 °C, Heinrich and Besch, 1992; Luhr and Aranda-Gómez, 1997; Levresse et al., 2016). Spinel lherzolites from Santo Domingo have a bimodal grain-size distribution characterized by medium-grained (0.5-2 mm) olivine and orthopyroxene porphyroclasts with undulose extinction, kink bands and subgrain boundaries, and a fine-grained matrix (< 0.5 mm) of unstrained olivine and orthopyroxene neoblasts with straight contacts locally converging to 120° triple junctions (Fig. 4.2a). Clinopyroxene and spinel form fine-grained (< 0.5 mm) anhedral grains or patches scattered in the peridotite matrix (Fig. 4.2b, c). Shape-preferred elongation of olivine and orthopyroxene, together with linear iso-orientation of spinel trails, marks a weak but pervasive foliation at the sample scale. Accessory amounts of amphibole are detected as tiny (~ 200 μm) grains located either at interstices (Fig. 4.2b) or surrounding anhedral spinel and

clinopyroxene (Fig. 4.2c). These petrographic observations are similar to those described before by Dávalos-Elizondo et al. (2016) and Levresse et al. (2016).

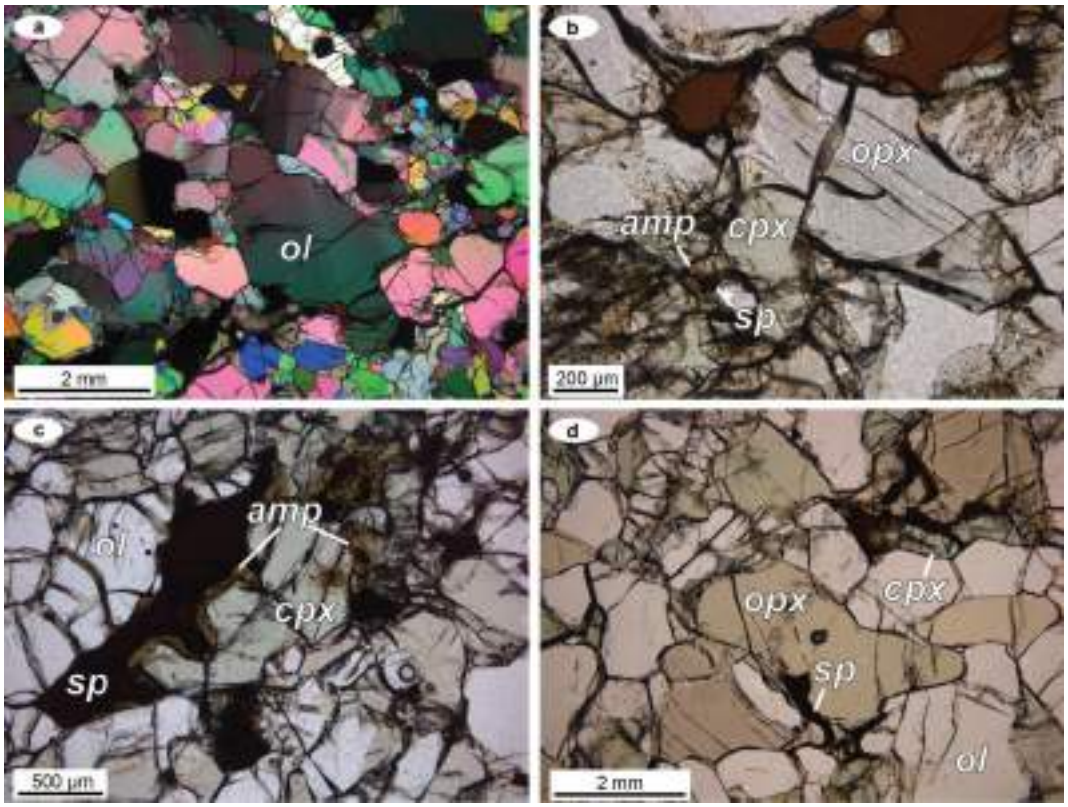

Figure 4.2. Photomicrographs under polarized light optical microscope of sulfide-bearing spinel peridotites from Santo Domingo (a, b, c) and Durango (d). Mineral abbreviations are: ol – olivine; opx – orthopyroxene; cpx – clinopyroxene; sp – spinel; amp – amphibole.

Coarse-granular spinel lherzolites from Ventura-Espíritu Santo and Durango have large (1-5 mm), slightly deformed crystals of olivine and orthopyroxene, and medium to fine-grained (0.5-2 mm), anhedral clinopyroxene and spinel (Fig. 4.2d) (Dávalos-Elizondo et al., 2016). Minerals are randomly oriented with no shape-preferred orientation. Grain boundaries between olivine and orthopyroxene are straight or interlobate. Vermicular spinel is commonly intergrown with anhedral orthopyroxene or clinopyroxene (Fig. 4.2d). Abundant glass veinlets are located at grain boundaries or in cracks within silicates and spinel. Glass veinlets show sharp and corroded contacts against the main rock-forming minerals.

4.3 Results

4.3.1 Major and trace element compositions of silicate minerals

The major element compositions of olivine and orthopyroxene in peridotite xenoliths from the volcanic fields of Santo Domingo, Ventura-Espíritu Santo and Durango are rather homogeneous (Table S4.1 in the Appendix). Olivine Mg# [100 x Mg/(Mg + Fe^{2+})] range from 88.1 to 91.0, and its NiO and CaO contents vary between 0.27-0.47 and 0.14-0.38 wt.%, respectively. The Mg# of orthopyroxene (88.6-90.8) are similar to those of olivine, and its Al_2O_3 abundances (3.21-5.05 wt.%) are correlated positively with CaO (0.64-0.91 wt.%) and negatively with MgO (31.6-33.5 wt.%) and SiO_2 (53.8-56.0 wt.%). TiO_2 concentrations in orthopyroxene are generally low (< 0.15 wt.%).

Contrary to olivine and orthopyroxene, the major element compositions of clinopyroxene show differences among samples from the three volcanic fields (Table S4.1). The Mg# of clinopyroxene ranges between 89.4-90.5 in Durango, 88.4-89.7 in Ventura-Espíritu Santo, and 88.9-91.4 in Santo Domingo. The Al_2O_3 concentrations span 5.54-6.06 wt.% in Durango, 6.13-6.62 wt.% in Ventura-Espíritu Santo, and 4.41-6.62 wt.% in Santo Domingo, and show no systematic co-variation with CaO (21.0-21.3 wt.% in Durango, 19.9-21.0 wt.% in Ventura-Espíritu Santo, and 20.0-22.1 wt.% in Santo Domingo). The abundances of FeO_T (2.57-3.59 wt.%) and Cr_2O_3 (0.63-1.12 wt.%) are generally similar in all the samples. The Na_2O and TiO_2 concentrations range between 0.82-1.89 and 0.23-0.54 wt.%, respectively, and the lowest values correspond to the Durango peridotites.

The chondrite-normalized REE patterns of clinopyroxene in Santo Domingo xenoliths display variable degree of LREE depletion (Ce_N/Yb_N = 0.14-0.51) coupled with relatively flat MREE-HREE segments (Gd_N/Yb_N = 0.84-1.23) at ~ 5 to 10 times the chondritic concentrations (Fig. 4.3a). Clinopyroxene grains in sample JH6 from Ventura-Espíritu Santo have REE compositions similar to xenoliths from Santo Domingo (Ce_N/Yb_N = 0.27-0.34), but are notably more fractionated in sample LP2 from the same volcanic field (Ce_N/Yb_N = 0.07-0.08) (Fig. 4.3a). Clinopyroxene in Durango peridotites is strongly LREE-depleted

(Ce_N/Yb_N = 0.01-0.02), in agreement with its lower Na_2O and TiO_2 contents (see above), except for two grains that display concave-upward patterns enriched in LREE up to supra-chondritic ratio (Ce_N/Yb_N = 1.37) (Fig. 4.3a).

The primitive upper mantle (PUM)-normalized trace element patterns of clinopyroxene in Santo Domingo xenoliths and sample JH6 from Ventura-Espíritu Santo have very variable positive Th-U spikes (Th_N/Nb_N up to 98.8), coupled with strong depletion in Nb relative to LREE (Fig. 4.3b). The more LREE-depleted clinopyroxene grains in sample LP2 from Ventura-Espíritu Santo and in the Durango xenoliths are also more depleted in Th, U and Nb, which are normally below their detection limits (Table S4.2 in the Appendix). Moreover, these grains show well-defined negative anomalies of Sr and Zr (Sr_N/Nd_N = 0.16-0.36; Zr_N/Sm_N = 0.10-0.45) (Fig. 4.3b), which are more pronounced with increasing degree of LREE depletion. Finally, the LREE-enriched clinopyroxene grains from Durango have also comparatively higher concentrations in other incompatible trace elements (Ba, Th, U, Nb, Sr, Zr and Hf), which define smoother trace element patterns that lack significant negative anomalies (Fig. 4.3b).

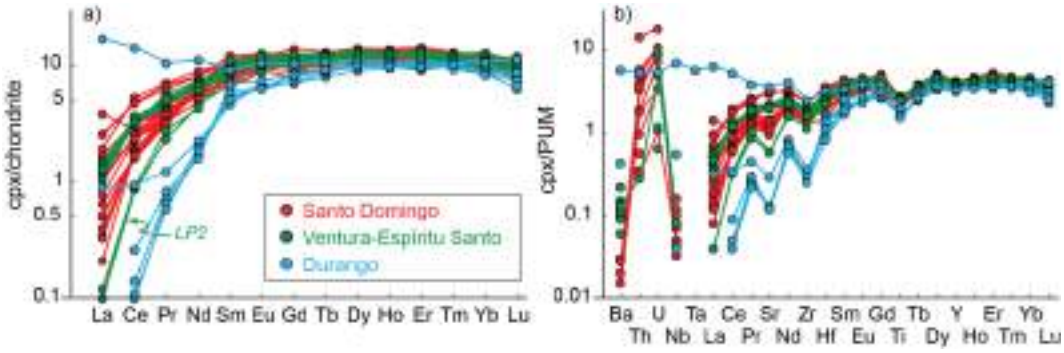

Figure 4.3. Chondrite-normalized concentrations of rare earth elements (a) and primitive upper mantle (PUM)-normalized concentrations of lithophile trace elements (b) (McDonough and Sun, 1995) in clinopyroxene (cpx) of spinel peridotites from Santo Domingo (red circles), Ventura-Espíritu Santo (green circles), and Durango (blue circles).

4.3.2 Major and trace element compositions of glass

The interstitial and fracture-filling glass in the mantle xenoliths from Ventura-Espíritu Santo and Durango has moderately high SiO_2 (52.1-60.8 wt.%) and Mg# (48.2-66.4) (Table S4.1). Silica shows poor negative correlations with TiO_2 (0.84-3.19 wt.%) and CaO (3.83-9.12 wt.%). Glass in all the samples is enriched in alkalis (Na_2O = 1.86-7.76 wt.%; K_2O = 2.07-3.38 wt.%) and Al_2O_3 (16.4-20.3 wt.%), and depleted in FeO_T (2.82-4.60 wt.%) and MgO (2.04-3.94 wt.%). There are no significant compositional differences between glasses in xenoliths from the two volcanic fields, except for the generally higher Na_2O/K_2O ratios of glass from Ventura-Espíritu Santo (~ 1.4-3.0) than from Durango (~ 0.6-2.0).

All analyzed silicate glasses have chondrite-normalized REE patterns with decreasing concentrations from light to heavy REE (La_N/Yb_N = 13.5-35.0; Gd_N/Yb_N = 1.6-4.8) (Fig. 4.4a), and smooth dome-shaped PUM-normalized patterns enriched in highly incompatible trace elements (Rb, Ba, Th, U, Nb, Ta) at ~ 100 times the PUM concentrations (Fig. 4.4b). Most of the patterns exhibit a negative anomaly of Pb relative to adjacent REE (Fig. 4.4b). These concentrations coincide with those of the alkali basalts and olivine-nephelinites/basanites that host the xenoliths (Aranda-Gómez et al., 2005) (Fig. 4.4).

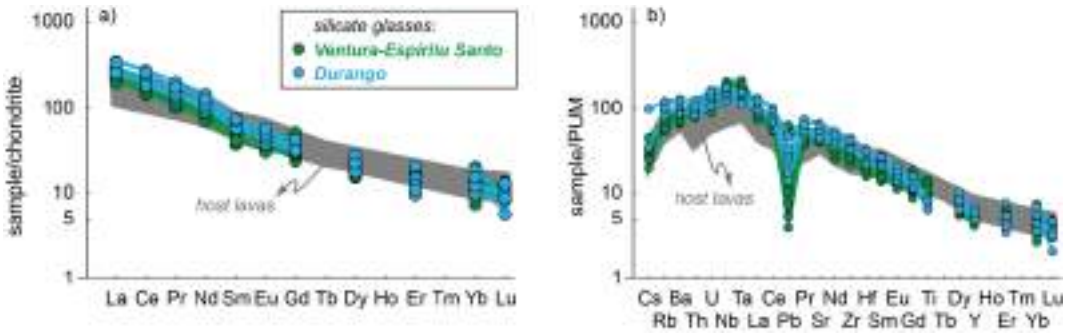

Figure 4.4. Chondrite-normalized concentrations of rare earth elements (a) and primitive upper mantle (PUM)-normalized concentrations of lithophile trace elements (b) (McDonough and Sun, 1995) in silicate glass of spinel peridotites from Ventura-Espíritu Santo (green circles) and Durango (blue circles). Grey field marks the composition of alkaline lavas that host the peridotite xenoliths (Heinrich and Besch, 1992; Aranda-Goméz et al., 2005).

4.3.3 Sulfide mineralogy

Based on their microstructural position and morphology, I identified three populations of BMS that are differently distributed in peridotites from the three volcanic fields. Intergranular sulfides (BMS_{int}) are the most common type in Santo Domingo, and they are also observed in Ventura-Espíritu Santo xenoliths. They consist of large (up to ~ 100 μm) grains with angular/polygonal shapes and straight-lined contacts against silicates and spinel, in part altered to iron oxides (Fig. 4.5a-c). Enclosed sulfides (BMS_{enc}) form tiny (~ 10 μm) subspherical blebs, which are included within silicates in Santo Domingo and Durango xenoliths (Fig. 4.5d-f). Finally, abundant grains of globular/rounded sulfide (10-50 μm) are scattered in interstitial glass veinlets (BMS_{gls}) in Ventura-Espíritu Santo and Durango xenoliths (Fig. 4.5g-i). These BMS_{gls} are occasionally attached to carbonates (Fig. 4.5g).

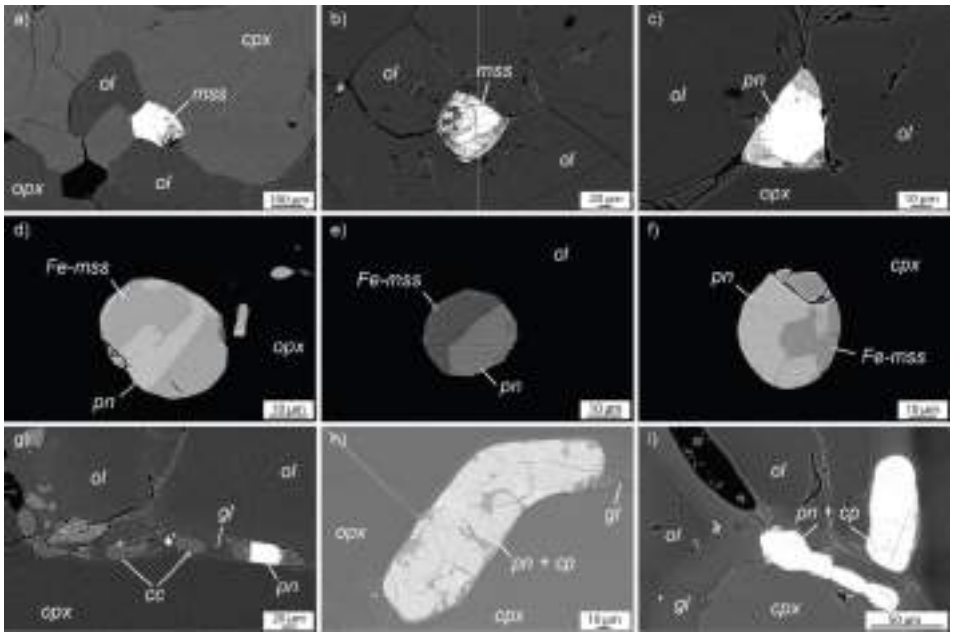

Figure 4.5. Backscattered electron images of intergranular (a, b, c), enclosed (d, e, f) and glass-hosted (g, h, i) base-metal sulfides in spinel peridotites from Santo Domingo, Ventura-Espíritu Santo and Durango volcanic fields. Mineral abbreviations are: mss – monosulfide solid solution; pn – pentlandite; cp – chalcopyrite; gl – silicate glass; cc - carbonate.

Intergranular BMS_{int} in Santo Domingo and Ventura-Espíritu Santo are mainly metal-deficient (metal/S = 0.83-0.95) monosulfide solid solution (mss_{int})

with Ni/(Ni+Fe) ranging between 0.09-0.56 (Fig. 4.6a) and Cu < 0.08 wt.% (Table S4.3 in the Appendix). However, several BMS_{int} are sulfur-deficient (metal/S = 1.09-1.15) pentlandite (pn_{int}) with Ni/(Ni+Fe) = 0.48-0.59 (Fig. 4.6a). Enclosed BMS_{enc} are either biphasic aggregates made up of Fe-rich mss [Ni/(Ni+Fe) = 0.09-0.29] and Ni-rich pentlandite [Ni/(Ni+Fe) = 0.54-0.57] in Santo Domingo (Fig. 4.5d-f), or single grains of mss with Ni/(Ni+Fe) = 0.36-0.59 in both Santo Domingo and Durango xenoliths (Fig. 4.6b).

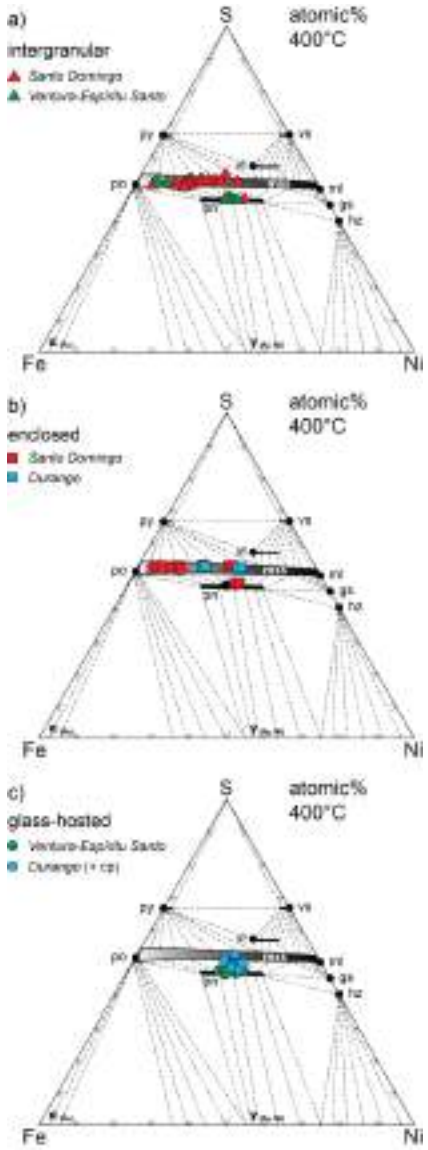

Figure 4.6. Major element compositions (atomic %) of intergranular (a, triangles), enclosed (b, squares) and glass-hosted (c, circles) base-metal sulfides in Santo Domingo (red), Ventura-Espíritu Santo (green) and Durango (blue) peridotite xenoliths, plotted in the Fe-Ni-S phase diagram at 400 °C (Kullerud et al., 1969). Mineral abbreviations are: mss – monosulfide solid solution; po – pyrrhotite; pn – pentlandite; ml – millerite; py – pyrite; hz – heazlewoodite; vs – vaesite; vl – violarite; gs – godlevskite.

Glass-hosted BMS_{gls} are single grains of pentlandite with Ni/(Ni+Fe) = 0.46-0.59 and Cu < 1.44 wt.% in Ventura-Espíritu Santo, or pentlandite + chalcopyrite intergrowths in Durango xenoliths (Fig. 4.6c). Abundant chalcopyrite intergrowths in the latter grains are reflected in high Cu contents (up to 9.85 wt.%) and slightly higher S contents (up to 35.0 wt.%) of their microprobe analyses (Table S4.3 in the Appendix).

4.3.4 In situ noble metals and Re-Os signatures of BMS

Base-metal sulfides have noble metal abundances that range 3.24-20.1 ppm for Os, 1.71-13.3 ppm for Ir, 2.62-31.5 ppm for Ru, 0.540-6.94 ppm for Rh, 0.164-61.5 ppm for Pt, 0.053-41.0 ppm for Pd, and 0.059-1.68 ppm for Au (Table S4.4 in the Appendix). Regardless of the sample locality, the different types of sulfide populations share similar concentrations of I-PGE (Os, Ir, Ru), Rh and Au (Fig. 4.7). However, both intergranular (pn_{int}) and glass-hosted (pn_{gls}) pentlandites are generally enriched in Pt (1.06-61.5 ppm) and Pd (7.74-41.0 ppm) compared with intergranular (mss_{int}) and enclosed (mss_{enc}) mss (Pt = 0.164-16.9 ppm; Pd = 0.050-11.2 ppm) (Fig. 4.7). The concentrations of I-PGE and Rh show well-defined positive mutual correlations, and they are uncorrelated with P-PGE (Pt, Pd) and Au. On the other hand, Pt and Pd abundances show rough co-variation in all the grains. The fact that all noble metals generally show constant count rates with respect to Ni in their time-resolved spectra (with the exception of Pt-Ir spikes in one mss_{enc}) suggests that these elements are mostly dissolved in the lattices of BMS. However, a sharp Au spike was detected in one pn_{gls} from Durango, which results in an anomalous high concentration of gold (5.98 ppm; Table S4.4). This observation is consistent with other grains analysed by LA-ICP-MS from La Breña (Durango), which contain nanosized inclusions of Pt and Au (González-Jiménez et al., 2020).

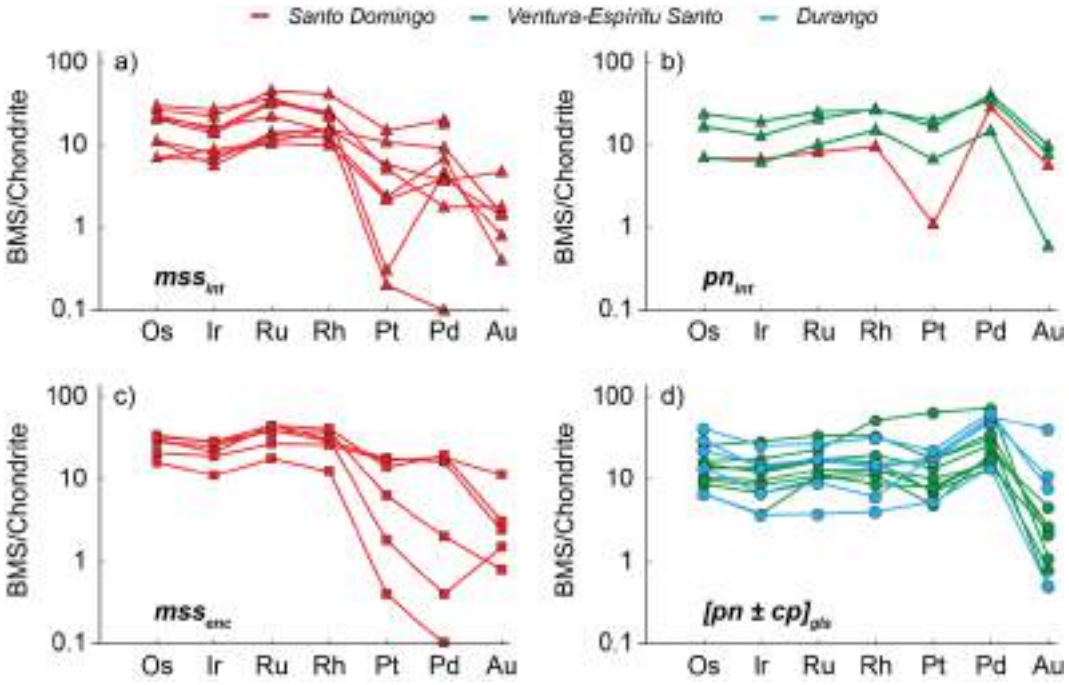

Figure 4.7. Chondrite-normalized abundances (Fischer-Gödde et al., 2010) of platinum-group elements and gold in intergranular monosulfide solid solutions (mss_{int}) (a), intergranular pentlandites (pn_{int}) (b), enclosed monosulfide solid solutions (mss_{enc}) (c), and glass-hosted pentlandite ± chalcopyrite aggregates ($pn \pm cp_{gls}$) (d) from Santo Domingo (red), Ventura-Espíritu Santo (green) and Durango (blue) peridotite xenoliths. Symbols as in Figure 4.6.

The shapes of chondrite-normalized PGE-Au patterns of BMS are rather homogeneous in each sulfide population. Intergranular mss_{int} in Santo Domingo xenoliths has mostly arch-shaped negatively sloping to flat patterns with Pd_N/Ir_N = 0.01-1.39 (Fig. 4.7a), whereas pn_{int} in Santo Domingo and Ventura-Espíritu Santo show slightly P-PGE enriched distributions (Pd_N/Ir_N = 1.88-4.14) (Fig. 4.7b). Enclosed mss_{enc} in Santo Domingo has patterns similar to those of intergranular mss, with flat I-PGE segments at ~ 10-100 times the chondritic proportions and negative slopes from Rh to Au (Pd_N/Ir_N = 0.01-0.97) (Fig. 4.7c). On the other hand, the chondrite-normalized PGE concentrations in glass-hosted BMS_{gls} from Ventura-Espíritu Santo and Durango mainly produce flat to positively sloping patterns with Pd_N/Ir_N = 1.07-8.40 (Fig. 4.7d).

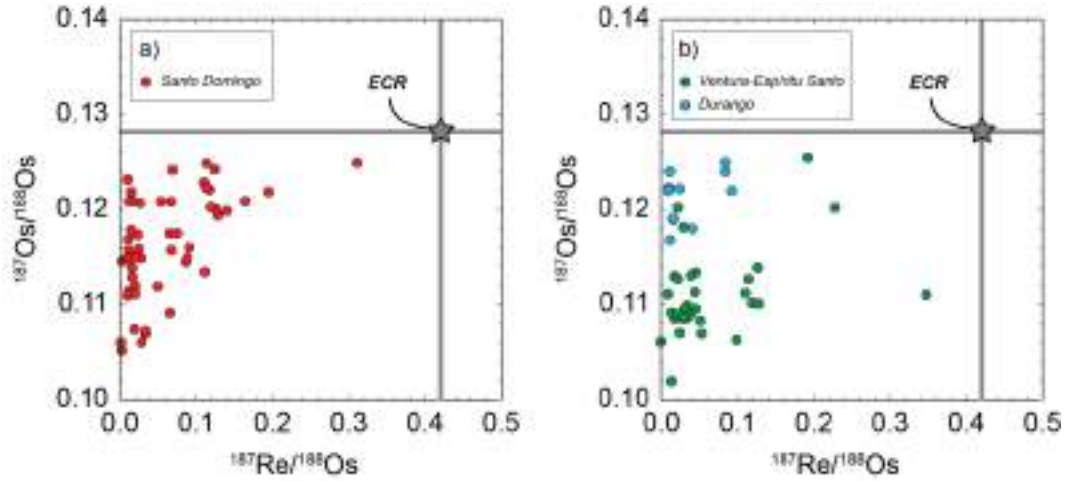

Figure 4.8. ***$^{187}Re/^{188}Os$ versus $^{187}Os/^{188}Os$ of base-metal sulfides in Santo Domingo (red circles) (a), and Ventura-Espíritu Santo (green circles) and Durango (blue circles) (b) peridotite xenoliths. Composition of the Enstatite Chondritic Reservoir (ECR, grey star) is from Walker et al. (2002).***

Intergranular and enclosed sulfides in Santo Domingo xenoliths (n = 55) have subchondritic $^{187}Os/^{188}$ Os ranging between 0.1053-0.1251 and $^{187}Re/^{188}Os$ spanning from 0.001 to 0.31 (Fig. 4.8a). Glass-hosted sulfides from Ventura-Espíritu Santo (n = 32) have subchondritic $^{187}Os/^{188}Os$ (0.1019-0.1255) that are uncorrelated with scattered $^{187}Re/^{188}Os$ (0.001-0.35) (Fig. 4.8b). Glass-hosted sulfides in Durango (n = 11) generally have more radiogenic $^{187}Os/^{188}Os$ compositions (0.1168-0.125) coupled with low $^{187}Re/^{188}Os$ (0.0108-0.093) (Fig. 4.8b). Re-depletion ages (T_{RD}) were plotted in probability density plots. Calculated T_{RD} for Santo Domingo and Ventura-Espíritu Santo sulfides yield similar peaks at 0.4-0.5, 1.0-1.1, 1.8-2.3, and 2.7-3.0 Ga (and a minor peak at 3.6 Ga in the case of Ventura-Espíritu Santo) (Fig. 4.9a, b), whereas for Durango sulfides they cluster at 0.5, 0.9 and 1.3 Ga (Fig. 4.9c).

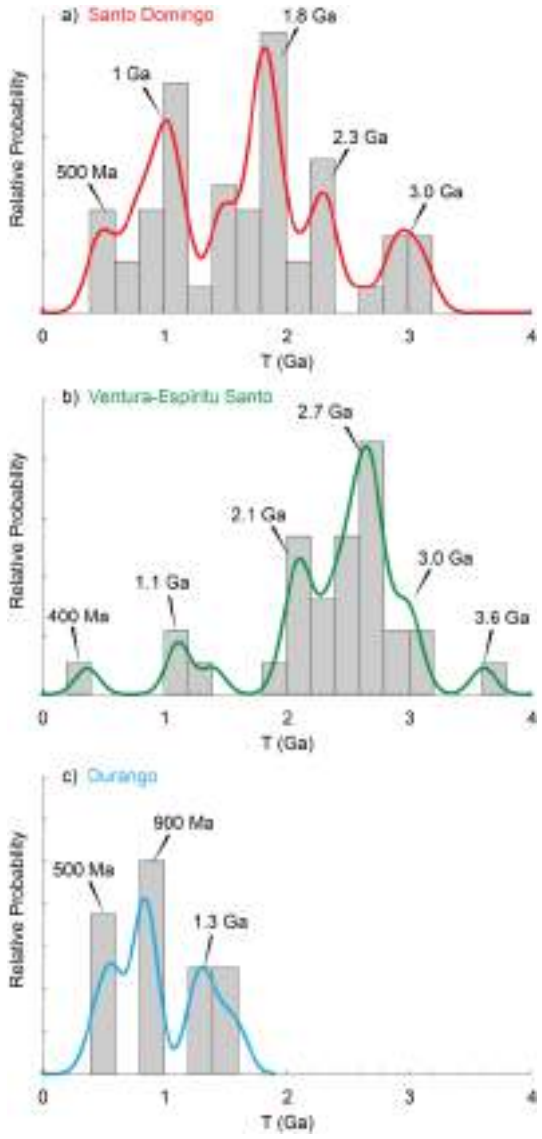

Figure 4.9. Probability density plots and histograms of rhenium-depletion model ages (T_{RD}) of base-metal sulfides in Santo Domingo (a), Ventura-Espíritu Santo (b) and Durango (c) peridotite xenoliths. A minimum uncertainty of 0.1 Ga was assumed for model ages, to avoid overemphasis on single data points determined by high internal precision (Pearson et al., 2007).

4.4 Discussion

4.4.1 Lithophile evidence for partial melting and alkaline metasomatism in the Mexican subcontinental lithospheric mantle

Most clinopyroxene grains from Durango (Ce_N/Yb_N = 0.01-0.02) and sample LP2 from Ventura-Espíritu Santo (Ce_N/Yb_N = 0.07-0.08) show strong fractionation of LREE relative to MREE-HREE (Figs. 4.3a, 4.10a). These clinopyroxenes also

have low concentrations of the most incompatible trace elements (Th, U, Nb) down to values below their detection limits (Fig. 4.3b), and strong depletion in Sr and Zr (Fig. 4.10b). All these characteristics are expected in residual clinopyroxene left after extraction of basaltic components from the mantle (e.g., Johnson et al., 1990). To constrain this process, I modelled the distribution of REE in mantle clinopyroxene in response to different degrees of non-modal fractional melting of garnet and spinel peridotites (Fig. 4.10c). The REE compositions of these clinopyroxenes match the model predictions for 2% initial partial melting in the garnet peridotite stability field, followed by 2% (sample LP2 from Ventura-Espíritu Santo) and 4% (samples from Durango) fractional melt extraction in the spinel-peridotite stability field (Fig. 4.10c).

Less LREE-depleted patterns (Ce_N/Yb_N = 0.14-0.51) in clinopyroxene from Santo Domingo and sample JH6 from Ventura-Espíritu Santo (Fig. 4.10a) are coupled with higher concentrations of other incompatible trace elements, such as Sr and Zr (Fig. 4.10b). This suggests that either trace elements systematics in this population of clinopyroxene reflect lower degrees of partial melting, or these grains partially re-equilibrated with silicate melts that interacted with the peridotite wall rock (e.g., Le Roux et al., 2007). The latter interpretation is most probable for two clinopyroxene grains from Durango, which have LREE-enriched patterns (Ce_N/Yb_N up to 1.37) that cannot be explained by models of mantle melting (Fig. 4.10c). Therefore, higher concentrations of Ba, Th, U, Nb, Sr and Zr in these grains (Fig. 4.3b) probably reflect interaction with alkaline melts enriched in highly incompatible trace elements (Baker et al., 1998).

Importantly, clinopyroxene in Santo Domingo and sample JH6 from Ventura-Espíritu Santo also have high Th-U concentrations (up to ~ 10 the PUM abundances, Fig. 4.3b) that are incompatible with a residual origin (e.g., Hauri et al., 1994). Positive anomalies of Th-U in mantle clinopyroxene are frequently coupled with progressive enrichment in LREE, and they are interpreted as products of chromatographic differentiation of melts during their percolation through the mantle (Navon and Stolper, 1987; Ionov et al., 2002; Raffone et al., 2009). However, increasing Th-U concentrations in clinopyroxene from Santo Domingo and Ventura-Espíritu Santo are not associated with a corresponding increase in LREE. This suggests that the Th-U enrichment in these clinopyroxenes

reflects the primitive signature of the metasomatic melt that reacted with this sector of lithospheric mantle, and is not due to melt differentiation during melt-rock reaction.

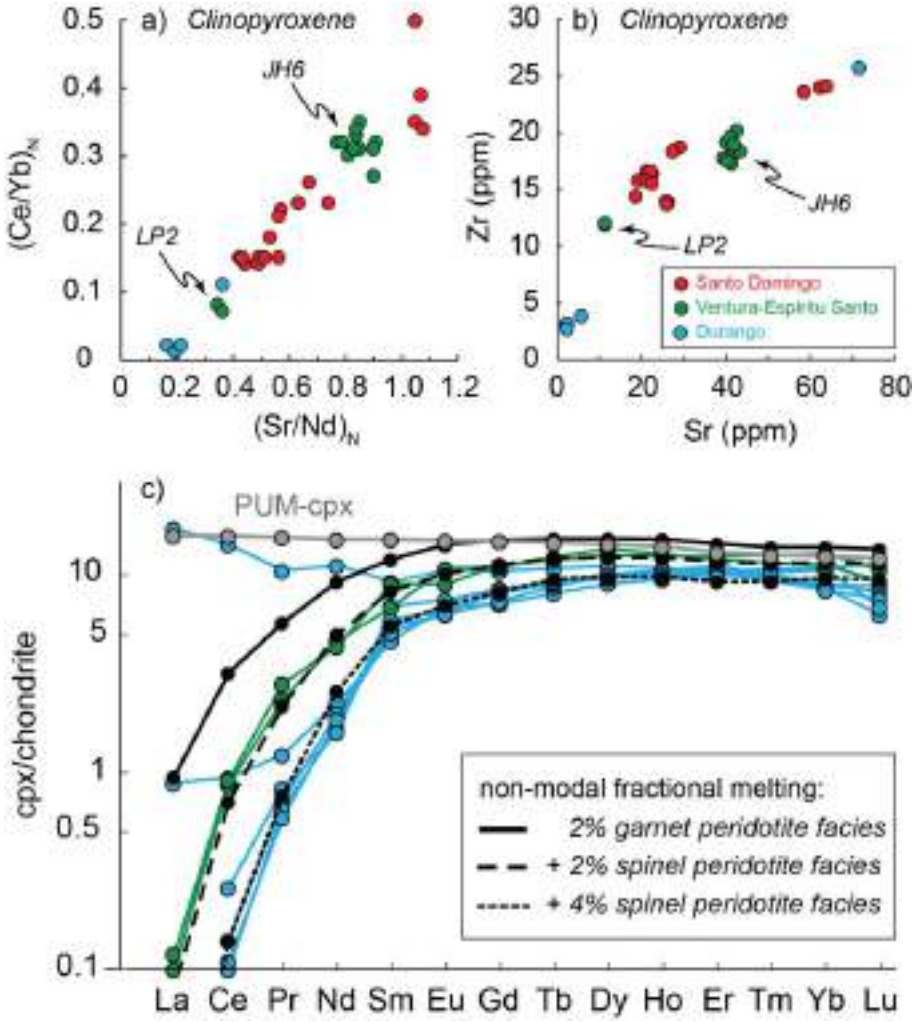

Figure 4.10. Chondrite-normalized (McDonough and Sun, 1995) $(Sr/Nd)_N$ vs. $(Ce/Yb)_N$ (a) and Sr vs. Zr concentrations (ppm) (b) of clinopyroxene in peridotite xenoliths from Santo Domingo (red circles), Ventura-Espíritu Santo (green circles) and Durango volcanic fields (blue circles). (c) Chondrite-normalized REE patterns of clinopyroxene in Ventura-Espíritu Santo (sample LP2) and Durango peridotite xenoliths compared with non-modal fractional melting curves of clinopyroxene in PUM (grey line, McDonough and Sun, 1995) in the garnet-peridotite facies (solid black line) [source and melting olivine:orthopyroxene:clinopyroxene:garnet modal proportions 0.57:0.21:0.13:0.09 and 0.05:0.15:0.97:0.14, respectively (Walter 1998 at 3 GPa)] followed by melting in the spinel peridotite facies (dashed black lines) [source and melting olivine:orthopyroxene:clinopyroxene modal proportions 0.54:0.28:0.18 and 0.11:0.59:0.53, respectively (Niu, 1997 at 1.5 GPa)]. Modes of the spinel peridotite source after partial melting in the garnet stability field are calculated using the equation of Johnson et al. (1990). Partition coefficients from Bedini and Bodinier (1999), Donnelly et al. (2004) and Su and Langmuir (2003).

This geochemical signature, together with the common presence of amphibole in the Santo Domingo peridotites, support a hydrous alkaline affinity of the melt that interacted with the SCLM beneath Central Mexico (e.g., Grégoire et al., 2002; Ionov et al., 2002; Raffone et al., 2009). This interpretation is also consistent with previous studies on spinel lherzolite xenoliths from La Joya maar (Ventura-Espíritu Santo volcanic field), which document the interaction of peridotites with basanite melt that produced FeO-Na_2O and LREE enrichments in clinopyroxene (Liang and Elthon 1990). Inclusions of CO_2-rich fluid and amphibole in clinopyroxene from Santo Domingo and Ventura-Espíritu Santo also support metasomatism by an alkaline agent with a hydrous/carbonate-rich component (Dávalos-Elizondo et al., 2016; Levresse et al., 2016). The variability of enrichment in incompatible elements shown by clinopyroxene from the three studied volcanic fields (Fig. 4.3) probably reflects local variation in the chemical-physical parameters of melt-rock reaction (e.g., melt fraction, melt velocity, crystal size) (Navon and Stolper, 1987; Takazawa et al., 1992). The strong depletion of Ba, Nb and Ta in clinopyroxene in the Santo Domingo and Ventura-Espíritu Santo peridotites (Fig. 4.3b) can be ascribed to the preferential subsolidus partitioning of these elements into coexisting amphibole (Tiepolo et al., 2000; Ionov et al., 2002).

In summary, the geochemical signatures of clinopyroxene in mantle xenoliths from the Santo Domingo, Ventura-Espíritu Santo and Durango volcanic fields indicate that the Mexican lithospheric mantle beneath Mesa Central experienced melt extraction that started within the stability field of garnet peridotite (> 20 kbar), and continued in different degrees within the spinel peridotite field. Moreover, this sector of the lithospheric mantle interacted with hydrous alkaline silicate melts, possibly during the intraplate magmatism that accompanied extensional tectonism in the Basin and Range Province since the Late Oligocene (Luhr et al., 2001; Ferrari et al., 2018).

4.4.2 Origin of enclosed and intergranular base-metal sulfides (BMS)

Enclosed BMS (BMS_{enc}) form tiny, silicate-hosted inclusions made of Fe-rich mss + pentlandite aggregates (Fig. 4.5d-f), which probably were formed by the sub-

solidus re-equilibration of former mss (mss_{enc}) upon cooling at T < 610 °C (Kullerud et al. 1969). In addition, mss_{enc} display arch-shaped negatively sloping chondrite-normalized PGE patterns (Pd_N/Ir_N < 1) (Fig. 4.7c), typical of residual mss that retained most compatible I-PGE after the extraction of Ni-Cu-rich sulfide melts enriched in incompatible P-PGE (Alard et al., 2000; Bockrath et al., 2004; Ballhaus et al., 2006; González-Jiménez et al., 2014; Lorand and Luguet, 2016). Interestingly, intergranular mss (mss_{int}) have chondrite-normalized PGE distributions rather similar to those of mss_{enc} (Fig. 4.7a), thus suggesting a common origin for both types of mss. Grain boundary migration during deformation/annealing of the peridotite matrix would have distributed residual mss either at junctions between rock-forming minerals (mss_{int}) (Fig. 4.5a-c) or within growing silicates (mss_{enc}) (Fig. 4.5d-f) (Griffin et al., 2002; Tassara et al., 2018).

Experimental work shows that the partitioning of PGE in the mantle is primarily governed by incongruent melting of mss at 1000-1200 °C, thus resulting in a crystalline residual Fe-rich mss and a Ni-Cu-rich sulfide melt counterpart (e.g., Bockrath et al., 2004; Ballhaus et al., 2006). To further constrain the origin of these BMS, I modelled the PGE variations produced by incongruent melting of "primitive sulfide" in a PUM source (280 ppm S and ~ 30 ppb ∑PGE, assumed to be entirely hosted in sulfides; Becker et al., 2006; Fischer-Gödde et al., 2011), by using the mss-sulfide melt partitioning coefficients of Ballhaus et al. (2006). I envisaged a fractional melting scenario based on the progressive extraction of different fractions of Ni-Cu-rich sulfide melt (X_{SL}) relative to mss left in the peridotite residuum. Segregation of X_{SL} ranging between 0.1 and 0.5 adequately reproduces the Pt-Pd depletion relative to compatible I-PGE of both mss_{enc} and mss_{int} in the Santo Domingo xenoliths (Fig. 4.11a). These fractions of sulfide melt, which are expected to be extracted from the mantle source along with the silicate melt, correspond to 2-12 % non-modal fractional melting assuming S solubility of 1000 ppm (Mavrogenes and O'Neill, 1999), and are therefore consistent with the melting degrees inferred from REE contents in clinopyroxene (see previous section). The fact that all mss_{enc}, with the exception of one grain, plot in a well-defined linear correlation between Pd_N/Ir_N and Ni/(Ni+Fe) (Fig. 4.11b) further indicates that these BMS formed by incongruent melting of mss

that became increasingly poorer in P-PGE as melting extracted Ni-Cu-rich sulfide melts.

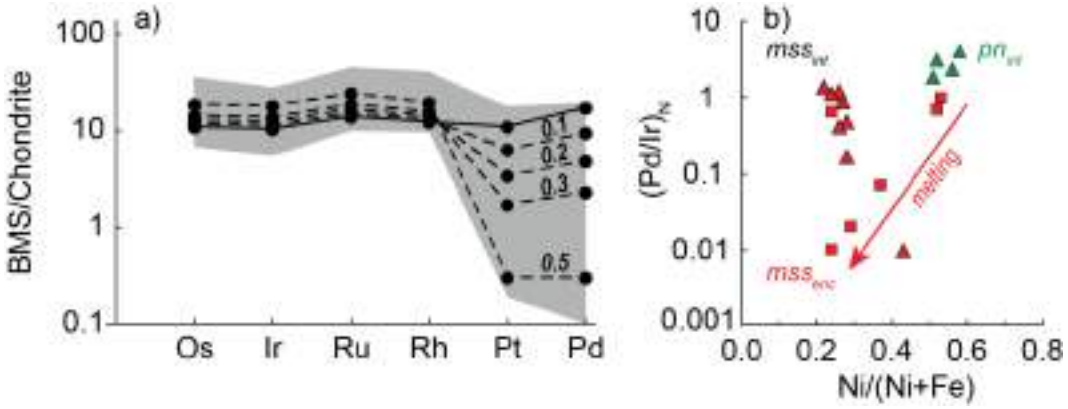

Figure 4.11. (a) Chondrite-normalized (Fischer-Gödde et al., 2010) PGE patterns of intergranular and enclosed mss in peridotite xenoliths from Central Mexico (grey field), compared with PGE variations computed for different extents of incongruent melting of "primitive sulfide" in PUM (dashed lines) (Becker et al., 2006; Fischer-Gödde et al., 2011). Labels indicate the fractions of Ni-Cu-rich sulfide melt (X_{SL}) extracted from mss. (b) Ni/(Ni+Fe) vs. $(Pd/Ir)_N$ of intergranular mss (mss_{int}), intergranular pentlandite (pn_{int}) and enclosed mss (mss_{enc}). Symbols as in Figure 4.6.

On the other hand, mss_{int} in the Santo Domingo xenoliths deviate from the correlation expected for such a melting trend (Fig. 4.11b), thus suggesting that their major element compositions may have shifted toward a Fe-enriched end-member. Ni/(Ni+Fe) ratios in mss_{int} show no co-variation with Fe/Ni ratios in coexisting olivine, which rules out that the sulfide-olivine partitioning equilibrium played any significant role in fixing the major element compositions of these BMS (Brenan and Caciagli, 2000). Moreover, Fe-Ni exchange with surrounding silicates would have affected all sulfide grains regardless of whether they are currently enclosed in silicates or intergranular. Therefore, all these observations favour the hypothesis that, despite preserving an original "residual" PGE signature, intergranular mss re-equilibrated with melts percolating through the SCLM while modifying their major element compositions, possibly during the same alkaline metasomatism event recorded by trace elements in clinopyroxene (see previous section). The iron enrichment observed in mss_{int} can be explained by the fact that primitive silicate magmas that attain sulfide saturation generally equilibrate with a Fe-rich sulfide (Patten et al., 2013).

In summary, both enclosed and intergranular mss preserve residual PGE signatures that are consistent with variable degrees of partial melting of the SCLM beneath Central Mexico. The subsequent interaction of Santo Domingo and Ventura-Espíritu Santo peridotites with metasomatic silicate melts likely changed the major element compositions of mss_{int} without disturbing their original PGE systematics (González-Jiménez et al., 2014). This metasomatic event may also have triggered the precipitation of intergranular Ni-rich pentlandite (pn_{int}), whose chondrite-normalized PGE patterns are flat to slightly positive (Pd_N/Ir_N = 1.88-4.14) (Fig. 4.7b), suggesting that they crystallized from trapped fractions of sulfide melt upon the percolation of silicate magmas (e.g., Wang et al., 2009).

4.4.3 Origin of glass-hosted sulfides in Ventura-Espíritu Santo and Durango xenoliths

The Ventura-Espíritu Santo and Durango mantle peridotites contain abundant droplet-shaped and globular base-metal sulfides that are embedded in interstitial silicate glass (BMS_{gls}) (Fig. 4.5g-i). This glass forms an interconnected network of films and veinlets with sharp contacts against silicates, thus suggesting that glass represents the infiltration of external melt into mantle peridotites (Neumann and Wulff-Pedersen, 1997; González-Jiménez et al., 2014; Tassara et al., 2018). Silicate glass displays trace element compositions enriched in most incompatible elements such as LREE, Rb, Ba, Th, U, Nb and Ta, overlapping those of alkaline basalts and basanites in which the xenoliths are hosted (Fig. 4.4) (Heinrich and Besch, 1992; Aranda-Gómez et al., 2005). However, compared to the host magmas, silicate glass in the Ventura-Espíritu Santo and Durango peridotites has higher concentrations of SiO_2, Al_2O_3 and Na_2O, and lower contents of MgO and FeO. This trend may be due to olivine fractionation upon infiltration and reaction with the host peridotites, as is also suggested by decreasing MgO/Al_2O_3 ratios with increasing SiO_2 contents (Fig. 4.12a). Therefore, textural and compositional observations indicate that interstitial silicate glass is the product of infiltration and quenching of Quaternary host-magmas during the entrapment and transport of mantle peridotite xenoliths to the surface (Neumann and Wulff-Pedersen, 1997; González-Jiménez et al., 2014; Tassara et al., 2018).

Glass-hosted sulfides (BMS_{gls}) are pentlandite ± chalcopyrite intergrowths with globular morphology (Fig. 4.5g-i), which suggests that they crystallized from droplets of molten Ni-Cu-rich sulfides that were immiscible in silicate melts (Andersen, 1987; Patten et al., 2012; Zelenski et al., 2017). These sulfide droplets may have formed by (1) incongruent melting of pre-existing mss and entrained in silicate magma during its segregation from the mantle source, or (2) sulfide saturation of a silicate magma undergoing differentiation upon its interaction with wall-rock peridotite (Jenner et al., 2010; Tassara et al., 2018). The Ni-Cu-rich sulfide melts extracted by incongruent melting of mantle mss usually have lower I-PGE concentrations than BMS_{gls} (Alard et al., 2000, 2011; Ballhaus et al., 2006). Instead, BMS_{gls} have flat to slightly positive PGE patterns (Fig. 4.7d), such as those that are commonly reported in mantle sulfides segregated from silicate magmas by liquid immiscibility (Tassara et al., 2018). However, early-segregated immiscible sulfide melts in equilibrium with primitive silicate melts have Fe-Ni-rich compositions (Li and Audètat, 2012; Zhang, 2015) that eventually precipitate assemblages dominated by mss (Jenner et al., 2010; Patten et al., 2012, 2013), which are in stark contrast with the pentlandite ± chalcopyrite nature of BMS_{gls}. These observations therefore indicate that BMS hosted in silicate glass of the Ventura-Espíritu Santo and Durango peridotites derive from crystallization of the sulfide fraction of evolved silicate magmas that reached sulfide saturation upon their interaction with wall-rock peridotite. Indeed, percolating silicate melts that undergo progressive differentiation towards silica-rich compositions may attain late-stage saturation in a highly evolved Cu-rich sulfide melt (Jenner et al., 2010; Greaney et al., 2017; Costa et al., 2021), which may explain the crystallization of the pentlandite ± chalcopyrite assemblage of BMS_{gls}. The rough correlation between Cu abundances of BMS_{gls} and SiO_2 concentrations of their host silicate glass (Fig. 4.12b) may underpin such explanation. Therefore, these observations support the hypothesis that progressive infiltration and interaction of host alkaline magmas within mantle peridotite caused their differentiation towards silica-rich compositions. This process would have triggered the segregation of immiscible droplets of Ni-Cu-rich sulfide melts that eventually precipitated glass-hosted sulfides as those present in the Ventura-Espíritu Santo and Durango mantle xenoliths.

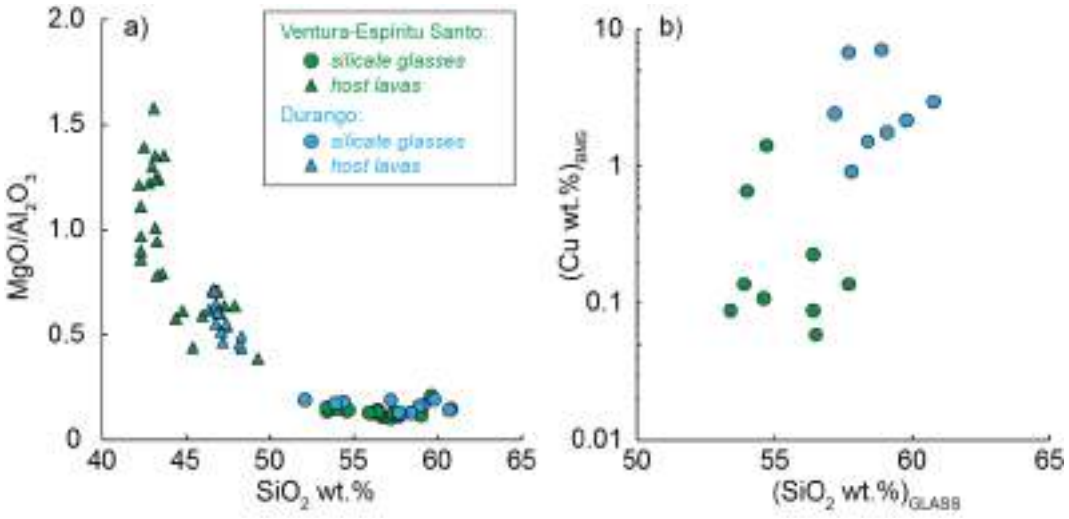

Figure 4.12. (a) SiO_2 abundances (wt.%) vs. MgO/Al_2O_3 of silicate glasses in peridotite xenoliths (circles) and their host alkaline lavas (triangles) from Ventura-Espíritu Santo (green) and Durango (blue) volcanic fields. (b) Cu abundances in glass-hosted sulfides vs. SiO_2 concentrations of their corresponding host silicate glass (wt.%) in Ventura-Espíritu Santo and Durango peridotite xenoliths.

4.4.4 Age and provenance of the lithospheric mantle blocks beneath central Mexico

Most enclosed and intergranular sulfides in the Santo Domingo xenoliths are residual mss left after variable degrees of partial melting in the mantle. Consistently, these BMS have subchondritic $^{187}Os/^{188}Os$ and $^{187}Re/^{188}Os$ values (Fig. 4.8a), which suggest that they evolved with low time-integrated Re/Os due to progressive extraction of incompatible Re by partial melting (Alard et al., 2002; Pearson et al., 2002; Griffin et al., 2002). Glass-hosted BMS from Ventura-Espíritu Santo and Durango have similar subchondritic $^{187}Os/^{188}Os$ uncorrelated with $^{187}Re/^{188}Os$ (Fig. 4.8b). This implies that BMS_{gls} inherited the heterogeneous Os-isotopic signature of the ancient mantle source of host-alkali lavas, now quenched into the glass. The fact that the BMS textural populations in each sample have homogeneous major and trace element signatures suggests that the also the Re-Os isotopes were not influenced by their mineralogical/compositional variability.

Probability density plots of T_{RD} from each volcanic field (Fig. 4.9) define multiple age peaks that partially overlap with global pulses of continental growth associated with major events of mantle melting (Fig. 4.13) (Condie, 1998; Pearson et al., 2007). The Santo Domingo and Ventura-Espíritu Santo BMS yield Mesoproterozoic (~ 1.1-1.0 Ga) age peaks that are broadly consistent with the Nd model ages and U-Pb zircon ages of the Grenville basement of the overlying Oaxaquia crust (Fig. 4.13a, b) (Ruíz et al., 1988; Weber et al., 2010). However, Paleoproterozoic (2.3, 2.1-1.8 Ga) and Archean (3.6, 3.0-2.7 Ga) age populations (Fig. 4.13a, b) reveal the presence of fragments of older SCLM beneath this sector of Oaxaquia, thus ruling out the idea that the whole terrane formed in the Mesoproterozoic as an intra-oceanic arc in the peri-Gondwana realm (Weber et al., 2010; Ortega-Gutiérrez et al., 2018).

On the other hand, the Durango BMS yield T_{RD} peaks at ~ 1.3 Ga and 900 Ma (Fig. 4.9c), thus indicating that the growth of continental crust in the Central terrane occurred mostly during the Grenville orogeny in the Mesoproterozoic. These major age peaks imply that the Central terrane did not accrete as a Cordilleran-type terrane during the Pacific evolution of western Mexico, like the adjacent Mesozoic Guerrero block that has notably younger T_{RD} ages of stabilization of the lithospheric mantle at ~ 300 Ma and subduction-related reworking at ~ 220 and 130 Ma (Centeno-García et al., 2008; Gonzáez-Jiménez et al., 2017a). Rather, the presence of Meso- to Neoproterozoic (1.3-0.9 Ga) and Paleozoic (~ 500 Ma) age populations in both the Oaxaquia and Central terranes suggests that the latter would have likely accreted to Oaxaquia during the Rodinia assembly (~ 1.0 Ga), before both were reworked in the Early Paleozoic as a single coherent block (Ruíz et al., 1988).

Paleoproterozoic (2.3-1.8 Ga) and Archean (3.6-2.7 Ga) ages in the Oaxaquia SCLM are not documented in crustal exposures of the region (Fig. 4.13a, b) (Solari et al., 2022). This observation provides further evidence that off-craton regions of the continental crust may be underlain by Archean-age and thin SCLM, becoming progressively fertile and unbuoyant as a consequence of protracted tectono-thermal activity (Lee et al., 2001; Griffin et al., 2011). The lack of a thick and buoyant cratonic root beneath Central Mexico may have caused the originally exposed early continental crust to be extensively reworked and/or

erased during multiple Wilson cycles. However, similar age peaks are characteristics of the Laurentia cratonic crust in SW United States (i.e., Mojavia terrane, Bennett and DePaolo, 1987; Rämö and Calzia, 1998; Lee et al., 2001; Rudnick and Lee, 2002), and the Amazonian craton in South America (Nance et al. 2009). Therefore, the presence of this ancient lithospheric mantle beneath Central Mexico raises the question whether part of the Oaxaquia block represents 1) a fragment of Laurentia displaced southeastwards by left-lateral transform movements during the break-up of Pangea (Anderson and Silver, 2005), or (2) a Gondwana-derived continental sliver, with an Archean-Paleoproterozoic SCLM that was accreted to North America during the assembly of Pangea in the Late Paleozoic (Appalachian orogeny, Steltenpohl et al., 2004; Tian et al., 2021). In order to assess these two hypotheses, I compared T_{RD} ages of mantle sulfides from Central Mexico with U-Pb ages of detrital zircons in Paleozoic metasedimentary rocks from NW (Laurentia-derived) and NE (Gondwana-derived) Mexico (Nance et al., 2007; Gehrels and Pecha, 2014). While a Late Archean event (~ 3.0-2.7 Ga) of continental growth is recorded in all continents, the massive production of juvenile crust at ~ 1.8 Ga is typical of the Laurentia craton (Fig. 4.13) (Condie et al., 1998; Whitmeyer and Karlstrom, 2007; Gehrels and Pecha, 2014). Moreover, both the crust and lithospheric mantle of the Mojavia terrane in SW United States share similar Paleoproterozoic (2.3-2.1 Ga) and Late Archean (2.6 Ga) ages (Bennett and DePaolo, 1987; Rämö and Calzia, 1998; Lee et al., 2001; Rudnick and Lee, 2002). However, an Early Paleozoic event of crustal production is not recorded in the SW margin of Laurentia, and the ~ 500 Ma peak in Central Mexico more closely resembles the age of the Pan-African-Brasiliano orogeny typical of Gondwana-derived terranes (Nance et al., 2007, 2009). Therefore, although the observed Paleoproterozoic ages are consistent with a Laurentia derivation, Early Paleozoic ages suggest that the Oaxaquia-Central composite block was detached from North America before the Pangea assembly event.

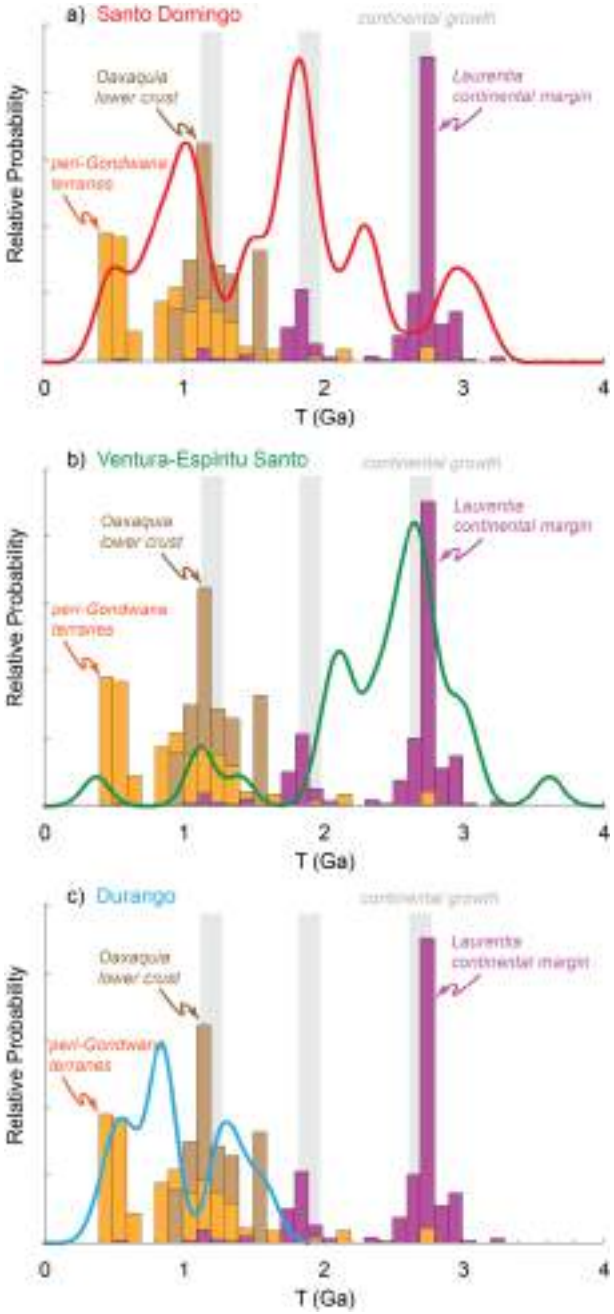

Figure 4.13. Probability density plots of T_{RD} model ages of sulfides in the SCLM of the Oaxaquia terrane (Santo Domingo and Ventura-Espíritu Santo peridotite xenoliths) and Central terrane (Durango peridotite xenoliths). Histograms of U-Pb ages of detrital zircons from peri-Gondwana terranes (orange) (Granjeno complex in NE Mexico, Nance et al., 2007), U-Pb ages of zircons from the Oaxaquia lower crust in central-southern Mexico (brown, Weber et al., 2010), and U-Pb ages in detrital zircons from the Laurentia continental margin (purple) (Paleozoic metasedimentary rocks from Sonora in NW Mexico, Gehrels and Pecha, 2014) are shown for comparisons. Grey columns mark the ages of global episodes of continental growth (Condie, 1998).

All these observations thus suggest that part of Oaxaquia could represent a fragment of the Laurentia craton (Fig. 4.14a), which split away from North America during the Rodinia break-up and evolved as a peri-Gondwana block from

the Neoproterozoic to Paleozoic (Fig. 4.14b). This interpretation reconciles kinematic reconstructions of Rodinia's configuration (AUSWUS model, Karlstrom et al., 1999; Burrett and Berry, 2000), which require the presence of Oaxaquia sliver as a linking segment of the Grenville belt between Australia and Laurentia, with paleontological evidence of Gondwana-type fauna in Oaxaquia throughout the Paleozoic (Ortega-Gutiérrez et al., 1995, 2018). In this scenario, the Mojave Sonora megashear might have acted as a major long-lived transfer fault associated with multiple orogenic cycles and continental break-up events (Silver and Anderson, 1974; Dickinson and Lawton, 2001; Anderson and Silver, 2005).

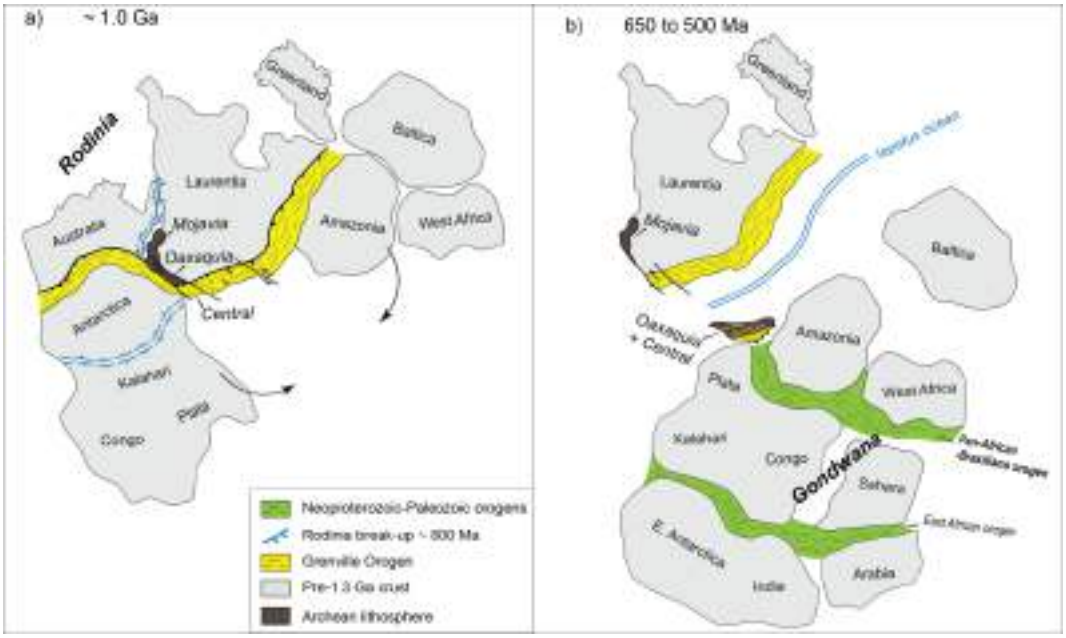

Figure 4.14. Reconstruction of the paleotectonic evolution of the Oaxaquia and Central terranes since Mesoproterozoic (a) to Neoproterozoic-Early Paleozoic (b). Modified from Karlstrom et al. (1999), Johansson (2014) and Stern (1994).

4.4.5 Metallogenic architecture of the continental lithosphere in central Mexico

The peridotite xenoliths from Santo Domingo, Ventura-Espíritu Santo and Durango volcanic fields provide a direct overview of the SCLM architecture beneath the Mesa Central (Fig. 4.1). This physiographic plateau corresponds to a

thin and topographically elevated continental crust, bounded by thickened crustal blocks both to the west (Sierra Madre Occidental volcanic belt) and to the east (Sierra Madre Oriental Laramide orogen) (see Fig. 4.2 in Nieto-Samaniego et al., 2007; Fitz-Díaz et al., 2018) (Fig. 4.15). An exceptional characteristic of this region is the anomalous number of distinct types of magmatic-hydrothermal ore deposits that are located along its structural limits, which coincide with regional WNW-ESE (San Luís – Tepehuanes, to the west) and N-S (Taxco – San Miguel de Allende, to the east) fault systems (Fig. 4.1b) (Camprubí and Albinson, 2007; Nieto-Samaniego et al., 2007). The hypermineralization around the Mesa Central can be explained by the conjoined role of the episodic reactivation of inherited structural corridors and the exceptionally vigorous continental arc volcanism of the Sierra Madre Occidental as it progressed eastward into the region, most notably culminating in the Oligocene (Camprubí et al., 2003; Camprubí, 2013). The concurrence of these geological factors particularly favourable for the genesis of ore deposits may explain why the San Luís – Tepehuanes fault zone, along the western and southern borders of the Mesa Central, hosts such a great diversity of ore mineralizations including: (1) the Cerro de Mercado shallow (hypabyssal to volcanic) IOCG deposit, (2) sulfide skarns or porphyry-type deposits (e.g., San Martín, Francisco I. Madeiro), (3) world-class (Fresnillo, Zacatecas, Guanajuato) and numerous smaller Ag-rich intermediate to low sulfidation epithermal deposits, and (4) Sn vein deposits associated with F-rich rhyolites and rhyodacites (Camprubí, 2013).

T_{RD} model ages of BMS in Santo Domingo, Ventura-Espíritu Santo and Durango peridotites (Fig. 4.9, 4.13) show that the hypermineralized crust along the boundaries of Mesa Central is controlled by inherited translithospheric boundaries defined by the underlying Archean-age subcontinental lithospheric mantle (Fig. 4.15). This fragment of originally cratonic SCLM formed in the Late Archean-Paleoproterozoic, reworked in the Mesoproterozoic (Grenville orogeny) and finally assembled with adjacent blocks along Paleozoic and Mesozoic suture zones (see previous section). Therefore, the western border of Mesa Central (i.e., the ~ 700 km long San Luís – Tepehuanes fault system) corresponds to the suture zone between the Archean-Proterozoic SCLM of the Oaxaquia-Central composite block and the Mesozoic Cordilleran-derived Guerrero terrane, which accreted

along the western Pacific margin of the Mexican lithosphere in the Jurassic (Camprubí, 2017; Centeno-García, 2017; González-Jiménez et al., 2017a, b). On the other hand, the nature and age of the SCLM lying beyond the eastern border of Mesa Central (i.e., the N-S trending Taxco – San Miguel de Allende fault system) is currently unknown. This fault system coincides with a paleogeographic boundary in the Mesozoic cover and a sharp increase in crustal thickness (Alaniz-Álvarez et al., 2005, 2007), suggesting it also marks a major trans-lithospheric structure (Nieto-Samaniego et al., 2007) that separates SCLM domains with different ages and/or provenance.

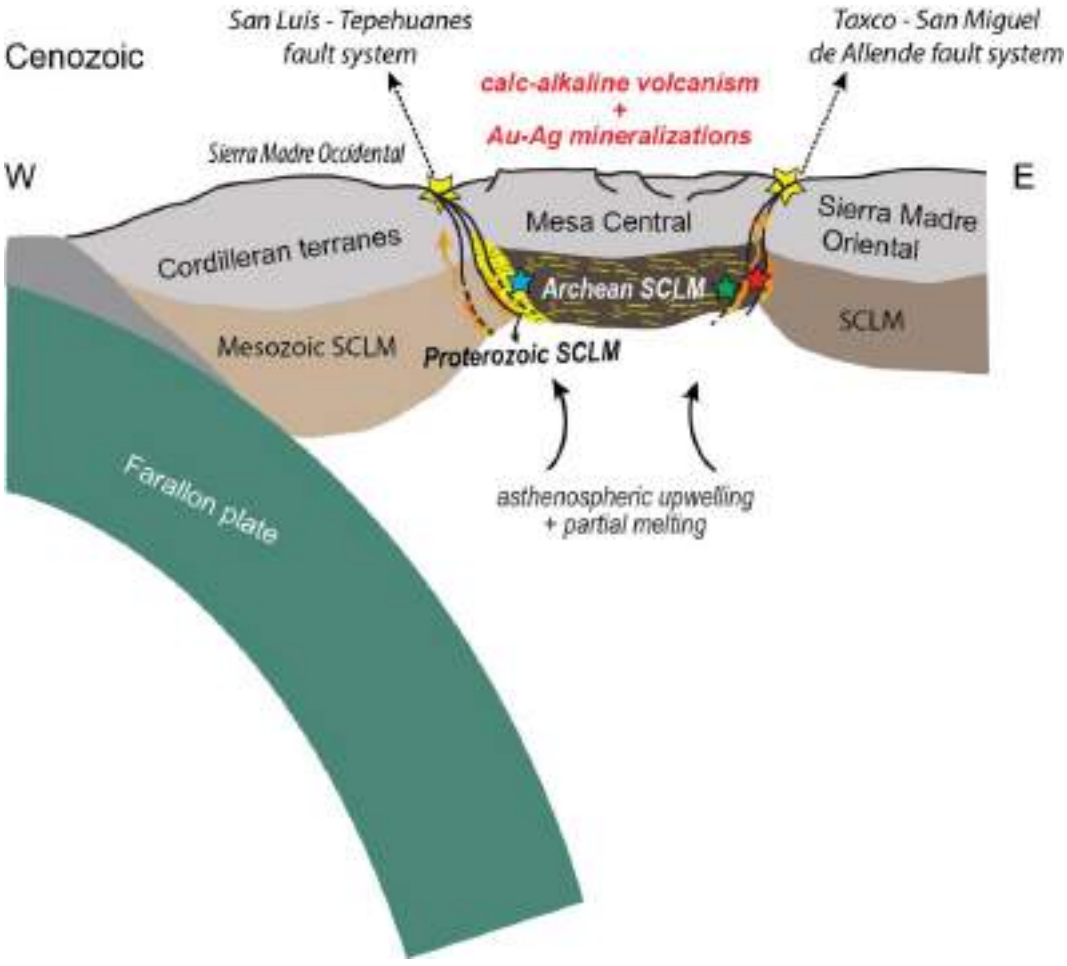

Figure 4.15. Geotectonic sketch proposed for the metallogenic evolution of Central Mexico during the Cenozoic. Stars indicate the inferred locations of mantle peridotite xenoliths studied in this work (Santo Domingo: red, Ventura-Espíritu Santo: green, and Durango: blue), and the locations of Au-Ag epithermal ores (yellow) associated with fault systems bordering the Mesa Central. The SCLM of the Oaxaquia and Central terrane are marked in dark grey and yellow, respectively. Orange arrows indicate the ascent of mineralizing magmas/fluids.

Overall, these observations support that the fault zones bordering the Mesa Central represent deep trans-lithospheric lineaments bounding a fragment of originally cratonic, thin and fertile Archean SCLM. The re-activation of these major trans-lithospheric boundaries during the subduction-related evolution of Mexico since the Mesozoic (Centeno-García, 2017) probably acted as 1st order pathways for focusing the ascent of ore-productive magmas and fluids feeding the crust (Fig. 4.15) (Begg et al., 2009). These observations provide further evidence for the key-role of large-scale terrane boundaries suturing the architecture of continental lithosphere in controlling the loci of deposition of magmatic-hydrothermal ores in the crust (Begg et al., 2010, 2018; Griffin et al., 2013).

4.5 Appendix

Table S4.1. Representative major element compositions (wt.%) of rock-forming minerals and silicate glass in Santo Domingo (SD), Ventura-Espíritu Santo (VES) and Durango (DU) volcanic fields. Samples labels refer to their maar locality: Joya Contreras (JC), Joya Prieta (JP), Santo Domingo (SD), Laguna de los Palau (LP), Joya Honda (JH) and La Breña (LB).

Volcanic field	*SD*	*SD*	*SD*	*SD*	*SD*	*SD*	*SD*	*SD*
Sample	JC11a	JC11a	JC11a	JC11a	JC15a	JC15a	JC15a	JC15a
Mineral	ol	opx	cpx	gl	ol	opx	cpx	gl
SiO_2	41.2	55.0	51.5	-	40.3	55.1	52.4	-
TiO_2	0.005	0.112	0.423	-	0.007	0.123	0.507	-
Al_2O_3	0.022	4.46	5.63	-	0.025	4.49	6.50	-
Cr_2O_3	0.000	0.388	0.983	-	0.000	0.417	0.880	-
FeO	9.56	6.94	2.79	-	10.4	6.88	3.12	-
MnO	0.138	0.158	0.080	-	0.172	0.122	0.099	-
MgO	48.7	32.0	15.3	-	48.5	32.2	14.9	-
CaO	0.252	0.807	20.9	-	0.282	0.827	20.2	-
Na_2O	-	0.153	1.63	-	-	0.105	1.81	-
K_2O	-	0.000	0.000	-	-	0.000	0.000	-
Total	100.3	100.1	99.2	-	100.0	100.3	100.4	-
Mg#	90.1	89.2	90.7	-	89.2	89.3	89.5	-

Volcanic field	*SD*	*SD*	*SD*	*SD*	*SD*	*SD*	*SD*	*SD*
Sample	JC21	JC21	JC21	JC21	SD10	SD10	SD10	SD10
Mineral	ol	opx	cpx	gl	ol	opx	cpx	gl
SiO_2	41.1	54.6	51.6	-	40.7	55.4	52.7	-
TiO_2	0.000	0.108	0.489	-	0.000	0.121	0.485	-
Al_2O_3	0.030	4.15	6.58	-	0.015	4.00	6.09	-
Cr_2O_3	0.000	0.371	0.935	-	0.023	0.409	0.933	-
FeO	10.4	6.95	3.06	-	10.0	6.63	2.57	-
MnO	0.152	0.139	0.124	-	0.148	0.138	0.082	-
MgO	48.5	32.7	14.9	-	48.5	32.8	15.3	-
CaO	0.217	0.741	20.7	-	0.211	0.638	21.1	-
Na_2O	-	0.119	1.79	-	-	0.083	1.58	-
K_2O	-	0.000	0.000	-	-	0.000	0.001	-
Total	100.8	99.9	100.1	-	99.9	100.2	100.8	-
Mg#	89.3	89.3	89.7	-	89.6	89.8	91.4	-

Volcanic field	*SD*	*SD*	*SD*	*SD*	*VES*	*VES*	*VES*	*VES*
Sample	SD11	SD11	SD11	SD11	LP2a	LP2a	LP2a	LP2a
Mineral	ol	opx	cpx	gl	ol	opx	cpx	gl
SiO_2	40.8	55.1	51.8	-	40.4	55.2	51.7	57.2
TiO_2	0.023	0.128	0.524	-	0.002	0.117	0.495	3.19
Al_2O_3	0.029	4.27	6.35	-	0.034	4.23	6.31	18.9
Cr_2O_3	0.000	0.433	1.06	-	0.027	0.339	0.877	0.000
FeO	10.3	6.76	3.07	-	10.0	6.94	3.10	3.82
MnO	0.147	0.116	0.104	-	0.114	0.126	0.105	0.105
MgO	48.3	32.4	15.1	-	48.5	32.2	14.8	2.04
CaO	0.216	0.836	20.1	-	0.379	0.751	20.9	7.30
Na_2O	-	0.118	1.89	-	-	0.098	1.56	6.00
K_2O	-	0.000	0.000	-	-	0.000	0.000	2.39
Total	100.2	100.1	100.1	-	99.7	100.0	99.9	101.2
Mg#	89.3	89.5	89.8	-	89.6	89.2	89.5	48.8

Table S4.1. (continued).

Volcanic field	*VES*	*VES*	*VES*	*VES*	*VES*	*VES*	*VES*	*VES*
Sample	JH6a	JH6a	JH6a	JH6a	JH6b	JH6b	JH6b	JH6b
Mineral	ol	opx	cpx	gl	ol	opx	cpx	gl
SiO_2	40.5	54.5	51.4	53.9	40.3	54.5	51.7	54.6
TiO_2	0.010	0.142	0.478	2.41	0.000	0.126	0.502	2.03
Al_2O_3	0.033	4.83	6.51	19.9	0.010	4.83	6.52	19.9
Cr_2O_3	0.000	0.459	0.928	0.025	0.000	0.468	0.915	0.000
FeO	10.4	6.68	3.15	4.00	10.4	6.74	3.19	3.91
MnO	0.151	0.112	0.077	0.084	0.103	0.126	0.103	0.056
MgO	48.5	32.0	15.4	3.10	48.7	32.4	15.4	2.89
CaO	0.265	0.875	20.2	7.97	0.351	0.891	19.9	6.72
Na_2O	-	0.115	1.67	6.04	-	0.133	1.65	6.99
K_2O	-	0.000	0.000	2.18	-	0.000	0.000	2.43
Total	100.3	99.7	99.9	99.7	100.2	100.3	99.8	99.7
Mg#	89.2	89.5	89.7	58.0	89.3	89.6	89.6	56.9

Volcanic field	*DU*	*DU*	*DU*	*DU*	*DU*	*DU*	*DU*	*DU*
Sample	LB1a	LB1a	LB1a	LB1a	LB3a	LB3a	LB3a	LB3a
Mineral	ol	opx	cpx	gl	ol	opx	cpx	gl
SiO_2	40.7	55.4	51.7	58.9	40.4	54.4	51.6	60.7
TiO_2	0.017	0.103	0.405	1.29	0.000	0.072	0.316	1.25
Al_2O_3	0.032	4.05	5.98	17.6	0.026	4.57	5.69	17.6
Cr_2O_3	0.000	0.470	1.12	0.000	0.000	0.511	1.014	0.000
FeO	10.3	6.55	2.90	3.73	10.4	6.83	3.20	3.15
MnO	0.127	0.134	0.082	0.089	0.121	0.131	0.055	0.051
MgO	48.3	32.8	15.1	2.92	48.6	32.6	15.5	2.617
CaO	0.267	0.652	21.1	6.27	0.296	0.802	21.0	6.11
Na_2O	-	0.065	1.63	5.10	-	0.065	1.36	5.62
K_2O	-	0.000	0.000	3.07	-	0.000	0.011	3.24
Total	100.1	100.2	100.0	99.1	100.2	100.0	99.9	100.6
Mg#	89.4	89.9	90.3	58.2	89.3	89.5	89.7	59.7

Volcanic field	*DU*	*DU*	*DU*	*DU*	*DU*	*DU*	*DU*	*DU*
Sample	LB3b	LB3b	LB3b	LB3b	LB3c	LB3c	LB3c	LB3c
Mineral	ol	opx	cpx	gl	ol	opx	cpx	gl
SiO_2	40.5	54.9	52.2	59.1	41.2	54.8	52.3	57.7
TiO_2	0.000	0.072	0.313	1.33	0.000	0.056	0.275	0.837
Al_2O_3	0.019	4.70	6.06	18.1	0.036	4.47	5.65	19.6
Cr_2O_3	0.000	0.547	1.04	0.012	0.000	0.445	0.878	0.040
FeO	10.1	6.86	3.06	3.51	9.75	6.84	3.14	3.29
MnO	0.159	0.141	0.082	0.021	0.107	0.160	0.070	0.084
MgO	48.7	32.3	15.3	3.07	48.3	32.0	15.7	2.69
CaO	0.303	0.801	21.2	5.96	0.251	0.857	21.0	6.88
Na_2O	-	0.096	1.33	5.24	-	0.120	1.29	5.57
K_2O	-	0.000	0.000	3.21	-	0.000	0.000	2.72
Total	100.2	100.4	100.6	99.8	100.0	99.7	100.2	99.5
Mg#	89.6	89.3	89.9	60.9	89.8	89.3	89.9	59.3

Table S4.2. Representative trace elements compositions [ppm] of clinopyroxene (cpx) and silicate glass (gl) in Santo Domingo (SV), Ventura-Espíritu Santo (VES) and Durango (DU) xenoliths (n.d. = not determined). Samples labels as in Table S4.1.

Volcanic field	*SD*	*SD*	*SD*	*SD*	*SD*	*SD*	*VES*	*VES*	*DU*	*DU*
Sample	JC11	JC15	JC21	JP3	SD10	SD11	LP2	JH6	LB3a	LB3c
Mineral	cpx	cpx	cpx	cpx	cpx	cpx	cpx	cpx	cpx	cpx
Ti^{47}	2591	3309	3107	2533	3239	3289	3121	2995	2349	1872
Rb^{85}	n.d.	n.d.	n.d.	n.d.	n.d.	n.d.	n.d.	n.d.	n.d.	n.d.
Sr^{88}	26.0	58.5	21.2	41.7	29.2	63.8	11.5	41.4	71.6	2.52
Y^{89}	15.4	15.1	17.9	14.1	16.4	16.4	17.6	17.0	15.0	13.6
Zr^{90}	13.9	23.5	16.5	18.6	18.6	24.0	11.8	19.2	25.6	3.05
Nb^{93}	0.065	0.106	0.022	0.033	0.029	0.044	n.d.	n.d.	4.57	n.d.
Cs^{133}	n.d.	n.d.	n.d.	n.d.	n.d.	n.d.	n.d.	n.d.	n.d.	n.d.
Ba^{137}	n.d.	1.46	0.118	n.d.	n.d.	n.d.	n.d.	0.970	37.8	n.d.
La^{139}	0.307	0.458	0.095	0.403	0.242	0.601	0.024	0.305	4.09	n.d.
Ce^{140}	1.40	3.26	1.09	1.95	1.55	2.91	0.532	1.98	8.79	0.065
Pr^{141}	0.352	0.663	0.320	0.365	0.430	0.586	0.217	0.423	0.979	0.055
Nd^{146}	2.58	4.12	2.71	2.50	3.25	3.75	2.12	3.22	5.13	0.850
Sm^{147}	1.59	1.57	1.46	1.12	1.67	1.58	1.02	1.51	1.37	0.760
Eu^{153}	0.565	0.652	0.663	0.530	0.703	0.715	0.611	0.683	0.597	0.361
Gd^{157}	2.26	2.35	2.32	1.79	2.20	2.49	2.19	2.17	2.09	1.71
Tb^{159}	n.d.	n.d.	n.d.	n.d.	n.d.	n.d.	n.d.	n.d.	n.d.	n.d.
Dy^{163}	2.71	2.77	3.49	2.40	3.24	3.12	3.36	2.94	2.75	2.38
Ho^{165}	n.d.	n.d.	n.d.	n.d.	n.d.	n.d.	n.d.	n.d.	n.d.	n.d.
Er^{166}	1.71	1.72	2.17	1.70	2.02	2.13	1.91	2.11	1.68	1.66
Tm^{169}	n.d.	n.d.	n.d.	n.d.	n.d.	n.d.	n.d.	n.d.	n.d.	n.d.
Yb^{172}	1.57	1.67	1.99	1.48	1.96	1.95	1.81	1.74	1.76	1.35
Lu^{175}	0.227	0.187	0.259	0.200	0.247	0.220	0.228	0.253	0.281	0.186
Hf^{178}	0.745	1.02	0.649	0.570	0.770	0.930	0.859	0.686	0.919	0.310
Ta^{181}	n.d.	n.d.	n.d.	n.d.	n.d.	n.d.	n.d.	n.d.	0.211	n.d.
Pb^{208}	n.d.	n.d.	n.d.	n.d.	n.d.	n.d.	n.d.	n.d.	n.d.	n.d.
Th^{232}	n.d.	n.d.	0.258	0.028	0.026	0.045	n.d.	n.d.	0.422	n.d.
U^{238}	n.d.	n.d.	0.188	n.d.	0.021	n.d.	n.d.	0.013	0.11	n.d.

Table S4.3. (continued).

Volcanic field	*VES*	*VES*	*VES*	*VES*	*VES*	*DU*	*DU*	*DU*	*DU*	*DU*
Sample	JH6	JH6	JH6	JH6	JH6	LB3	LB3	LB3	LB3	LB3
Mineral	gl	gl	gl	gl	gl	gl	gl	gl	gl	gl
Ti^{47}	16793	11397	13943	17010	15445	8790	8892	8002	8069	10699
Rb^{85}	40.1	35.2	45.2	39.5	36.7	49.4	70.3	59.3	61.9	73.0
Sr^{88}	1095	803	1005	1074	1037	1040	1064	903	902	1328
Y^{89}	25.9	18.2	22.2	22.0	23.8	25.0	21.3	22.5	21.5	30.3
Zr^{90}	345	239	289	315	296	399	362	361	350	473
Nb^{93}	127	87.9	114	124	113	97.7	91.8	82.1	79.9	121
Cs^{133}	0.700	0.610	n.d.	n.d.	n.d.	n.d.	2.10	n.d.	0.740	n.d.
Ba^{137}	588	439	599	603	505	691	713	600	581	859
La^{139}	68.5	48.4	64.3	66.6	62.1	68.3	62.2	60.7	61.9	85.5
Ce^{140}	128	90.3	122	131	118	140	126	115	115	171
Pr^{141}	14.3	9.56	12.3	14.7	13.5	14.1	13.2	12.8	13.7	19.0
Nd^{146}	52.2	32.0	39.2	53.5	49.7	52.9	50.4	45.6	50.6	67.6
Sm^{147}	9.02	6.10	5.69	9.61	11.4	10.4	10.3	8.52	8.65	10.8
Eu^{153}	2.80	1.76	2.10	2.72	2.48	2.73	2.20	2.54	2.54	2.81
Gd^{157}	7.73	5.88	4.86	6.62	5.83	8.90	6.31	6.52	7.52	8.69
Tb^{159}	n.d.	n.d.	n.d.	n.d.	n.d.	n.d.	n.d.	n.d.	n.d.	n.d.
Dy^{163}	5.08	3.85	3.89	5.92	5.71	5.08	4.86	4.45	4.47	7.09
Ho^{165}	n.d.	n.d.	n.d.	n.d.	n.d.	n.d.	n.d.	n.d.	n.d.	n.d.
Er^{166}	2.94	1.57	2.56	2.09	2.59	2.43	2.04	2.04	1.59	3.44
Tm^{169}	n.d.	n.d.	n.d.	n.d.	n.d.	n.d.	n.d.	n.d.	n.d.	n.d.
Yb^{172}	2.01	1.91	1.79	2.06	1.21	2.15	3.13	2.11	1.61	2.00
Lu^{175}	0.339	0.266	0.245	n.d.	n.d.	0.144	0.218	0.245	0.209	0.222
Hf^{178}	6.83	4.53	5.08	6.43	5.97	9.55	7.09	6.66	6.45	9.39
Ta^{181}	7.06	4.72	6.17	6.84	5.79	5.48	5.05	4.49	4.21	5.60
Pb^{208}	1.09	0.840	3.37	2.87	1.59	2.17	2.65	3.79	4.51	7.04
Th^{232}	9.81	6.99	7.04	7.65	8.12	7.39	6.99	6.46	6.51	10.0
U^{238}	3.02	1.80	3.03	3.09	3.02	3.26	2.73	2.83	2.24	3.33

Table S4.4. Major element compositions of base-metal sulfides (in wt.%) in Santo Domingo (SV), Ventura-Espíritu Santo (VES) and Durango (DU) xenoliths (n.d. = not determined). Samples labels as in Table S4.1.

Volcanic field	*SD*	*SD*	*SD*	*SD*	*SD*	*SD*	*SD*	*SD*	*SD*	*SD*
Sample	JC15	JC15	JC15	JC15	JC15	JC15	JC15	JC15	JC15	JC15
Mineral	mss_{enc}	pn_{int}	pn_{int}	mss_{enc}	mss_{enc}	pn_{int}	mss_{enc}	pn_{enc}	mss_{enc}	mss_{enc}
O	*n.d.*	*n.d.*	*n.d.*	*n.d.*	*n.d.*	*n.d.*	*n.d.*	*n.d.*	*n.d.*	*n.d.*
S	38.3	32.7	32.8	37.6	37.8	32.7	38.4	33.0	38.3	38.0
Fe	45.5	27.7	28.0	45.9	45.6	32.0	52.8	29.0	48.9	48.0
Ni	15.0	38.3	38.4	15.4	15.7	32.9	7.61	36.7	12.1	12.7
Co	0.209	0.343	0.326	0.170	0.178	0.519	0.098	0.647	0.174	0.141
Cu	0.029	0.078	0.053	0.038	0.027	0.111	0.071	0.134	0.073	0.063
Total	99.1	99.2	99.6	99.2	99.3	98.3	98.9	99.5	99.5	99.0
met/S	0.90	1.13	1.14	0.93	0.92	1.12	0.90	1.13	0.91	0.91
[Ni/(Ni+Fe)]	0.24	0.57	0.57	0.24	0.25	0.49	0.12	0.55	0.19	0.20

Volcanic field	*SD*	*SD*	*SD*	*SD*	*SD*	*SD*	*SD*	*SD*	*SD*	*SD*
Sample	JC15	JC21	JC21	JC21	JC21	JC21	JC21	JC21	JC21	JC21
Mineral	cp_{enc}	mss_{enc}	mss_{int}	mss_{int}	mss_{int}	mss_{int}	mss_{int}	mss_{int}	mss_{enc}	mss_{enc}
O	*n.d.*	*n.d.*	*n.d.*	*n.d.*	*n.d.*	*n.d.*	*n.d.*	*n.d.*	*n.d.*	*n.d.*
S	34.3	38.2	38.0	37.7	36.9	37.0	36.9	37.0	38.1	38.4
Fe	30.6	43.1	48.3	43.3	43.4	45.0	44.0	42.9	27.5	27.6
Ni	0.739	18.3	13.3	18.3	17.7	16.1	17.3	18.3	32.9	32.9
Co	0.041	0.294	0.308	0.347	0.417	0.219	0.252	0.401	0.337	0.360
Cu	33.0	0.010	0.043	0.028	0.010	0.027	0.042	0.022	0.562	0.067
Total	98.8	99.9	100.0	99.7	98.5	98.5	98.6	98.6	99.5	99.4
met/S	1.01	0.91	0.92	0.93	0.94	0.94	0.95	0.94	0.90	0.89
[Ni/(Ni+Fe)]	0.02	0.29	0.21	0.29	0.28	0.25	0.27	0.29	0.53	0.53

Volcanic field	*SD*	*SD*	*SD*	*SD*	*SD*	*SD*	*SD*	*SD*	*SD*	*SD*
Sample	JC21	JC21	JC21	JC21	JC21	JC21	JC21	JC21	JC21	JC21
Mineral	mss_{int}	mss_{int}	mss_{int}	mss_{int}	mss_{int}	mss_{int}	pn_{int}	pn_{int}	mss_{int}	mss_{int}
O	*n.d.*	*n.d.*	*n.d.*	*n.d.*	*n.d.*	*n.d.*	*n.d.*	*n.d.*	*n.d.*	*n.d.*
S	37.3	37.6	37.7	37.5	38.2	37.4	32.6	32.2	38.6	37.8
Fe	41.4	46.0	47.2	44.9	31.4	46.7	27.2	25.7	42.6	43.3
Ni	19.2	15.4	14.2	16.3	29.9	14.3	38.7	38.8	17.9	17.8
Co	0.602	0.221	0.227	0.347	0.136	0.328	0.376	0.383	0.311	0.317
Cu	0.051	0.028	0.039	0.038	0.047	0.036	0.856	0.875	0.041	0.063
Total	98.7	99.2	99.4	99.2	99.8	98.8	99.8	98.2	99.5	99.3
met/S	0.93	0.93	0.93	0.93	0.90	0.93	1.15	1.14	0.89	0.92
[Ni/(Ni+Fe)]	0.31	0.24	0.22	0.26	0.48	0.23	0.58	0.59	0.28	0.28

Table S4.5. (continued).

Volcanic field	*SD*	*SD*	*SD*	*SD*	*SD*	*SD*	*SD*	*SD*	*SD*	*SD*
Sample	JC21	JP2	JP2	JP2	JP2	JP2	JP3	SD10	SD10	SD10
Mineral	mss_{int}	mss_{int}	mss_{int}	mss_{int}	mss_{int}	mss_{int}	mss_{int}	mss_{enc}	mss_{enc}	mss_{enc}
O	*n.d.*	*n.d.*	*n.d.*	*n.d.*	*n.d.*	*n.d.*	*n.d.*	*n.d.*	*n.d.*	*n.d.*
S	38.1	38.8	38.8	38.8	39.0	38.5	39.6	38.5	38.5	38.4
Fe	44.6	34.3	34.3	39.0	38.1	43.2	28.6	37.4	37.8	28.4
Ni	16.6	26.9	26.9	21.8	23.2	17.5	29.8	23.3	23.3	32.2
Co	0.135	0.156	0.134	0.167	0.120	0.157	0.307	0.246	0.232	0.271
Cu	0.071	0.034	0.015	0.018	0.025	0.024	0.078	0.014	0.035	0.042
Total	99.5	100.3	100.2	99.8	100.5	99.5	98.4	99.5	99.9	99.4
met/S	0.91	0.89	0.89	0.89	0.89	0.90	0.83	0.89	0.90	0.89
[Ni/(Ni+Fe)]	0.26	0.43	0.43	0.35	0.37	0.28	0.50	0.37	0.37	0.52

Volcanic field	*SD*	*SD*	*SD*	*SD*	*SD*	*SD*	*SD*	*SD*	*SD*	*SD*
Sample	SD10	SD10	SD10	SD11	SD11	SD11	SD11	SD11	SD11	SD11
Mineral	pn_{enc}	pn_{enc}	mss_{enc}	mss_{int}	pn_{int}	pn_{enc}	mss_{enc}	mss_{enc}	mss_{enc}	pn_{enc}
O	*n.d.*	*n.d.*	*n.d.*	*n.d.*	*n.d.*	*n.d.*	*n.d.*	*n.d.*	*n.d.*	*n.d.*
S	32.9	32.8	38.5	37.9	32.7	32.8	37.9	37.9	38.4	32.8
Fe	27.4	27.3	51.2	55.2	29.7	29.7	55.2	53.2	53.5	29.1
Ni	37.4	37.3	8.85	5.96	36.1	36.2	5.92	6.85	6.53	36.2
Co	0.808	0.798	0.140	0.108	0.643	0.666	0.100	0.093	0.113	0.739
Cu	0.059	0.070	0.082	0.026	0.055	0.073	0.040	0.038	0.067	0.078
Total	98.6	98.3	98.8	99.2	99.3	99.4	99.2	98.1	98.6	98.9
met/S	1.11	1.11	0.89	0.93	1.14	1.14	0.92	0.91	0.90	1.12
[Ni/(Ni+Fe)]	0.57	0.56	0.14	0.09	0.54	0.54	0.09	0.11	0.10	0.54

Volcanic field	*VES*	*VES*	*VES*	*VES*	*VES*	*VES*	*VES*	*VES*	*VES*	*VES*
Sample	JH6	JH6	JH6	JH6	JH6	JH6	JH6	JH6	JH6	JH6
Mineral	pn_{gls}	pn_{gls}	pn_{gls}	pn_{gls}	pn_{gls}	pn_{gls}	pn_{gls}	pn_{gls}	pn_{gls}	pn_{gls}
O	*n.d.*	*n.d.*	*n.d.*	*n.d.*	*n.d.*	*n.d.*	*n.d.*	*n.d.*	*n.d.*	*n.d.*
S	33.3	33.1	32.6	33.2	32.5	32.9	32.9	33.3	33.1	32.7
Fe	30.9	29.2	29.1	27.8	32.3	30.3	27.6	31.4	32.4	31.3
Ni	35.2	37.4	36.4	38.1	33.6	36.2	38.7	34.5	33.9	34.7
Co	0.305	0.338	0.327	0.320	0.300	0.341	0.405	0.311	0.313	0.302
Cu	0.142	0.115	0.753	0.078	0.113	0.059	0.347	0.070	0.095	0.668
Total	99.9	100.2	99.3	99.5	99.0	99.8	99.9	99.7	99.8	99.7
met/S	1.12	1.13	1.14	1.11	1.14	1.14	1.14	1.11	1.13	1.15
[Ni/(Ni+Fe)]	0.52	0.55	0.54	0.57	0.50	0.53	0.57	0.51	0.50	0.51

Table S4.6. (continued).

Volcanic field	*VES*	*VES*	*VES*	*VES*	*VES*	*VES*	*VES*	*VES*	*VES*	*VES*
Sample	JH6	JH6	JH6	JH6	JH6	JH6	LP1	LP1	LP1	LP1
Mineral	pn_{gls}	pn_{gls}	pn_{gls}	pn_{gls}	pn_{gls}	pn_{gls}	pn_{gls}	pn_{gls}	pn_{int}	cp_{int}
O	*n.d.*	*n.d.*	*n.d.*	*n.d.*	*n.d.*	*n.d.*	*n.d.*	*n.d.*	*n.d.*	*n.d.*
S	32.1	32.8	33.0	33.0	32.4	32.7	32.0	32.1	32.7	33.5
Fe	32.7	29.0	34.4	31.4	31.9	31.7	28.6	28.6	27.9	30.0
Ni	33.5	37.5	31.3	34.6	34.0	32.9	36.5	36.4	37.6	0.490
Co	0.304	0.362	0.250	0.307	0.325	0.288	0.326	0.345	0.350	0.057
Cu	0.090	0.118	0.107	0.144	0.231	1.44	0.000	0.000	0.000	32.6
Total	98.8	99.8	99.1	99.6	99.0	99.1	97.4	97.5	98.6	96.7
met/S	1.16	1.14	1.12	1.12	1.15	1.13	1.14	1.14	1.13	1.01
[Ni/(Ni+Fe)]	0.49	0.55	0.46	0.51	0.50	0.50	0.55	0.55	0.56	0.02

Volcanic field	*VES*	*VES*	*VES*	*VES*	*VES*	*VES*	*VES*	*VES*	*VES*	*VES*
Sample	LP1	LP1	LP1	LP1	LP1	LP1	LP1	LP1	LP2	LP2
Mineral	mss_{int}	pn_{gls}	pn_{gls}	pn_{gls}	mss_{int}	mss_{int}	pn_{int}	pn_{int}	pn_{int}	pn_{int}
O	*n.d.*	*n.d.*	*n.d.*	*n.d.*	*n.d.*	*n.d.*	*n.d.*	*n.d.*	*n.d.*	*n.d.*
S	37.9	32.7	32.4	32.3	38.2	37.6	32.5	32.0	32.6	32.6
Fe	49.3	30.0	30.0	25.9	53.2	52.7	28.4	28.1	31.8	31.0
Ni	10.5	35.5	34.6	38.6	6.3	6.6	35.9	35.6	33.3	34.2
Co	0.080	0.355	0.454	0.424	0.148	0.145	0.773	0.671	0.365	0.363
Cu	0.014	0.000	0.008	0.000	0.000	0.000	0.000	0.000	0.000	0.692
Total	97.8	98.5	97.5	97.3	97.8	97.0	97.5	96.3	98.0	98.8
met/S	0.90	1.13	1.12	1.12	0.89	0.90	1.12	1.12	1.12	1.14
[Ni/(Ni+Fe)]	0.17	0.53	0.52	0.59	0.10	0.11	0.55	0.55	0.50	0.51

Volcanic field	VES	VES	VES	VES	VES	VES	VES	DU	DU	DU
Sample	LP2	LP2	LP2	LP2	LP2	LP2	LP2	LB1	LB1	LB1
Mineral	pn_{gls}	pn_{gls}	cp_{gls}	cp_{gls}	pn_{int}	pn_{int}	pn_{int}	mss_{enc}	mss_{enc}	mss_{enc}
O	*n.d.*	*n.d.*	*n.d.*	*n.d.*	*n.d.*	*n.d.*	*n.d.*	0.267	0.151	0.185
S	33.2	32.8	33.9	34.1	33.5	32.4	32.5	38.6	38.0	38.3
Fe	30.6	27.1	30.1	30.4	30.6	31.7	31.2	36.9	37.3	38.6
Ni	34.3	37.7	0.317	0.259	34.2	30.2	34.1	24.3	24.3	23.0
Co	0.378	0.356	0.057	0.045	0.354	0.308	0.330	0.316	0.324	0.263
Cu	0.173	0.226	32.4	32.2	0.145	2.770	0.487	0.173	0.400	0.408
Total	98.6	98.2	96.7	97.1	98.7	97.3	98.6	100.6	100.5	100.7
met/S	1.10	1.11	1.00	0.99	1.09	1.12	1.14	0.90	0.92	0.92
[Ni/(Ni+Fe)]	0.52	0.57	0.01	0.01	0.52	0.48	0.51	0.38	0.38	0.36

Table S4.7. (continued).

Volcanic field	*DU*	*DU*	*DU*	*DU*	*DU*	*DU*	*DU*	*DU*	*DU*	*DU*
Sample	LB3	LB3	LB3	LB3	LB3	LB3	LB3	LB3	LB3	LB3
Mineral	pn_{gls}	pn_{gls}	*pn+cp*	*pn+cp*	cp_{gls}	pn_{gls}	*pn+cp*	pn_{gls}	*pn+cp*	*pn+cp*
O	0.198	0.176	1.16	1.80	0.000	0.215	0.316	0.607	0.190	1.08
S	33.7	33.7	33.8	34.0	35.4	33.9	34.8	35.3	35.0	34.9
Fe	28.0	28.0	27.5	24.8	35.5	27.5	25.1	36.3	31.0	30.8
Ni	36.9	37.4	34.9	32.4	0.647	38.5	31.8	0.529	30.2	31.0
Co	0.343	0.336	0.297	0.251	0.077	0.326	0.294	0.125	0.421	0.428
Cu	0.684	0.597	2.20	7.19	29.3	0.573	8.33	27.6	2.46	1.80
Total	99.8	100.2	99.9	100.5	100.9	101.0	100.7	100.5	99.3	100.1
met/S	1.09	1.10	1.07	1.05	1.00	1.10	1.04	1.00	1.02	1.02
[Ni/(Ni+Fe)]	0.56	0.56	0.55	0.55	0.02	0.57	0.55	0.01	0.48	0.49

Volcanic field	*DU*	*DU*	*DU*	*DU*	*DU*	*DU*	*DU*	*DU*	*DU*	*DU*
Sample	LB3	LB3	LB3	LB3	LB3	LB3	LB3	LB3	LB3	LB3
Mineral	*pn+cp*	*pn+cp*	*pn+cp*	*pn+cp*	*pn+cp*	*pn+cp*	*pn+cp*	*pn+cp*	*pn+cp*	*pn+cp*
O	0.189	0.144	0.234	0.174	0.314	0.209	0.194	0.191	0.085	0.200
S	34.0	34.3	33.8	33.2	33.6	33.7	33.8	34.2	34.5	33.5
Fe	29.9	29.8	27.6	26.7	24.4	29.2	29.4	28.4	25.3	26.2
Ni	34.5	35.0	36.3	37.5	37.2	34.6	34.9	29.4	31.9	38.6
Co	0.344	0.327	0.375	0.374	0.356	0.330	0.348	0.317	0.242	0.293
Cu	1.54	1.31	1.36	0.772	3.00	0.933	0.923	6.89	8.29	0.924
Total	100.5	100.9	99.7	98.7	98.9	99.0	99.5	99.3	100.3	99.7
met/S	1.09	1.08	1.08	1.10	1.07	1.08	1.08	1.05	1.05	1.10
[Ni/(Ni+Fe)]	0.52	0.53	0.56	0.57	0.59	0.53	0.53	0.50	0.55	0.58

Volcanic field	*DU*	*DU*	*DU*	*DU*	*DU*
Sample	LB3	LB7	LB7	LB7	LB7
Mineral	*pn+cp*	mss_{enc}	mss_{enc}	mss_{enc}	mss_{enc}
O	0.429	0.215	0.173	0.290	0.167
S	34.0	36.8	37.4	36.8	38.2
Fe	24.7	25.4	25.7	25.5	24.5
Ni	30.5	36.5	35.6	36.5	37.1
Co	0.242	0.361	0.346	0.316	0.355
Cu	9.85	0.283	0.291	0.342	0.203
Total	99.7	99.5	99.6	99.7	100.5
met/S	1.06	0.95	0.92	0.95	0.91
[Ni/(Ni+Fe)]	0.54	0.58	0.57	0.58	0.59

Table S4.4. Concentrations (ppm) of chalcophile and siderophile elements in base-metal sulfides from Santo Domingo (SV), Ventura-Espíritu Santo (VES) and Durango (DU) xenoliths (n.d. = not determined). Samples labels as in Table S4.1.

Volcanic field	*SD*	*SD*	*SD*	*SD*	*SD*	*SD*	*SD*	*SD*	*SD*
Sample	JC15	JC15	JC21	JC21	JC21	JC21	JC21	JC21	JC21
Mineral	mss_{enc}	mss_{enc}	mss_{enc}	mss_{int}	mss_{enc}	mss_{int}	mss_{int}	mss_{int}	pn_{int}
Zn^{66}	408	4.57	25.7	26.7	864	61.4	50.4	5.12	73.6
As^{75}	47.0	1.15	8.73	11.8	93.9	39.9	176	2.61	305
Se^{82}	129	101	129	213	190	227	234	121	163
Ru^{101}	26.9	12.2	30.8	31.5	18.5	24.4	9.69	9.31	5.73
Rh^{103}	3.81	1.64	4.04	5.55	3.45	3.05	2.07	1.63	1.29
Ag^{107}	4.41	0.169	0.151	0.090	17.6	0.286	5.24	n.d.	19.1
Pd^{108}	9.15	0.053	0.201	11.2	10.4	9.59	5.23	3.83	16.1
Cd^{111}	0.610	n.d.	0.426	0.810	0.834	1.34	0.610	n.d.	1.74
In^{115}	0.040	n.d.	n.d.	n.d.	0.047	n.d.	0.031	n.d.	0.290
Sb^{121}	n.d.	n.d.	n.d.	n.d.	12.4	n.d.	n.d.	n.d.	27.6
Te^{125}	19.4	1.33	2.01	6.61	28.1	3.21	23.4	2.08	22.5
Os^{189}	13.7	7.86	14.9	13.1	10.3	11.5	3.43	5.50	3.50
Ir^{193}	11.7	5.14	9.74	10.3	8.76	7.18	3.09	2.57	3.19
Pt^{195}	16.9	0.420	1.74	14.2	16.0	n.d.	10.2	2.27	1.06
Au^{197}	0.358	n.d.	0.218	n.d.	1.68	n.d.	0.225	0.059	0.850
Pb^{208}	22.5	0.345	5.87	2.41	219	41.6	42.8	0.600	36.0
Bi^{209}	0.992	0.075	0.030	0.125	2.060	0.169	0.571	0.057	1.14

Volcanic field	*SD*	*SD*	*SD*	*SD*	*SD*	*SD*	*VES*	*VES*	*VES*
Sample	JC21	JC21	JP2	JP3	SD10	SD10	LP1	LP1	LP1
Mineral	mss_{int}	mss_{int}	mss_{int}	mss_{int}	mss_{enc}	mss_{enc}	pn_{gls}	pn_{int}	pn_{gls}
Zn^{66}	2.86	51.7	4.64	13.2	10.4	129	26.0	42.9	50.7
As^{75}	14.0	31.8	11.0	8.120	14.1	40.2	39.6	0.950	32.3
Se^{82}	119	237	101	234	109	233	101	147	169
Ru^{101}	7.27	7.66	15.2	22.3	25.8	30.5	7.58	7.00	15.8
Rh^{103}	1.33	2.07	1.94	3.47	4.97	5.35	1.14	2.02	6.94
Ag^{107}	n.d.	3.75	1.08	28.0	1.11	14.7	9.44	17.1	15.1
Pd^{108}	2.19	2.09	0.080	1.02	1.11	10.9	9.96	8.38	41.0
Cd^{111}	n.d.	0.810	0.208	n.d.	0.450	3.85	0.660	6.64	2.76
In^{115}	n.d.	0.103	n.d.	0.019	n.d.	0.272	0.181	0.212	0.279
Sb^{121}	n.d.	0.460	n.d.	0.280	0.370	2.54	8.67	1.17	8.05
Te^{125}	2.79	42.0	1.35	8.68	26.3	32.2	24.9	28.6	46.5
Os^{189}	5.56	3.51	10.4	10.1	16.5	15.8	3.24	3.50	8.12
Ir^{193}	3.68	4.10	7.68	6.39	13.1	13.1	1.77	2.88	8.19
Pt^{195}	2.10	5.51	0.164	4.80	5.98	13.2	7.59	6.37	61.5
Au^{197}	0.215	0.695	n.d.	0.263	0.119	0.457	0.112	0.096	0.169
Pb^{208}	1.40	66.6	2.06	17.9	9.14	84.2	9.71	13.9	6.81
Bi^{209}	0.098	0.882	0.544	3.39	1.44	10.6	1.08	0.735	1.05

Table S4.4. (continued).

Volcanic field	*VES*	*VES*	*VES*	*VES*	*VES*	*VES*	*VES*	*VES*	*DU*
Sample	LP2	LP2	JH6	JH6	JH6	JH6	JH6	JH6	LB3
Mineral	pn_{int}	pn_{int}	pn_{gls}	pn_{gls}	pn_{gls}	pn_{gls}	pn_{gls}	pn_{gls}	pn_{gls}
Zn^{66}	126	60.0	236	30.7	102	32.0	40.6	47.5	103
As^{75}	157	152.680	33.9	10	89.3	45.8	24.6	14.5	11.5
Se^{82}	220	160.480	192	154	169	156	148	123	103
Ru^{101}	14.3	17.5	6.95	12.2	23.2	11.9	11.5	8.91	7.49
Rh^{103}	3.66	3.535	1.45	2.15	4.44	2.61	1.90	1.71	1.72
Ag^{107}	48.8	25.8	27.4	8.52	25.7	17.8	14.7	14.4	11.3
Pd^{108}	23.2	20.3	11.6	7.74	17.4	14.6	20.0	9.96	8.67
Cd^{111}	3.15	2.070	4.57	2.30	3.81	1.94	3.58	4.90	3.48
In^{115}	0.784	0.284	0.499	0.183	0.40	0.151	0.140	0.058	0.180
Sb^{121}	18.5	21.3	1.41	0.440	4.95	1.64	1.87	0.920	0.830
Te^{125}	57.5	34.1	34.4	13.8	31.1	29.4	16.2	12.2	16.4
Os^{189}	8.25	11.7	4.21	7.05	12.5	6.62	7.60	5.17	4.73
Ir^{193}	6.01	8.880	3.11	5.96	13.3	6.44	5.59	4.37	3.89
Pt^{195}	15.7	18.6	4.64	6.57	16.5	12.8	16.3	6.960	9.53
Au^{197}	1.48	1.181	0.692	0.351	0.078	0.405	0.319	n.d.	n.d.
Pb^{208}	18.7	13.9	110	17.7	44.6	36.5	14.3	23.1	14.3
Bi^{209}	3.72	3.730	3.54	1.47	3.44	3.71	2.15	2.15	1.84

Volcanic field	*DU*	*DU*	*DU*	*DU*
Sample	LB3	LB3	LB3	LB3
Mineral	*pn+cp*	*pn+cp*	*pn+cp*	
Zn^{66}	29.3	39.0	37.1	9.38
As^{75}	24.9	38.5	109	38.5
Se^{82}	216	295	216	58.2
Ru^{101}	12.5	6.18	18.4	2.62
Rh^{103}	2.04	0.81	4.18	0.540
Ag^{107}	23.3	25.0	21.6	4.78
Pd^{108}	28.8	31.9	36.0	7.57
Cd^{111}	7.19	13.1	5.13	1.98
In^{115}	0.064	0.304	0.118	0.044
Sb^{121}	n.d.	n.d.	n.d.	2.39
Te^{125}	39.4	56.2	26.4	11.4
Os^{189}	14.5	6.75	20.1	3.24
Ir^{193}	6.33	3.12	11.7	1.71
Pt^{195}	16.0	17.9	21.1	5.00
Au^{197}	1.64	5.98	1.16	0.076
Pb^{208}	51.7	183	94.2	37.0
Bi^{209}	4.44	5.87	4.21	1.82

Table S4.5. Re-Os composition and calculated Re-delpetion model ages (Ga) of base-metal sulfides from Santo Domingo (SD), Ventura-Espíritu Santo (VES) and Durango (DU) mantle xenoliths. Samples labels as in Table S4.1.

Volcanic field	Sample	$^{187}Os/^{188}Os$	2σ	$^{187}Re/^{188}Os$	2σ	$T_{RD}ECR$	2σ
SD	JC	0.11149	2.60E-04	0.01298	2.20E-04	2.32	0.04
SD	JC	0.11953	2.60E-04	0.12976	2.20E-03	1.21	0.04
SD	JC	0.11582	4.00E-04	0.01272	8.00E-04	1.73	0.06
SD	JC	0.10703	1.36E-04	0.03532	3.00E-03	2.93	0.02
SD	JC	0.11469	7.00E-03	0.00412	9.20E-04	1.88	0.97
SD	JC	0.12095	1.20E-04	0.06836	3.20E-04	1.01	0.02
SD	JC	0.10728	1.36E-04	0.03532	3.00E-03	2.90	0.02
SD	JC	0.11763	7.60E-04	0.06649	1.68E-04	1.47	0.11
SD	JC	0.11200	3.80E-04	0.05100	1.84E-02	2.25	0.05
SD	JC	0.11763	4.40E-04	0.07600	3.20E-02	1.47	0.06
SD	JC	0.11584	1.40E-03	0.06860	3.20E-04	1.72	0.19
SD	JC	0.12100	9.00E-04	0.01750	8.20E-04	1.00	0.13
SD	JC	0.11500	7.40E-04	0.01283	8.60E-04	1.84	0.10
SD	JC	0.12200	1.60E-04	0.01580	1.40E-04	0.86	0.02
SD	JC	0.12100	1.02E-04	0.01290	1.80E-04	1.00	0.01
SD	JC	0.11500	3.40E-04	0.01150	2.00E-04	1.84	0.05
SD	JC	0.11400	5.20E-04	0.01685	5.60E-03	1.98	0.07
SD	JC	0.11153	8.60E-03	0.01304	5.20E-03	2.32	1.18
SD	JC	0.10528	1.36E-04	0.00353	7.60E-04	3.17	0.02
SD	JC	0.10925	1.60E-03	0.06680	7.80E-03	2.63	0.22
SD	JP	0.11749	2.00E-04	0.02499	5.60E-04	1.49	0.03
SD	JP	0.12019	3.40E-04	0.12652	3.20E-04	1.12	0.05
SD	JP	0.12096	9.20E-05	0.05524	3.20E-03	1.01	0.01
SD	JP	0.12508	7.20E-04	0.31254	2.00E-04	0.43	0.10
SD	JP	0.11510	3.20E-04	0.01210	5.20E-03	1.83	0.04
SD	JP	0.11700	1.56E-04	0.01205	7.80E-04	1.56	0.02
SD	JP	0.12100	9.00E-04	0.16600	8.80E-04	1.00	0.13
SD	JP	0.11800	7.00E-04	0.01580	4.20E-04	1.42	0.10
SD	JP	0.12080	1.94E-04	0.02800	2.10E-03	1.03	0.03
SD	JP	0.11460	7.60E-04	0.08790	1.60E-03	1.89	0.10
SD	JP	0.11500	7.00E-04	0.08950	8.60E-04	1.84	0.10
SD	JP	0.11500	5.80E-04	0.08950	3.20E-03	1.84	0.08
SD	JP	0.11300	4.00E-04	0.01720	9.80E-03	2.12	0.06
SD	JP	0.12300	9.60E-04	0.11200	6.80E-04	0.72	0.14
SD	JP	0.11600	1.32E-04	0.02640	5.00E-03	1.70	0.02
SD	JP	0.10610	1.32E-04	0.00240	5.00E-04	3.06	0.02
SD	JP	0.11500	1.00E-04	0.02940	4.60E-04	1.84	0.01
SD	JP	0.12000	2.20E-04	0.14110	1.20E-04	1.14	0.03
SD	JP	0.11610	1.92E-04	0.09230	1.22E-04	1.69	0.03
SD	JP	0.11500	1.92E-04	0.01301	1.40E-03	1.84	0.03
SD	JP	0.10610	1.00E-04	0.02940	4.06E-03	3.06	0.01
SD	SD	0.12224	9.60E-05	0.11865	1.46E-04	0.83	0.01
SD	SD	0.12243	1.02E-04	0.11479	1.56E-04	0.80	0.01
SD	SD	0.11511	2.60E-04	0.02209	3.20E-04	1.82	0.04

Table S4.5. (continued).

Volcanic field	Sample	$^{187}Os/^{188}Os$	2σ	$^{187}Re/^{188}Os$	2σ	$T_{RD}ECR$	2σ
SD	SD	0.11104	1.04E-04	0.01101	1.22E-04	2.38	0.01
SD	SD	0.11206	9.80E-04	0.02133	1.36E-04	2.24	0.13
SD	SD	0.12039	6.80E-04	0.12058	1.14E-03	1.09	0.10
SD	SD	0.12503	1.90E-04	0.11490	3.60E-04	0.44	0.03
SD	SD	0.12430	1.16E-03	0.07023	6.20E-04	0.54	0.16
SD	SD	0.12330	1.16E-03	0.01123	6.20E-04	0.68	0.16
SD	SD	0.10748	9.80E-04	0.02013	1.36E-04	2.87	0.13
SD	SD	0.12436	1.10E-04	0.12580	1.18E-04	0.53	0.02
SD	SD	0.11355	1.10E-03	0.11280	1.18E-02	2.04	0.15
SD	SD	0.11120	9.80E-04	0.02133	1.36E-04	2.36	0.13
VES	LP	0.11301	1.80E-04	0.01886	2.80E-04	2.11	0.02
VES	LP	0.12549	1.88E-04	0.19363	8.40E-04	0.37	0.03
VES	LP	0.10610	3.00E-05	0.00100	2.20E-04	3.06	0.00
VES	LP	0.10992	7.80E-04	0.03531	9.40E-03	2.54	0.11
VES	LP	0.11019	2.80E-04	0.12099	1.62E-04	2.50	0.04
VES	JH	0.10701	3.40E-03	0.02540	6.00E-02	2.93	0.47
VES	JH	0.10830	3.00E-03	0.05286	9.40E-03	2.76	0.41
VES	JH	0.10850	3.00E-04	0.01900	9.40E-04	2.73	0.04
VES	JH	0.10920	1.12E-04	0.01467	2.40E-02	2.64	0.03
VES	JH	0.11340	1.12E-03	0.04669	2.40E-02	2.06	0.16
VES	JH	0.10862	2.80E-03	0.03505	7.00E-02	2.72	0.39
VES	JH	0.12021	1.16E-04	0.02296	1.38E-03	1.12	0.02
VES	JH	0.11270	1.16E-04	0.02296	1.38E-03	2.16	0.02
VES	JH	0.12021	1.16E-03	0.22958	1.38E-03	1.12	0.16
VES	JH	0.10193	2.60E-03	0.01469	1.56E-03	3.62	0.35
VES	JH	0.10696	2.60E-03	0.05469	1.56E-03	2.94	0.35
VES	JH	0.11817	1.18E-04	0.03023	2.60E-03	1.40	0.02
VES	JH	0.10958	2.60E-05	0.03184	2.60E-04	2.58	0.00
VES	JH	0.11011	2.00E-04	0.12932	2.00E-04	2.51	0.03
VES	JH	0.10900	2.00E-04	0.02253	8.00E-04	2.66	0.03
VES	JH	0.10900	2.20E-04	0.03965	1.10E-04	2.66	0.03
VES	JH	0.11104	2.80E-03	0.34920	3.80E-03	2.38	0.38
VES	JH	0.11391	9.80E-04	0.12814	1.16E-03	1.99	0.14
VES	JH	0.11110	1.44E-04	0.01000	1.14E-04	2.38	0.02
VES	JH	0.10956	1.46E-03	0.04688	1.60E-04	2.59	0.20
VES	JH	0.11120	2.80E-04	0.11206	9.00E-03	2.36	0.04
VES	JH	0.11130	1.48E-03	0.04566	8.60E-04	2.35	0.20
VES	JH	0.10630	2.20E-04	0.10016	9.80E-04	3.03	0.03
VES	JH	0.10850	1.08E-04	0.03087	8.60E-04	2.73	0.01
VES	JH	0.11307	1.20E-04	0.04029	5.20E-04	2.10	0.02
VES	JH	0.10870	1.24E-04	0.03019	5.60E-04	2.70	0.02
VES	JH	0.11270	1.24E-04	0.11630	5.60E-04	2.16	0.02

Table S4.5. (continued).

Volcanic field	Sample	$^{187}Os/^{188}Os$	2σ	$^{187}Re/^{188}Os$	2σ	$T_{RD}ECR$	2σ
DU	LB	0.12231	7.80E-05	0.01138	4.80E-04	0.82	0.01
DU	LB	0.11800	1.54E-04	0.04250	2.00E-04	1.42	0.02
DU	LB	0.12200	9.40E-04	0.01083	2.20E-04	0.86	0.13
DU	LB	0.12200	8.60E-04	0.09344	2.60E-04	0.86	0.12
DU	LB	0.11680	1.58E-03	0.01282	3.80E-04	1.59	0.22
DU	LB	0.12400	9.80E-04	0.01292	5.40E-04	0.58	0.14
DU	LB	0.12400	7.60E-04	0.08521	1.62E-04	0.58	0.11
DU	LB	0.12500	6.80E-04	0.08532	2.20E-04	0.44	0.10
DU	LB	0.12220	2.80E-03	0.02521	8.00E-05	0.84	0.39
DU	LB	0.11900	6.00E-04	0.01688	2.80E-05	1.28	0.08
DU	LB	0.11911	1.28E-04	0.01676	5.80E-04	1.27	0.02

5. Metallogenic fingerprint of a metasomatized lithospheric mantle feeding gold endowment in the western Mediterranean basin**

***This chapter has been published in Schettino, E., Marchesi, C., González-Jiménez, J. M., Saunders, E., Hidas, K., Gervilla, F., and Garrido, C., 2022, Metallogenic fingerprint of a metasomatized lithospheric mantle feeding gold endowment in the western Mediterranean basin: Geological Society of America Bulletin, v. 134, no. 5/6, p. 1468-1484, https://doi.org/10.1130/B36065.1.*

5.1 Introduction

Accretionary orogens host a wide range of magmatic and hydrothermal ore deposits that provide the largest world resources of copper, gold and silver, as well as significant reserves of base metals, such as zinc, lead, iron, tin, and molybdenum (Bierlein et al., 2009; Groves et al., 2019). These ore deposits are fed by the ascent of ore-productive magmas scavenging metals from metal-rich sources in the subcontinental lithospheric mantle (SCLM; McInnes et al., 1999; Griffin et al., 2013; Tassara et al., 2017; Holwell et al., 2019; Wang et al., 2019; Chong et al., 2021). In these mantle sources, noble metals (platinum-group elements, PGE: Ru, Rh, Pd, Os, Ir and Pt, plus Au) and semi-metals (Se, As, Te, Bi, Sb, Sn) are mostly concentrated in base-metal sulfides (BMS), nano-to-micrometer-sized platinum-group minerals (PGM) and native alloys (Alard et al., 2000; Luguet et al., 2001; Lorand et al., 2008; O'Driscoll and González-Jiménez, 2016). Several studies have used the variability of PGE and semi-metals systematics in distinct populations of BMS and PGM as geochemical markers for assessing the mobility of chalcophile metals during partial melting and metasomatism in the SCLM (González-Jiménez et al., 2014, 2019, 2020; Saunders et al., 2015, 2016; Hughes et al., 2017; Tassara et al., 2018). However, BMS and PGM data of peridotite xenoliths from ore-productive regional settings are still scarce and, therefore, the melt-rock reaction processes enhancing the metallogenic fertility of the SCLM are still poorly constrained.

The peridotite xenoliths entrained in the alkaline basalts from Tallante (Eastern Betic Cordillera, Southeast Spain) provide an excellent scenario for exploring the metallogenic role of the SCLM beneath a crustal volcanic province hosting a wide range of magmatic-hydrothermal ore deposits. Several studies employed these mantle xenoliths to investigate the multi-stage history of partial melting and metasomatism of the SCLM beneath the western Mediterranean (Beccaluva et al., 2004; Shimizu et al., 2008; Rampone et al., 2010; Bianchini et al., 2011, 2015; Hidas et al., 2016; Marchesi et al., 2017). This well-studied sector of SCLM offers the opportunity to constrain how melting and metasomatism may control the mobility and storage of metals in the mantle. In this chapter, I present an integrated study coupling a detailed microstructural description of a suite of peridotite xenoliths from Tallante with in situ chemical characterization of their BMS and associated PGM. These results have been employed to infer how the metasomatic evolution of the lithospheric mantle may affect the metallogenic fertility of an ore-productive domain of continental crust.

5.2 Geological setting

The Pliocene alkaline volcanic field of Tallante represents the youngest magmatic episode (2.93-2.29 Ma, Duggen et al., 2005) of the Neogene Volcanic Province (NVP) in Southeast Spain (Gómez-Pugnaire et al., 2019, for a review). This province is located in the eastern sector of the Betic Cordillera and consists of a volcanic belt extending NE-SW for ~ 150 km along the Mediterranean coast (Fig. 5.1). The NVP comprises Miocene calc-alkaline to ultrapotassic (shoshonitic and lamproitic) volcanic suites. This volcanism changed to alkaline-basaltic activity in the Pliocene-Pleistocene (Duggen et al., 2005). This magmatic evolution, from subduction-related to intraplate magmatism, relates to the complex interplay between compressional shortening along the Iberian-African plate boundary and coeval extensional tectonics in the westward migrating Alborán micro-continent, which eventually collided against the south Iberian and Maghrebian passive margins, thereby generating the arched Betic-Rif Cordillera (e.g., Platt et al., 2013). Stretching of continental lithosphere in response to the westward rollback

of the Tethyan subducting slab properly accounts for the regional evolution of the Alborán domain in the Cenozoic (Lonergan and White, 1997). This geodynamic model is supported by geophysical evidence of an east-dipping detached slab beneath the Gibraltar arc (Bezada et al., 2013), and by geochemical signatures of subduction-related fluids/melts in the mantle sources of Miocene tholeiitic and calc-alkaline lavas from the westernmost Mediterranean (Duggen et al., 2004, 2008; Varas-Reus et al., 2017). Westward retreat of the subduction front during the Miocene caused lateral tearing along the continental margin, which was accommodated by subduction transform edge propagator (STEP) faults yielding the topographic uplift of the eastern Betics (Mancilla et al., 2015, 2018). Continental edge delamination of Iberian lithosphere since the Late Miocene then marked a shift in the associated magmatism towards high-K calc-alkaline, shoshonitic, and lamproitic compositions in response to the asthenosphere upwelling and melting of metasomatized SCLM beneath the southern Iberian margin (Duggen et al., 2005).

Medium- to high-K calc-alkaline volcanism in the NVP (15-6 Ma, Duggen et al., 2008 and references therein) is spatially and genetically associated with important epithermal auriferous (Roadalquilar-Carboneras district) and Pb-Zn-Cu-(Ag) (Mazarrón-La Unión district) ore deposits emplaced in volcanic domes at ~11 Ma (Fig. 5.1) (Arribas et al., 1995; Morales-Ruano et al., 2000; Esteban-Arispe et al., 2016). Hydrothermal fluids, migrating through faults and fractures that acted as magma conduits for the Miocene volcanism (e.g., Carboneras, Palomares, Alhama de Murcia faults), deposited ores in strongly altered calc-alkaline volcanic rocks by mixing of hypersaline magmatic fluids with cooler meteoric solutions (Sänger-von Oepen et al., 1989). Intraplate-type alkaline basalts from Tallante postdate the subduction-related calc-alkaline volcanism associated with ores. Anorogenic signature of these volcanic rocks reflects a sub-lithospheric mantle source and magma contamination by SCLM components (Duggen et al., 2005). The suite of mantle xenoliths carried by such lavas preserves extreme lithological heterogeneity, which records multiple metasomatic episodes associated with the evolution of the transitional lithosphere underlying the southern Iberian margin. Therefore, these mantle peridotites are expected to

provide relevant information on the lithospheric mantle reservoir that possibly fed metal endowment in the overlying crust.

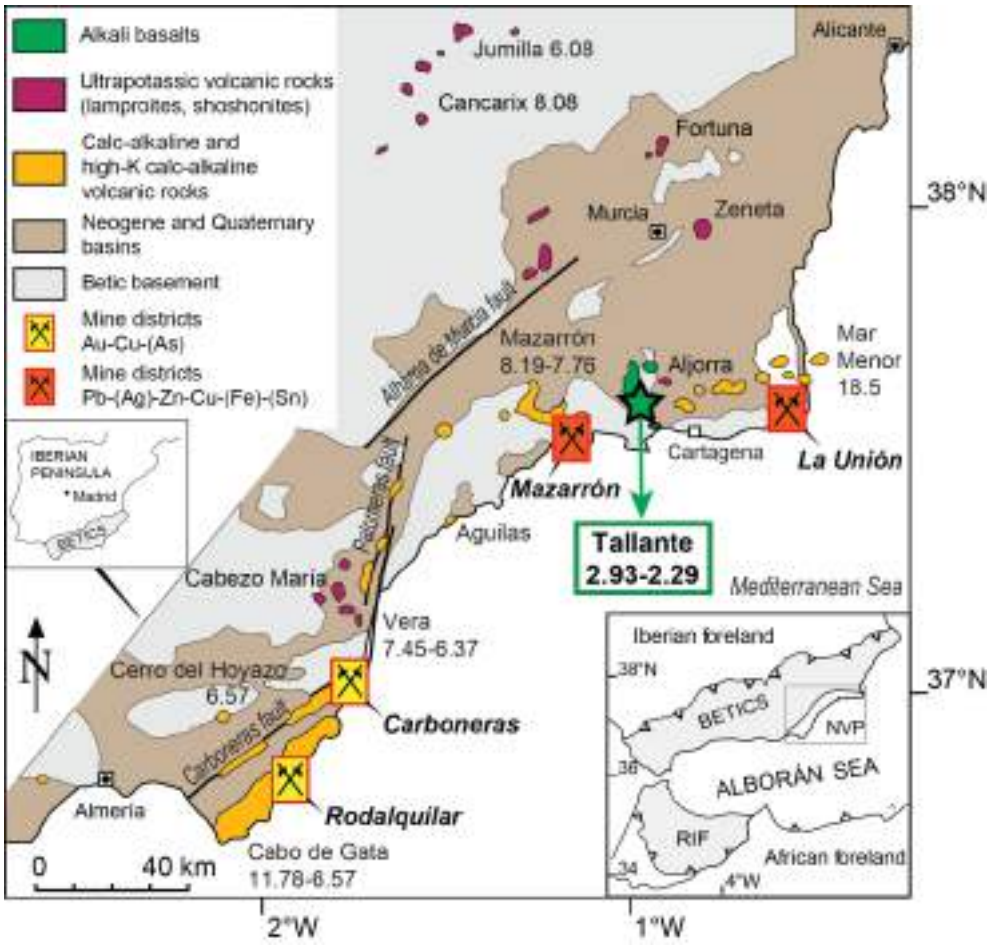

Figure 5.1. Geological sketch map of the Neogene Volcanic Province (NVP) of Southeast Spain with the location of outcrops of different volcanic suites and mining districts (modified from Gómez-Pugnaire et al., 2019). Geochronological data in million years (Ma) of volcanic suites are from Duggen et al. (2008) and references therein.

5.3 Petrogenesis of Tallante mantle xenoliths

Ultramafic mantle xenoliths entrained in the Pliocene lavas of Tallante have been largely used to investigate the petrological, geochemical, and rheological evolution of the subcontinental lithospheric mantle (SCLM) beneath the westernmost Mediterranean. Heterogeneous lithologies preserved in this xenolith suite comprises “fertile” spinel lherzolites, clinopyroxene-poor harzburgites,

orthopyroxene-free wehrlites, plagioclase-impregnated peridotites and composite veined xenoliths, which reflect a complex sequence of metasomatic events that transformed this mantle portion in terms of modal mineralogy and lithophile element distribution. Likewise, systematic variations in textural relations between rock-forming minerals have been thoroughly applied to recognize different microstructural domains, from porphyroclastic to equigranular fabrics, recording variable degrees of crystal-plastic deformation, recrystallization, and melt-rock interaction processes.

The microstructural relations tracking the progressive exhumation of Tallante mantle peridotites have been partially to totally erased by the development of a well-recrystallized equigranular microstructure that overprints a prior porphyroclastic fabric (Rampone et al., 2010). The increasingly granoblastic to polygonal texture within equigranular peridotites formed by an extended stage of melt-assisted annealing, which was likely triggered by melt percolation coeval to the late Neogene formation of veins in composite xenoliths (Hidas et al., 2016). Olivine cystallographic preferred orientation (CPO) in Tallante peridotites are consistent with a subhorizontal ENE directed mantle flow, likely reflecting transtensional deformational regime in response to the Late Miocene slab tearing and continental edge delamination of the Iberian lithosphere (Hidas et al., 2016). Moreover, the occurrence of spinel-orthopyroxene-clinopyroxene clusters within porphyroclastic domains was interpreted as the subsolidus decompression product of former garnet (Shimizu et al., 2008). These clusters range in geometry from rounded aggregates to heavily stretched linear trails, thus representing the mineralogical and microstructural markers of the high-temperature crystal-plastic ductile flow related to mantle upwelling from garnet- to spinel-facies stability fields (Rampone et al., 2010).

The multi-stage metasomatic evolution affecting the SCLM sampled by Tallante xenoliths is then documented by the formation of distinct metasomatic parageneses. Indeed, modal metasomatism in anhydrous Tallante spinel (± plagioclase) peridotites caused widespread precipitation of clinopyroxene + orthopyroxene in “fertile” lherzolites, crystallization of olivine grains dissolving orthopyroxene in pyroxene-poor harzburgites, or crystallization of interstitial plagioclase patches. Such a modal heterogeneity, together with the variability in

REE abundances and isotopic systematics in both clinopyroxene separates and whole rocks, was ascribed either to the multi-stage interaction with different metasomatic agents (Beccaluva et al., 2004; Marchesi et al., 2017), or to a single percolation event involving the upwards migration of silicate melts interacting with peridotite wall-rocks at different lithospheric depths (Rampone et al., 2010). In particular, Marchesi et al. (2017) interpreted the different metasomatic parageneses as the interaction products of peridotites with melts with different silica activities derived from an isotopically heterogeneous mantle reservoir during the Late Oligocene-Miocene evolution of the western Mediterranean. On the other hand, Bianchini et al. (2011) linked the multi-stage metasomatic history to different tectono-magmatic events, namely a Permo-Triassic alkaline magmatism followed by reaction with Jurassic MORB-like basalts. Finally, Rampone et al. (2010) ascribed the litho-diversity recorded by Tallante spinel (± plagioclase) peridotites to the Cenozoic subalkaline magmatism permeating the Alborán SCLM by reactive porous flow of tholeiitic melts shifting from olivine- to orthopyroxene- saturation while rising adiabatically through the lithosphere. Late-stage interaction with SiO_2-undersaturated alkaline magmas finally promoted the consumption of orthopyroxene and the generation of wehrlites in proximity of magma conduits for the ascent of host Pliocene alkali basalts (Marchesi et al., 2017).

The generation of "hybrid" composite lithologies is documented by the formation of hydrous (± amphibole/phlogopite-bearing) orthopyroxenite lenses characterized by extremely enriched Sr-Nd-Hf isotopic signatures (Bianchini et al., 2011). Composite xenoliths are crosscut by felsic veinlets including gabbronorites (Bianchini et al., 2015) and quartz-diorites enveloped by orthopyroxene-rich metasomatic aureole, which display adakite-like geochemical signatures (Arai et al., 2003; Shimizu et al., 2004). These felsic veins have been ascribed to the focused channelization at shallow depths of alkali-rich silica-oversaturated melts with anomalously high $\delta^{18}O$ values and Sr-Nd-Pb isotopic signatures that record the recycling of continental crustal components in the shallow supra-subduction lithospheric mantle (Dallai et al., 2019; Avanzinelli et al., 2020).

5.4 Sampling

I carried out a careful preliminary examination under transmitted/reflected light optical microscope in multiple thin sections of 48 peridotite xenolith from Tallante in order to identify petrographic domains hosting BMS and PGM. Additional details about the microstructure, geochemistry and petrology of these xenoliths can be found in Hidas et al. (2016) and Marchesi et al. (2017). Tallante mantle peridotites pervasively record modal metasomatism involving the formation of orthopyroxene and clinopyroxene at the expense of olivine (Rampone et al., 2010; Marchesi et al., 2017). Petrographic evidence documented that this main type of silicate metasomatism is routinely associated with the presence of BMS, which were detected in clinopyroxene-rich (fertile) lherzolites. Therefore, 14 thin sections from six different samples of these rocks were selected to investigate for the first time the mineral repositories of noble metals and semi-metals in the SCLM beneath the southern Iberian margin.

5.5 Petrography and mineral chemistry of sulfide-bearing peridotites

All the sulfide-bearing mantle xenoliths from Tallante selected for this study are spinel lherzolites (see Fig. S1 in Marchesi et al., 2017), which mainly consist of medium- to fine-grained (0.5–2 mm) olivine, orthopyroxene, clinopyroxene, and spinel (Fig. 5.2a-d). Interstitial films and/or patches of glass are common around clinopyroxene and spinel grains (Fig. 5.2e, f). Plagioclase is present only in one sample (TAL128), both as rims around spinel and interstitial anhedral patches. Accessory amphibole (pargasite) is locally included in clinopyroxene. Base-metal sulfides always constitute inclusions hosted in clinopyroxene and, to a lesser extent, orthopyroxene (Fig. 5.2d-f).

5.5.1 Silicates and spinel

Slightly strained, polygonal olivine grains generally have granoblastic to equigranular texture, which likely formed during pervasive melt percolation at the expense of former porphyroclastic microstructure (Rampone et al., 2010). Few relics of olivine porphyroclasts show kink bands, subgrain boundaries and shape-preferred orientation, marking a weak foliation, indicative of crystal-plastic deformation prior to the equigranular recrystallization. On the other hand, orthopyroxene and clinopyroxene usually form amoeboid, unstrained crystals or irregular patches interstitially scattered between olivine (Fig. 5.2a-d).

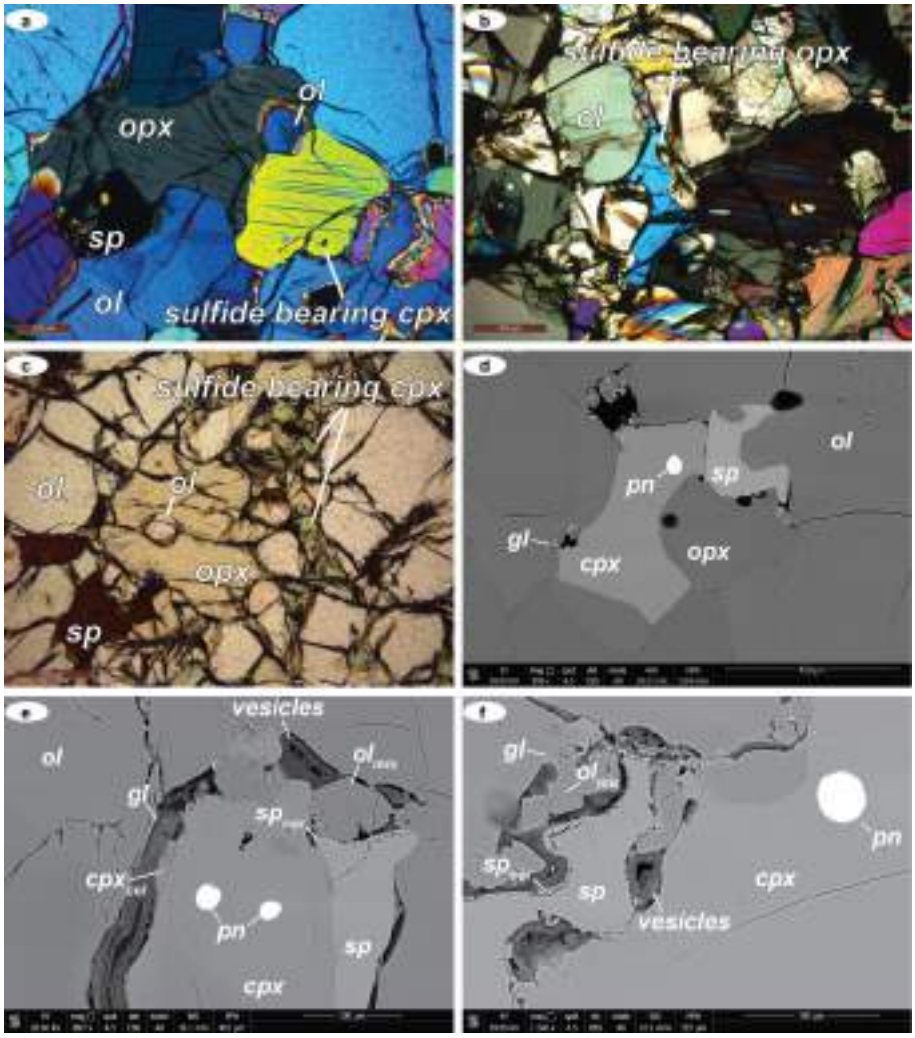

Figure 5.2. Photomicrographs of polarized light optical microscope (a, b, c) and backscattered electron (BSE) images (d, e, f) of sulfide-bearing domains in spinel lherzolites from Tallante. Mineral abbreviations are: ol, olivine; cpx, clinopyroxene; opx, orthopyroxene; sp, spinel; gl, glass; cpx_{cor}, spongy coronae of clinopyroxene; sp_{cor}, spongy coronae of spinel; ol_{mic}, olivine microlites; pn, pentlandite.

Orthopyroxene also forms tabular to anhedral crystals that seem to replace olivine, as suggested by lobate rims and poikilitic textures (Fig. 2a, c). Closely-spaced cleavage planes and exsolution lamellae are locally observed within both types of pyroxene (Fig. 5.2a-b). Dark brown spinel forms subspherical blebs or amoeboid grains interstitial between olivine, locally iso-oriented into linear trails sub-parallel to the sample foliation (Rampone et al., 2010). Moreover, anhedral spinel is commonly in close contact with sulfide-hosting clino- and orthopyroxene forming mineral intergrowths (Fig. 5.2a, c, d) that are scattered between matrix olivine, uncontrolled by the macroscopic foliation and without penetrative shape preferred orientation. In places, these sulfide-bearing clinopyroxene-orthopyroxene-spinel intergrowths have straight internal contacts (Fig. 5.2a, d), whereas both types of pyroxene and spinel display curvilinear grain boundaries and cusp-shaped terminations against olivine (Fig. 5.2a-d).

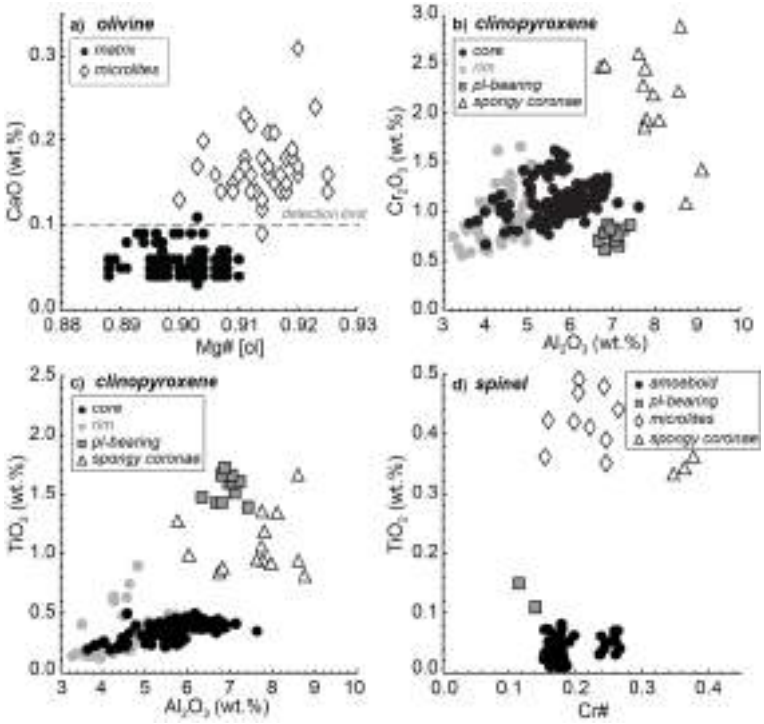

Figure 5.3. Mg# [100 x Mg/(Mg+Fe^{2+})] versus CaO (wt.%) in olivine (a), Al_2O_3 versus Cr_2O_3 (b) and TiO_2 (wt.%) (c) in clinopyroxene, and Cr# [Cr/(Cr+Al)] versus TiO_2 (wt.%) in spinel (d). Black and grey circles indicate the compositions of cores and rims of grains in the matrix, respectively; white diamonds and triangles mark the compositions of microlites and spongy coronae, respectively; grey squares represent the compositions of minerals in the plagioclase-bearing lherzolite samples (TAL128).

Olivine in the matrix has Mg# [100 x Mg/(Mg+Fe^{2+})] from 88.8 to 91.1 and CaO contents below the EMPA detection limit (Fig. 5.3a). Orthopyroxene has Mg# ranging from 89.6 to 91.8, and its Al_2O_3 contents (2.46-5.66 wt.%) are positively correlated with Cr_2O_3 (0.22-1.05 wt.%) and TiO_2 (0.01-0.47 wt.%), and negatively with SiO_2 (53.2-56.8 wt.%). Clinopyroxene shows a preferential distribution pattern defined by decreasing Al_2O_3, Cr_2O_3 and TiO_2 (Fig. 5.3b, c), and increasing Mg# (89.8-93.6) and SiO_2 (49.1-53.7 wt.%) from core to rim. These variations have been interpreted to reflect re-equilibration of clinopyroxene during mantle decompression and cooling (Hidas et al., 2016). Clinopyroxene grains in the plagioclase-bearing lherzolite (TAL128) have TiO_2 abundances that are significantly higher than those in plagioclase-free samples, coupled with relatively low Cr_2O_3 and high Al_2O_3 contents (Fig. 5.3b, c). Similar compositional trends were described in clinopyroxene from plagioclase-bearing peridotites impregnated by exotic melts (Rampone et al., 1997). Amoeboid spinel between olivine or associated with pyroxenes has Mg# = 74.5-81.6, Cr# [Cr/(Cr+Al)] = 0.11-0.27 and low TiO_2 abundances (<0.15 wt.%) (Table S5.1 in the Appendix), which are slightly higher in the plagioclase-bearing sample (Fig. 5.3d).

5.5.2 Interstitial glass pockets

Glass forms lobate pockets and interstitial patches with irregular contacts against clinopyroxene and spinel grains (Fig. 5.2e, f). These pockets consist of a matrix of silicate glass, small (<50 μm) euhedral crystals (microlites) of olivine and spinel, and abundant subspherical vugs and vermicular vesicles (Fig. 5.2e, f). Coarse spinel and clinopyroxene in contact with interstitial glass usually exhibit secondary rims made of spongy coronae and porous overgrowths (Fig. 5.2e, f).

Interstitial glass has silica-rich (54.6-61.2 wt.%) major element compositions, also enriched in Al_2O_3 (19.7-23.2 wt.%), and Na_2O (2.14-5.92 wt.%), and depleted in MgO (1.34-3.59 wt.%), FeO (1.70-2.95 wt.%) and K_2O (< 0.03 wt.%), and present variably low total oxides (Table S5.1 in the Appendix). Both euhedral microlites and coronitic overgrowths in contact with glass pockets have major element compositions that clearly differ from those of the grain cores and coarse grains in the matrix (Fig. 5.3). Olivine microlites have higher Mg#

(90.0-92.5) and CaO contents (0.10-0.31 wt.%) than matrix olivine (Fig. 5.3a), and spinel microlites are enriched in TiO_2 (0.35-0.49 wt.%) compared with coarse spinel (Fig. 3d). On the other hand, clinopyroxene in spongy coronae is usually enriched in Al_2O_3 (5.76-8.75 wt.%), Cr_2O_3 (1.09-2.88 wt.%) and TiO_2 (0.81-1.65 wt.%) compared with inner portions of the grains (Fig. 5.3b, c). The spongy coronae of spinel have higher Cr# (0.35-0.38) and TiO_2 (0.33-0.36 wt.%) compared with the grain core (Fig. 5.3b).

5.5.3 Base-metal sulfides

Base-metal sulfides are droplet-like inclusions (10-50 μm) always hosted in anhedral clinopyroxene and orthopyroxene (Fig. 5.2d-f), without any textural relationship with internal fractures or cracks of the host pyroxene. They are monomineralic or polyphase aggregates consisting of pentlandite locally coexisting with chalcopyrite and/or bornite grains (Fig. 5.4a-c). Chalcopyrite also forms spatially arranged planar intergrowths within larger pentlandite grains (Fig. 5.4d). Locally, grains of pentlandite and bornite are rimmed either by millerite or chalcocite (Fig. 5.4b).

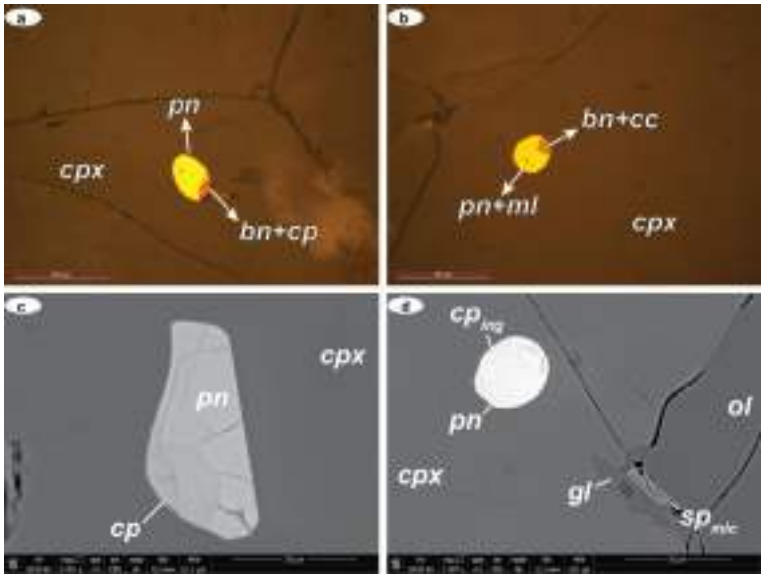

Figure 5.4. Photomicrographs of base-metal sulfide (BMS) assemblages in Tallante peridotite xenoliths: reflected light optical (a, b) and BSE images (c ,d). Mineral abbreviations as in Figure 5.2, and cp, chalcopyrite (ing: intergrowths); bn, bornite; cc, chalcocite; ml, millerite sp_{mic}, spinel microlites.

Pentlandite has metal/S atomic ratios ranging from 1.10 to 1.13, and Ni/(Ni+Fe) atomic ratios from 0.56 to 0.68 (Fig. 5.5a). Cobalt and Cu contents are generally below 0.32 wt.% and 0.90 wt.%, respectively (Table S5.2 in the Appendix). However, Cu contents up to 4.37 wt.% are detected in pentlandite grains with abundant chalcopyrite intergrowths (cf. *mixed analyses, Table S5.2). Chalcopyrite coexisting with pentlandite in composite aggregates has metal/S ratio ~ 1 (Fig. 5.5b) and Ni contents up to ~ 5 wt.% probably due to analytical interference with adjacent pentlandite. Bornite spans from Fe-enriched (Fe = 13.7 wt.%) to sulfur-deficient, Cu-enriched compositions (Cu = 68.9 wt.%) approaching that of chalcocite (Fig. 5.5b). The retrieved bulk compositions of polyphase aggregates have metal/S atomic ratios ranging from 1.07 to 1.14, Ni/(Ni+Fe) = 0.51-0.59, which is slightly lower than in monomineralic pentlandite, and high Cu contents ranging from 6.24 to 14.8 wt.% (Table S5.2).

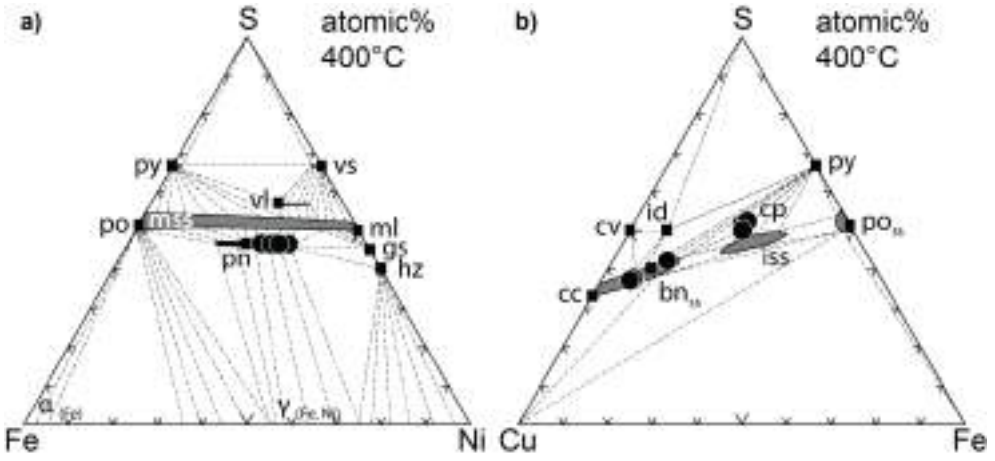

Figure 5.5. Major element compositions (atomic %) of base-metal sulfides (BMS) in Tallante peridotites (black circles) plotted in the Fe-Ni-S (a) and Cu-Fe-S (b) phase diagrams. Phase relations at 400 °C are from Kullerud et al. (1969) for the Fe-Ni-S system, and Cabri (1973) for the Cu-Fe-S system. Mineral abbreviations are: pn, pentlandite; po, pyrrhotite; mss, monosulfide solid solution; ml, millerite; hz, heazlewoodite; py, pyrite; vs, vaesite; vl, violarite; gs, godlevskite; bn_{ss}, bornite solid solution; iss, intermediate solid solution; cv, covellite; cc, chalcocite; cp, chalcopyrite; id, idaite.

Some BMS in the Tallante peridotite xenoliths contain nano-to-micrometer sized PGM. These grains consist of euhedral inclusions, usually less than 1 to ~ 5 µm in size, which commonly occur close to the grain boundary

between sulfide and pyroxene (Fig. 5.6a) without any connection to internal fractures or cracks (Fig. 5.6b). Qualitative identification by EDS microanalyses indicates that these PGM usually consist of Pt(-Pd)-Sn (Fig. 5.6a, b). The focused ion beam (FIB) and transmission electron microscopy (TEM) analysis carried out by González-Jiménez et al. (2020) revealed that these PGM are crystals of tatyanite (ideally $Pt_9Cu_3Sn_4$) with no crystallographic continuity with host pentlandite. Furthermore, several grains of native gold (± platinum) were detected as nanosized inclusions in pentlandite grains. Gold particles display well defined crystal shapes and needle-like morphologies (Fig. 5.6c). Again, there is no textural feature, such as fractures or cracks, controlling the location of the gold particles in the host sulfide. A more precise qualitative identification by EDS microanalyses of these grains is partially hindered by the matrix interferences of major elements (S, Fe, Ni, Cu) in the host sulfide.

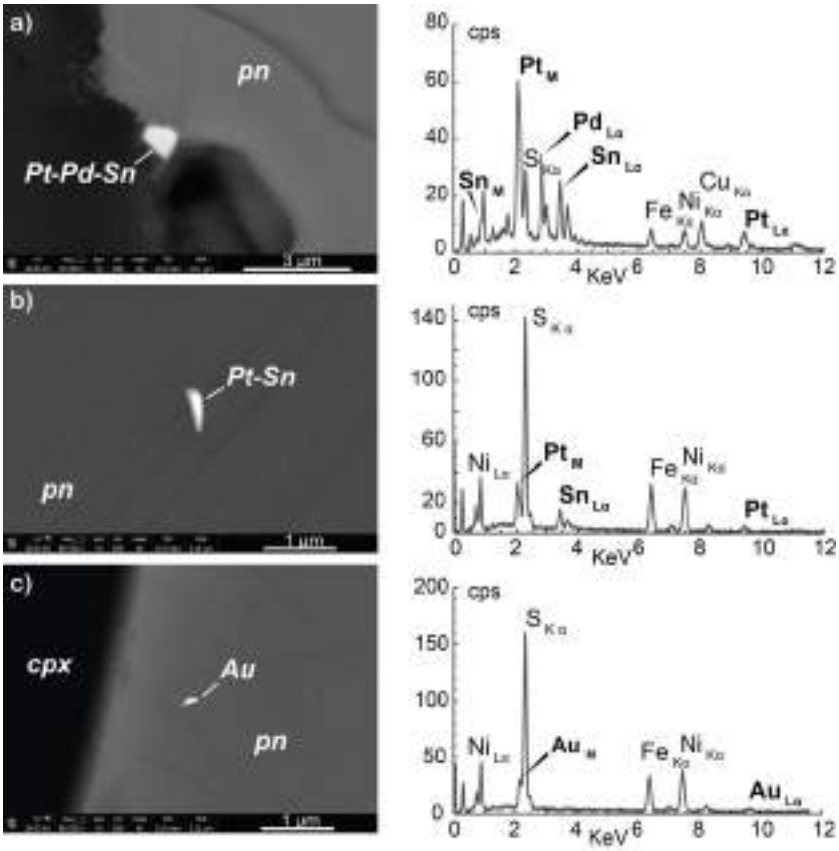

Figure 5.6. BSE images and corresponding EDS spectra of sulfide-hosted tatyanite ($Pt_9Cu_3Sn_4$) (a), Pt-Sn rich platinum-group mineral (PGM) (b), and native gold (c). S-Ni-Fe-Cu peaks in EDS spectra in part reflect contamination by the host sulfide.

5.6 Trace element compositions

5.6.1 Sulfide-hosting clinopyroxene

Coarse clinopyroxene displays rare earth element (REE) concentrations from ~ 3 to 40 times the chondritic values (McDonough and Sun, 1995), with concentrations of most samples between 4 and 10 times chondritic (Fig. 5.7a, b). Clinopyroxene grains in plagioclase-free spinel lherzolites are, in general, light REE (LREE)-depleted (La_N/Sm_N = 0.35-0.85), and present variable middle REE (MREE) over heavy REE (HREE) fractionation (Sm_N/Yb_N = 0.68-1.25) and rather homogeneous HREE contents (Yb_N = 6-11; Fig. 5.7a). These data are consistent with previous results of clinopyroxene in spinel lherzolites from Tallante (Beccaluva et al., 2004; Rampone et al., 2010; Bianchini et al., 2011; Marchesi et al., 2017). However, clinopyroxene from different samples has slightly different REE distributions (Fig. 5.7a). Analyzed grains in TAL110, TAL129, TAL143 and TAL146 exhibit rectilinear enrichment from LREE to MREE (La_N/Sm_N = 0.35-0.85) (type 1a), while grains in sample TAL099 generally have more fractionated LREE-MREE segments (La_N/Sm_N = 0.39-0.49) (type 1b). Furthermore, a few clinopyroxene grains from TAL110 and TAL129 are enriched in LREE relative to MREE (La_N/Sm_N = 1.46-3.06) (type 1c). Clinopyroxene from plagioclase-bearing lherzolite (sample TAL128) displays convex-upward MREE-enriched patterns (La_N/Sm_N = 0.32-0.40; Sm_N/Yb_N = 1.81-2.02) (type 2), analogous to previous observations in clinopyroxene from plagioclase-bearing lherzolites from Tallante (Rampone et al., 2010). Finally, spongy coronae of clinopyroxene in contact with interstitial glass are in general more depleted in LREE (especially La and Ce) than coarser clinopyroxene from the matrix, whereas MREE and HREE have similar concentrations (Fig. 5.7a).

Heterogeneous LREE/MREE patterns are coupled with different concentrations of other incompatible trace elements (Fig. 5.7c, d). Clinopyroxene in plagioclase-free spinel lherzolites displays chondrite-normalized multi-element diagrams (Fig. 5.7c) characterized by variable negative anomalies of high-field strength elements (Nb, Ta, Zr, Hf, Ti) relative to adjacent REE of similar compatibility, coupled with Th-U positive spikes. However, the extent of Th-U

enrichment is linked to LREE/MREE fractionation. Thus, LREE-enriched clinopyroxene (type 1c) has higher concentrations of Th-U relative to Nb-Ta (Th_N/Nb_N = 10.3-98.6), whereas clinopyroxene with lower LREE/MREE ratios (type 1b) has a weaker positive Th-U anomaly (Th_N/Nb_N = 1.08-11.7) and lower Nb_N/Ta_N ratio (0.16-0.52). The less fractionated LREE/MREE type1a clinopyroxene exhibits transitional features between these two signatures (Th_N/Nb_N = 1.61-56.9). Grains with stronger enrichment of Th-U (type 1c) are also more depleted in Ti and Zr relative to adjacent REEs. Lead (Pb) is notably poor in all types of grains (Fig. 5.7c). Clinopyroxene in plagioclase-bearing peridotites (TAL128: type 2) displays low Th-U enrichment (Th_N/Nb_N = 1.18-7.74) coupled with strong subchondritic Nb_N/Ta_N (0.04-0.15) (Fig. 5.7d). Moreover, these grains also have higher Zr-Ti and lower Sr contents compared with clinopyroxene in plagioclase-free lherzolites. Similar clinopyroxene patterns in other plagioclase-impregnated peridotites from Tallante have been ascribed to melt-rock reaction at decreasing melt mass and/or entrapment of small fractions of melt (Rampone et al., 2010).

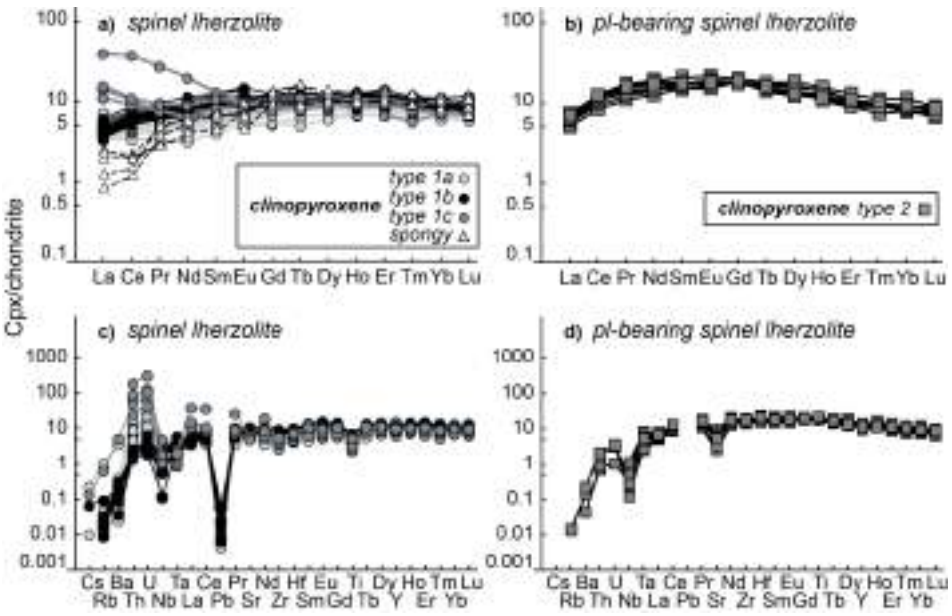

Figure 5.7. Chondrite-normalized concentrations of rare earth elements (REE) and other lithophile trace elements in clinopyroxene of spinel lherzolites (a, c) and plagioclase-bearing lherzolite (b ,d) from Tallante. Light grey, black and dark grey circles in (a) and (c) indicate the compositions of grains with different La_N/Sm_N fractionations (types 1a, 1b, 1c), and white triangles the compositions of spongy coronae of clinopyroxene in spinel lherzolites; pl: plagioclase. Normalizing values from McDonough and Sun (1995).

5.6.2 Base-metal sulfides

In situ chalcophile and siderophile elements data were obtained for BMS inclusions in pyroxene consisting of monomineralic pentlandite (e.g., Fig. 5.2e, f), pentlandite with chalcopyrite intergrowths (e.g., Fig. 5.4d), and pentlandite coexisting with chalcopyrite and/or bornite grains (e.g., Fig. 5.4a, c). The concentrations of PGE and Au in the analyzed BMS (n = 67) are variable and range from 0.470 to 75.3 ppm for Os, 0.370 to 44.0 ppm for Ir, 1.08 to 79.9 ppm for Ru, 0.442 to 14.4 ppm for Rh, 0.194 to 383 ppm for Pt, 0.970 to 247 ppm for Pd, and 0.104 to 46.3 ppm for Au (Table S5.4 in the Appendix).

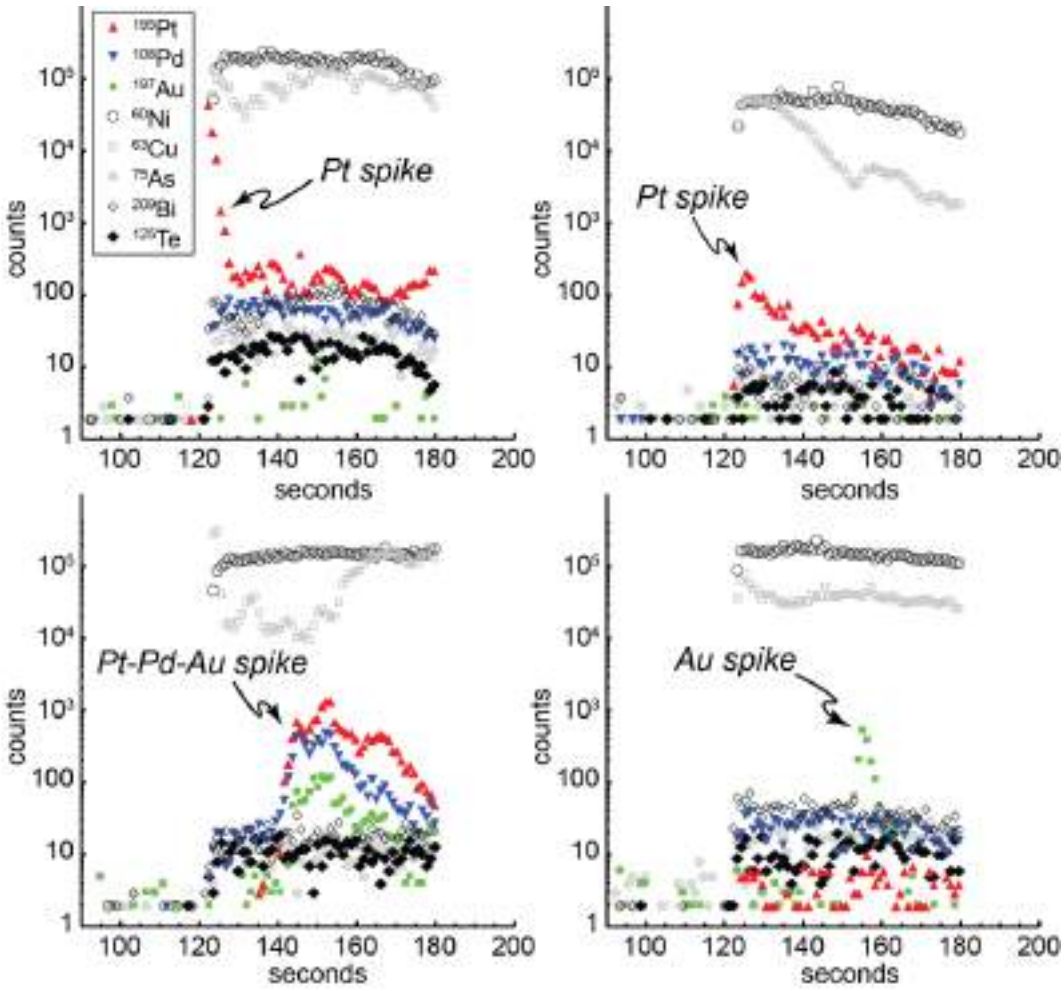

Figure 5.8. Representative time-resolved spectra of LA-ICP-MS analyses for selected isotopes in base-metal sulfides of Tallante peridotites.

The time-resolved spectra of I-PGE (Os, Ir, Ru) and Rh show constant count rates with respect to Ni as a function of ablation time, suggesting that these elements are structurally bound in the BMS. In contrast, the signals of Pt, Au and in some cases Pd show sharp peaks in the time-resolved spectra of several sulfides, revealing the presence of discrete Pt-, Au- and Pt-Pd-Au-bearing micro-inclusions dispersed within the host BMS (Fig. 5.8). These submicrometer-sized nuggets, which were already observed as crystal phases during SEM analyses (Fig. 5.6), are thought to be the reason for the high contents of Pt, Au, and sometimes Pd in several analyzed BMS, whereas low concentrations of these elements are generally associated with the lack of positive spikes in the time-resolved spectra.

Three distinct groups of chondrite-normalized PGE patterns (normalizing values from Fischer-Gödde et al., 2010) were identified based on their Pd_N/Ir_N ratios in the whole suite of BMS (Fig. 5.9), regardless of the assemblage constituting the analyzed inclusion: (1) nearly flat PGE patterns with variable enrichment in P-PGE (Pd_N/Ir_N = 1.03-4.56) (n = 37; Fig. 5.9a), (2) arch-shaped PGE patterns with an almost flat segment from Os to Rh and a negatively fractionated segment from Rh to Pd (Pd_N/Ir_N = 0.14-0.90) (n = 19; Fig. 5.9b), and (3) positively fractionated PGE patterns with low I-PGE contents and suprachondritic Pd_N/Ir_N ratios (5.28-30.74) (n = 11; Fig. 5.9c). Interestingly, the analyzed BMS may display depletion in Pt and Au down to less than 0.5 times the chondritic concentrations, regardless of the compositional group (Pd_N/Ir_N ratio) to which they belong (Fig. 5.9a-c). A careful inspection of their respective time-resolved spectra reveals that negative anomalies are detected when Au- or Pt-spikes (Fig. 5.8) are lacking.

Abundances of semi-metals vary from 91.3 to 225 ppm for Se, 5.36 to 116 ppm for As, 10.3 to 42.6 ppm for Te, 0.274 to 3.02 ppm for Sb, and 0.350 to 9.79 ppm for Bi (Table S5.4). Their signals in the time-resolved spectra are homogeneous with respect to Ni, suggesting they entered in solid solution in the BMS (Fig. 5.8). The normalized concentrations of these elements ordered from left to right according to their atomic radius are similar for the three sulfide groups with different Pd_N/Ir_N fractionations (Fig. 5.9d-f). Noteworthy, Te and, especially, Bi are slightly enriched in all grains, whereas As has variable abundances defining

significant positive anomalies (Fig. 5.9d-f). The extent of the positive As anomaly does not show any correlation with either Pd_N/Ir_N fractionation or with depletion in Pt and Au.

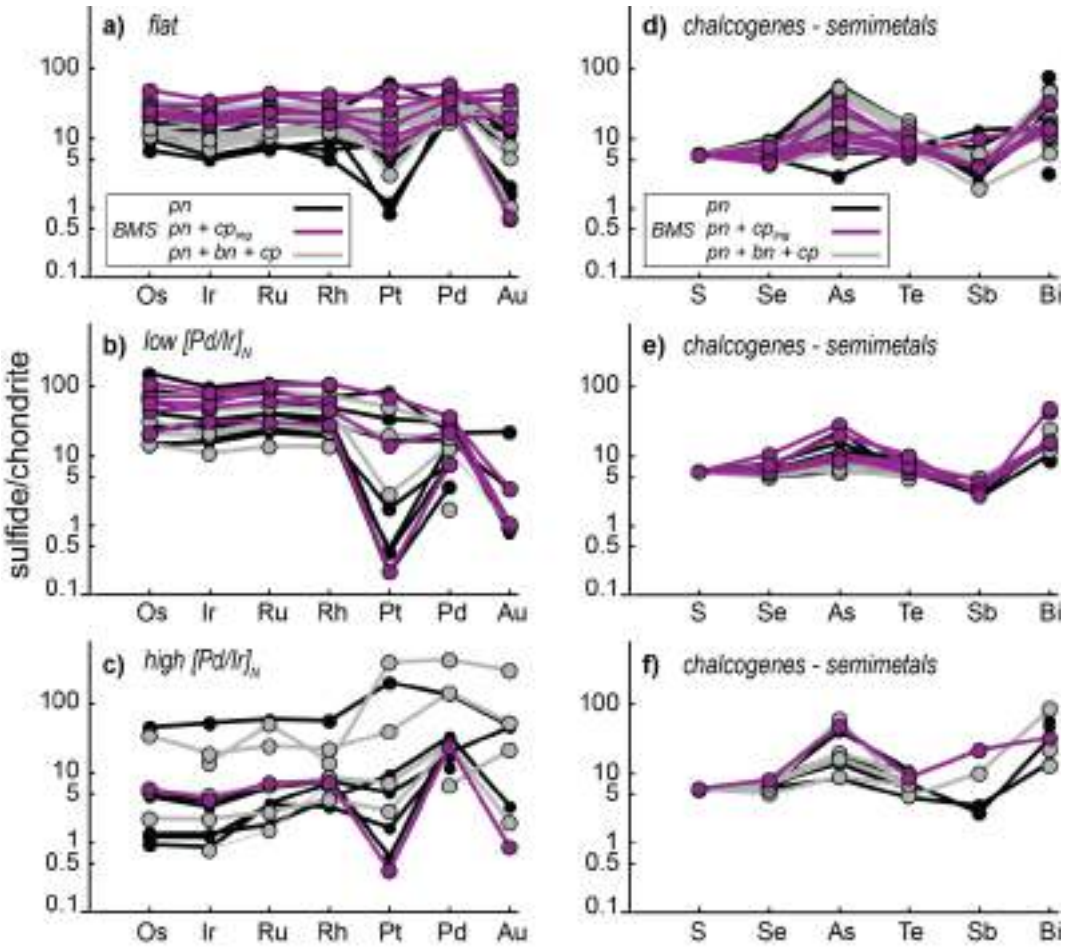

Figure 5.9. Chondrite-normalized abundances of platinum-group elements (PGE) (a, b, c) and semi-metals (d, e, f) in BMS with different Pd_N/Ir_N fractionations from Tallante peridotites. Both PGE and semi-metals are ordered from left to right according to decreasing compatibility in mss coexisting with a sulfide liquid. Black lines indicate patterns of monomineralic pentlandite (pn), purple lines of pentlandite + chalcopyrite intergrowths (cp_{ing}), and grey lines of pentlandite + bornite + chalcopyrite (pn + bn + cp). Normalizing values are from Fischer-Gödde et al. (2010), and McDonough and Sun (1995).

5.7 Discussion

5.7.1 Metasomatic origin of sulfide-hosting clinopyroxene

The granoblastic texture of the sulfide-bearing peridotite xenoliths from Tallante records annealing recrystallization of the olivine fabric in response to pervasive percolation of silicate melts (Rampone et al., 2010; Hidas et al., 2016). Sulfide-hosting anhedral pyroxenes are commonly associated with spinel, forming irregular intergrowths scattered between olivine grains (Fig. 5.2). The distribution of these clinopyroxene + orthopyroxene + spinel intergrowths lack of any geometric control by the olivine fabric, suggesting they formed subsequently to the deformational stage that produced the sample foliation. Moreover, both pyroxenes and spinel frequently corrode or include olivine through lobate rims or poikilitic texture (Fig. 5.2a-d), supporting they formed by melt-rock interaction rather than by garnet breakdown as proposed by Shimizu et al. (2008) and Rampone et al. (2010). This interpretation is consistent with modal metasomatism causing FeO-SiO_2 enrichment in these fertile spinel lherzolites (Marchesi et al., 2017). Reactive percolation of silicate melts by porous flow in peridotite xenoliths from Tallante is further documented by crystallization of olivine rims replacing orthopyroxene, or vice versa (Rampone et al., 2010). Sulfide droplets are systematically included within metasomatic clino- and orthopyroxene (Fig. 5.2d-f, 5.4), suggesting that their precipitation took place when the percolating silicate melt shifted from olivine- to pyroxene-saturation while rising adiabatically and interacting with host peridotites (Rampone et al., 2010).

Variations in the abundances of trace elements in clinopyroxene (Fig. 5.7) likely reflect their chromatographic fractionation during interaction of lithospheric mantle with percolating melt (Navon and Stolper, 1987). As chemical exchange between melt and peridotite wall-rock is faster for the more incompatible elements, comparatively stronger compositional heterogeneities are expected for large ion lithophile elements (LILE: Cs, Rb, Ba), LREE and high-field strength elements (HFSE: Nb, Ta, Th, and U). Therefore, the progressive shift from LREE-depleted (types 1a and 1b) to LREE-enriched patterns (type 1c) of sulfide-hosting clinopyroxene (Fig. 5.7a) was probably produced by the reaction with

silicate melts at decreasing melt/rock ratios (Bedini et al., 1997; Ionov et al., 2002). The stronger positive U-Th peaks coupled with higher LREE concentrations and Nb_N/Ta_N ratios observed in a few clinopyroxene grains (type 1c, Fig. 5.7c) are possibly due to late-stage interaction with small melt fractions, which finally evolved towards compositions more enriched in incompatible elements as a consequence of their progressive differentiation and percolation through the SCLM (Bedini et al., 1997; Rampone et al., 2010).

The age of norite veins cross-cutting peridotites in composite mantle xenoliths from Tallante (6.8 ± 2.0 Ma) (Bianchini et al., 2015) indicates that the metasomatic event producing the formation of sulfide-hosting pyroxene predated the Late Miocene-Pleistocene alkaline magmatic cycle in the eastern Betic Cordillera (Duggen et al., 2005). According to Bianchini et al. (2011), Sr-Nd-Hf isotopes of clinopyroxene corroborate that Jurassic MORB-type silicate melts were the main metasomatic agent in the Tallante lithospheric mantle. However, the lack of geochemical equilibrium between different clinopyroxene grains at the thin section scale (Fig. 5.7) argues against an old Mesozoic percolation event in these rocks. Indeed, the general LREE-depleted signature of clinopyroxene in extensively percolated peridotites from Tallante has been ascribed to pervasive re-equilibration with Cenozoic tholeiites of subduction-related affinity (Rampone et al., 2010). Based on the wide variability of Sr-Nd-Pb isotopic signatures, Marchesi et al. (2017) ascribed the microstructural and compositional features of metasomatic clinopyroxene to reactive porous flow of melts from a pyroxenite-bearing heterogeneous mantle source.

Melts with a pyroxenite component played a key role in the geochemical refertilization of the SCLM beneath the western Mediterranean (Lambart et al., 2012; Marchesi et al., 2014). Thermodynamic and experimental work indicates that clinopyroxene, orthopyroxene and spinel crystallize from a pyroxenite-derived melt interacting with peridotite (Lambart et al., 2012). Depending on the silica activity of this melt, either olivine or orthopyroxene occurs on the liquidus surface together with clinopyroxene ± spinel (Lambart et al., 2012), properly accounting for the coupled dissolution of olivine and formation of orthopyroxene, or vice versa, recorded by the whole set of Tallante spinel peridotites (Rampone et al., 2010; Marchesi et al., 2017). In the context of the geodynamic evolution of the

western Mediterranean, partial melting of a pyroxenite-peridotite veined mantle was likely caused by lithospheric extension and asthenosphere upwelling due to westward rollback retreat of the subduction system in the Cenozoic (Duggen et al., 2005, 2008). In summary, previous works and these new compositional and textural observations on Tallante xenoliths support the hypothesis that the metasomatic event leading to crystallization of sulfide-hosting pyroxene was due to the Miocene subduction-related subalkaline metasomatism permeating the southern Iberian lithosphere in response to the upwelling of a hot asthenospheric mantle upon slab rollback and tearing of the continental paleomargin (Mancilla et al., 2015; Hidas et al., 2016).

5.7.2 In situ melting of metasomatic domains

Interstitial glass within Tallante spinel lherzolites forms vug-rich lobate pockets that border clinopyroxene and spinel (Fig. 5.2e, f). The absence of glass around domains constituted by olivine, the main rock-forming mineral, rules out the hypothesis that it represents external melt infiltrating the peridotites. In addition, glass pockets are remarkably enriched in SiO_2 and Al_2O_3 (Fig. 5.10), and depleted in MgO, FeO, TiO_2 and K_2O (not shown) compared with host alkali basalts (Fig. 5.10), supporting the idea that they are not simply portions of host magma trapped in the xenoliths (Coltorti et al., 2000; González-Jiménez et al., 2014; Tassara et al., 2018). Homogeneous TiO_2/Al_2O_3 ratios (~ 0.04 to 0.07) over the whole range of SiO_2 abundances in glass (Fig. 5.10) are also inconsistent with reaction between peridotite and infiltrating alkali basaltic melts (Neumann and Wulff-Pedersen, 1997). Moreover, amphibole and phlogopite relics are absent in the matrix of the studied spinel lherzolites, arguing against an origin of glass by incongruent breakdown of these phases (Yaxley et al., 1997).

On the other hand, the exclusive association of glass with metasomatic clinopyroxene-spinel assemblages supports its generation by in situ melting of small-scale mineral domains formed during Miocene refertilization. Indeed, the compositions of glass (Table S5.1) resemble those of near-solidus melts of fertile spinel peridotites at low pressure (1 GPa) (Fig. 5.10) (Baker et al., 1995; Falloon et al., 2008). Empty vugs and subspherical vesicles in glass pockets (Fig. 5.2e, f)

suggest that a significant amount of volatiles were originally dissolved in the melt now quenched to silicate glass. This supports that melting occurred under hydrous conditions, possibly explaining the SiO_2-rich composition of several interstitial glass patches compared with anhydrous near-solidus melts (Fig. 5.10) (Gaetani and Grove, 1998). In this scenario, volatiles likely lowered the solidus temperature of spinel lherzolites at low pressure, promoting the small-scale melting of sulfide-hosting clinopyroxene and spinel (Ionov et al., 1994). This local event should have occurred at very low melting degrees, thus preserving most of the clinopyroxene-spinel assemblages and generating small amounts of melts, which were unable to segregate through interconnected channels (von Bargen and Waff, 1986) and were instead trapped at interstices in close contact with their source minerals. The irregularly shaped geometries of glass patches (Fig. 5.2e, f) contrast with the equilibrium melt distribution predicted for a partially molten peridotite at mantle conditions (Jin et al., 1994), suggesting that the entrapment of melt pockets occurred in a relatively short time.

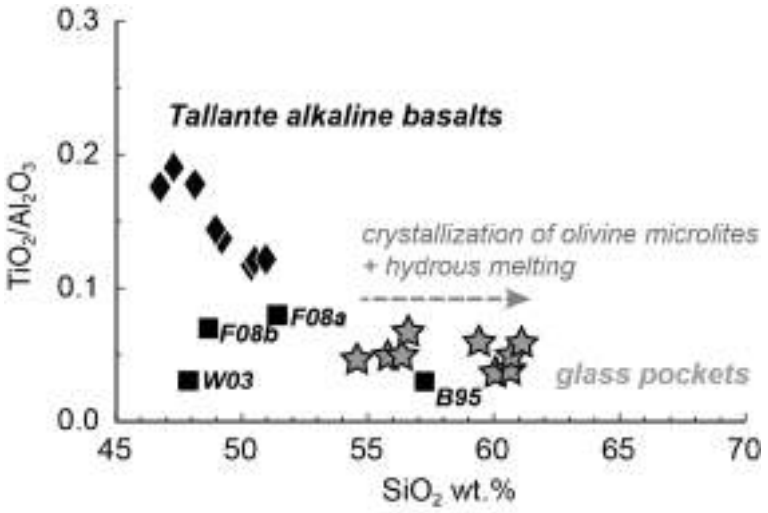

Figure 5.10. TiO_2/Al_2O_3 versus SiO_2 (wt.%) for glasses in spinel lherzolites from Tallante (grey stars) compared with data of host alkali basalts (black diamonds, Duggen et al. 2005) and experimentally-determined near-solidus melts of lherzolites at 1 GPa (B95-Baker et al. 1995; F08a-Falloon et al. 2008), 1.5 GPa (F08b-Fallon et al. 2008), and of depleted harzburgite at 1 GPa (W03-Wasylenki et al. 2003) (black squares).

At contacts with glass, clinopyroxene and spinel usually display spongy coronae (Fig. 5.2e, f) that constitute a reaction zone with quenched melt ("spongy

textures" in Kovács et al., 2007; Pan et al., 2018). This melt-mineral reaction led to higher contents of Al_2O_3, TiO_2 and Cr_2O_3 in spongy clinopyroxene, as well as of TiO_2 in spongy spinel, in comparison with the inner portion of the grains (Fig. 5.3b-d). In addition, enhanced partitioning of Ti in clinopyroxene at near-solidus melting conditions (Baker et al., 1995) may have contributed to enrich TiO_2 in spongy clinopyroxene. Low degrees of partial melting at grain rims may explain lower LREE concentrations in spongy clinopyroxene (Fig. 5.7a) and slightly higher Cr# in spongy spinel (Fig. 5.3b) (Yaxley et al., 1997; Kovács et al., 2007). However, higher Cr# in spinel may also reflect low-pressure re-equilibration of spongy coronae with Si-rich hydrous melts now quenched to glass (Dick and Bullen, 1984).

Small euhedral microlites of olivine and spinel randomly dispersed within glass pockets likely represent the crystallization products of the melt quenched to silicate glass in which microlites are now included (Yaxley et al., 1997). Relatively high CaO in olivine (Fig. 5.3a) and TiO_2 in spinel microlites (Fig. 5.3d) are consistent with this interpretation (Dick and Bullen, 1984). High Mg# values of olivine microlites (90.0-92.5) support their precipitation from a primitive mantle melt that experienced minor fractional crystallization. This interpretation is consistent with experimental results that show how highly silicic mantle melts may reach saturation in high-Mg# olivine at relatively low pressure (1 GPa) (Draper and Green, 1997). Fractional crystallization of olivine likely contributed to increase SiO_2 (Fig. 5.10) and decrease MgO and FeO in the coexisting melt, accounting for the compositional variability of these glasses (Table S5.1). In the context of the petrological evolution of the Tallante peridotites, in situ low degrees of partial melting of metasomatic clinopyroxene and spinel are likely the results of supply of heat and volatiles from the Pliocene alkaline magmas that finally carried the xenoliths to the surface.

5.7.3 Fingerprinting the origin of BMS included in metasomatic pyroxene

All the BMS grains identified in the Tallante xenoliths are included in metasomatic pyroxene and exhibit rounded morphology (Figs. 5.2, 5.4). This

suggests that BMS are the solidified products of immiscible droplets of sulfide melt entrained in subalkaline silicate melts (e.g., Andersen et al., 1987) that produced the refertilization of Tallante peridotites via formation of clinopyroxene + orthopyroxene + spinel assemblages (Aulbach et al., 2021).

These sulfide inclusions consist of Ni-rich pentlandite coexisting with minor chalcopyrite and/or bornite (Fig. 5.4). At the temperature conditions (850-1050 °C) estimated for the equilibration of this set of mantle xenoliths (Hidas et al., 2016), phase relations in the Fe-Ni-Cu-S system predict that Fe-rich monosulfide solid solution (*mss*) should be the first solid to crystallize from sulfide melt droplets (Kullerud et al., 1969). If so, the fractionation of such sulfide melts must be governed by the sequential crystallization of monosulfide (*mss*) and/or intermediate (*iss*) [$(Cu_{1\pm x}Fe_{1\pm y})S_2$] solid solutions (Ballhaus et al., 2001). In this scenario, pentlandite may crystallize either at ~865 °C as a result of peritectic reaction between Fe-rich *mss* (pyrrhotite) and residual Ni-rich liquid (Sugaki and Kitakaze, 1998), or at lower temperature (< 610 °C) as the subsolidus re-equilibration product of former *mss* reacting with heazlewoodite [$(Ni, Fe)_{3\pm x}S_2$] solid solution (*hzss*) (Kullerud et al., 1969). However, such a crystallization pathway does not explain the compositions of BMS from Tallante because: (1) their reconstructed bulk compositions have Cu contents (up to 14.8 wt.%) exceeding the solubility limit of Cu in *mss* (maximum of 7.5 wt.% Cu in *mss* structure at 935 °C; Cabri, 1973), and (2) pyrrhotite (the low temperature product of equilibration of the high-temperature *mss*) does not occur in Tallante composite BMS, ruling out the formation of pentlandite by re-equilibration of former *mss*, either by subsolidus or peritectic reaction (Mansur et al., 2019).

Conversely, the reconstructed bulk compositions of these sulfides point out that their parental melts had compositions arising from the central portion of the Fe-Ni-Cu-S tetrahedron (see Fig. 1a in Peregoedova and Ohnenstetter, 2002) as is typical for sulfides precipitated from metasomatic Cu-(Ni-Fe)-rich melt formed by incongruent melting of pre-existing Fe-Ni-Cu sulfides (Bockrath et al., 2004; Luguet and Reisberg, 2016). The bulk Ni-Cu rich compositions, together with high metal/S (~1.1, Table S5.2) and low Fe/(Fe+Cu) ratios of the Tallante sulfides (Fig. 5.11), are more consistent with their formation in a portion of the Fe-Ni-Cu-S system dominated by the early (850-900 °C) crystallization of the

quaternary solid solution comprising the compositional range between heazlewoodite (*hzss*) and intermediate (*iss*) solid solutions (Peregoedova and Ohnenstetter, 2002). Once cooling, this quaternary solid solution may increase its bulk Ni/Cu ratio breaking down to pentlandite from *hzss* at ~760 °C and chalcopyrite (and/or bornite) from *iss* below 557 °C (Fleet and Pan, 1994; Kullerud et al., 1969; Peregoedova and Ohnenstetter, 2002), explaining the observed *pn* ± *cp* ± *bn* assemblages in the Tallante peridotites (Fig. 5.4).

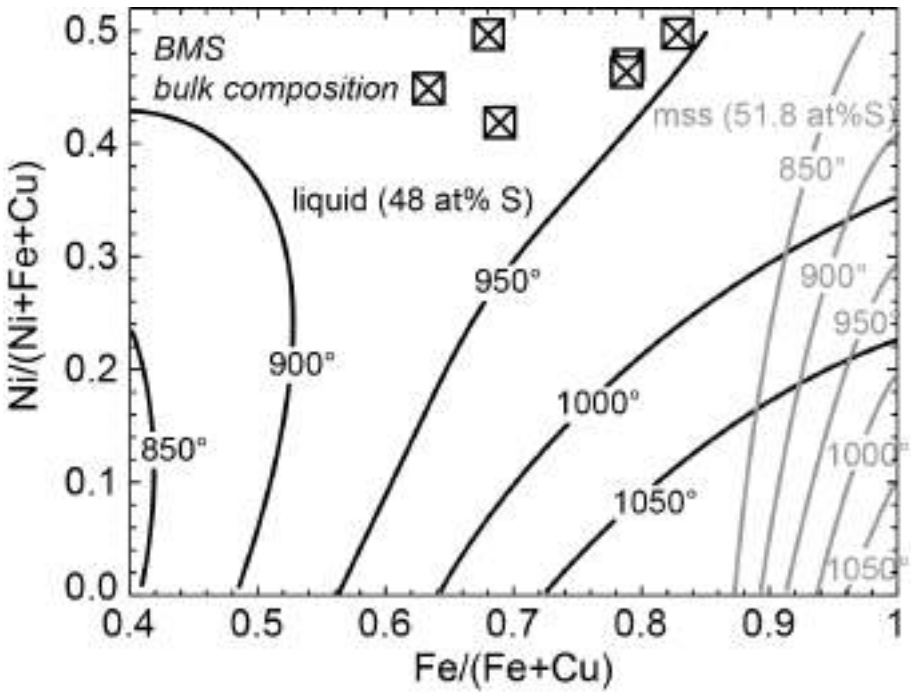

Figure 5.11. Reconstructed bulk compositions of BMS from Tallante peridotites (squares) in the Fe/(Fe+Cu) versus Ni/(Ni+Fe+Cu) plot. Grey and black lines are calculated isopleths of mss (51.8 at.% S) and coexisting sulfide liquid (48 at.% S) at different temperatures, respectively (Fleet and Pan, 1994).

On the other hand, BMS from Tallante exhibit broad variability of chondrite-normalized PGE patterns ($0.14 < Pd_N/Ir_N < 30.74$) (Fig. 5.9), which can be grouped into three main types: (1) sulfides with nearly chondritic PGE relative abundances ($Pd_N/Ir_N \sim 1$), which are commonly observed in "pristine" mantle *mss* (Bockrath et al., 2004); (2) sulfides with negatively trending PGE patterns ($Pd_N/Ir_N < 1$) as is typical of residual *mss* left after partial melting (i.e., Type 1 BMS in Luguet and Reisberg, 2016), and (3) sulfides with positively trending PGE patterns ($Pd_N/Ir_N > 5$) as those reported for BMS precipitated from

metasomatic Ni-Cu rich sulfide melts migrating through the SCLM (i.e., Type 2 BMS in Luguet and Reisberg, 2016). These three types of chondrite-normalized PGE patterns characterize sulfide aggregates with almost constant Ni-Fe-Cu compositions (i.e., *pn* ± *cp* ± *bn*) (Fig. 5.5), suggesting that the fractionation of PGE was not governed by the known melt-solid and solid-solid partition coefficients at equilibrium. Moreover, these sulfides exhibit remarkably homogeneous concentrations of semi-metals (Fig. 5.9d-f), which provides additional evidence that PGE abundances were not controlled by the expected chalcophile partitioning during fractionation of a sulfide melt, as commonly predicted by experimental results (Ballhaus et al., 2006) and empirical studies (Alard et al., 2000; Lorand and Alard, 2001). Furthermore, there is no correlation between Pd_N/Ir_N of BMS and indicators of silicate melt fractionation (e.g., La_N/Sm_N) in their host pyroxene (Fig. 5.12), suggesting that the variability in PGE systematics did not originate from variable extents of interaction with the agents of silicate metasomatism (e.g., Saunders et al., 2015; Tassara et al., 2018).

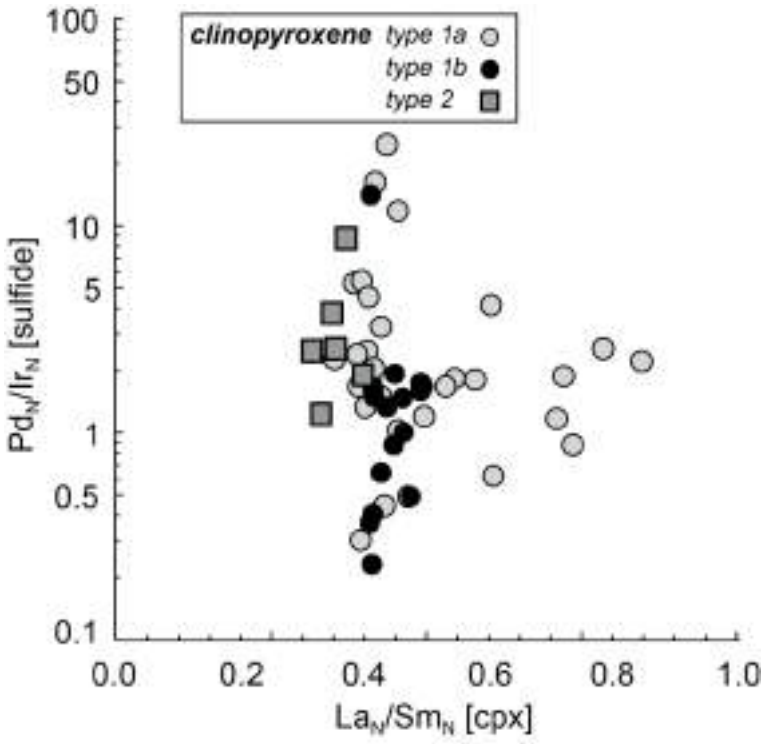

Figure 5.12. Pd_N/Ir_N ratio of BMS in Tallante peridotites versus La_N/Sm_N of host clinopyroxene. Symbols as in Fig. 5.7.

All these observations point out that Tallante BMS crystallized from Ni-Cu rich sulfide melt(s) that inherited the PGE signatures of distinct populations of pre-existing sulfides and/or PGM, each one with its own distinct PGE systematics, which melted incongruently during extraction and/or migration of silicate melts in the SCLM. Several works have shown that the PGE composition of the SCLM is highly heterogeneous at different scales (Aulbach et al., 2016; Aulbach et al., 2021), as the PGE budget is controlled by various populations of BMS and PGM recording multiple episodes of partial melting and metasomatism (González-Jiménez et al., 2014; Hughes et al., 2017; Tassara et al., 2018). As the melting region in subduction settings is normally several tens to hundreds of kilometers across and may extend to depths greater than 100 km (e.g., The MELT Seismic Team 1998), individual melt batches ascending through the upper mantle above a subduction zone may carry PGE signatures inherited from distinct BMS/PGM populations. The preservation of variable PGE signatures in the Tallante sulfides implies that melt extraction, melt-rock interaction, and melt crystallization did not erase the original noble metal systematics of the pre-existing sulfides and/or PGM, despite producing relatively homogeneous bulk Ni-Fe-Cu and semi-metal signatures.

5.7.4 The role of nano-to-micrometer sized PGM and gold particles

Careful examination of the time-resolved spectra signals collected during the in situ LA-ICP-MS analyses of the Tallante BMS reveals the frequent presence of ^{195}Pt, ^{108}Pd, and ^{197}Au positive spikes (Fig. 5.8). This observation is consistent with BSE images, acquired by FEG-ESEM, confirming the presence of several types of nano-to-micrometer sized inclusions of Pt(-Pd)-Sn rich PGM (including tatyanite $Pt_9Cu_3Sn_4$, González-Jiménez et al., 2020) and gold particles in BMS (Fig. 5.6). The high-magnification imaging of tatyanite nanoparticles by combining high-resolution SEM and high-resolution TEM revealed a predominantly euhedral morphology and the absence of crystallographic continuity with the host BMS (i.e., pentlandite or chalcopyrite, González-Jiménez et al., 2020). These observations suggest that the formation of nano-to-micrometer sized PGM likely preceded the precipitation of their host BMS. This hypothesis is

consistent with the fact that refractory Pt(-Pd)-Te-Sn compounds have higher solidus temperature (>1200 °C) than the liquidus temperature of Cu-Fe-Ni-S melts (Sinyakova et al., 2016, 2019), suggesting they crystallize before being trapped into BMS. The enrichment in Sn in such Pt-rich PGM (Fig 6a, b) suggests that this semi-metal enhanced the formation of immiscible Pt-rich nanomelts or nanoparticles in both the silicate and sulfide liquids (Helmy et al., 2007, 2013; Anenburg and Mavrogenes, 2020; González-Jiménez et al., 2019, 2020). Interestingly, (sub)-micrometer sized PGM consisting of Pt bounded with semi-metals (As, Te, Bi) have been reported in other mantle BMS, including pentlandite (Luguet et al., 2007; Lorand et al., 2010; Alard et al., 2011; González-Jiménez et al., 2019). Experimental works also support the more refractory nature of these Pt-rich minerals than BMS, owing to the strong tendency of Pt to form semi-metal complexes in both silicate and sulfide melts (Helmy et al., 2013; Helmy and Bragagni, 2017; Anenburg and Mavrogenes, 2020).

Similarly, gold particles in the Tallante peridotites also exhibit euhedral morphology and no specific microstructure that might control their location within the host BMS, suggesting that they crystallized prior to BMS rather than by low-temperature exsolution. Previous works have shown that gold is almost insoluble into pentlandite (Piña et al., 2012) or its potential precursors such as *mss*, *hzss*, or *iss* (Barnes et al., 2006; Holwell et al., 2015). Indeed, Sinyakova et al. (2019) synthetised nano-to-micrometer sized gold alloys at high temperatures (>1000 °C) directly from Ni-Cu-Fe sulfide melts, demonstrating that, if these types of melts become sufficiently enriched in gold, this metal can form its own mineral phases instead of being trapped in the lattice of BMS. Moreover, experimental studies have shown that gold solubility in silicate melts is strongly related to melt sulfur content (Li and Audétat, 2013; Li et al., 2019). Therefore, once a fractionating silicate melt achieves sulfide saturation, a rapid drop in $S_{[melt]}$ may cause local precipitation of native gold, as supported by the occurrence of several gold-bearing silicate glasses in mantle xenoliths worldwide (Tassara et al., 2017; González-Jiménez et al., 2020).

An attentive analysis of the LA-ICP-MS signals of BMS indicates that negative Pt and Au anomalies in chondrite-normalized PGE patterns (Fig. 5.9) are systematically associated with lack of positive spikes in their respective time-

resolved spectra. In contrast, positive anomalies and/or nearly chondritic proportions of Pt and Au relative to adjacent PGEs (Fig. 5.9) are systematically correlated with pronounced Pt and Au spikes in the time-resolved spectra (Fig. 5.8), confirming that the presence or absence of (sub)-micrometric particles largely controls the Pt-Au budget of the BMS. These observations suggest that a selective uptake of Pt and Au by nanoparticles (or nanomelts) preceding the formation of the Tallante BMS may have strongly depleted these two elements in the crystallizing sulfides, whereas the mechanical assimilation of these pre-existing metal particles produced nearly chondritic or superchondritic concentrations. Thus, the presence or lack of PGM and metal-bearing particles exerted a strong "disturbing impact" on the PGE systematics of the analyzed BMS.

This interpretation corroborates recent experimental (Anenburg and Mavrogenes, 2020) and empirical works (Zelenski et al., 2017; Kamenetsky and Zelensky, 2020), showing that mantle-derived sulfide droplets may preserve their variable PGE systematics over distances covering the whole lithospheric column, especially whether they transport discrete nano-to-micrometer sized particles or melts. As discussed above, the metal-bearing particles may have been segregated at any stage of the evolution of the Tallante peridotites, either directly from silicate melt prior to sulfide saturation, or from droplets of immiscible sulfide melt, once sulfide saturation was already achieved. Alternatively, Pt-rich PGM and Au-bearing minerals may have been also assimilated and transported in the silicate melt during melt extraction and migration in the SCLM in the form of solid nanoparticles or nanomelts (González-Jiménez et al., 2019, 2020; Kamenetsky and Zelenski).

5.8 Metallogenic model

The peculiar position of the Tallante volcanic field, in the western Mediterranean, provides a perspective onto the evolution of a transitional lithospheric mantle sector between southern Iberia and the westward migrating Alborán micro-continent (Fig. 5.13a, b). Fertile spinel lherzolites from Tallante sampled volumes

of subcontinental lithospheric mantle affected by pervasive crystallization of metasomatic sulfide-hosting pyroxenes. This refertilization event was due to the percolation of subalkaline subduction-related magmas generated by upwelling of hot mantle asthenosphere upon slab rollback and tearing of the Iberian continental lithosphere during the Miocene. Subvertical translithospheric STEP faults, which accommodated the lateral propagation of slab rupture, likely provided preferential pathways for the upward migration of silicate melts and the generation of metasomatized domains in the SCLM underlying the southern Iberian margin.

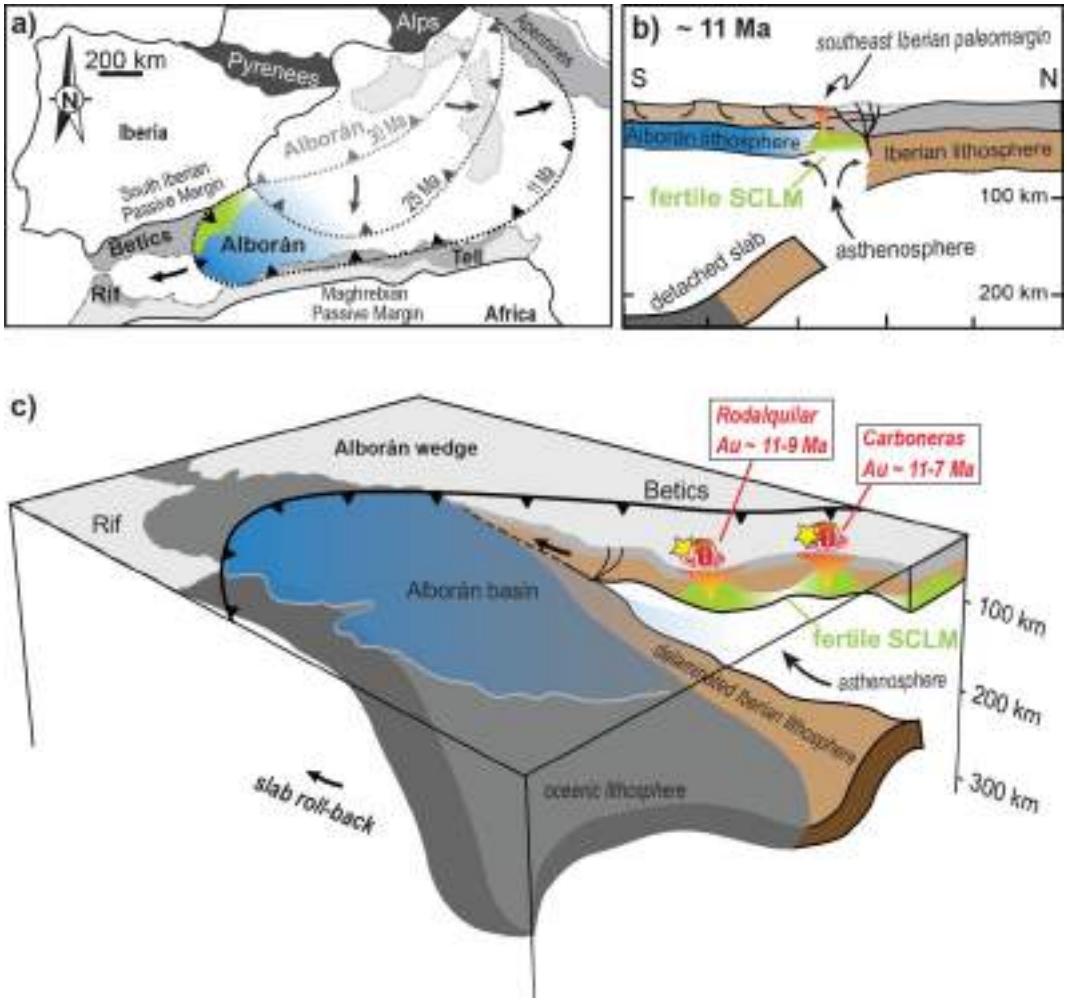

Figure 5.13. a) Cartoon of the geotectonic evolution of the western Mediterranean in response to westward migration of the Alborán micro-continent in the Cenozoic. b) N-S cross-section close to the southeast Iberian margin, as inferred by seismic profiles in Mancilla et al. (2015, 2018). c) Conceptual 3D geodynamic sketch of the lithospheric architecture beneath the western Mediterranean (modified after Mancilla et al., 2015).

The precipitation of Ni-Cu rich BMS with strongly heterogeneous PGE systematics (Fig. 5.9), Pt-Pd-rich PGM, and Au-bearing microinclusions (Fig. 5.6) hosted in the metasomatic (clinopyroxene + orthopyroxene + spinel) assemblages (Fig. 5.2, 5.4) suggests that ascending silicate melts incorporated different populations of sulfide droplets and metal nanoparticles, which were finally concentrated in the shallower domains of the SCLM by melt-rock reaction at decreasing melt volumes. The possible presence of pyroxenites in the mantle source of these silicate melts (Marchesi et al., 2017) may have enhanced their Au budget, as pyroxenites are considered relevant sources of gold in the mantle (Saunders et al., 2018).

Precipitation of metasomatic sulfides, PGM, and metal nanoparticles provided an efficient mechanism for the storage of metals, in particular gold, in the SCLM beneath the southern Iberian margin. Indeed, BMS in Tallante peridotites have Au concentrations (median 1.78 ppm) up to 4-5 times higher than Au abundances in BMS from other xenoliths of common oceanic or continental mantle (~ 0.02 ppm in intraplate oceanic mantle; 0.01-0.28 ppm in depleted cratonic mantle; 0.20-0.414 ppm in metasomatized SCLM; see references in Fig. 5.14). Similarly to the SCLM beneath southern Patagonia (Tassara et al., 2018), high contents of Au in BMS from Tallante are linked to the presence of Au-metallogenic provinces in the upper crust (Fig. 5.1). This observation suggests a close link between Au abundances in mantle BMS and the metallogenic fertility of the overlying crust, supporting previous evidence of the key contribution of the metasomatized lithospheric mantle as a source of gold endowment in the upper crust (McInnes et al., 1999; Hronsky et al., 2012; Griffin et al., 2013; Tassara et al., 2017; Holwell et al., 2019; Wang et al., 2019). In this scenario, the fertile domains of SCLM sampled by sulfide-bearing Tallante peridotites may have sourced the parental magmas of middle- to high-K calc-alkaline volcanic suites genetically related to gold mineralizations in Southeast Spain (Fig. 5.13c). The occurrence of gold magmatic particles in lamproitic dykes of the NVP (Toscani, 1999) further supports the presence of Au-rich domains in the SCLM beneath the southern Iberian margin. Gold fertility of magmas from this sector of SCLM was enhanced by relatively low melting temperature of the sulfide-bearing metasomatic assemblages, as well as by low thermal stability of their gold

repositories (Ni-Cu rich BMS). Melting of fertile SCLM occurred in response to continuous asthenosphere upwelling and continental edge delamination of the Iberian lithosphere since the Middle Miocene, driving the generation of ore-productive volcanic suites, progressively shifting from calc-alkaline to alkaline affinities. Such a metallogenic evolution may account for other regional settings related to the emplacement of Cu-Au deposits associated to post-subduction calc-alkaline to alkaline magmas sourced from subduction-metasomatized lithospheric mantle (Richards, 2009; Fiorentini et al., 2018; Holwell et al., 2019; Rabayrol and Hart, 2021).

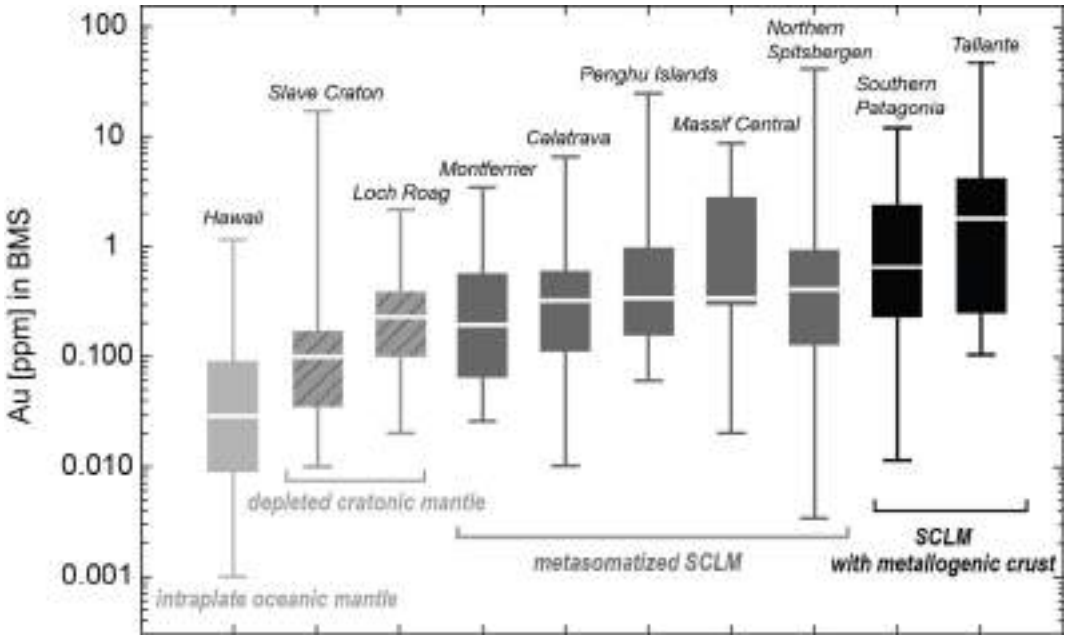

Figure 5.14. Box plots showing the concentrations of gold (ppm) in BMS of peridotite xenoliths from oceanic and continental mantle. The box depicts the central part of the sampling distribution, between the 25th and 75th percentile. The line across the box displays the median value of the distribution. Lines extending from the box represent the range of the observed values. Data sources are from Sen et al. (2010) (intraplate oceanic mantle, light grey boxes); Aulbach et al. (2004) and Hughes et al. (2017) (depleted cratonic mantle, striped grey boxes); Alard et al. (2011), González-Jiménez et al. (2014), Wang et al. (2009), Lorand and Alard (2001), and Saunders et al. (2015) (metasomatized SCLM, grey boxes); Tassara et al. (2018) and this study (SCLM with metallogenic crust, black boxes).

In conclusion, the modification of the SCLM during the subduction-related Miocene evolution of the western Mediterranean impacted on the metallogenesis of its overlying crust by a two-stage process: 1) subalkaline silicate metasomatism efficiently stored metals, especially Au, in fertile domains of the SCLM beneath

the southern Iberian margin by the precipitation of sulfide-bearing metasomatic pyroxenes during the Miocene; 2) partial melting of these fertile domains in response to continental edge delamination and asthenosphere upwelling transferred their metal budget to calc-alkaline magmas feeding mineralization and gold endowment in the overlying crust (Fig. 5.13). Regardless of the metasomatising agent, the two-stage process documented here, which is at the core of the metallogenic enrichment of the western Mediterranean lithospheric domain, is akin to the one that was recently documented and numerically modelled in the Ivrea Zone of NW Italy (Fiorentini et al., 2018). It is proposed that a two-stage process, characterized by metal-volatile enrichment and subsequent focuzed reactivation, may represent the most important first-order control on the localization of world-class mineralized camps worldwide.

5.9 Appendix

Table S5.1. Representative major element compositions (wt.%) of minerals in Tallante xenoliths (b.d.l. = below detection limits). Mineral abbreviations are: ol, olivine; opx, orthopyroxene; cpx, clinopyroxene; cpx_{rim}, clinopyroxene rim; sp, spinel; gl, glass; ol_{mic} and sp_{mic}, olivine and spinel microlites; cpx_{cor} and sp_{cor}, clinopyroxene and spinel spongy coronae.

					TAL099					
wt.%	ol	opx	cpx	cpx_{rim}	sp	gl	ol_{mic}	sp_{mic}	cpx_{cor}	sp_{cor}
SiO_2	40.97	55.26	51.19	52.63	0.02	60.76	41.23	0.22	49.60	-
TiO_2	*b.d.l.*	0.11	0.42	0.34	0.03	0.83	0.01	0.42	1.27	-
Al_2O_3	*b.d.l.*	4.51	6.87	4.81	52.8	21.74	0	54.1	5.76	-
Cr_2O_3	*b.d.l.*	0.54	1.27	0.98	16.88	*b.d.l.*	0.12	15.36	2.34	-
FeO*	9.26	5.90	2.31	2.34	10.07	1.89	7.17	8.2	1.96	-
MnO	0.14	0.16	0.06	0.09	0.09	0.07	0.11	0.04	0.07	-
MgO	49.47	33.72	15.14	16.11	19.86	2.21	50.88	20.50	15.82	-
CaO	0.05	0.71	21.58	21.94	0.01	7.66	0.31	0.26	22.31	-
Na_2O	*b.d.l.*	0.05	1.28	1.02	0.03	3.36	0.01	0.04	0.38	-
K_2O	*b.d.l.*	*b.d.l.*	*b.d.l.*	*b.d.l.*	0.01	0.02	0.01	*b.d.l.*	*b.d.l.*	-
Total	99.89	100.96	100.13	100.25	99.8	98.54	99.85	99.14	99.5	-
Mg#	90.3	91.1	92.5	92.7	77.9	67.6	92.0	81.7	93.5	-
Cr#	-	-	0.111	0.120	0.176	-	-	0.160	0.214	-

					TAL110					
wt.%	ol	opx	cpx	cpx_{rim}	sp	gl	ol_{mic}	sp_{mic}	cpx_{cor}	sp_{cor}
SiO_2	40.78	54.78	51.57	51.36	0.04	-	41.73	0.10	48.47	-
TiO_2	0.01	0.03	0.25	0.64	0.03	-	0.02	0.35	0.94	-
Al_2O_3	0.01	4.18	5.83	4.57	47.98	-	0.06	47.81	7.78	-
Cr_2O_3	*b.d.l.*	0.72	1.41	1.38	22.15	-	*b.d.l.*	23.18	2.45	-
FeO*	9.08	5.81	2.34	2.47	10.63	-	7.67	6.96	2.18	-
MnO	0.14	0.14	0.07	0.07	0.08	-	0.14	0.06	0.05	-
MgO	49.59	33.38	15.85	17.35	18.69	-	50.36	20.08	15.49	-
CaO	0.09	0.81	21.79	20.9	0.01	-	0.21	0.15	21.31	-
Na_2O	*b.d.l.*	0.01	1.08	0.58	*b.d.l.*	-	0.06	0.02	0.72	-
K_2O	*b.d.l.*	*b.d.l.*	*b.d.l.*	0.01	0.01	-	0.01	*b.d.l.*	*b.d.l.*	-
Total	99.69	99.86	100.2	99.34	99.61	-	100.26	98.72	99.39	-
Mg#	90.4	91.2	93.0	92.6	75.8	-	91.5	83.7	92.7	-
Cr#	-	-	0.140	0.169	0.236	-	-	0.245	0.174	-

					TAL128					
wt.%	ol	opx	cpx	cpx_{rim}	sp	gl	ol_{mic}	sp_{mic}	cpx_{cor}	sp_{cor}
SiO_2	40.14	54.73	49.88	-	0.04	-	41.05	-	-	-
TiO_2	*b.d.l.*	0.32	1.44	-	0.15	-	0.05	-	-	-
Al_2O_3	0.01	4.35	6.66	-	57.83	-	0.03	-	-	-
Cr_2O_3	*b.d.l.*	0.39	0.71	-	11.15	-	0.03	-	-	-
FeO*	10.66	6.75	2.62	-	10.80	-	9.33	-	-	-
MnO	0.14	0.15	0.09	-	0.08	-	0.11	-	-	-
MgO	48.26	32.89	15.41	-	19.84	-	49.32	-	-	-
CaO	0.04	0.68	22.35	-	0.01	-	0.13	-	-	-
Na_2O	*b.d.l.*	0.01	0.6	-	0.03	-	*b.d.l.*	-	-	-
K_2O	*b.d.l.*	0.01	*b.d.l.*	-	*b.d.l.*	-	*b.d.l.*	-	-	-
Total	99.24	100.27	99.76	-	99.92	-	100.05	-	-	-
Mg#	88.8	89.7	91.4	-	76.6	-	90.0	-	-	-
Cr#	-	-	0.066	-	0.115	-	-	-	-	-

Table S5.1. (continued).

					TAL129					
wt.%	ol	opx	cpx	cpx_{rim}	sp	gl	ol_{mic}	sp_{mic}	cpx_{cor}	sp_{cor}
SiO_2	40.21	55.36	50.72	51.99	0.05	56.51	40.28	0.12	48.46	-
TiO_2	0.02	0.01	0.43	0.35	0.05	1.00	0.09	0.49	1.34	-
Al_2O_3	*b.d.l.*	3.04	5.57	4.78	53.14	19.71	0.06	49.3	8.10	-
Cr_2O_3	*b.d.l.*	0.24	1.01	0.91	15.62	0.08	0.03	19.33	1.93	-
FeO*	9.76	6.19	2.32	2.42	10.45	2.86	8.65	10.2	3.01	-
MnO	0.15	0.15	0.07	0.09	0.06	0.07	0.11	0.05	0.07	-
MgO	49.23	33.93	15.79	16.24	19.2	3.52	50.02	20.15	16.04	-
CaO	0.05	0.64	22.3	22.14	0.01	7.51	0.16	0.10	19.95	-
Na_2O	0.02	0.04	0.81	0.77	0.02	4.63	0.02	0.01	0.93	-
K_2O	*b.d.l.*	*b.d.l.*	*b.d.l.*	*b.d.l.*	*b.d.l.*	0.02	0.01	0.01	*b.d.l.*	-
Total	99.44	99.6	99.02	99.68	98.6	95.92	99.43	99.77	99.84	-
Mg#	89.7	90.9	92.6	92.5	76.6	68.7	90.6	78.0	90.8	-
Cr#	-	-	0.108	0.113	0.165	-	-	0.206	0.138	-

					TAL143					
wt.%	ol	opx	cpx	cpx_{rim}	sp	gl	ol_{mic}	sp_{mic}	cpx_{cor}	sp_{cor}
SiO_2	40.92	55.99	51.97	51.54	0.03	-	-	0.11	-	0.30
TiO_2	*b.d.l.*	0.02	0.31	0.32	0.07	-	-	0.44	-	0.36
Al_2O_3	0.02	2.79	5.27	5.08	45.21	-	-	45.19	-	36.28
Cr_2O_3	0.27	0.59	1.43	1.48	24.3	-	-	24.63	-	33.3
FeO*	8.77	5.74	2.25	2.32	10.99	-	-	8.04	-	10.92
MnO	0.12	0.14	0.08	0.08	0.07	-	-	0.04	-	0.07
MgO	50.17	34.36	15.97	15.9	18.27	-	-	19.84	-	16.74
CaO	0.06	0.62	21.85	22.07	*b.d.l.*	-	-	0.12	-	0.03
Na_2O	*b.d.l.*	0.01	1.09	0.96	*b.d.l.*	-	-	*b.d.l.*	-	0.04
K_2O	*b.d.l.*	*b.d.l.*	*b.d.l.*	*b.d.l.*	*b.d.l.*	-	-	*b.d.l.*	-	*b.d.l.*
Total	100.32	100.26	100.21	99.76	98.94	-	-	98.4	-	98.99
Mg#	90.6	91.6	93.1	92.8	74.8	-	-	81.5	-	73.9
Cr#	-	-	0.154	0.164	0.265	-	-	0.268	-	0.365

					TAL146					
wt.%	ol	opx	cpx	cpx_{rim}	sp	gl	ol_{mic}	sp_{mic}	cpx_{cor}	sp_{cor}
SiO_2	41.16	56.18	52.18	52.39	0.05	-	41.33	-	49.01	0.19
TiO_2	0.02	0.06	0.24	0.49	0.05	-	*b.d.l.*	-	0.94	0.33
Al_2O_3	*b.d.l.*	3.5	5.65	4.45	47.21	-	0.03	-	8.61	39.18
Cr_2O_3	*b.d.l.*	0.43	1.43	1.16	22.97	-	0.16	-	2.88	31.13
FeO*	8.94	5.76	2.08	2.61	10.61	-	7.76	-	2.18	10.34
MnO	0.14	0.14	0.09	0.11	0.06	-	0.12	-	0.06	0.06
MgO	50.24	34.25	15.76	18.29	18.79	-	51.61	-	15.32	18.69
CaO	0.05	0.66	21.65	20.12	0.04	-	0.14	-	20.83	0.08
Na_2O	*b.d.l.*	0.02	1.12	0.64	*b.d.l.*	-	*b.d.l.*	-	0.79	0.03
K_2O	0.01	0.01	0.01	*b.d.l.*	0.01	-	0.01	-	*b.d.l.*	*b.d.l.*
Total	100.56	101.01	100.22	100.25	99.78	-	101.16	-	100.62	100.05
Mg#	90.7	91.5	93.3	92.6	75.9	-	91.8	-	92.6	76.4
Cr#	-	-	0.145	0.149	0.246	-	-	-	0.183	0.346

Table S5.2. Major element compositions of base-metal sulfides (in wt.%) in Tallante mantle xenoliths.

Sample	S	Fe	Ni	Co	Cu	Total	M/S	Ni/(Ni+Fe)
pentlandite								
TAL099a-C1-1	33.17	25.32	40.83	0.29	0.05	99.75	1.11	0.61
TAL099a-C1-2	33.03	25.37	40.67	0.29	0.05	99.49	1.11	0.60
TAL099a-C2-1	32.90	24.09	41.42	0.30	0.08	98.83	1.11	0.62
TAL099a-C3-1	32.90	24.33	40.88	0.29	0.07	98.54	1.10	0.62
TAL099a-C4-1	32.63	25.00	40.99	0.28	0.17	99.12	1.13	0.61
TAL099a-C4-4	32.95	25.80	40.65	0.30	0.10	99.88	1.12	0.60
TAL099a-C5-1	32.96	25.79	39.56	0.29	0.08	98.75	1.11	0.59
TAL099a-C6-1	32.81	23.39	42.60	0.29	0.03	99.19	1.12	0.63
*TAL099a-C7-1**	32.96	25.12	37.16	0.26	4.37	99.93	1.12	0.58
*TAL099b-C1-1**	32.90	26.29	37.49	0.27	1.91	98.92	1.11	0.58
TAL099b-C2-1	32.62	24.47	42.02	0.25	0.03	99.46	1.13	0.62
TAL099b-C3-1	32.82	25.45	40.93	0.28	0.03	99.61	1.13	0.60
TAL099b-C4-1	32.77	25.98	40.67	0.28	0.08	99.84	1.13	0.60
TAL099b-C5-1	32.78	24.89	41.28	0.30	0.05	99.36	1.12	0.61
TAL099b-C5-2	32.73	24.40	40.92	0.31	0.07	98.49	1.11	0.61
TAL099b-C6-1	32.83	23.43	41.80	0.28	0.04	98.45	1.11	0.63
TAL099b-C6-2	32.91	23.51	41.67	0.25	0.04	98.44	1.10	0.63
TAL099b-C7-1	32.58	24.91	40.25	0.25	0.07	98.11	1.11	0.61
TAL099b-C8-1	32.74	24.72	41.12	0.31	0.07	99.02	1.12	0.61
*TAL099c-C1-1**	32.99	26.86	38.16	0.27	1.62	99.97	1.12	0.57
TAL099c-C3-1	33.07	22.18	43.38	0.27	0.03	98.99	1.10	0.65
TAL099c-C6-1	33.05	24.43	40.60	0.29	0.91	99.37	1.11	0.61
TAL099c-C7-1	33.00	27.58	38.54	0.27	0.17	99.63	1.12	0.57
TAL099c-C8-1	32.93	26.12	39.08	0.28	0.29	98.76	1.11	0.59
TAL099c-C11-1	32.92	24.40	41.69	0.28	0.06	99.43	1.12	0.62
TAL129c-C1-1	32.69	24.28	41.78	0.25	0.08	99.15	1.13	0.62
TAL129c-C3-1	32.69	24.46	40.78	0.27	0.12	98.41	1.11	0.61
TAL129c-C4-1	32.49	24.72	40.31	0.27	0.20	98.10	1.12	0.61
TAL129c-C5-1	32.79	28.14	37.49	0.32	0.07	98.89	1.12	0.56
TAL129c-C7-1	32.34	24.04	41.09	0.27	0.30	98.11	1.13	0.62
TAL129c-C8-1	32.81	25.12	40.70	0.27	0.12	99.07	1.12	0.61
TAL129-C2-1	32.91	25.15	40.47	0.28	0.14	99.02	1.11	0.60
TAL129-C2-3	33.15	25.11	40.22	0.25	0.09	98.87	1.10	0.60
TAL129-C2-4	32.75	24.03	41.10	0.29	0.07	98.30	1.11	0.62
TAL129-C3-1	32.84	24.95	40.54	0.27	0.14	98.83	1.11	0.61
TAL129-C3-2	32.96	24.23	41.17	0.28	0.11	98.83	1.11	0.62
TAL129-C7-1	32.81	24.94	40.27	0.27	0.09	98.43	1.11	0.61
TAL129-C8-1	32.82	23.15	42.38	0.27	0.24	98.93	1.11	0.64
TAL129-C9-1	32.88	24.88	40.46	0.25	0.17	98.70	1.11	0.61
*TAL129-C9-2**	33.01	24.14	39.35	0.28	2.02	98.89	1.10	0.61
TAL129-C10-1	32.97	25.87	38.92	0.27	0.05	98.13	1.10	0.59
TAL099-C3-1	32.71	20.24	45.15	0.30	0.08	98.55	1.11	0.68
TAL099-C3-3	32.91	21.66	43.88	0.32	0.09	98.93	1.11	0.66
TAL099-C4-1	32.86	24.87	40.58	0.30	0.09	98.75	1.11	0.61
TAL099-C5-1	33.02	24.57	40.90	0.29	0.05	98.88	1.10	0.61
TAL099-C5-2	32.47	24.18	40.98	0.27	0.16	98.13	1.12	0.62

Table S5.2. (continued).

Sample	S	Fe	Ni	Co	Cu	Total	M/S	Ni/(Ni+Fe)
pentlandite								
*TAL110b-C1-1**	32.97	24.42	39.06	0.28	1.89	98.69	1.10	0.60
*TAL110b-C5-1**	33.19	25.36	34.04	0.29	5.56	98.50	1.08	0.56
*TAL110b-C5-3**	32.99	25.77	37.75	0.29	1.89	98.78	1.10	0.58
TAL110b-C6-1	32.82	22.64	41.75	0.27	0.65	98.19	1.10	0.64
TAL110b-C7-1	32.82	22.97	42.92	0.26	0.08	99.11	1.12	0.64
TAL110c-C1-1	32.70	23.90	41.74	0.25	0.05	98.70	1.12	0.62
TAL110c-C3-1	32.90	24.33	41.51	0.25	0.07	99.15	1.11	0.62
TAL110c-C3-2	32.87	23.52	41.52	0.27	0.13	98.36	1.10	0.63
TAL129a-C4-1	32.71	24.78	40.92	0.26	0.05	98.78	1.12	0.61
TAL129a-C5-1	32.58	25.30	40.74	0.27	0.09	99.06	1.13	0.61
*TAL129a-C6-1**	32.70	22.65	41.63	0.27	1.32	98.65	1.11	0.64
TAL129a-C7-1	32.64	24.10	41.51	0.27	0.07	98.66	1.12	0.62
TAL129a-C8-1	32.85	25.92	39.02	0.23	0.59	98.70	1.11	0.59
*TAL129b-C1-1**	32.77	24.64	39.77	0.26	1.35	98.88	1.12	0.61
*TAL129b-C3-1**	32.94	27.30	36.35	0.29	1.61	98.56	1.10	0.56
TAL129b-C4-1	32.77	25.65	39.88	0.28	0.14	98.78	1.12	0.60
TAL128b1-C2-1	32.55	26.18	39.20	0.29	0.08	98.35	1.12	0.59
TAL128b1-C3-1	32.81	26.56	38.91	0.28	0.22	98.87	1.12	0.58
TAL128b1-C3-3	32.78	27.46	38.13	0.31	0.12	98.86	1.12	0.57
TAL128b1-C4-2	32.80	26.34	38.77	0.28	0.15	98.40	1.11	0.58
TAL143-C1-1	32.75	23.43	41.69	0.28	0.04	98.28	1.11	0.63
TAL143-C2-1	32.80	24.77	40.05	0.31	0.38	98.39	1.11	0.61
TAL143-C3-1	32.80	25.47	39.51	0.30	0.12	98.27	1.11	0.60
TAL146-C1-1	32.82	22.24	43.76	0.27	0.17	99.32	1.12	0.65
TAL146-C2-1	32.76	24.28	41.07	0.26	0.06	98.50	1.11	0.62
TAL146-C2-2	32.61	22.17	43.13	0.27	0.08	98.31	1.11	0.65
chalcopyrite								
*TAL99c-C8-2**	34.70	29.23	4.83	0.04	29.66	98.49	0.99	-
*TAL099-C3-2**	33.96	27.36	4.82	0.04	31.13	97.34	1.00	-
*TAL099-C3-4**	33.83	29.58	1.72	0.02	32.19	97.37	1.01	-
TAL129b-C4-2	34.08	29.54	0.55	0.02	33.57	97.79	1.00	-
bornite								
TAL099a-C4-2	23.36	7.43	0.86	0.03	68.08	99.82	1.67	-
TAL099a-C4-3	23.04	6.98	0.69	0.02	68.92	99.72	1.70	-
TAL099a-C4-5	23.36	7.84	0.38	0.03	68.39	100.06	1.68	-
TAL110b-C7-2	27.06	13.73	0.34	0.01	57.68	98.86	1.37	-
Reconstructed bulk composition								
TAL099-C3-1	33.23	21.81	33.30	-	11.66	100.00	1.10	-
TAL099-C3-2	33.93	25.27	27.81	-	12.99	100.00	1.07	-
TAL110b-C7-1	32.40	22.48	30.32	-	14.81	100.00	1.14	-
TAL129-2-3	33.92	26.58	31.43	-	8.07	100.00	1.08	-
TAL129b-C4-1	33.66	27.04	31.04	-	8.25	100.00	1.09	-
TAL143-C3-1	33.80	26.57	33.38	-	6.24	100.00	1.08	-

Table S5.3. Representative trace elements abundances (ppm) of clinopyroxene grains in Tallante xenoliths (n.d. = not determined) and LA-ICP-MS reference material.

Sample	TAL110	TAL110	TAL129	TAL129	TAL143	TAL143	TAL146	TAL146
Type	1a	1a	1a	1a	1a	1a	1a	1a
Cs	*n.d.*	*n.d.*	*n.d.*	*n.d.*	*n.d.*	*n.d.*	*n.d.*	*n.d.*
Rb	*n.d.*	0.020	0.020	*n.d.*	0.100	*n.d.*	*n.d.*	*n.d.*
Ba	0.080	*n.d.*	0.270	*n.d.*	0.850	*n.d.*	*n.d.*	0.120
Th	0.170	0.180	0.210	0.140	0.240	0.130	0.120	0.240
U	0.070	0.070	0.070	0.050	0.140	0.090	0.040	0.070
Nb	0.290	0.390	*n.d.*	0.170	0.830	0.260	0.180	0.320
Ta	0.040	0.040	*n.d.*	*n.d.*	0.050	0.040	0.030	0.030
La	1.42	1.25	1.00	0.97	0.92	0.88	0.97	1.01
Ce	3.96	3.67	3.36	3.40	2.99	2.94	2.81	2.96
Pb	*n.d.*	0.010	*n.d.*	*n.d.*	*n.d.*	*n.d.*	*n.d.*	0.020
Pr	0.620	0.550	0.670	0.640	0.490	0.520	0.460	0.510
Sr	58.0	50.7	39.5	47.4	60.6	49.7	35.4	35.2
Nd	3.48	2.89	4.03	4.27	2.60	2.62	2.17	2.54
Zr	20.3	15.5	20.3	22.7	25.0	22.2	14.9	13.4
Hf	0.810	0.600	0.900	0.740	0.660	0.670	0.460	0.450
Sm	1.26	1.06	1.44	1.55	1.15	1.01	0.84	0.96
Eu	0.460	0.360	0.480	0.600	0.670	0.490	0.390	0.350
Gd	1.70	1.58	1.68	2.07	2.01	1.72	1.53	1.36
Ti	161	1626	226	232	166	170	153	1462
Tb	0.300	0.330	0.320	0.350	0.310	0.320	0.280	0.290
Dy	2.34	2.72	2.22	2.51	2.06	2.21	2.17	2.19
Y	19.5	16.4	13.0	15.4	16.5	13.7	14.4	12.3
Ho	0.590	0.550	0.490	0.600	0.570	0.510	0.460	0.460
Er	2.15	1.76	1.36	1.77	1.94	1.39	1.52	1.36
Tm	0.240	0.240	0.210	0.260	0.240	0.210	0.200	0.210
Yb	1.32	1.56	1.44	1.72	1.19	1.28	1.15	1.35
Lu	0.240	0.260	0.240	0.250	0.210	0.200	0.170	0.190

Table S5.3. (continued).

Sample	TAL099	TAL099	TAL099	TAL099	TAL099	TAL099	TAL099	TAL099
Type	1b	1b	1b	1b	1b	1b	1b	1b
Cs	*n.d.*	*n.d.*	*n.d.*	*n.d.*	*n.d.*	*n.d.*	*n.d.*	*n.d.*
Rb	*n.d.*	*n.d.*	0.040	*n.d.*	*n.d.*	*n.d.*	*n.d.*	*n.d.*
Ba	*n.d.*	*n.d.*	0.270	0.530	0.670	0.090	0.090	*n.d.*
Th	*n.d.*	0.050	0.050	*n.d.*	0.050	0.050	0.060	*n.d.*
U	*n.d.*	*n.d.*	0.020	0.020	0.020	0.020	*n.d.*	*n.d.*
Nb	0.240	0.260	0.400	0.140	0.170	0.270	0.170	0.200
Ta	0.030	0.050	*n.d.*	0.050	0.050	0.050	0.040	0.050
La	0.97	1.03	1.03	0.91	0.97	1.07	1.02	0.92
Ce	3.38	3.65	3.78	3.29	3.63	3.64	3.43	3.33
Pb	*n.d.*	*n.d.*	*n.d.*	0.020	*n.d.*	*n.d.*	*n.d.*	*n.d.*
Pr	0.590	0.720	0.690	0.600	0.690	0.680	0.670	0.650
Sr	53.0	54.1	64.7	51.4	56.5	56.2	55.1	55.1
Nd	3.42	4.19	3.99	3.54	3.90	3.80	3.74	3.65
Zr	27.9	29.7	3-	29.7	28.4	29.2	30.3	29.2
Hf	0.850	0.810	0.870	0.840	0.860	0.840	0.960	0.850
Sm	1.31	1.56	1.55	1.37	1.41	1.41	1.46	1.35
Eu	0.510	0.620	0.580	0.540	0.610	0.570	0.540	0.570
Gd	2.07	2.40	2.43	2.13	2.48	2.11	2.10	2.21
Ti	223	279	258	268	268	232	255	2639
Tb	0.340	0.430	0.450	0.430	0.400	0.390	0.410	0.420
Dy	2.53	2.82	2.86	2.61	2.72	2.61	2.95	2.88
Y	15.2	16.9	16.8	16.3	15.4	15.7	16.5	17.1
Ho	0.580	0.620	0.620	0.560	0.580	0.590	0.640	0.620
Er	1.54	1.81	1.85	1.78	1.69	1.78	1.98	1.87
Tm	0.230	0.240	0.260	0.250	0.250	0.270	0.280	0.290
Yb	1.41	1.75	1.66	1.54	1.44	1.51	1.66	1.49
Lu	0.220	0.220	0.210	0.190	0.210	0.230	0.240	0.210

Table S5.3. (continued).

Sample	TAL128	TAL128	TAL128	TAL128	TAL099	TAL099	TAL146	TAL143
Type	2	2	2	2	spongy	spongy	spongy	spongy
Cs	*n.d.*	*n.d.*	*n.d.*	*n.d.*	*n.d.*	*n.d.*	*n.d.*	*n.d.*
Rb	*n.d.*	*n.d.*	*n.d.*	*n.d.*	*n.d.*	*n.d.*	*n.d.*	*n.d.*
Ba	*n.d.*	*n.d.*	*n.d.*	0.100	*n.d.*	*n.d.*	*n.d.*	*n.d.*
Th	*n.d.*	0.020	0.030	0.020	*n.d.*	*n.d.*	*n.d.*	*n.d.*
U	*n.d.*	*n.d.*	*n.d.*	*n.d.*	*n.d.*	*n.d.*	*n.d.*	*n.d.*
Nb	*n.d.*	0.030	0.210	0.110	*n.d.*	*n.d.*	*n.d.*	*n.d.*
Ta	0.030	0.040	0.100	0.080	*n.d.*	*n.d.*	*n.d.*	*n.d.*
La	1.20	1.36	1.77	1.28	0.56	0.20	0.46	0.61
Ce	5.09	5.71	7.59	6.46	1.37	0.73	1.26	1.19
Pb	*n.d.*	*n.d.*	*n.d.*	*n.d.*	*n.d.*	*n.d.*	*n.d.*	*n.d.*
Pr	1.02	1.14	1.59	1.34	0.450	0.350	0.280	0.270
Sr	17.7	21.9	64.2	45.3	*n.d.*	*n.d.*	*n.d.*	*n.d.*
Nd	5.80	6.43	8.76	7.02	2.98	2.50	1.62	1.89
Zr	63.3	55.0	68.1	60.7	*n.d.*	*n.d.*	*n.d.*	*n.d.*
Hf	2.320	1.950	1.620	1.500	*n.d.*	*n.d.*	*n.d.*	*n.d.*
Sm	2.26	2.68	3.07	2.20	1.03	*n.d.*	*n.d.*	0.67
Eu	0.850	0.950	1.220	0.950	0.380	0.540	0.260	0.410
Gd	3.64	3.55	4.01	3.66	2.44	2.78	1.91	2.71
Ti	950	948	935	750	*n.d.*	*n.d.*	*n.d.*	*n.d.*
Tb	0.600	0.630	0.650	0.530	0.300	0.610	0.330	0.600
Dy	3.83	4.06	4.49	3.25	3.20	2.56	3.52	*n.d.*
Y	17.6	17.5	20.9	15.7	*n.d.*	*n.d.*	*n.d.*	*n.d.*
Ho	0.810	0.770	0.860	0.680	0.630	0.550	0.710	0.690
Er	1.75	1.77	2.08	1.57	1.89	1.62	2.34	1.67
Tm	0.230	0.240	0.270	0.220	0.310	0.230	*n.d.*	*n.d.*
Yb	1.22	1.53	1.85	1.32	1.69	1.89	*n.d.*	1.31
Lu	0.180	0.210	0.220	0.160	0.160	0.210	0.170	0.290

Table S5.3. (continued).

Sample	TAL128	TAL128	TAL128	TAL128	TAL099	TAL099	TAL146	TAL143
Type	2	2	2	2	spongy	spongy	spongy	spongy
Cs	*n.d.*	*n.d.*	*n.d.*	*n.d.*	*n.d.*	*n.d.*	*n.d.*	*n.d.*
Rb	*n.d.*	*n.d.*	*n.d.*	*n.d.*	*n.d.*	*n.d.*	*n.d.*	*n.d.*
Ba	*n.d.*	*n.d.*	*n.d.*	0.100	*n.d.*	*n.d.*	*n.d.*	*n.d.*
Th	*n.d.*	0.020	0.030	0.020	*n.d.*	*n.d.*	*n.d.*	*n.d.*
U	*n.d.*	*n.d.*	*n.d.*	*n.d.*	*n.d.*	*n.d.*	*n.d.*	*n.d.*
Nb	*n.d.*	0.030	0.210	0.110	*n.d.*	*n.d.*	*n.d.*	*n.d.*
Ta	0.030	0.040	0.100	0.080	*n.d.*	*n.d.*	*n.d.*	*n.d.*
La	1.20	1.36	1.77	1.28	0.56	0.20	0.46	0.61
Ce	5.09	5.71	7.59	6.46	1.37	0.73	1.26	1.19
Pb	*n.d.*	*n.d.*	*n.d.*	*n.d.*	*n.d.*	*n.d.*	*n.d.*	*n.d.*
Pr	1.02	1.14	1.59	1.34	0.450	0.350	0.280	0.270
Sr	17.7	21.9	64.2	45.3	*n.d.*	*n.d.*	*n.d.*	*n.d.*
Nd	5.80	6.43	8.76	7.02	2.98	2.50	1.62	1.89
Zr	63.3	55.0	68.1	60.7	*n.d.*	*n.d.*	*n.d.*	*n.d.*
Hf	2.320	1.950	1.620	1.500	*n.d.*	*n.d.*	*n.d.*	*n.d.*
Sm	2.26	2.68	3.07	2.20	1.03	*n.d.*	*n.d.*	0.67
Eu	0.850	0.950	1.220	0.950	0.380	0.540	0.260	0.410
Gd	3.64	3.55	4.01	3.66	2.44	2.78	1.91	2.71
Ti	950	948	935	750	*n.d.*	*n.d.*	*n.d.*	*n.d.*
Tb	0.600	0.630	0.650	0.530	0.300	0.610	0.330	0.600
Dy	3.83	4.06	4.49	3.25	3.20	2.56	3.52	*n.d.*
Y	17.6	17.5	20.9	15.7	*n.d.*	*n.d.*	*n.d.*	*n.d.*
Ho	0.810	0.770	0.860	0.680	0.630	0.550	0.710	0.690
Er	1.75	1.77	2.08	1.57	1.89	1.62	2.34	1.67
Tm	0.230	0.240	0.270	0.220	0.310	0.230	*n.d.*	*n.d.*
Yb	1.22	1.53	1.85	1.32	1.69	1.89	*n.d.*	1.31
Lu	0.180	0.210	0.220	0.160	0.160	0.210	0.170	0.290

Table S5.3. (continued).

Sample Type	LA-ICP-MS Reference Material		
	BHVO-2G (n=23)	RSD (%)	GeoRem database
Cs	0.113	7	0.100
Rb	10.3	4	9.20
Ba	148	7	131
Th	1.36	8	1.22
U	0.451	7	0.403
Nb	20.6	6	18.3
Ta	1.290	9	1.15
La	17.2	7	15.2
Ce	42.3	5	37.6
Pb	1.91	7	1.70
Pr	6.04	6	5.35
Sr	445	3	396
Nd	27.7	5	24.5
Zr	191	5	170
Hf	4.88	8	4.32
Sm	6.93	5	6.10
Eu	2.33	6	2.07
Gd	6.94	6	6.16
Ti	18703	5	16300
Tb	1.03	5	0.920
Dy	6.01	8	5.28
Y	29.3	4	26.0
Ho	1.12	9	0.980
Er	2.87	8	2.56
Tm	0.374	8	0.340
Yb	2.26	9	2.01
Lu	0.310	8	0.279

Table S5.4. Concentrations (ppm) of chalcophile and siderophile elements of base-metal sulfides (n.d. = not determined) in Tallante mantle xenoliths and LA-ICP-MS reference materials.

Sample	TAL099_c3-1	TAL099_c3-2	TAL099_c4-1	TAL099_c5-1	TAL099_c5-2	TAL099a_c1-1	TAL099a_c2-1	TAL099a_c4-2	TAL099a_c4-1
Mineral	*pn+cp*	*pn + cp*	*pn*	*pn*	*pn + bn*	*pn + bn*	*pn + bn*	*pn + bn*	*pn + bn*
S	327103	329118	328550	330201	324656	331683	331633	326251	329538
Co	1714	1905	1935	1753	1533	1600	1607	1650	1481
Ni	439102	399640	481165	451077	509560	421359	392964	442456	393192
Cu	1824	13798	9304	3671	939	13254	541	6348	2216
Zn	2.93	9.90	10.5	7.37	37.0	16.5	36.2	11.7	5.62
Se	*n.d.*	*n.d.*	153	103	*n.d.*	129	*n.d.*	111	135
Ag	3.83	1.80	2.26	2.16	2.62	2.56	*n.d.*	0.440	1.49
Cd	*n.d.*	1.76	*n.d.*	*n.d.*	*n.d.*	0.560	*n.d.*	*n.d.*	*n.d.*
In	0.201	*n.d.*	0.156	*n.d.*	0.460	0.085	0.640	0.222	0.071
As	29.4	14.1	22.6	11.3	*n.d.*	14.6	*n.d.*	17.4	10.8
Te	42.6	15.1	17.7	15.0	15.8	15.2	*n.d.*	15.9	13.6
Pb	3.23	7.75	43.5	35.4	39.2	41.3	40.4	35.0	29.1
Sb	*n.d.*	*n.d.*	1.88	*n.d.*	*n.d.*	*n.d.*	*n.d.*	*n.d.*	*n.d.*
Bi	5.64	1.38	1.63	0.960	1.90	1.47	*n.d.*	1.49	1.83
Os	18.4	18.0	9.10	15.1	75.3	32.1	*n.d.*	17.5	7.23
Ir	12.7	11.8	5.24	10.3	44.0	20.8	6.60	8.93	5.05
Ru	22.2	18.8	7.74	15.5	80.0	35.9	36.3	17.3	9.49
Rh	3.50	3.65	1.90	3.08	13.8	6.16	1.93	3.02	1.82
Pt	22.2	25.0	*n.d.*	*n.d.*	*n.d.*	2.63	383	38.7	*n.d.*
Pd	25.1	25.4	9.64	2.07	18.2	8.02	247	82.3	0.970
Au	*n.d.*	1.20	*n.d.*	*n.d.*	*n.d.*	*n.d.*	46.3	8.18	*n.d.*

Sample	TAL099a_c5-1	TAL099a_c6-1	TAL099a_c7-1	TAL099b_c1-1	TAL099b_c2-1	TAL099b_c3-1	TAL099b_C4-1	TAL099b_c5-1	TAL099b_c6-1
Mineral	*pn + cp_{exs}*	*pn*	*pn + cp_{exs}*	*pn + cp + bn*	*pn + bn*	*pn*	*pn*	*pn*	*pn*
S	329608	328066	329563	328962	326248	328176	327721	327772	328312
Co	1573	1665	1678	1365	1687	1635	1686	1890	1502
Ni	383600	449381	391230	329465	432714	399369	409509	446160	397913
Cu	29859	6470	6230	133890	4735	1344	40555	1517	9045
Zn	30.6	28.5	5.88	67.1	14.7	5.50	44.5	8.86	32.8
Se	118	123	126	113	123	140	125	122	159
Ag	9.96	0.354	3.87	16.6	1.24	0.699	12.2	1.53	0.478
Cd	2.32	1.28	0.220	8.74	0.455	0.285	3.26	0.219	0.500
In	0.239	0.288	0.044	0.440	0.075	0.083	0.446	0.092	0.230
As	14.2	22.3	18.5	15.1	20.2	14.0	20.9	17.4	11.8
Te	13.1	18.2	13.5	19.0	16.3	13.7	18.7	17.1	15.2
Pb	37.4	16.8	41.0	100	40.5	38.3	44.5	42.6	1.58
Sb	*n.d.*	0.530	0.500	*n.d.*	0.710	0.390	0.450	0.440	*n.d.*
Bi	1.27	1.56	1.75	3.87	1.73	1.87	1.70	1.70	1.35
Os	10.9	10.8	10.4	9.34	10.1	11.6	23.1	7.29	9.56
Ir	10.2	9.72	14.7	9.38	8.96	11.8	25.1	7.15	9.08
Ru	19.9	20.5	21.2	18.1	19.1	20.9	42.5	14.8	19.9
Rh	2.94	3.13	3.73	4.46	3.02	3.43	7.78	2.51	3.42
Pt	6.57	58.8	0.200	2.90	*n.d.*	0.190	194	1.65	5.92
Pd	12.8	17.7	4.31	19.0	7.24	2.01	76.1	4.36	14.9
Au	*n.d.*	5.73	*n.d.*	*n.d.*	0.140	*n.d.*	7.36	*n.d.*	*n.d.*

Table S5.4. (continued).

Sample	*TAL099 b_c8-1*	*TAL099 c_c1-1*	*TAL099 c_c3-1*	*TAL099 c_c6-1*	*TAL099 c_c7-1*	*TAL099 c_c8-1*	*TAL099 c_c11-1*	*TAL110 b_C6*	*TAL110 b_c7*
Mineral	*pn + cp_{exs}*	*pn + cp_{exs}*	*pn*	*pn*	*pn + cp_{exs}*	*pn + cp*	*pn*	*pn + cp + bn*	*pn + cp + bn*
S	327401	329894	330688	330514	329959	329286	329172	328210	328206
Co	1774	1684	1685	1870	1696	1625	1879	1641	1540
Ni	451264	358180	439535	411713	379338	355868	425052	328887	341603
Cu	22007	37547	1994	7491	34334	29599	4534	89322	79946
Zn	37.5	41.4	74.9	14.5	15.9	60.3	21.9	67.2	87.3
Se	112	134	111	139	122	105	131	118	120
Ag	10.7	13.0	*n.d.*	2.87	1.87	0.28	3.26	2.86	4.35
Cd	0.570	1.12	0.620	0.270	1.35	1.88	1.18	9.84	2.72
In	0.269	0.222	0.330	0.093	0.189	0.456	0.096	0.423	0.600
As	22.9	19.4	19.3	20.2	16.3	13.3	15.7	12.5	29.0
Te	16.8	19.0	15.7	12.5	16.6	15.4	10.3	11.2	19.1
Pb	55.2	40.3	37.9	48.7	36.1	14.4	30.6	73.7	89.0
Sb	0.580	0.610	*n.d.*	0.680	0.460	*n.d.*	0.480	*n.d.*	0.750
Bi	1.87	1.81	1.56	1.67	1.78	1.37	1.57	2.73	2.19
Os	14.7	22.0	6.64	13.4	34.7	37.1	0.470	15.9	12.4
Ir	14.3	22.8	7.72	12.9	33.4	34.3	0.400	9.67	8.66
Ru	30.1	43.0	16.8	28.3	71.8	58.5	2.56	21.7	23.7
Rh	4.40	7.95	2.81	4.75	13.9	9.76	1.00	3.61	3.47
Pt	50.5	*n.d.*	0.430	0.39	*n.d.*	47.8	*n.d.*	18.6	9.64
Pd	34.1	14.4	8.37	4.32	17.0	15.7	6.88	10.6	12.6
Au	2.20	0.140	*n.d.*	*n.d.*	0.500	*n.d.*	*n.d.*	*n.d.*	*n.d.*

Sample	*TAL110 c_c1*	*TAL110 c_c2*	*TAL110 c_c3*	*TAL128 a_c1*	*TAL128 a_c2*	*TAL128 ba_c2*	*TAL128 b1_c3*	*TAL128 b1_c4*	*TAL128 b1C4-1*
Mineral	*pn*	*pn*	*pn + cp*	*pn + cp_{exs}*	*pn + cp*	*pn*	*pn + cp*	*pn + cp*	*pn + cp_{exs}*
S	326976	328597	329031	325817	321264	325539	327844	330000	330000
Co	1902	1810	1665	1680	1739	2078	1731	1931	1629
Ni	430676	404966	382207	360208	338088	415927	329929	386885	347180
Cu	6324	292	26806	59460	35799	13706	25175	19783	34101
Zn	87.9	105	44.8	52.0	39.4	20.0	20.6	23.6	29.8
Se	134	160	134	91.8	116	140	133	136	102
Ag	1.39	1.01	0.087	13.8	12.9	7.34	6.83	7.43	7.91
Cd	0.327	2.23	2.50	2.70	3.24	1.79	1.44	2.54	4.02
In	0.386	0.568	0.227	0.337	0.356	0.191	0.392	0.320	0.404
As	22.1	26.3	18.8	18.6	75.0	74.8	83.0	100	62.6
Te	21.9	22.7	16.6	15.2	26.6	26.1	33.5	34.9	17.4
Pb	17.8	96.6	6.16	51.3	21.3	20.2	22.6	23.0	22.6
Sb	0.360	*n.d.*	0.270	1.46	*n.d.*	*n.d.*	*n.d.*	0.770	0.530
Bi	1.19	0.350	0.700	1.71	1.51	1.55	1.36	1.60	1.57
Os	29.1	10.7	6.75	10.7	5.80	2.40	6.31	9.52	12.9
Ir	21.8	8.27	4.83	7.30	5.39	1.87	4.03	11.6	7.63
Ru	38.6	15.6	9.43	12.3	8.68	4.46	8.01	15.7	17.1
Rh	6.60	2.69	1.75	2.28	2.25	1.12	1.65	4.61	3.07
Pt	32.4	16.7	8.63	9.83	17.3	0.590	8.35	18.4	25.2
Pd	17.0	26.1	13.3	11.1	16.5	19.7	18.7	27.4	24.1
Au	0.120	*n.d.*	0.100	3.07	*n.d.*	*n.d.*	0.160	5.22	7.38

Table S5.4. (continued).

Sample	*TAL129 b_c1-1*	*TAL129 b_c3-1*	*TAL129 c_c1-1*	*TAL129 c_c3-1*	*TAL129 c_c6-1*	*TAL129 c_c7-1*	*TAL129 c_c8-1*	*TAL143 _c1-1*	*TAL143 _c2-1*
Mineral	*pn + cp_{exs}*	*pn + cp_{exs}*	*pn*	*pn*	*pn*	*pn*	*pn*	*pn*	*pn + cp*
S	327747	329423	326884	326948	322310	323433	328076	327536	328042
Co	1010	1298	996	1179	1091	1076	1024	1239	1005
Ni	400701	336548	385773	405958	385050	364818	402125	433107	312164
Cu	21299	9349	21956	14559	14444	14662	2895	2152	46304
Zn	27.4	355	14.4	44.2	49.4	32.0	125	14.8	43.4
Se	170	225	166	213	160	150	192	131	124
Ag	6.99	14.9	9.74	9.45	11.3	10.9	2.45	2.51	18.0
Cd	1.46	1.45	2.30	1.30	2.00	0.810	0.900	0.326	4.32
In	0.184	*n.d.*	0.132	0.320	0.235	0.199	0.059	0.064	0.313
As	88.4	53.5	34.4	56.8	37.9	42.3	35.9	14.9	19.8
Te	20.5	17.1	16.8	17.5	24.2	10.6	24.5	14.7	18.4
Pb	103	23.5	48.1	35.6	45.8	40.3	20.1	3.22	43.2
Sb	3.02	*n.d.*	0.380	*n.d.*	*n.d.*	*n.d.*	0.370	*n.d.*	*n.d.*
Bi	3.57	4.85	3.47	3.40	3.16	2.12	2.74	0.84	1.68
Os	2.97	28.6	0.620	4.57	9.42	20.7	7.40	14.9	10.5
Ir	1.92	25.8	0.570	5.21	6.58	15.3	4.31	10.9	6.95
Ru	5.07	64.8	2.46	5.90	16.4	28.0	14.5	20.1	13.8
Rh	1.01	6.21	0.440	0.660	1.91	3.91	2.10	3.71	2.87
Pt	0.38	13.4	1.58	1.09	7.34	15.4	0.780	18.5	13.7
Pd	13.5	12.5	11.3	11.6	14.5	9.41	17.9	16.4	15.8
Au	0.130	*n.d.*	7.06	0.300	1.20	0.490	*n.d.*	*n.d.*	3.86

Sample	*TAL143 _c3-1*	*TAL143 _c4-1*	*TAL146 _c1-1*	*TAL129 _c1-1*	*TAL129 _c2-3*	*TAL129 _c2-2*	*TAL129 _c2-1*	*TAL129 _c3-1*	*TAL129 _c3-2*
Mineral	*pn + cp*	*pn + cp*	*pn + cp_{exs}*	*pn*	*pn + cp*	*pn*	*pn + cp_{exs}*	*pn*	*pn*
S	328044	329924	328236	330629	327457	331515	329110	328406	329628
Co	949	344	1212	1835	1653	1466	1566	1296	1679
Ni	301111	213750	399933	420061	388420	406172	379026	318585	394277
Cu	58603	186786	29540	12757	20474	26280	39320	50336	35378
Zn	77.8	239	14.7	207	29.7	65.6	16.2	117	46.7
Se	91.3	129	147	185	169	145	160	150	154
Ag	9.07	53.0	1.85	13.7	9.29	1.71	12.1	14.8	12.0
Cd	4.12	5.17	0.800	5.37	1.46	2.40	6.20	3.21	5.95
In	0.303	1.53	0.088	1.44	-	0.220	0.184	0.585	0.409
As	12.2	116	20.2	114	43.3	31.2	37.4	25.8	36.7
Te	18.6	11.5	30.3	36.9	26.4	19.6	24.1	13.7	20.3
Pb	41.2	103	6.52	280	24.3	35.6	113	67.2	80.3
Sb	0.89	1.47	*n.d.*	*n.d.*	*n.d.*	*n.d.*	0.390	*n.d.*	0.460
Bi	1.19	9.79	1.26	8.70	1.48	3.40	5.44	5.29	4.84
Os	10.9	*n.d.*	12.6	9.89	6.88	9.42	53.8	2.29	5.40
Ir	9.76	0.370	9	8.79	7.37	7.48	37.6	1.54	4.72
Ru	20.4	1.08	16.5	12.2	12.9	12.4	71.4	4.40	8.65
Rh	4.72	0.930	2.95	2.86	2.85	3.1	14.4	1.06	2.18
Pt	12.1	*n.d.*	13.9	19.4	17.2	4.13	66.8	5.04	14.0
Pd	20.1	3.86	20.9	24.5	22.5	15.5	20.8	9.91	12.4
Au	0.790	3.30	0.110	1.78	*n.d.*	0.230	0.160	*n.d.*	3.25

Table S5.4. (continued).

Sample	*TAL129 _c5-1*	*TAL129 _c7-1*	*TAL129 _c8-1*	*TAL129 _c9-1*	*TAL129 _c9-2*	*TAL129 _c10-1*	*TAL129 a_c1-1*	*TAL129 a_c2-1*	*TAL129 a_c4-1*
Mineral	*pn*	*pn + cp + bn*	*pn*	*pn + cp*	*pn + cp + bn*	*pn*	*pn*	*pn + cp*	*pn + cp*
S	329013	328099	328237	328797	330134	329698	323703	325248	327095
Co	1425	1507	1575	1304	1718	1759	1753	1920	1868
Ni	350924	379981	415292	325466	417805	390929	362009	377315	409594
Cu	15456	20274	19166	79208	16586	8058	17297	13927	15973
Zn	66.6	46.8	45.6	313	25.5	45.0	33.7	118	54.8
Se	111	159	166	154	140	137	162	164	156
Ag	2.93	10.3	1.60	3.47	6.64	10.7	7.17	8.30	0.656
Cd	1.27	2.36	2.76	11.9	0.470	1.41	3.96	2.82	1.96
In	0.686	0.235	0.344	1.42	0.247	0.146	0.185	0.316	0.320
As	5.36	37.3	39.9	32.4	38.4	30.9	36.0	49.7	32.5
Te	17.6	23.7	19.8	22.5	20.9	25.7	18.9	23.7	13.0
Pb	1.90	62.4	47.4	266	43.8	17.7	47.9	31.4	27.0
Sb	*n.d.*	*n.d.*	*n.d.*	0.590	0.560	*n.d.*	1.08	*n.d.*	*n.d.*
Bi	4.13	3.61	3.25	5.39	3.57	6.34	2.84	1.28	1.60
Os	8.08	2.76	3.32	5.43	6.98	0.680	4.76	14.8	13.5
Ir	5.13	2.31	2.30	3.33	4.59	0.640	2.60	13.5	9.18
Ru	12.3	4.65	4.87	7.47	9.23	1.29	5.54	21.3	18.3
Rh	2.08	1.19	1.20	1.62	1.72	0.580	0.900	2.69	3.65
Pt	11.6	7.08	7.09	6.18	13.9	9.21	8.13	11.9	17.0
Pd	20.4	15.3	12.8	9.83	11.6	19.1	13.3	22.3	17.1
Au	*n.d.*	*n.d.*	1.81	*n.d.*	3.50	0.500	*n.d.*	*n.d.*	4.30

Sample	*TAL129 a_c6-1*	*TAL129 a_c7-1*	*TAL129 a_c8-1*	*Po-725*			*IMER-2*		
Mineral	*pn* + cp_{exs}	*pn*	*pn*	*X* (n =44)	RSD%	pref. value	*X* (n =44)	RSD%	pref. value
S	327043	326397	328505						
Co	2124	1997	1719						
Ni	441447	416968	394451						
Cu	18049	12517	8918						
Zn	26.3	49.3	73.7						
Se	170	155	166				90.7	4	85.2
Ag	11.4	7.53	2.00				1673	2	1603
Cd	1.89	1.40	2.40				0.069	21	0.064
In	0.373	0.201	1.10						
As	46.4	31.2	29.1				45.2	2	46.1
Te	21.5	17.4	15.0				213	2	210
Pb	65.4	45.7	39.5				195	4	191
Sb	0.570	*n.d.*	*n.d.*				285391	1	285400
Bi	3.87	2.52	5.11				407	4	397
Os	24.4	1.12	44.0	50.4	14	48.2			
Ir	16.4	1.04	31.2	44.5	8	42.4			
Ru	31.3	1.94	54.6	31.1	5	38.0			
Rh	5.79	0.570	9.29	41.4	6	41.3			
Pt	37.6	2.75	80.8	38.6	5	36.3	0.418	12	0.468
Pd	21.0	14.9	11.9	57.2	5	42.9	0.199	10	0.218
Au	5.48	0.300	3.27	36.8	6	44.5	1339	4	1305

6. Mantle-to-crust metal transfer by nanomelts

6.1 Introduction

Ore deposits are regarded as local manifestations of large-scale geological processes that optimally align to maximize the flux and storage of metals from background levels in a source region to economic abundances in the accessible crust (e.g., Hronsky et al., 2012; Barnes et al., 2016). The flux of precious and semi-metals through the continental lithosphere is traditionally modelled according to their relative solubility within ascending silicate magmas and/or immiscible droplets of Fe-Ni-Cu sulfide melt (Zelenski et al., 2018; Blanks et al., 2020; Heinrich and Connolly, 2022; Holwell et al., 2022), which collect most of the budget of chalcophile (i.e., sulfide-loving) metals by chemical equilibrium partitioning (Li and Audétat, 2012). This assumption has been recently challenged by an increasing number of mineralogical studies reporting the occurrence of metal-rich, insoluble nanoparticles controlling a large fraction of the metals inventory in mantle rocks (González-Jiménez et al., 2019, 2020), mantle-derived magmas (Kamenetsky et al., 2015; Zelenksi et al., 2017; Kamenetsky and Zelenski, 2020), and hydrothermal ore-forming fluids (Petrella et al., 2020; Hastie et al., 2021; McLeish et al., 2021; Petrella et al., 2022). Nevertheless, the origin of metal-rich nanoparticles in mantle rocks, as well as their fate during transport upwards through the crust are still contentious questions.

Experimental work shows that precious and semi-metals in magmas tend to self-organize into insoluble nanoclusters even before attaining concentrations for their saturation in sulfide liquids (Helmy et al., 2013). Moreover, recent experiments ascribed the formation of insoluble nanoparticles to the segregation of metal-rich nanomelts immiscible in the sulfide melt (Anenburg and Mavrogenes, 2020), thus arguing against the effective role of sulfide melts on metal dissolution. However, the geological record still lacks direct evidence of lithospheric-scale metal transport via immiscible metal-rich nanomelts, with little knowledge of their impact on the mobility and storage of metals in ore-productive domains of the continental lithosphere.

To address this knowledge gap, I investigated rocks from the Neogene Volcanic Province of Eastern Betics (Southeastern Spain), which hosts a wide range of magmatic-hydrothermal ores associated with subduction-related magmatism in the western Mediterranean. This volcanic province includes calcalkaline to alkaline magmas (Duggen et al., 2005), which are genetically associated with epithermal Au and Pb-Zn-Cu-(Ag) mineralization at ~ 9-11 Ma in the Roadalquilar-Carboneras and Mazarrón-La Unión districts, respectively (Fig. 6.1a; Arribas et al., 1995; Milot et al., 2022). The last eruptive stages of alkaline basalt magmatism (Tallante volcanic field, 2.93-2.29 Ma; Fig. 6.1a) brought up to the surface abundant mantle xenoliths representative of the underlying SCLM, which was inferred to have originally fed the ore-productive volcanism in the region (Chapter 5). Moreover, alkaline magmatism in the region also produced lamproite dykes, which extruded at ~ 9.3-7.1 Ma (e.g., Fortuna volcanic field, Fig. 6.1a; Pérez-Valera et al., 2013) and were sourced by partial melting of the subduction-metasomatized SCLM sampled by the Tallante mantle xenoliths (Bianchini et al., 2015; Avanzinelli et al., 2020; Casalini et al., 2021). Therefore, the Neogene Volcanic Province is an excellent natural laboratory for documenting the transfer mechanisms that controlled the flux of metals from the SCLM to magmatic-hydrothermal ores in the upper crust across a trans-lithospheric plumbing network.

In this chapter, I discuss the mechanisms accounting for mantle-to-crust metal transfer by describing the nature of Pb-rich nanoparticles preserved in metasomatized mantle xenoliths (Tallante volcanic field) and spatially/genetically associated lamproite dykes (Fortuna volcanic field). These observations provide snapshots of metal transport in a trans-lithospheric continuum and document how mechanical entrapment of metal-rich nanomelts immiscible in sulfide liquid may have played a key role in regulating the metal endowment of an ore-productive sector of continental lithosphere.

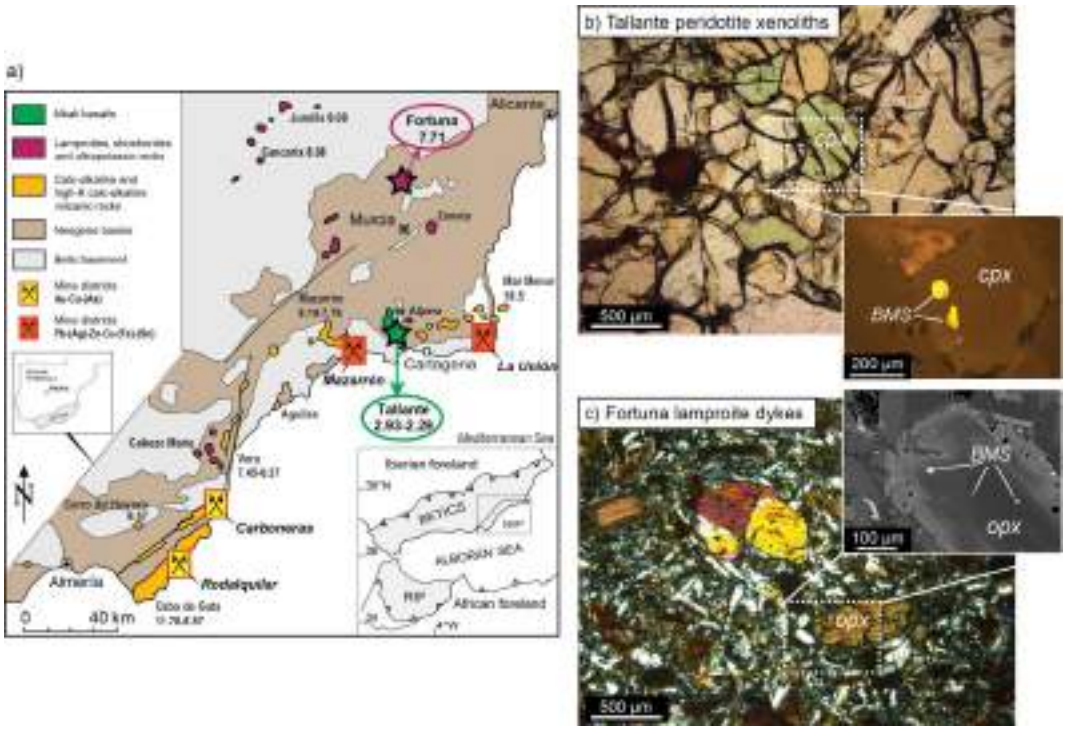

Figure 6.1. Geological sketch of the Neogene Volcanic Province of Southeast Spain (modified from Gómez-Pugnaire et al., 2019), with the location of the volcanic localities of Tallante and Fortuna (a), photomicrographs and backscatter electron images of the studied pyroxene-hosted sulfides from Tallante xenoliths (b) and Fortuna lamproite dyke (c). Mineral abbreviations are: cpx – clinopyroxene; opx – orthopyroxene; BMS – base-metal sulfides. Geochronological data in million years (Ma) of volcanic suites are from Duggen et al. (2005).

6.2 Petrological background

The studied nanoparticle-bearing peridotite xenoliths come from the Tallante volcanic field, and represent a volume of fertile SCLM that experienced metal endowment through the crystallization of precious metal-rich nanoparticles incorporated in metasomatic sulfides (González-Jiménez et al., 2020; Chapter 5). The targeted xenoliths have a medium-to-fine grained (0.5-2 mm) granular texture characterized by the presence of olivine porphyroclasts in a granoblastic matrix of poorly strained olivine neoblasts and amoeboid orthopyroxene, clinopyroxene and spinel (Chapter 5). The major element compositions of the rock-forming minerals record cooling and decompression of this portion of lithospheric mantle from 1100 °C at 1.8-1.9 GPa to 850 °C at 0.7-0.9 GPa (Rampone et al., 2010; Hidas et al., 2016). The estimated fO_2 conditions based on the olivine-spinel oxybarometer (Ballhaus et al., 1991) vary between -1.5 to +1.5 relative to the fayalite-magnetite-

quartz buffer (FMQ), which fall within the range typically observed in a subduction-metasomatized lithospheric mantle (Bénard et al., 2018). Spherical droplets of base-metal sulfides enriched in metals (Au ~ 1.78 ppm) up to 20-50 μm across (González-Jiménez et al., 2020; Chapter 5) are systematically enclosed within metasomatic clino and orthopyroxene. The trace element signatures of sulfide-bearing clinopyroxene record silicate metasomatism by Miocene subalkaline subduction-related magmas (Chapter 5).

The suite of lamproite dykes and lava flows extruded in this region ca. 9.3-7.1 (Pérez-Valera et al., 2013) along the STEP faults that accommodated the lateral tearing and edge delamination of the Iberian continental margin (Duggen et al., 2005; Cambeses et al., 2016). The lamproite dykes from the locality of Fortuna (~ 7.71 Ma; Kuiper et al., 2006) studied here display a porphyritic texture with euhedral phenocrysts and microlites of olivine, phlogopite, orthopyroxene and apatite that are dispersed in a glassy to microcrystalline groundmass (Venturelli et al., 1988). The lamproite magma started crystallizing at T < 1100 °C and FMQ ± 1 as it settled ~ 45 km depth near the mantle-crust boundary zone before crustal emplacement (Cambeses et al., 2016). Base-metal sulfides in these rocks occur as rounded droplets included within the grain core of prismatic orthopyroxene phenocrysts (Sharygin et al., 2003), indicating that they were trapped during the early stages of magmatic differentiation of the ascending lamproite melt.

6.3 Results

6.3.1 Nanoparticle-bearing sulfide droplets

Pb-rich nanoparticles were found included in base-metal sulfides (BMS) from peridotite mantle xenoliths of Tallante and the nearby Fortuna lamproite dykes (Fig. 6.1). The nanoparticle-bearing BMS at Tallante is a spherical droplet, ~ 30 μm in diameter, included within a metasomatic clinopyroxene (Fig. 6.1b). The trace element signature of the sulfide-bearing clinopyroxene records mantle metasomatism by asthenosphere-derived silicate magmas, released during the

subduction-related evolution of the western Mediterranean in the Miocene (Hidas et al., 2016; Chapter 5). The nanoparticle-bearing sulfide droplet consists of a composite aggregate of pentlandite [$(Ni,Fe)_9S_8$] with lesser amounts of chalcopyrite [$CuFeS_2$] and bornite [Cu_5FeS_4] (Fig. 6.2a). This pyroxene-hosted BMS precipitated from a Fe-Ni-Cu sulfide melt transported as immiscible droplets by the asthenosphere-derived silicate magmas percolating through the shallow portions of the SCLM (see Chapter 5). The lack of pyrrhotite exsolutions or subsolidus flame-like textures suggests that the Fe-Ni-Cu sulfide melt solidified to pentlandite ± chalcopyrite intergrowth once the xenoliths were rapidly brought up to the surface during the eruption of the Pliocene host lava (Anenburg and Mavrogenes, 2020; Helmy et al., 2021).

The nanoparticle-bearing sulfides in the Fortuna lamproites form rounded droplets that are included within the magnesium-rich core (Mg# = 94.5-87.3) of prismatic orthopyroxene phenocrysts (Fig. 6.1c), which crystallized as the lamproite magmas differentiated while ascending through the mantle-crust transition (Cambeses et al., 2016). The sulfide droplets are ~ 10 μm (Fig. 6.3a) in size and are commonly associated with fluid inclusions and/or silicate melt inclusions (Fig. S6.1 of the Appendix). They consist of pentlandite and chalcopyrite intergrowths, with rare amounts of pyrrhotite. These characteristics suggest that the immiscible sulfide droplets originally present in the silicate magma were mechanically trapped by growing orthopyroxene as the lamproite magma ascended through the base of the crust, and finally exsolved into pentlandite ± chalcopyrite intergrowths during fast cooling upon magma eruption (Helmy et al., 2021).

6.3.2 Metal-rich nanoparticles

Several Au- and Pb-rich nanoparticles are found in sulfide droplets from Tallante mantle xenoliths (Fig. 6.2) and lamproite dykes (Fig. 6.3). Magmatic nanoparticles of gold were reported as euhedral inclusions hosted in sulfide blebs from Tallante mantle peridotites (González-Jiménez et al., 2020; Chapter 5), or as spheroidal grains within the glassy groundmass of the Fortuna lamproite dyke (Toscani et al., 1999). Here, I document the first evidence of Pb-rich nanoparticles

in Fe-Ni-Cu sulfide droplets from these rocks. The nanoparticles from the interior of the sulfide blebs and at their interface with hosting pyroxene (Figs. 6.2, 6.3) were extracted from polished thin sections by focusing ion beam scanning electron microscopy (FIB-SEM) and thinned to ~ 90 nm electron transparent foils for subsequent high resolution transmission electron microscopy (HR-TEM; Fig. S6.2 of the Appendix, Wirth, 2009; Ciobanu et al., 2011).

HR-TEM examination of the FIB section from the inner part of the sulfide bleb included in the Tallante clinopyroxene (Fig. 6.2a) indicates the presence of a nanosized Pb-Cu-S domain (100-200 nm; Fig. 6.2b) yielding selected area electron diffraction (SAED) patterns consistent with crystalline galena (Table 6.1). The TEM-EDS elemental mapping also reveals the presence of a Fe-oxide euhedral inclusion (~ 500 nm; Fig. S6.3 of the Appendix), displaying fast Fourier diffraction patterns calculated from high resolution images consistent with a single crystal of magnetite in crystallographic continuity with the host pentlandite (Fig. S6.4 of the Appendix). The presence of magnetite nanoinclusions within Tallante sulfides was already reported by González-Jiménez et al. (2020), who concluded that they crystallized from the unmixed oxygen-rich fraction of an oxy-sulfide melt (Doyle and Naldrett, 1987) due to local fO_2 increase around the FMQ buffer (Naldrett, 1969; Larocque et al., 2000). The galena nanoinclusion displays well-defined crystal faces and polygonal grain boundaries against the surrounding pentlandite matrix (Fig. 6.2b-c). The analysis of HR-TEM images highlights a distinct lattice orientation between the galena nanoinclusion, identified by (2 2 0) and (2 0 0) planes (2.10 Å and 2.97 Å d-spacings, respectively), and the adjacent pentlandite, identified by (3 1 1) plane (3.08 Å d-spacings) (Fig. 6.2d). The lack of crystallographic continuity with the host pentlandite, together with the perfectly idiomorphic shape of the galena nanoinclusion, argue against an origin by alteration or low-temperature exsolution of PbS previously dissolved in a homogeneous sulfide solution. Rather, these characteristics support the hypothesis that galena crystallized prior to the solidification of the Fe-Ni sulfide melt that precipitated the host sulfide.

The FIB section extracted along the margin of the sulfide bleb crosscuts the pentlandite-chalcopyrite interface (Fig. 6.2a). The chalcopyrite portion of the sulfide aggregate contains a ~ 1 μm Pb-rich idiomorphic grain enveloped by a

subspherical Cu-rich halo (Fig. 6.2e-f), which yields single-crystal diffraction patterns corresponding with galena and digenite, respectively (Table 6.1). The HR-TEM imaging reveals that the galena inclusion, identified by (1 1 1) plane (3.42 Å d-spacing), shares a common crystallographic orientation with the adjacent digenite halo, identified by (3 2 2) plane (3.05 Å d-spacing) (Fig. 6.2g). This observation supports the hypothesis that galena and digenite co-precipitated upon cooling. The galena + digenite envelope exhibits a droplet-shaped morphology located at the external edge of the sulfide bleb (Fig. 6.2a, e-f), which points against the idea that it formed via exsolution from the Fe-Ni-Cu sulfide melt that finally precipitated their host sulfide matrix.

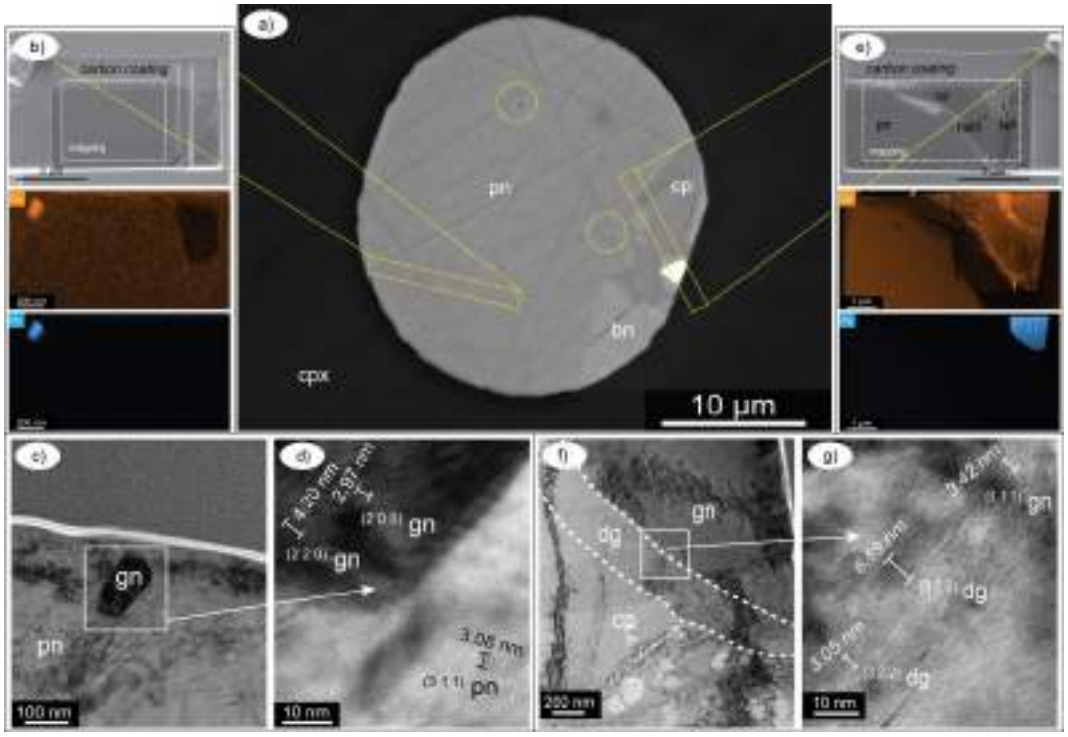

Figure 6.2. Backscatter electron image acquired at scanning electron microscope on polished thin section, showing the location of two metal-rich nanoparticles in the studied sulfide droplet from Tallante peridotite xenolith (a). Backscatter electron images and EDS elemental maps (Cu, Pb) on the two thin foil focused-ion beam (FIB) sections analyzed by transmission electron microscopy (TEM) (b, e). Bright field scanning electron images (STEM; c, f) and high-resolution TEM images (d, g) of the contact between the galena nanoinclusions and the adjacent sulfide minerals. Estimated measurements (nm) of 10 spacings and corresponding lattice parameters are shown for each mineral domain. Mineral abbreviations are: cpx – clinopyroxene; gn – galena; pn – pentlandite; cp – chalcopyrite; bn – bornite; dg – digenite.

The four FIB cross-sections of sulfide droplets hosted in the Fortuna lamproites also intersected several Pb-Cu-rich nanoparticles surrounded by a Ni-

Fe sulfide matrix (Fig. 6.3 and Figs. S6.5-6.8 of the Appendix). These Pb-Cu-rich nanoparticles occur either as very small (< 10 nm) particles randomly dispersed within the sulfide matrix, or as larger (0.1-1 μm) particles located along the external interface of the sulfide droplet (Fig. 6.3a).

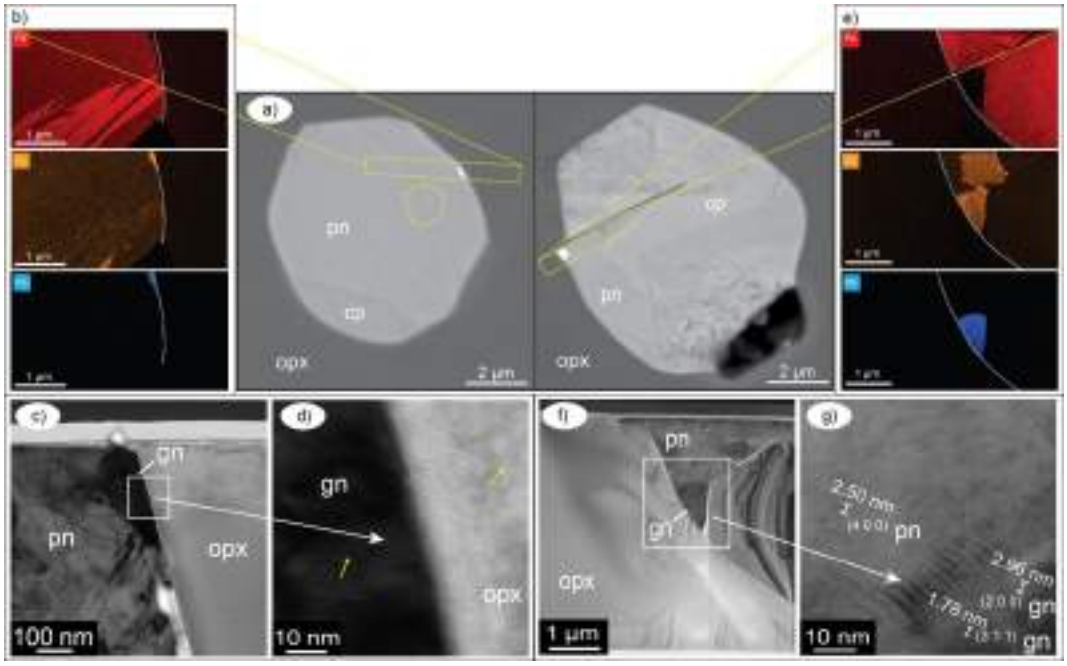

Figure 6.3. Backscatter electron images of nanoparticle-bearing sulfide droplets acquired at scanning electron microscope on polished thin sections of Fortuna lamproite dykes (a). EDS elemental maps (Fe, Cu, Pb) on thin-foil focused-ion beam (FIB) samples analyzed by transmission electron microscopy (TEM) (b, e). Bright field scanning electron images (STEM; c, f) and high-resolution TEM images (d, g) of the contact between the galena nano-inclusions and the adjacent minerals. Estimated measurements (nm) of 10 spacings and corresponding lattice parameters are shown for each mineral domain. Mineral abbreviations are: opx – orthopyroxene; gn – galena; pn – pentlandite; cp – chalcopyrite.

In all cases, the SAED patterns are consistent with the presence of single crystals of galena (Table 6.1), which have semi-circular morphologies with an outer border adapting along the curvilinear surface of the sulfide droplet (Fig. 6.3b-c, e-f). The galena nanoparticles share crystallographic continuity with the adjacent pentlandite matrix (Fig. 6.3g), suggesting that they both co-precipitated upon fast ascent of the lamproite magma. However, the galena nanoparticles show no preferential orientation relative to the subparallel planar intergrowths of chalcopyrite and pyrrhotite (Fig. 6.3b), nor crystallographic continuity with the adjacent orthopyroxene phenocryst (Fig. 6.3d). The curvilinear morphologies of

galena nanoparticles, together with the lack of flame-like textures within the pentlandite-chalcopyrite intergrowths, contrast with the textural characteristics that would be expected if PbS was originally dissolved in the sulfide melt that finally solidified to the host BMS (Anenburg and Mavrogenes, 2020).

Table 6.1. Indexed lattice parameters of identified minerals derived from selected area electron diffraction (SAED) analysis and fast Fourier Transform (FFT) diffraction patterns calculated from high-resolution images.

Tallante peridotite xenolith										
d-spacings (Å)	pentlandite		chalcopyrite		galena		digenite		magnetite	
	Å	*(h k l)*	Å	*(h k l)*	Å	*(h k l)*	Å	*(h k l)*	Å	*(h k l)*
3.54	3.50	2 2 0								
3.02	3.08	3 1 1								
2.89	2.85	2 2 2								
3.03			3.04	1 1 2						
1.87			1.87	2 2 0						
3.42					3.42	1 1 1				
2.96					2.99	2 0 0				
2.09					2.10	2 2 0				
1.78					1.79	3 1 1				
3.38							3.38	1 0 0		
3.04							3.05	3 2 2		
2.96									2.95	2 2 0
2.53									2.56	3 1 1
Fortuna lamproite dyke										
d-spacings (Å)	pentlandite		chalcopyrite		galena		digenite		magnetite	
	Å	*(h k l)*	Å	*(h k l)*	Å	*(h k l)*	Å	*(h k l)*	Å	*(h k l)*
5.79	5.79	1 1 1								
3.54	3.55	2 2 0								
3.02	3.01	3 1 1								
2.89	2.87	2 2 2								
1.77	1.80	4 4 0								
3.04			3.07	1 1 2						
1.87			1.88	2 2 0						
3.42					3.42	1 1 1				
2.96					2.96	2 0 0				
2.09					2.06	2 2 0				

6.4 Discussion

The nanoparticle-bearing sulfides in the Tallante mantle xenoliths and the Fortuna lamproite dykes share very similar textural and compositional characteristics. They consist of ~ 10-30 µm spherical droplets made of pentlandite ± chalcopyrite intergrowths and host an identical suite of nanoparticles inclusions of native gold and galena (Figs. 6.2, 6.3; Toscani et al., 1999; González-Jiménez et al., 2020; Chapter 5). These observations support the hypothesis that the lamproite magmas, generated by partial melting of the underlying subduction-metasomatized SCLM (Avanzinelli et al., 2020; Casalini et al., 2021), mechanically entrained Fe-Ni-Cu molten sulfides from the mantle source and physically transported them as immiscible droplets upwards to the crust (Fig. 6.4; Bockrath et al., 2004; Ballhaus et al., 2006).

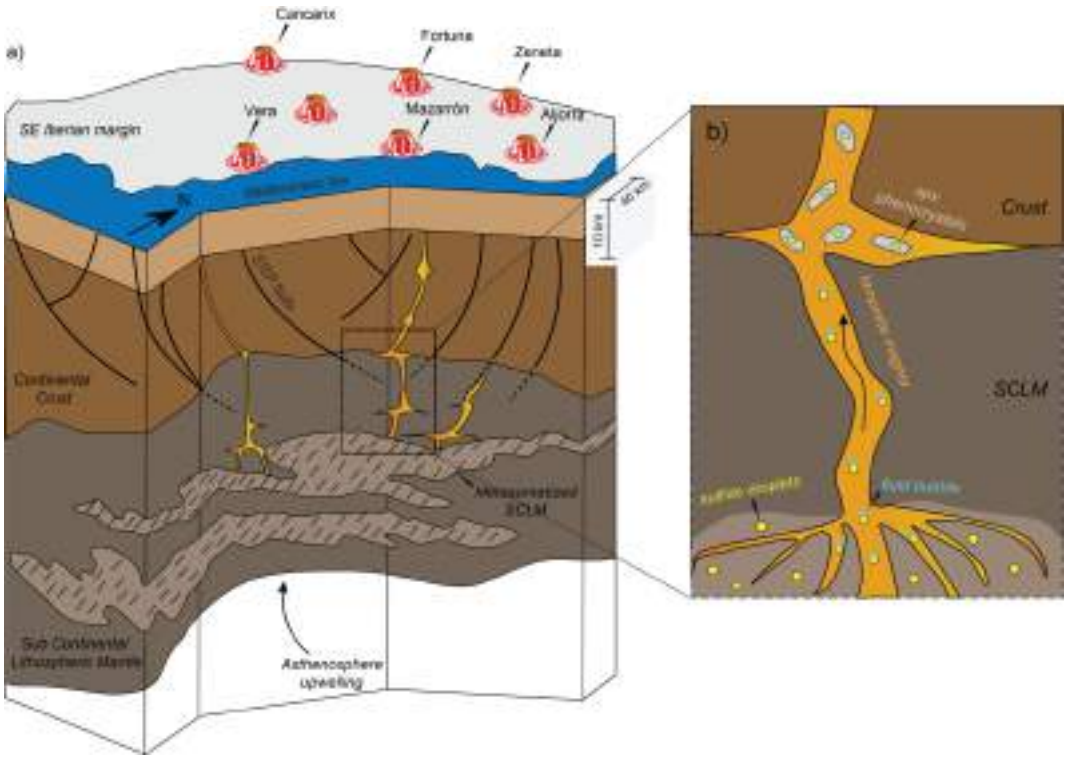

Figure 6.4. Schematic model for metal transport across the ore-productive sector of continental lithosphere beneath the Neogene Volcanic Province of Southeast Spain. Modified after Cambeses et al. (2016). STEP faults: subduction transform edge propagator fault systems.

The presence of sulfide droplets as clinopyroxene-hosted inclusions in fusible domains of the SCLM likely favored the mechanical removal of sulfide liquid during partial melting events in the mantle (Wang et al., 2020). Because sulfide liquids are denser (~ 4000 kg/m^3; Dobson et al., 2000) compared with silicate magmas (~ 2460-2710 kg/m^3 for lamproite magmas; Rao et al., 2008), the upwards transport of sulfide droplets necessarily requires that the sinking velocity of sulfide melt is lower than the ascent velocity of the host lamproite magma. Subduction-zone magmas usually rise very fast (ascent rates ranging between 100-1000 m/yr, Turner and Costa, 2007). On the other hand, the sinking velocity of sulfide droplets can be calculated according to the Stokes' law for spherical bodies (Holzheid, 2010):

$$v = \frac{(\Delta\rho)}{18 * \mu} * g * d^2$$

using the density difference between sulfide and silicate melts ($\Delta\rho$), the diameter of the sulfide melt droplets (d ~ 30 µm maximum), and the temperature-dependent viscosity (μ) of the silicate melt (Giordano et al., 2008). The calculated sinking velocities of sulfide melt droplets range from ~ 3 to 14 m/yr between 700-1200 °C (Table 6.2).

Table 6.2. Calculated settling velocities of immiscible droplets of sulfide melt in lamproite magmas, based on relative density contrast ($\rho_{sulfide} - \rho_{lamproite}$), diameter of sulfide droplets (d), and temperature-dependent viscosities of the lamproite magmas (µ). Ascent rates of lamproite magmas are provided by Turner and Costa (2007).

	Settling velocities of sulfide melt droplets					
	$\rho_{sulfide}$ = 4000 kg/m^3		$\rho_{lamproite}$ = 2585 kg/m^3		**d** = 30 µm	
T [°C]	700	800	900	1000	1100	1200
µ [Kg/ms]	6.16	4.79	3.73	2.89	2.20	1.63
v [m/yr]	3.55	4.56	5.85	7.55	9.90	13.35
	Ascent rate of lamproite magmas					
v [m/yr]	100-1000					

The comparison between these velocities shows that the fraction of Fe-Ni-Cu sulfide melt incorporated during mantle melting may be efficiently transported upwards by ascending lamproite melts throughout the mantle-to-crust magma route (Fig. 6.4). This transport mechanism is especially effective through high-strain domains of the continental lithosphere (Wang et al., 2020), such as the trans-lithospheric fault zones that provide the locus of lamproite volcanism in Southeast Spain (Cambeses et al., 2016). Moreover, the close textural association of sulfides with fluid inclusions in Fortuna lamproites (Fig. S6.1 of the Appendix) provides evidence of the formation of buoyant compounds (Mungall et al., 2015; Iacono-Marziano et al., 2021) that possibly boosted the rapid upwards flux of dense sulfide melt included in silicate magmas (Blanks et al., 2020; Heinrich and Connolly, 2022).

The entrapment and transport of sulfide melt droplets within silicate magmas likely drove the collection of chalcophile elements, such as precious and semi-metals (Li and Audétat, 2012). Nevertheless, the occurrence of sulfide-hosted galena nanosized inclusions, as well as native gold and Pt-(Pd)-Sn compounds in both Tallante peridotite xenoliths and Fortuna lamproite dykes (Toscani et al., 1999; González-Jiménez et al., 2020; Chapter 5), shows that these metals did not dissolve in sulfide melts according to the expected chalcophile partitioning behavior.

Experimental work has shown that pure galena [PbS] has melting temperatures around 1115 °C, although it should fully dissolve within Fe-Ni-Cu sulfide liquid at the high temperatures that are typical of mantle-derived magmas (> 850 °C; Brett and Kullerud, 1967). Therefore, according to experimental results, galena nanoparticles in mantle sulfides should form during the subsolidus re-equilibration of the BMS assemblage exsolving at low temperatures. However, the galena nanoparticles identified in the Tallante mantle xenolith and Fortuna lamproite dyke lack flame-like textures or orientation relationship with the adjacent sulfide matrix, indicating that they were not produced by low-temperature exsolution of PbS previously dissolved in the sulfide liquid (Wirth et al., 2013; Junge et al., 2015; González-Jiménez et al., 2020). Moreover, the galena nanoparticles in the Tallante peridotite xenoliths are commonly close to magnetite nanoinclusions (Fig. S6.3 of the Appendix). This spatial proximity rules out that

they crystallized by decreasing sulfur fugacity into reducing domains of the subarc lithospheric mantle, as proposed by Kepezhinskas et al. (2022).

The Cu-bearing galena nanoinclusion in the Tallante mantle peridotite has well-defined crystal shapes and polygonal grain boundaries (Fig. 6.2a-c). Together with the distinct lattice orientation relative to the host pentlandite (Fig. 6.2d), these features support the hypothesis that the Cu-bearing galena nanoinclusion crystallized as an early magmatic phase from the (oxy)-sulfide melt before the solidification of the host sulfide droplet. The high-temperature crystallization of galena in a Fe-Ni-Cu-(Pb) sulfide system necessarily requires the segregation of immiscible Pb-(Cu)-rich liquid from the Ni-Fe sulfide melt (Fig. 6.5). Immiscibility between Ni-Fe sulfide melts and liquids enriched in semi-metals (e.g., TABS: Te, As, Bi, Se) has been experimentally demonstrated (Anenburg and Mavrogenes, 2020; Helmy and Botcharnikov, 2020), but it has never been reported for Pb-bearing liquids in nature. According to experimental data, the co-existence of euhedral galena with a digenite subspherical halo in crystallographic continuity (Fig. 6.2e-g) records the monotectic reaction below ~ 500 °C involving the solidification of galena + digenite from a Pb-Cu-rich liquid covering the central portion of the Pb-Cu-S system (Fig. 6.5; Craig and Kullerud, 1968; Johto and Taskinen, 2013; Shishin et al., 2020). Therefore, the attainment of the galena-digenite eutectic point necessarily requires the derivation from a Pb-Cu liquid that was originally immiscible within the Ni-Fe sulfide melt at high temperature (Fig. 6.5). Depending on the relative abundances of Cu and Pb (Fig. 6.5), the immiscible liquid may have fully crystallized at high temperature as Cu-bearing galena (Fig. 6.2b; Chang et al., 1988), or precipitated at low temperature (< 500 °C) as galena + digenite upon xenolith ascent (Fig. 6.2e). The fact that the galena + digenite spherical envelope is located at the edge surface of the host sulfide droplet (Fig. 6.2a, e-f) is consistent with a two-phase separation by liquid immiscibility at high temperature (Anenburg and Mavrogenes, 2020).

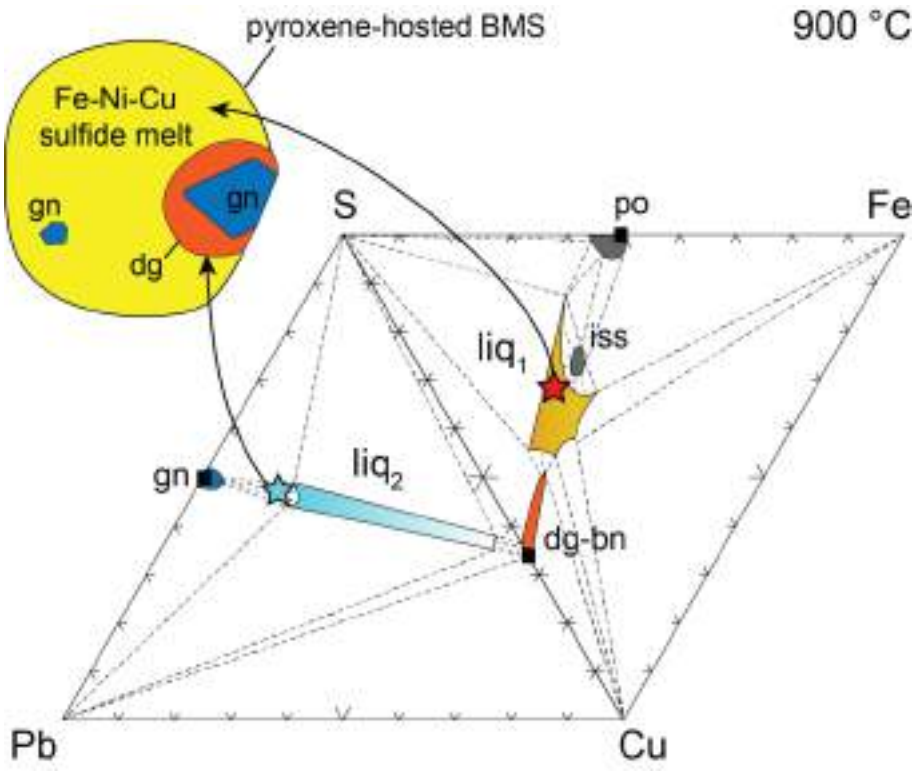

Figure 6.5. Experimentally-determined phase relations at 900 °C in the Pb-Cu-S (Craig and Kullerud, 1968; Shishin et al., 2020) and Fe-Cu-S systems (Kitakaze et al., 2018) applied for interpreting the origin of galena nanoinclusions in sulfide droplets from Tallante peridotites and Fortuna lamproites.

An analogous interpretation explains the origin of galena nanoparticles in the Fortuna lamproites, which likewise display curvilinear morphologies adapting to the rounded surface of the host sulfide droplet (Fig. 6.3). The lack of any orientation relationships relative to the pentlandite-chalcopyrite intergrowths (Fig. 6.3b), together with the rounded morphologies at the edge surface of the sulfide droplet (Fig. 6.3c, e-f), support that the galena nanoparticles crystallized from a Pb-Cu rich liquid entrained within the Ni-Fe sulfide melt that precipitated their host BMS. Therefore, these observations reinforce the idea that metal transfer across the ore-productive continental lithosphere of the southeastern Iberian margin occurred through the entrapment of metal-rich nanomelts within sulfide melt droplets, which were transported upwards by ascending lamproitic magmas across the entire lithospheric column. A similar mechanism may address the mantle-to-crust transfer of native gold, which occurs as euhedral crystals in sulfide droplets from the Tallante peridotite xenoliths (Chapter 5) and immiscible spheroids in silicate glasses from the Fortuna lamproite dykes (Toscani et al.,

1999). This transport mechanism explains why similar parageneses of metal-rich nanoinclusions are hosted in analogous sulfide droplets in both magmatic products (the Fortuna lamproite) and their mantle source (sampled by the Tallante peridotite xenolith). According to this model, the metallogenic fertility of mantle-derived silicate magmas may be partially dictated by the fractions of sulfide liquid and metal-rich nanomelts that are scavenged from the source and physically transported during magma ascent through the lithosphere (Bockrath et al., 2004; Ballhaus et al., 2006).

These observations provide the first-ever direct geological record of the experimental predictions that metal-rich insoluble clusters, such as those commonly reported in BMS worldwide (Wirth et al., 2013; Junge et al., 2015; González-Jiménez et al., 2020; Kamenetsky and Zelensky, 2020), may precipitate from small droplets of nanomelts that were originally immiscible within Fe-Ni-Cu sulfide liquids (Helmy et al., 2013; Anenburg and Mavrogenes, 2020; Helmy and Botcharnikov, 2020). Therefore, the close association of metal-rich nanoparticles with magmatic sulfides may be due to mechanical entrapment, rather than to chalcophile equilibrium partitioning (Wirth et al., 2013; Junge et al., 2015). In this scenario, sulfide melts may act as a physical trap for metal-rich clusters insoluble in silicate magmas (Kamenetsky et al., 2015; González-Jiménez et al., 2019), favoring their coalescence into immiscible liquids that may segregate close to the external surface of the sulfide droplet (Helmy et al., 2013; Anenburg and Mavrogenes, 2020). These findings further highlight the necessity to revise the reliability of traditional models of metal transport based solely on sulfide solubility and sulfide/silicate equilibrium partitioning, and require considering transport as nanomelts governed by surface energy properties (Tredoux et al., 1995; Ballhaus and Sylvester, 2000). If the inventory of metal-rich nanoparticles could be finally transferred to the hydrothermal fluids exsolving from magmas at shallow crustal depths, metals may accumulate as colloidal metal-rich nanoparticles (Petrella et al., 2020, 2022; González-Jiménez et al., 2021; Hastie et al., 2021; McLeish et al., 2021) that can be distributed by mineralizing fluids at various crustal levels.

6.5 Appendix

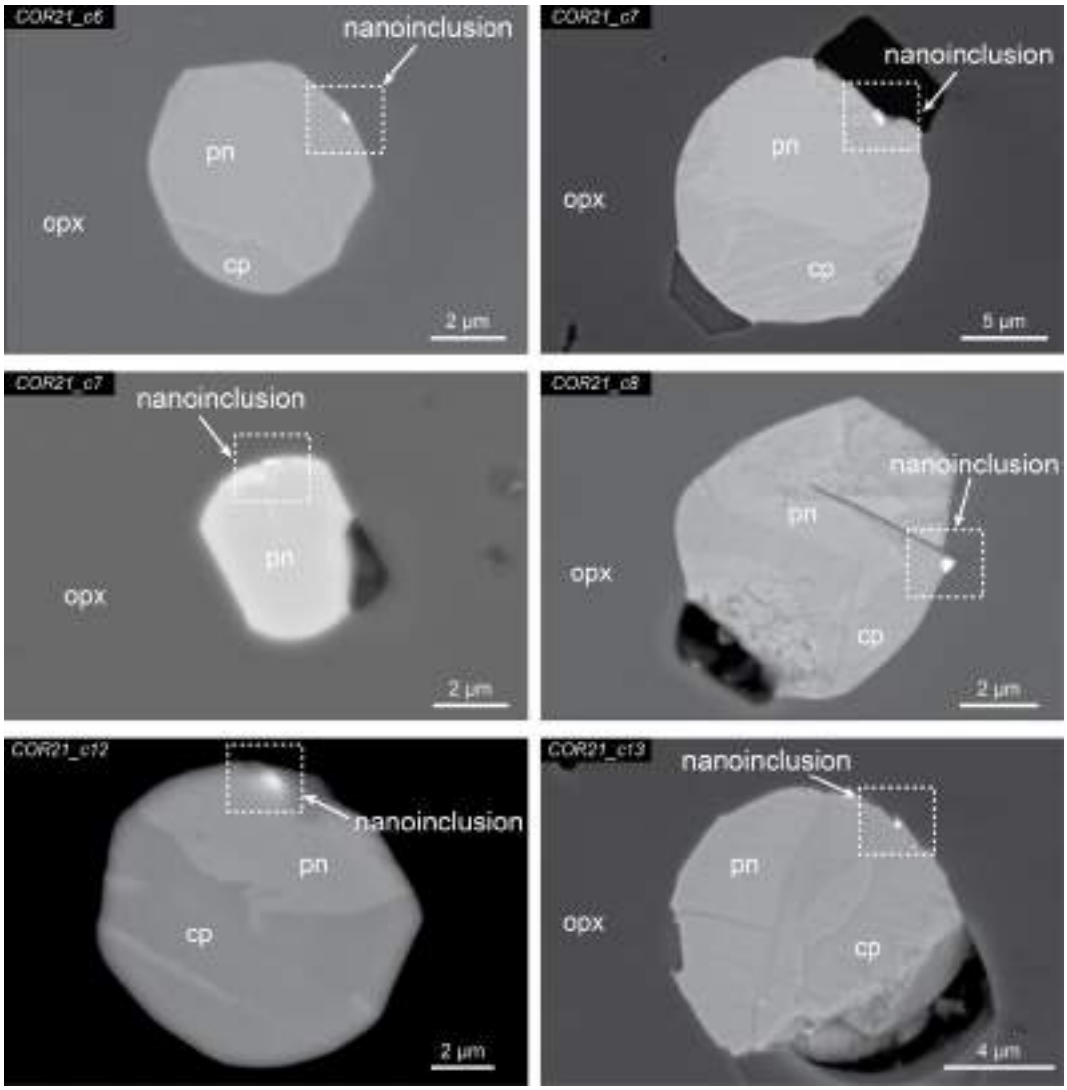

Figure S6.1. Backscattered electron images of nanoparticle-bearing sulfide droplets in the Fortuna lamproite dykes (COR21).

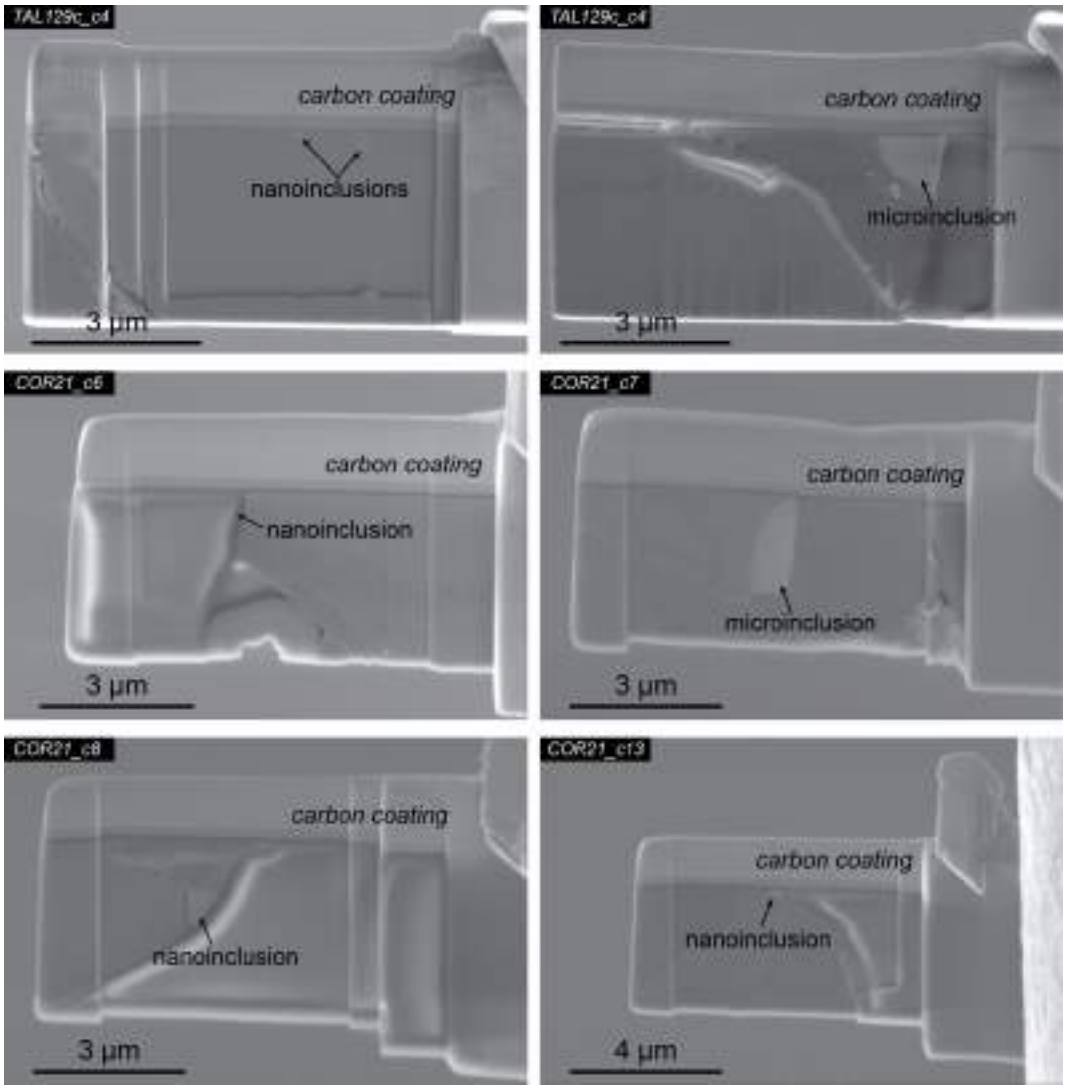

Figure S6.2. Electro transparent thin-foil samples extracted from selected nanoparticle-bearing sulfide droplets in Tallante peridotite xenoliths (TAL129c) and Fortuna lamproite dykes (COR21)

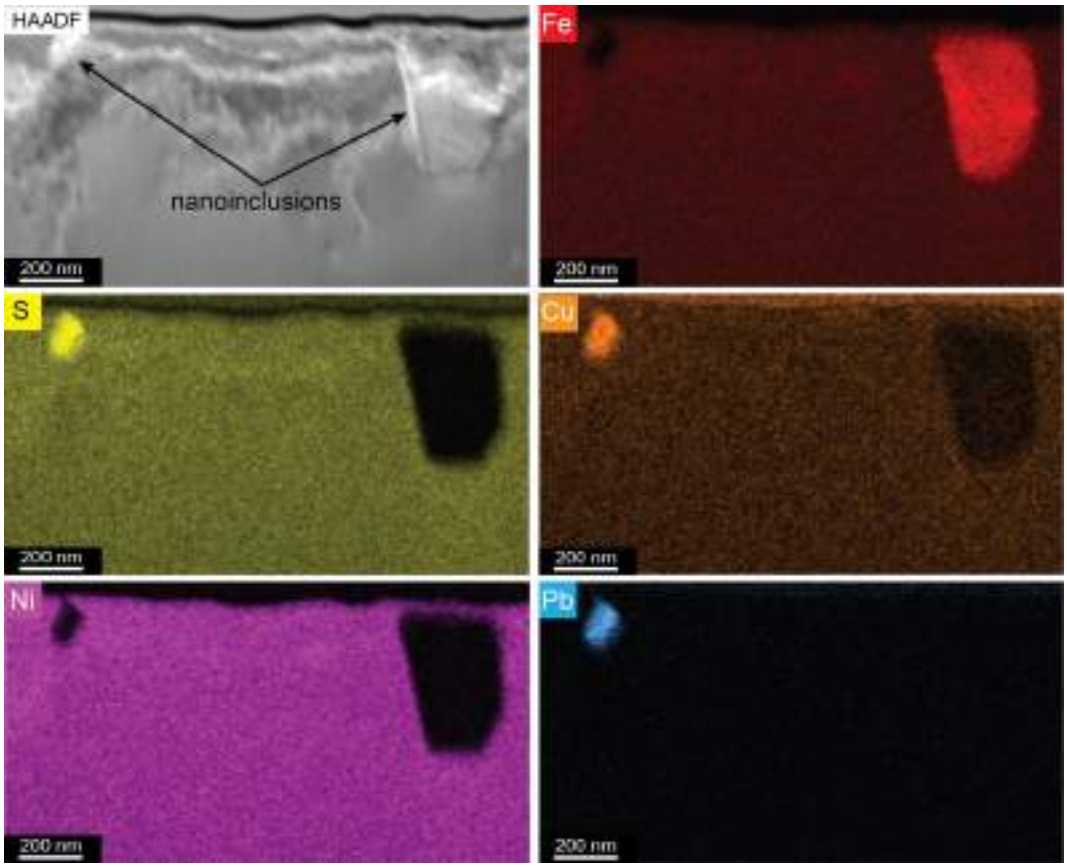

Figure S6.3. High angle-annular dark field (HAADF) Z-contrast image and elemental maps in scanning transmission electron microscopy (STEM-EDS) acquired on TAL129_c4 thin foil sample by high resolution-transmission electron microscopy (HR-TEM).

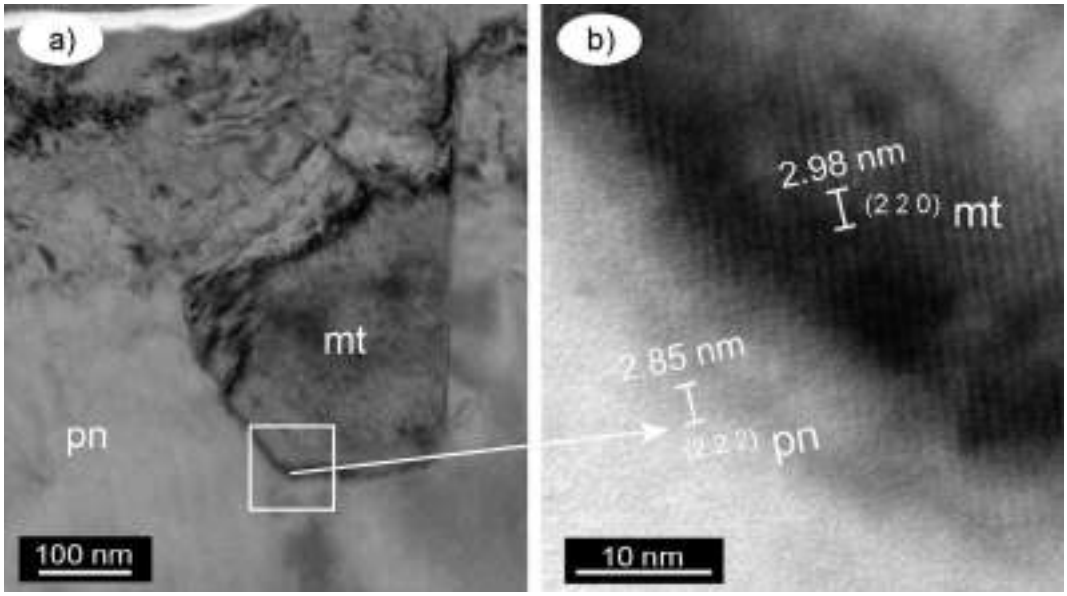

Figure S6.4. Bright field scanning electron images (a) and high-resolution transmission electron microscopy images (HR-TEM, b) of magnetite nanoinclusion in thin foil sample TAL129c_c4.

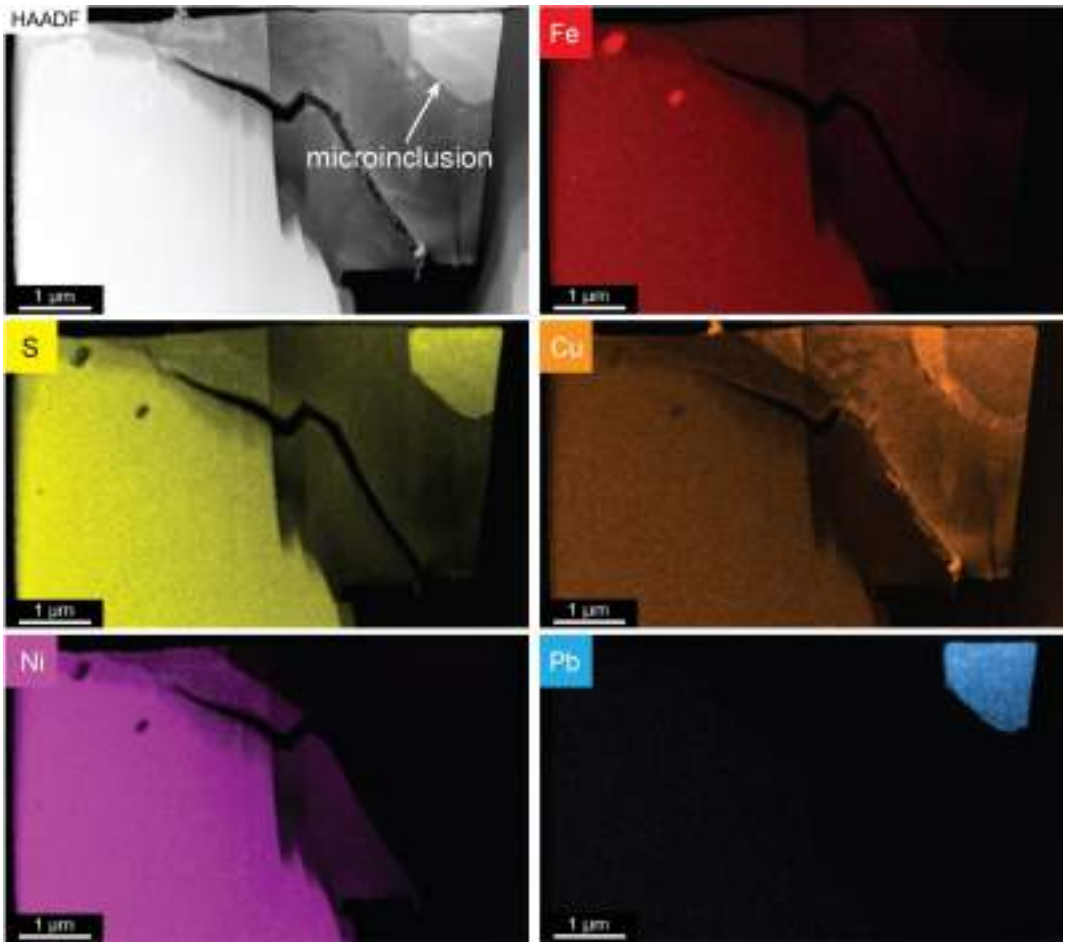

Figure S6.5. High angle-annular dark field (HAADF) Z-contrast image and elemental maps in scanning transmission electron microscopy (STEM-EDS) acquired on TAL129_c4 thin foil sample by high resolution-transmission electron microscopy (HR-TEM).

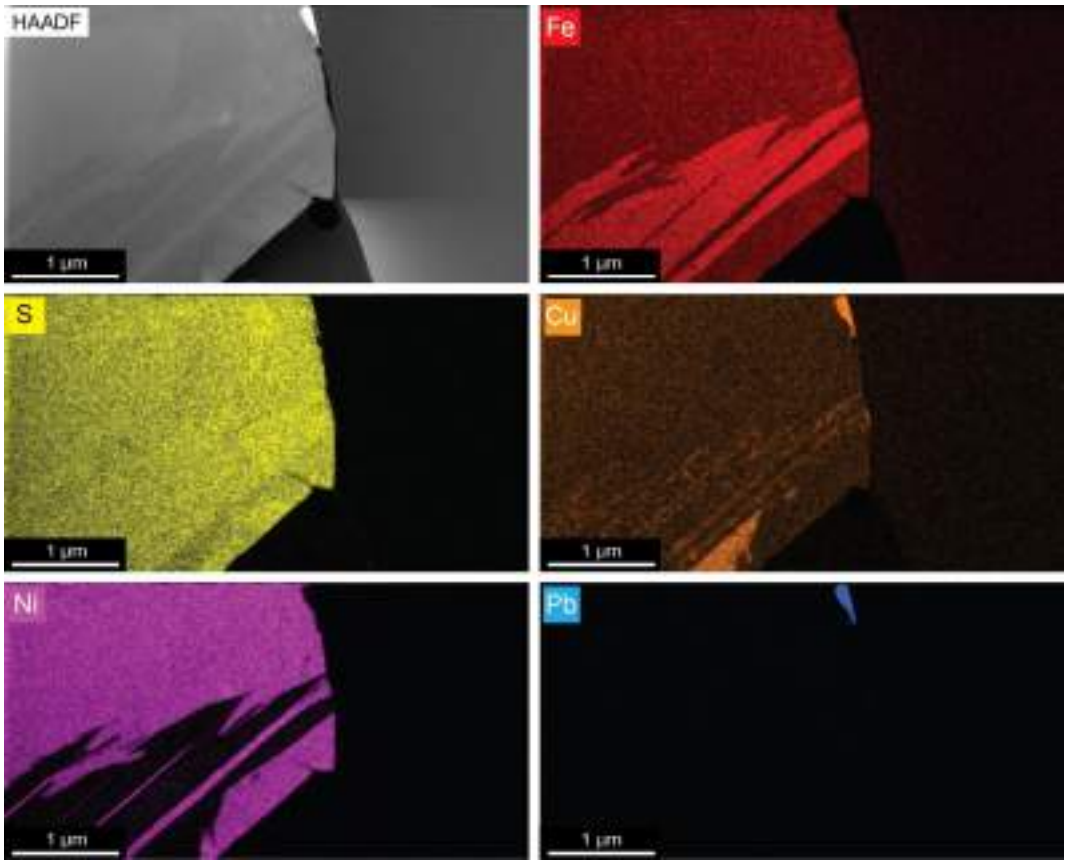

Figure S6.6. High angle-annular dark field (HAADF) Z-contrast image and elemental maps in scanning transmission electron microscopy (STEM-EDS) acquired on COR21_c6 thin foil sample by high resolution-transmission electron microscopy (HR-TEM).

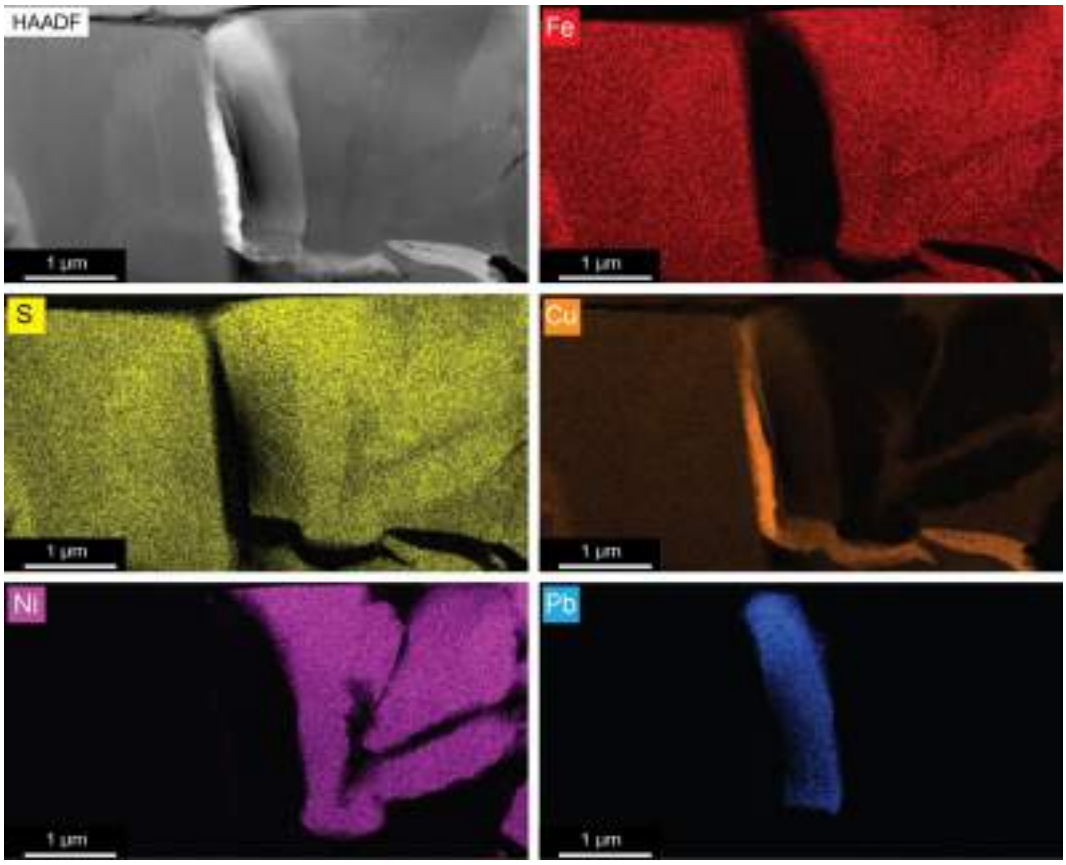

Figure S6.7. High angle-annular dark field (HAADF) Z-contrast image and elemental maps in scanning transmission electron microscopy (STEM-EDS) acquired on COR21_c7 thin foil sample by high resolution-transmission electron microscopy (HR-TEM).

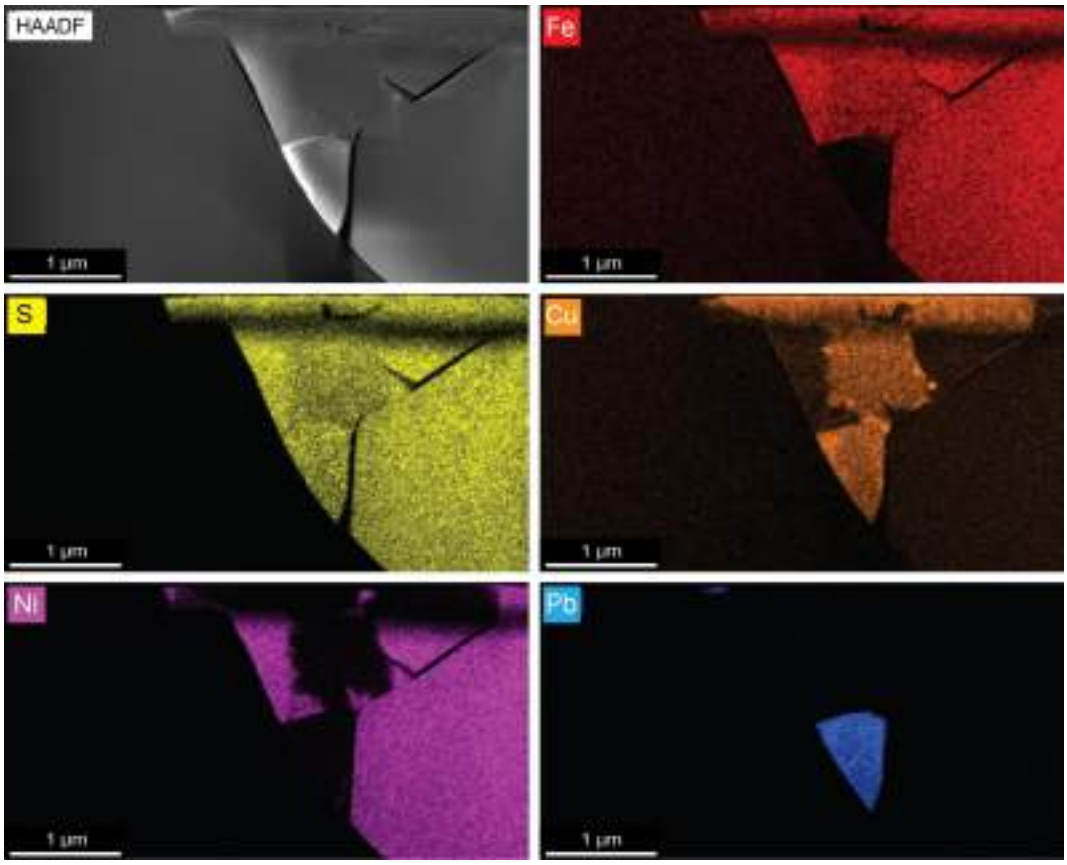

Figure S6.8. High angle-annular dark field (HAADF) Z-contrast image and elemental maps in scanning transmission electron microscopy (STEM-EDS) acquired on COR21_c8 thin foil sample by high resolution-transmission electron microscopy (HR-TEM).

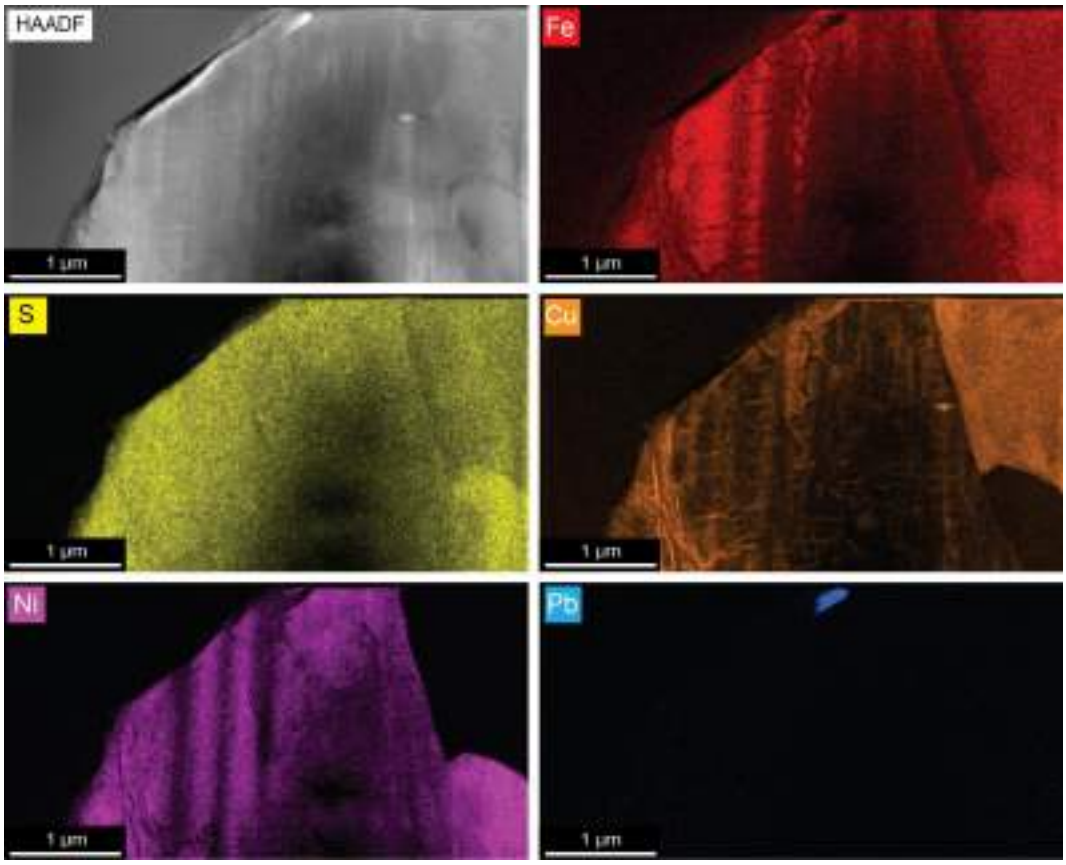

Figure S6.9. High angle-annular dark field (HAADF) Z-contrast image and elemental maps in scanning transmission electron microscopy (STEM-EDS) acquired on COR21_c13 thin foil sample by high resolution-transmission electron microscopy (HR-TEM).

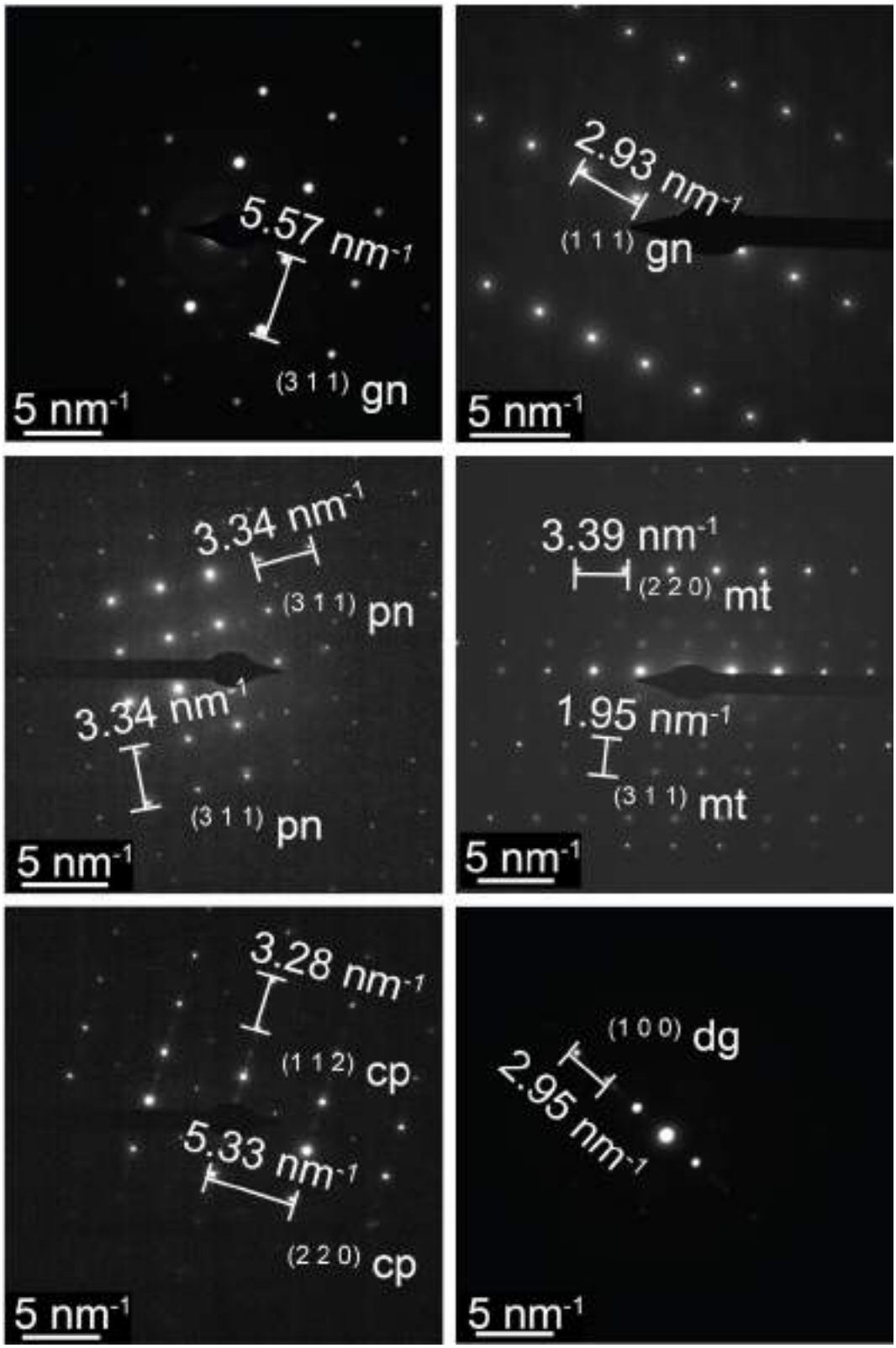

Figure S6.10. Representative selected area electron diffraction (SAED) patterns and fast Fourier transform diffraction patterns from high resolution images of minerals identified in the Tallante peridotite xenoliths and Fortuna lamproite dykes. Abbreviations are: gn – galena; pn – pentlandite; mt – magnetite; cp – chalcopyrite; dg – digenite.

Part III

Conclusions

7. Conclusions

7.1 Outcomes of the thesis

This Ph.D thesis provides new insights into the geological factors that control the mobility, transport and storage of chalcophile metals in the subcontinental lithospheric mantle (SCLM). To achieve these goals, I interpreted petrographic and microstructural characteristics, and in situ chemical data of minerals in mantle-derived rocks, principally peridotite xenoliths, which allowed to define: 1) the key control of the SCLM architecture on determining the regional distribution of metallogenic provinces (Chapter 4); 2) the melt/rock reaction processes boosting the metallogenic fertility of the SCLM (Chapter 5); 3) the transfer media and mechanisms ruling the flux of chalcophile metals across the lithospheric-scale magma route (Chapter 6). Therefore, these results provide key constraints upon both the active and passive roles of the subcontinental lithospheric mantle on governing the metallogenic endowment in ore-productive regions of the continental crust (e.g., Central Mexico, Southeast Spain).

The role of the SCLM architecture on determining the heterogeneous distribution of ore mineralizations in the crust was assessed by studying mantle xenoliths from the Santo Domingo, Ventura-Espíritu Santo and Durango volcanic fields in Central Mexico (Mesa Central). Clinopyroxene grains in these lherzolites record different degrees of partial melting in the garnet (2%) and spinel peridotite (2-4%) stability fields, and interaction with hydrous alkaline silicate melts possibly produced by intraplate magmatism due to extensional tectonics since Late Oligocene. Grains of intergranular and enclosed monosulfide solid solution (mss) in Santo Domingo peridotites formed by the extraction of 0.1-0.5 fractions of Ni-Cu-rich sulfide melt from mss during mantle melting events. Glass-hosted sulfides (pentlandite ± chalcopyrite) in Ventura-Espíritu Santo and Durango lherzolites formed by the segregation of immiscible droplets of Ni-Cu-rich sulfide melts during the infiltration and fractionation of the host basalts. Notably, T_{RD} model ages of Santo Domingo and Ventura-Espíritu Santo sulfides indicate that the SCLM beneath the Oaxaquia lithospheric block formed in the Archean-Paleoproterozoic as part of the Laurentia craton, and was reworked together with

the currently adjacent Central terrane (beneath Durango) in the Mesoproterozoic (~ 1.0 Ga). Early Paleozoic (~ 500 Ma) T_{RD} ages of sulfides in peridotites from the three volcanic fields indicate that the Oaxaquia-Central composite block split away from Laurentia and experienced Pan-African-Brasiliano orogeny before being emplaced in its present position in the Late Paleozoic. During the Mesozoic-Cenozoic evolution of the Cordilleran margin of western Mexico, the translithospheric faults bounding this Archean-Proterozoic SCLM probably acted as preferential pathways for ore-productive melts and fluids associated with the subduction-related metallogeny of Central Mexico.

The melt-rock reaction processes controlling the metallogenic fertility of the SCLM were assessed by studying a suite of spinel lherzolite xenoliths from Tallante (Eastern Betic Cordillera, Southeast Spain). These rocks preserve evidence of the percolation of Miocene subalkaline silicate melts in the SCLM beneath the southern Iberian margin, which caused the crystallization of metasomatic sulfide-hosting clinopyroxene, orthopyroxene and spinel. In the Pliocene, these sulfide-bearing metasomatic assemblages underwent small-scale partial melting in response to the influx of heat/volatiles from host alkaline magmas shortly before the xenoliths' ascent, as evidenced by interstitial silicate glass associated with spongy coronae around clinopyroxene and spinel. Base-metal sulfides (pentlandite ± chalcopyrite ± bornite) in the Tallante peridotites represent the breakdown product of quaternary (Ni-Fe-Cu-S) sulfide solution between heazlewoodite and intermediate solid solutions, which originally precipitated from Ni-Cu-rich sulfide melts. Incongruent melting of monosulfide solid solution produced these melts during extraction and transport of the silicate magmas that finally precipitated the sulfide-hosting pyroxenes. Despite sharing homogeneous compositions in terms of major elements and semi-metals, these BMS have a wide variability of PGE systematics inherited from distinct populations of sulfides and/or PGM during melting and melt percolation to the shallower SCLM. The early magmatic segregation of (sub)-micrometric PGM and metal particles, either from silicate or sulfide melts, controlled the noble metal distribution in BMS (especially of Pt and Au), depending on whether they were incorporated or not within sulfides. Overall, BMS in Tallante peridotites have remarkably higher Au abundances than BMS in oceanic or continental mantle not

associated with metallogenic crustal provinces. It is proposed that metasomatic crystallization of sulfide-hosting pyroxene provided an efficient mechanism for the storage of metals, especially Au, in this sector of SCLM underlying the ore-productive continental margin of southeast Iberia. Partial melting of this fertile source region, during progressive asthenosphere upwelling and continental edge delamination, may have effectively fed the metal cargoes of the calc-alkaline volcanism genetically associated with ore mineralization in the upper crust.

The transfer media and mechanisms controlling the flux of metals across the continental lithosphere were assessed by investigating peridotite mantle xenoliths (Tallante volcanic field) and lamproite dykes (Fortuna volcanic field) from the Neogene Volcanic Province of Southeast Spain. These lamproite dykes are interpreted to have been sourced by partial melting of the underlying metasomatized SCLM, sampled by the Tallante peridotite xenoliths. Therefore, these rocks as a whole portray snapshots of a trans-lithospheric continuum linking the transfer of metals from a fertile mantle source to subduction-related alkaline magmas genetically associated with the emplacement of magmatic-hydrothermal ores in the crust. Both peridotite mantle xenoliths and lamproite dykes contain 10-30 μm sized sulfide droplets made up of pentlandite ± chalcopyrite intergrowths, included in metasomatic clinopyroxene (in the Tallante peridotite xenoliths) or orthopyroxene phenocrysts (in the Fortuna lamproite dykes). I propose that these sulfides represent droplets of immiscible sulfide melt entrained in lamproite magmas during mantle melting, and physically transported in the silicate magmas while ascending across the lithosphere. Importantly, sulfides in both peridotites and lamproites contain metal-rich nanosized inclusions of galena, magnetite and native gold. The crystallographic and microstructural properties of the galena nanoparticles support that these minerals crystallized from small droplets of Pb(-Cu)-rich nanomelts, which were originally immiscible within the Fe-Ni-Cu sulfide melts that precipitated their host sulfide grains. These nanosized inclusions are the first-ever direct evidence in nature of immiscibility between metal (Pb-Cu)-rich nanomelts and sulfide liquids, thus questioning the effective role of sulfide melts on dissolving metals by chalcophile partitioning. These conclusions claim for the necessity to revise the reliability of traditional models of metal transport based solely on sulfide solubility and sulfide/silicate equilibrium partitioning, and

require to consider the role of surface energy properties in governing the physical entrapment and transport of insoluble metal-rich nanoclusters within sulfide liquids.

7.2 Perspectives

The results of this thesis provide a step forward for the understanding of the physico-chemical behavior of chalcophile metals in the subcontinental lithospheric mantle, as well as new insights into the mantle processes leading to the genesis of magmatic-hydrothermal ore deposits in the crust. Furthermore, the major outcomes of this study highlight several controversial topics that open up new research space in which directing the lines of future investigation.

This study shows that a better understanding of the architecture of the SCLM provides key tools to develop exploration strategies for targeting the distribution of magmatic-hydrothermal ore deposits in the continental crust. In particular, the *in situ* Re-Os age data of Santo Domingo, Ventura-Espíritu Santo and Durango peridotite xenoliths point out that the metallogenic productivity of the continental crust in Central Mexico is strongly controlled by the architecture of a previously undiscovered, Archean-age SCLM root. Such increasing evidence for the occurrence of cryptic, Archean-age lithospheric mantle roots beneath off-craton regions of Proterozoic/Pharenozoic exposed crust demands to better constrain the origin, age and evolution of off-craton SCLM, beyond the long-lasting genetic dichotomy traditionally assumed between old, depleted and thick cratonic SCLM vs. young, fertile and thin off-craton SCLM.

Furthermore, this thesis evidences that the mobility of precious and semi-metals in the SCLM cannot be entirely accounted for by their chalcophile affinity for sulfide liquids. In particular, platinum-group elements and semi-metals systematics in base-metal sulfides from Tallante mantle xenoliths indicate that these elements did not behave according to their expected equilibrium partitioning between mss, sulfide melts and silicate magmas. Instead, the abundances and distribution of precious metals in mantle sulfides may be governed by the mechanical incorporation of insoluble Au-rich, and Pt-Pd-rich minerals, which

may directly crystallize from silicate magmas prior to the solidification of sulfide melts. Notably, these results show that such mechanisms provide an effective way for enhancing the metallogenic fertility of metasomatized domains of the SCLM beneath ore-productive regions of the continental crust. Therefore, future work will need to revise the role of base-metal sulfides and sulfide melts on dissolving precious metals, especially considering the increasing evidence of precious metal-rich minerals insoluble in silicate magmas ascending through the mantle.

Finally, high-resolution textural characterization of nanosized inclusions of galena within sulfide droplets from Tallante mantle xenoliths and Fortuna lamproite dykes documents previously unreported liquid immiscibility between Pb(-Cu)-rich nanomelts and Fe-Ni-Cu sulfide melts, persisting across the whole lithospheric-scale magma route. Such a breakthrough provides a new scenario for the mechanisms of metal flux from mantle source to extruded magmas, which may bypass the conventional solubility and equilibrium partitioning models between sulfides, sulfide melts and silicate magmas. Future lines of investigation will need to assess whether physical entrapment ruled by surface energy properties of insoluble metal-rich nanomelts/nanominerals provides an effective process for boosting the metal transport required for generating ore deposits.

Part IV

References

8. References

Ackerman, L., Walker, R. J., Puchtel, I. S., Pitcher, L., Jelínek, E., and Strnad, L., 2009, Effects of melt percolation on highly siderophile elements and Os isotopes in subcontinental lithospheric mantle: a study of the upper mantle profile beneath Central Europe: Geochimica et Cosmochimica Acta, v. 73, p. 2400-2414, https://doi.org/10.1016/j.gca.2009.02.002.

Alaniz-Álvarez, S. A., and Nieto-Samaniego, Á. F., 2005, El sistema de fallas Taxco-San Miguel de Allende y la Faja Volcánica Transmexicana, dos fronteras tectónicas del centro de México activas durante el Cenozoico: Boletín de la Sociedad Geológica Mexicana, v. 57, p. 65-82, doi: 10.18268/BSGM2005v57n1a4.

Alaniz-Álvarez, S. A., and Nieto-Samaniego, Á. F., 2007, The Taxco-San Miguel de Allende fault system and the Trans-Mexican Volcanic Belt: Two tectonic boundaries in central México active during the Cenozoic: in Alaniz-Álvarez, S. A., and Nieto-Samaniego, Á. F., eds., Geology of México: Celebrating the Centenary of the Geological Society of México: Boulder, Colorado, USA, The Geological Society of America. Geological Society of America Special Paper, v. 442, p. 301-316, doi: 10.1130/2007.2422(10).

Alard, O., Griffin, W. L., Lorand, J. P., Jackson, S. E., and O'Reilly, S. Y., 2000, Non-chondritic distribution of the highly siderophile elements in mantle sulphides: Nature, v. 407, p. 891-894, https://doi.org/10.1038/35038049.

Alard, O., Griffin, W. L., Pearson, N. J., Lorand, J. P., and O'Reilly, S. Y., 2002, New insights into the Re–Os systematics of sub-continental lithospheric mantle from in situ analysis of sulphides: Earth and Planetary Science Letters, v. 203, p. 651-663, https://doi.org/10.1016/S0012-821X(02)00799-9.

Alard, O., Lorand, J. P., Reisberg, L., Bodinier, J. L., Dautria, J. M., and O'reilly, S. Y., 2011, Volatile-rich metasomatism in Montferrier xenoliths (Southern France): Implications for the abundances of chalcophile and

highly siderophile elements in the subcontinental mantle: Journal of Petrology, v. 52, p. 2009-2045, https://doi.org/10.1093/petrology/egr038.

Andersen, T., Griffin, W. L., and O'Reilly, S. Y., 1987, Primary sulphide melt inclusions in mantle-derived megacrysts and pyroxenites: Lithos, v. 20, p. 279-294, https://doi.org/10.1016/S0024-4937(87)80002-6.

Anderson, D. L., 1995, Lithosphere, asthenosphere, and perisphere: Reviews of Geophysics, v. 33, p. 125-149, https://doi.org/10.1029/94RG02785.

Anderson, T.H., and Silver, L.T., 2005, The Mojave-Sonora megashear—Field and analytical studies leading to the conception and evolution of the hypothesis, in Anderson, T.H., Nourse, J.A., McKee, J.W., and Steiner, M.B., eds., The Mojave-Sonora Megashear Hypothesis: Development, Assessment, and Alternatives: Geological Society of America Special Paper, v. 393, p. 1–50, doi: 10.1130/2005.2393 (01).

Anenburg, M., and Mavrogenes, J. A., 2020, Noble metal nanonugget insolubility in geological sulfide liquids: Geology, v. 48, p. 939-943, https://doi.org/10.1130/G47579.1.

Arai, S., Shimizu, Y., and Gervilla, F., 2003, Quartz diorite veins in a peridotite xenolith from Tallante, Spain: implications for reaction and survival of slab-derived SiO_2-oversaturated melt in the upper mantle: Proceedings of the Japan Academy, Series B, v. 79, p. 145-150.

Aranda-Gómez, J. J., Luhr, J. F., and Pier, J. G., 1992, The La Breña-El Jagüey maar complex, Durango, México: I Geological evolution: Bulletin of Volcanology, v. 54, p. 393-404.

Aranda-Gómez, J. J., Luhr, J. F., Housh, T. B., Valdez-Moreno, G., and Chávez-Cabello, G., 2005, El volcanismo tipo intraplaca del Cenozoico tardío en el centro y norte de México: una revisión: Boletín de la Sociedad Geológica Mexicana, v. 57, p. 187-225.

Arndt, N. T., Fontboté, L., Hedenquist, J. W., Kesler, S. E., Thompson, J. F., and Wood, D. G., 2017, Future global mineral resources: Geochemical Perspectives, v. 6, p. 1-171.

Arribas, A., Cunningham, C. G., Rytuba, J. J., Rye, R. O., Kelly, W. C., Podwysocki, M. H., McKee, E. H., and Tosdal, R. M., 1995, Geology, geochronology, fluid inclusions, and isotope geochemistry of the Rodalquilar gold alunite deposit, Spain: Economic Geology, v. 90, p. 795-822, https://doi.org/10.2113/gsecongeo.90.4.795.

Artemieva, I. M., 2009, The continental lithosphere: Reconciling thermal, seismic, and petrologic data: Lithos, v. 109, p. 23-46, https://doi.org/10.1016/j.lithos.2008.09.015.

Audétat, A., Pettke, T., Heinrich, C. A., and Bodnar, R. J., 2008, Special paper: the composition of magmatic-hydrothermal fluids in barren and mineralized intrusions: Economic Geology, v. 103, p. 877-908, https://doi.org/10.2113/gsecongeo.103.5.877.

Aulbach, S., Griffin, W. L., Pearson, N. J., O'Reilly, S. Y., Kivi, K., and Doyle, B. J., 2004, Mantle formation and evolution, Slave Craton: constraints from HSE abundances and Re–Os isotope systematics of sulfide inclusions in mantle xenocrysts: Chemical Geology, v. 208, p. 61-88, https://doi.org/10.1016/j.chemgeo.2004.04.006.

Aulbach, S., Mungall, J. E., and Pearson, D. G., 2016, Distribution and processing of highly siderophile elements in cratonic mantle lithosphere: Reviews in Mineralogy and Geochemistry, v. 81, p. 239-304, https://doi.org/10.2138/rmg.2016.81.5.

Aulbach, S., Giuliani, A., Fiorentini, M. L., Baumgartner, R. J., Savard, D., Kamene.tsky, V. S., Caruso, S., Danyushevky, L. V., Powell, W., and Griffin, W. L., 2021, Siderophile and chalcophile elements in spinels, sulphides and native Ni in strongly metasomatised xenoliths from the Bultfontein kimberlite (South Africa): Lithos, v. 380-381, p. 105880, https://doi.org/10.1016/j.lithos.2020.105880.

Avanzinelli, R., Bianchini, G., Tiepolo, M., Jasim, A., Natali, C., Braschi, E., Dallai, L., Beccaluva, L., and Conticelli, S., 2020, Subduction-related hybridization of the lithospheric mantle revealed by trace element and Sr-Nd-Pb isotopic data in composite xenoliths from Tallante (Betic Cordillera, Spain): Lithos, v. 352, 105316.

Baker, J., Chazot, G., Menzies, M., and Thirlwall, M., 1998, Metasomatism of the shallow mantle beneath Yemen by the Afar plume—implications for mantle plumes, flood volcanism, and intraplate volcanism: Geology, v. 26, p. 431-434, https://doi.org/10.1130/0091-7613(1998)026<0431:MOTSMB>2.3.CO;2.

Baker, M. B., Hirschmann, M. M., Ghiorso, M. S., and Stolper, E. M., 1995, Compositions of near-solidus peridotite melts from experiments and thermodynamic calcuations: Nature, v. 375, p. 308-311, https://doi.org/10.1038/375308a0.

Ballhaus, C., and Ulmer, P., 1995, Platinum-group elements in the Merensky Reef: II. Experimental solubilities of platinum and palladium in Fe1− xS from 950 to 450° C under controlled *f*S2 and *f*H2: Geochimica et Cosmochimica Acta, v. 59, p. 4881-4888, https://doi.org/10.1016/0016-7037(95)00355-X.

Ballhaus, C., and Sylvester, P., 2000, Noble metal enrichment processes in the Merensky Reef, Bushveld Complex: Journal of Petrology, v. 41, p. 545-561, https://doi.org/10.1093/petrology/41.4.545.

Ballhaus, C., Tredoux, M., and Späth, A., 2001, Phase relations in the Fe–Ni–Cu–PGE–S system at magmatic temperature and application to massive sulphide ores of the Sudbury igneous complex: Journal of Petrology, v. 42, p. 1911-1926, https://doi.org/10.1093/petrology/42.10.1911.

Ballhaus, C., Bockrath, C., Wohlgemuth-Ueberwasser, C., Laurenz, V., and Berndt, J., 2006, Fractionation of the noble metals by physical processes: Contributions to Mineralogy and Petrology, v. 152, p. 667-684, https://doi.org/10.1007/s00410-006-0126-z.

Barnes, S. J., Makovicky, E., Makovicky, M., Rose-Hansen, J., and Karup-Moller, S., 1997, Partition coefficients for Ni, Cu, Pd, Pt, Rh, and Ir between monosulfide solid solution and sulfide liquid and the formation of compositionally zoned Ni–Cu sulfide bodies by fractional crystallization of sulfide liquid: Canadian Journal of Earth Sciences, v. 34, p. 366-374, https://doi.org/10.1139/e17-032.

Barnes, S. J., Cox, R. A., and Zientek, M. L., 2006, Platinum-group element, gold, silver and base metal distribution in compositionally zoned sulfide droplets from the Medvezky Creek Mine, Noril'sk, Russia: Contributions to Mineralogy and Petrology, v. 152, p. 187-200, https://doi.org/10.1007/s00410-006-0100-9.

Barnes, S. J., Mungall, J. E., and Maier, W. D., 2015, Platinum group elements in mantle melts and mantle samples: Lithos, v. 232, p. 395-417, https://doi.org/10.1016/j.lithos.2015.07.007.

Barnes, S. J., Cruden, A. R., Arndt, N., and Saumur, B. M., 2016, The mineral system approach applied to magmatic Ni–Cu–PGE sulphide deposits: Ore Geology Reviews, v. 76, p. 296-316.

Beccaluva, L., Bianchini, G., Bonadiman, C., Siena, F., and Vaccaro, C., 2004, Coexisting anorogenic and subduction-related metasomatism in mantle xenoliths from the Betic Cordillera (southern Spain): Lithos, v. 75, p. 67-87, https://doi.org/10.1016/j.lithos.2003.12.015.

Becker, H., Horan, M. F., Walker, R. J., Gao, S., Lorand, J. P., and Rudnick, R. L., 2006, Highly siderophile element composition of the Earth's primitive upper mantle: constraints from new data on peridotite massifs and xenoliths: Geochimica et Cosmochimica Acta, v. 70, p. 4528-4550, https://doi.org/10.1016/j.gca.2006.06.004.

Bedini, R. M., Bodinier, J. L., Dautria, J. M., and Morten, L., 1997, Evolution of LILE-enriched small melt fractions in the lithospheric mantle: a case study from the East African Rift: Earth and Planetary Science Letters, v. 153, p. 67-83, https://doi.org/10.1016/S0012-821X(97)00167-2.

Bedini, R. M., and Bodinier, J.-L., 1999, Distribution of incompatible trace elements between the constituents of spinel peridotite xenoliths: ICP-MS data from the East African Rift: Geochimica et Cosmochimica Acta, v. 63, p. 3883-3900.

Begg, G.C., Griffi n, W.L., Natapov, L.M., O'Reilly, S.Y., Grand, S.P., O'Neill, C.J., Hronsky, J.M.A., Djomani, Y.P., Swain, C.J., Deen, T., and Bowden, P., 2009, The lithospheric architecture of Africa: Seismic tomography,

mantle petrology, and tectonic evolution: Geosphere, v. 5, p. 23–50, doi:10.1130/GES00179.1.

Begg, G. C., Hronsky, J. A., Arndt, N. T., Griffin, W. L., O'Reilly, S. Y., and Hayward, N., 2010, Lithospheric, cratonic, and geodynamic setting of Ni-Cu-PGE sulfide deposits: Economic Geology, v. 105, p. 1057-1070, https://doi.org/10.2113/econgeo.105.6.1057.

Begg, G. C., Hronsky, J. M., Griffin, W. L., and O'Reilly, S. Y., 2018, Global-to deposit-scale controls on orthomagmatic Ni-Cu (-PGE) and PGE reef ore formation, in Mondal, S. K., Griffin, W. L., eds., Processes and Ore Deposits of Ultramafic-Mafic Magmas through Space and Time: Elsevier, p. 1-46, https://doi.org/10.1016/B978-0-12-811159-8.00002-0.

Beccaluva, L., Bianchini, G., Bonadiman, C., Siena, F., and Vaccaro, C., 2004, Coexisting anorogenic and subduction-related metasomatism in mantle xenoliths from the Betic Cordillera (southern Spain): Lithos, v. 75, p. 67-87.

Bekker, A., Barley, M. E., Fiorentini, M. L., Rouxel, O. J., Rumble, D., and Beresford, S. W., 2009, Atmospheric sulfur in Archean komatiite-hosted nickel deposits. Science, v. 326, p. 1086-1089, DOI: 10.1126/science.1177742.

Bénard, A., Klimm, K., Woodland, A. B., Arculus, R. J., Wilke, M., Botcharnikov, R. E., Shimizu, N., Nebel, O., Rivard, C., and Ionov, D. A., 2018, Oxidising agents in sub-arc mantle melts link slab devolatilisation and arc magmas: Nature Communications, v. 9, p. 1-10, https://doi.org/10.1038/s41467-018-05804-2.

Bennett, V. C., and DePaolo, D. J., 1987, Proterozoic crustal history of the western United States as determined by neodymium isotopic mapping: Geological Society of America Bulletin, v. 99, p. 674-685, https://doi.org/10.1130/0016-7606(1987)99<674:PCHOTW>2.0.CO;2.

Bezada, M. J., Humphreys, E. D., Toomey, D. R., Harnafi, M., Dávila, J. M., and Gallart, J., 2013, Evidence for slab rollback in westernmost Mediterranean from improved upper mantle imaging: Earth and Planetary Science Letters, v. 368, p. 51-60, https://doi.org/10.1016/j.epsl.2013.02.024.

Bianchini, G., Beccaluva, L., Nowell, G. M., Pearson, D. G., and Siena, F., 2011, Mantle xenoliths from Tallante (Betic Cordillera): insights into the multi-stage evolution of the south Iberian lithosphere: Lithos, v. 124, p. 308-318, https://doi.org/10.1016/j.lithos.2010.12.004.

Bianchini, G., Braga, R., Langone, A., Natali, C., and Tiepolo, M., 2015, Metasedimentary and igneous xenoliths from Tallante (Betic Cordillera, Spain): Inferences on crust–mantle interactions and clues for post-collisional volcanism magma sources: Lithos, v. 220, p. 191-199, https://doi.org/10.1016/j.lithos.2015.02.011.

Bierlein, F. P., Groves, D. I., and Cawood, P. A., 2009, Metallogeny of accretionary orogens—the connection between lithospheric processes and metal endowment: Ore Geology Reviews, v. 36, p. 282-292, https://doi.org/10.1016/j.oregeorev.2009.04.002.

Blanks, D. E., Holwell, D. A., Fiorentini, M. L., Moroni, M., Giuliani, A., Tassara, S., González-Jiménez, J. M., Boyce, A. J., and Ferrari, E., 2020, Fluxing of mantle carbon as a physical agent for metallogenic fertilization of the crust: Nature Communications, v. 11, p. 1-11, https://doi.org/10.1038/s41467-020-18157-6.

Bockrath, C., Ballhaus, C., and Holzheid, A., 2004, Fractionation of the platinum-group elements during mantle melting: Science, v. 305, p. 1951-1953, DOI: 10.1126/science.1100160.

Brenan, J. M., and Caciagli, N. C., 2000, Fe–Ni exchange between olivine and sulphide liquid: implications for oxygen barometry in sulphide-saturated magmas: Geochimica et Cosmochimica Acta, v. 64, p. 307-320, https://doi.org/10.1016/S0016-7037(99)00278-1.

Brett, R., and Kullerud, G., 1967, The Fe-Pb-S system: Economic Geology, v. 62, p. 354-369, https://doi.org/10.2113/gsecongeo.62.3.354.

Burness, S., Smart, K. A., Tappe, S., Stevens, G., Woodland, A. B., and Cano, E., 2020, Sulphur-rich mantle metasomatism of Kaapvaal craton eclogites and its role in redox-controlled platinum group element mobility: Chemical Geology, v. 542, 119476, https://doi.org/10.1016/j.chemgeo.2020.119476.

Burrett, C., and Berry, R., 2000, Proterozoic Australia–Western United States (AUSWUS) fit between Laurentia and Australia: Geology, v. 28, p. 103-106, https://doi.org/10.1130/0091-7613(2000)28<103:PAUSAF>2.0.CO;2.

Cabri, L. J., 1973, New data on phase relations in the Cu-Fe-S system: Economic Geology, v. 68, p. 443-454, https://doi.org/10.2113/gsecongeo.68.4.443.

Cambeses, A., Garcia-Casco, A., Scarrow, J. H., Montero, P., Pérez-Valera, L. A., and Bea, F., 2016, Mineralogical evidence for lamproite magma mixing and storage at mantle depths: Socovos fault lamproites, SE Spain: Lithos, v. 266, p. 182-201, https://doi.org/10.1016/j.lithos.2016.10.006.

Campa, M. F., and Coney, P. J., 1983, Tectono-stratigraphic terranes and mineral resource distributions in Mexico: Canadian Journal of Earth Sciences, v. 20, p. 1040-1051, https://doi.org/10.1139/e83-094.

Campbell, I. H., and Naldrett, A. J., 1979, The influence of silicate: sulfide ratios on the geochemistry of magmatic sulfides: Economic Geology, v. 74, p. 1503-1506.

Camprubí, A., 2009, Major metallogenic provinces and epochs of Mexico: SGA News, v. 25, p. 1-20.

Camprubí, A., 2013, Tectonic and metallogenic history of Mexico: in Colpron, M., Bissig, T., Rusk, B. G., Thompson, J. F. H., eds., Tectonics, Metallogeny, and Discover: The North American Cordillera and Similar Accretionary Settings, Society of Economic Geologists, Special Publications, v. 17, p. 201-243.

Camprubí, A., 2017, The metallogenic evolution in Mexico during the Mesozoic, and its bearing in the Cordillera of Western North America: Ore Geology Reviews, v. 81, p. 1193-1214, https://doi.org/10.1016/j.oregeorev.2015.11.007.

Camprubí, A., Ferrari, L., Cosca, M. A., Cardellach, E., and Canals, À., 2003, Ages of epithermal deposits in Mexico: regional significance and links

with the evolution of Tertiary volcanism: Economic Geology, v. 98, p. 1029-1037, https://doi.org/10.2113/gsecongeo.98.5.1029.

Camprubí, A., and Albinson, T., 2007, Epithermal deposits in México—Update of current knowledge, and an empirical reclassification: in Alaniz-Álvarez, S. A., Nieto-Samaniego, A. F., eds., Geology of México: Celebrating the Centenary of the Geological Society of México, v. 422, 377-415.

Capitanio, F. A., Nebel, O., and Cawood, P. A., 2020, Thermochemical lithosphere differentiation and the origin of cratonic mantle: Nature, v. 588, p. 89-94, https://doi.org/10.1038/s41586-020-2976-3.

Carlson, R. W., Pearson, D. G., and James, D. E., 2005, Physical, chemical, and chronological characteristics of continental mantle: Reviews of Geophysics, v. 43, https://doi.org/10.1029/2004RG000156.

Casalini, M., Avanzinelli, R., Tommasini, S., Natali, C., Bianchini, G., Prelević, D., Mattei, M., and Conticelli, S., 2022, Petrogenesis of Mediterranean lamproites and associated rocks: The role of overprinted metasomatic events in the post-collisional lithospheric upper mantle: Geological Society, London, Special Publications, v. 513, p. 271-296.

Cawthorn, R. G., 2010, The platinum group element deposits of the Bushveld Complex in South Africa: Platinum Metals Review, v. 54, p. 205-215, doi:10.1595/147106710X520222.

Centeno-García, E., 2005, Review of upper Paleozoic and lower Mesozoic stratigraphy and depositional environments, central and west Mexico: Constraints on terrane analysis and paleogeography: in Anderson, T. H., Nourse, J. A., McKee, J. W., Steiner, M. B., eds., The Mojave-Sonora Megashear Hypothesis: Development, Assessment, and Alternatives: Geological Society of America Special Paper, v. 393, p. 233-258.

Centeno-García, E., 2017, Mesozoic tectono-magmatic evolution of Mexico: An overview: Ore Geology Reviews, v. 81, p. 1035-1052, https://doi.org/10.1016/j.oregeorev.2016.10.010.

Centeno-García, E., Guerrero-Suastegui, M., and Talavera-Mendoza, O., 2008, The Guerrero composite terrane of western Mexico: Collision and

subsequent rifting in a supra-subduction zone: in Draut, A., Clift, P.D., and Scholl, D.W., eds., Formation and Applications of the Sedimentary Record in Arc Collision Zones: Geological Society of America Special Paper 436, p. 279–308.

Chang, J., and Audétat, A., 2023, Post-subduction porphyry Cu magmas in the Sanjiang region of southwestern China formed by fractionation of lithospheric mantle–derived mafic magmas: Geology, v. 51, p. 64-68, https://doi.org/10.1130/G50502.1.

Chang, L. L., Wu, D., and Knowles, C. R., 1988, Phase relations in the system Ag_2S-Cu_2S-PbS-Bi_2S_3: Economic Geology, v. 83, p. 405-418, https://doi.org/10.2113/gsecongeo.83.2.405.

Chen, K., Tang, M., Lee, C. T. A., Wang, Z., Zou, Z., Hu, Z., and Liu, Y., 2020, Sulfide-bearing cumulates in deep continental arcs: The missing copper reservoir: Earth and Planetary Science Letters, v. 531, 115971, https://doi.org/10.1016/j.epsl.2019.115971.

Chen, L., Tang, L., Wang, W., Li, X., Zhang, J., Li, J., Li, Z., Wang, H., and Zhu, Z., 2022, Highly siderophile element behavior in the subduction zone mantle: Constraints from data on the Yap Trench peridotites: Lithos, v. 432, 106893, https://doi.org/10.1016/j.lithos.2022.106893.

Chistyakova, S., Latypov, R., Hunt, E. J., and Barnes, S., 2019, Merensky-type platinum deposits and a reappraisal of magma chamber paradigms: Scientific Reports, v. 9, p. 1-12, https://doi.org/10.1038/s41598-019-45288-8.

Chong, J., Fiorentini, M. L., Holwell, D. A., Moroni, M., Blanks, D. E., Dering, G. M., Davis, A., and Ferrari, E., 2021, Magmatic cannibalisation of a Permo-Triassic Ni-Cu-PGE-(Au-Te) system during the breakup of Pangea – Implications for craton margin metal and volatile transfer in the lower crust: Lithos, v. 388-389, p. 106079, 10.1016/j.lithos.2021.106079.

Chowdhury, P., and Dasgupta, R., 2019, Effect of sulfate on the basaltic liquidus and sulfur Concentration at Anhydrite Saturation (SCAS) of hydrous basalts–Implications for sulfur cycle in subduction zones: Chemical

Geology, v. 522, p. 162-174, https://doi.org/10.1016/j.chemgeo.2019.05.020.

Chowdhury, P., Dasgupta, R., Phelps, P. R., Lee, C. T. A., and Anselm, R. A., 2021, Partitioning of chalcophile and highly siderophile elements (HSEs) between sulfide and carbonated melts–Implications for HSE systematics of kimberlites, carbonatites, and melt metasomatized mantle domains: Geochimica et Cosmochimica Acta, v. 305, p. 130-147, https://doi.org/10.1016/j.gca.2021.05.006.

Ciobanu, C. L., Cook, N. J., Utsunomiya, S., Pring, A., and Green, L., 2011, Focussed ion beam–transmission electron microscopy applications in ore mineralogy: Bridging micro-and nanoscale observations: Ore Geology Reviews, v. 42, p. 6-31, https://doi.org/10.1016/j.oregeorev.2011.06.012.

Coltorti, M., Beccaluva, L., Bonadiman, C., Salvini, L., and Siena, F., 2000, Glasses in mantle xenoliths as geochemical indicators of metasomatic agents: Earth and Planetary Science Letters, v. 183, p. 303-320, https://doi.org/10.1016/S0012-821X(00)00274-0.

Condie, K. C., 1998, Episodic continental growth and supercontinents: a mantle avalanche connection?: Earth and Planetary Science Letters, v. 163, p. 97-108, https://doi.org/10.1016/S0012-821X(98)00178-2.

Condie, K. C., 2021, Earth as an evolving planetary system. Academic Press.

Connors, K. A., Noble, D. C., Bussey, S. D., and Weiss, S. I., 1993, Initial gold contents of silicic volcanic rocks: Bearing on the behavior of gold in magmatic systems: Geology, v. 21, p. 937-940, https://doi.org/10.1130/0091-7613(1993)021<0937:IGCOSV>2.3.CO;2.

Core, D. P., Kesler, S. E., and Essene, E. J., 2006, Unusually Cu-rich magmas associated with giant porphyry copper deposits: Evidence from Bingham, Utah: Geology, v. 34, p. 41-44, https://doi.org/10.1130/G21813.1.

Costa, S., Fulignati, P., Gioncada, A., Pistolesi, M., Bosch, D., and Bruguier, O., 2021, Tracking metal evolution in arc magmas: Insights from the active volcano of La Fossa, Italy: Lithos, v. 380, p. 105851, https://doi.org/10.1016/j.lithos.2020.105851.

Craig, J. R., and Kullerud, G., 1968, Phase relations and mineral assemblages in the copper-lead-sulfur system: American Mineralogist, v. 53, p. 145-161.

Dallai, L., Bianchini, G., Avanzinelli, R., Natali, C., and Conticelli, S., 2019, Heavy oxygen recycled into the lithospheric mantle: Scientific Reports, v. 9, p. 1-7.

Dávalos-Elizondo, M. G., Aranda-Gómez, J. J., Levresse, G., and Cervantes de la Cruz, K. E., 2016, Química mineral y geoquímica de xenolitos del manto del campo volcánico Santo Domingo, San Luis Potosí: evidencias de procesos metasomáticos del manto bajo porciones de la Mesa Central, México: Revista mexicana de ciencias geológicas, v. 33, p. 81-104.

Delpech, G., Lorand, J. P., Grégoire, M., Cottin, J. Y., and O'Reilly, S. Y., 2012, In-situ geochemistry of sulfides in highly metasomatized mantle xenoliths from Kerguelen, southern Indian Ocean: Lithos, v. 154, p. 296-314, https://doi.org/10.1016/j.lithos.2012.07.018.

Dick, H. J., and Bullen, T., 1984, Chromian spinel as a petrogenetic indicator in abyssal and alpine-type peridotites and spatially associated lavas: Contributions to Mineralogy and Petrology, v. 86, p. 54-76, https://doi.org/10.1007/BF00373711.

Dickinson, W. R., and Lawton, T. F., 2001, Carboniferous to Cretaceous assembly and fragmentation of Mexico: Geological Society of America Bulletin, v. 113, p. 1142-1160, https://doi.org/10.1130/0016-7606(2001)113<1142:CTCAAF>2.0.CO;2.

Dobson, D. P., Crichton, W. A., VOCadlo, L. I. D. U. N. K. A., Jones, A. P., Wang, Y., Uchida, T., Rivers, M., Sutton, S., and Brodholt, J. P., 2000, In situ measurement of viscosity of liquids in the Fe-FeS system at high pressures and temperatures: American Mineralogist, v. 85, p. 1838-1842, https://doi.org/10.2138/am-2000-11-1231.

Donnelly, K. E., Goldstein, S. L., Langmuir, C. H., and Spiegelman, M., 2004, Origin of enriched ocean ridge basalts and implications for mantle dynamics: Earth and Planetary Science Letters, v. 226, p. 347-366.

Doyle, C. D., and Naldrett, A. J., 1987, The oxygen content of "sulfide" magma and its effect on the partitioning of nickel between coexisting olivine and molten ores: Economic Geology, v. 82, p. 208-211.

Draper, D. S., and Green, T. H., 1997, P–T phase relations of silicic, alkaline, aluminous mantle-xenolith glasses under anhydrous and C–O–H fluid-saturated conditions: Journal of Petrology, v. 38, p. 1187-1224, https://doi.org/10.1093/petroj/38.9.1187.

Duggen, S., Hoernle, K., van den Bogaard, P., and Harris, C., 2004, Magmatic evolution of the Alboran region: The role of subduction in forming the western Mediterranean and causing the Messinian Salinity Crisis: Earth and Planetary Science Letters, v. 218, p. 91-108, https://doi.org/10.1016/S0012-821X(03)00632-0.

Duggen, S., Hoernle, K., van den Bogaard, P., and Garbe-Schönberg, D., 2005, Post-collisional transition from subduction-to intraplate-type magmatism in the westernmost Mediterranean: evidence for continental-edge delamination of subcontinental lithosphere: Journal of Petrology, v. 46, p. 1155-1201, https://doi.org/10.1093/petrology/egi013.

Duggen, S., Hoernle, K., Klügel, A., Geldmacher, J., Thirlwall, M., Hauff, F., Lowry, D., and Oates, N., 2008, Geochemical zonation of the Miocene Alborán Basin volcanism (westernmost Mediterranean): geodynamic implications: Contributions to Mineralogy and Petrology, v. 156, p. 577-593, https://doi.org/10.1007/s00410-008-0302-4.

Edmonds, M., Mather, T. A., and Liu, E. J., 2018, A distinct metal fingerprint in arc volcanic emissions: Nature Geoscience, v. 11, p. 790-794, https://doi.org/10.1038/s41561-018-0214-5.

Esteban-Arispe, I., Velasco, F., Boyce, A. J., Morales-Ruano, S., Yusta, I., and Carrillo-Rosúa, J., 2016, Unconventional non-magmatic sulfur source for the Mazarrón Zn–Pb–Cu–Ag–Fe epithermal deposit (SE Spain): Ore Geology Reviews, v. 72, p. 1102-1115, https://doi.org/10.1016/j.oregeorev.2015.10.005.

Evans, K. A., Elburg, M. A., and Kamenetsky, V. S., 2012, Oxidation state of subarc mantle: Geology, v. 40, p. 783-786, https://doi.org/10.1130/G33037.1.

Falloon, T. J., Green, D. H., Danyushevsky, L. V., and McNeill, A. W., 2008, The composition of near-solidus partial melts of fertile peridotite at 1 and 1· 5 GPa: implications for the petrogenesis of MORB: Journal of Petrology, v. 49, p. 591-613, https://doi.org/10.1093/petrology/egn009.

Ferrari, L., Conticelli, S., Vaggelli, G., Petrone, C. M., and Manetti, P., 2000, Late Miocene volcanism and intra-arc tectonics during the early development of the Trans-Mexican Volcanic Belt: Tectonophysics, v. 318, p. 161-185, https://doi.org/10.1016/S0040-1951(99)00310-8.

Ferrari, L., Valencia-Moreno, M., and Bryan, S., 2005, Magmatismo y tectónica en la Sierra Madre Occidental y su relación con la evolución de la margen occidental de Norteamérica: Boletín de la Sociedad Geológica Mexicana, v. 57, p. 343-378, doi: 10.18268/BSGM2005v57n3a5.

Ferrari, L., Valencia-Moreno, M., and Bryan, S., 2007, Magmatism and tectonics of the Sierra Madre Occidental and its relation with the evolution of the western margin of North America: in Alaniz-Álvarez, S. A., Nieto-Samaniego, A. F., eds., Geology of México: Celebrating the Centenary of the Geological Society of México Boulder, Colorado, USA, The Geological Society of America. Geological Society of America Special Paper, v. 422, p. 1-39, https://doi.org/10.1130/2007.2422(01).

Ferrari, L., Orozco-Esquivel, T., Bryan, S. E., Lopez-Martinez, M., and Silva-Fragoso, A., 2018, Cenozoic magmatism and extension in western Mexico: Linking the Sierra Madre Occidental silicic large igneous province and the Comondú Group with the Gulf of California rift: Earth-Science Reviews, v. 183, p. 115-152, https://doi.org/10.1016/j.earscirev.2017.04.006.

Finnigan, C. S., Brenan, J. M., Mungall, J. E., and McDonough, W. F., 2008, Experiments and models bearing on the role of chromite as a collector of platinum group minerals by local reduction: Journal of Petrology, v. 49, p. 1647-1665, https://doi.org/10.1093/petrology/egn041.

Fiorentini, M. L., LaFlamme, C., Denyszyn, S., Mole, D., Maas, R., Locmelis, M., Caruso, S., and Bui, T-H., 2018, Post-collisional alkaline magmatism as gateway for metal and sulfur enrichment of the continental lower crust: Geochimica et Cosmochimica Acta, v. 223, p. 175-197, https://doi.org/10.1016/j.gca.2017.11.009.

Fischer-Gödde, M., Becker, H., and Wombacher, F., 2010, Rhodium, gold and other highly siderophile element abundances in chondritic meteorites: Geochimica et Cosmochimica Acta, v. 74, p. 356-379, https://doi.org/10.1016/j.gca.2009.09.024.

Fischer-Gödde, M., Becker, H., and Wombacher, F., 2011, Rhodium, gold and other highly siderophile elements in orogenic peridotites and peridotite xenoliths: Chemical Geology, v. 280, p. 365-383, https://doi.org/10.1016/j.chemgeo.2010.11.024.

Fitz-Díaz, E., Lawton, T. F., Juárez-Arriaga, E., and Chávez-Cabello, G., 2018, The Cretaceous-Paleogene Mexican orogen: Structure, basin development, magmatism and tectonics: Earth-Science Reviews, v. 183, p. 56-84, https://doi.org/10.1016/j.earscirev.2017.03.002.

Fleet, M. E., and Pan, Y., 1994, Fractional crystallization of anhydrous sulfide liquid in the system Fe-Ni-Cu-S, with application to magmatic sulfide deposits: Geochimica et Cosmochimica Acta, v. 58, p. 3369-3377, https://doi.org/10.1016/0016-7037(94)90092-2.

Fonseca, R. O., Campbell, I. H., O'Neill, H. S. C., and Allen, C. M., 2009, Solubility of Pt in sulphide mattes: Implications for the genesis of PGE-rich horizons in layered intrusions: Geochimica et Cosmochimica Acta, v. 73, p. 5764-5777, https://doi.org/10.1016/j.gca.2009.06.038.

Fonseca, R. O., Mallmann, G., O'Neill, H. S. C., Campbell, I. H., and Laurenz, V., 2011, Solubility of Os and Ir in sulfide melt: Implications for Re/Os fractionation during mantle melting: Earth and Planetary Science Letters, v. 311, p. 339-350, https://doi.org/10.1016/j.epsl.2011.09.035.

Fonseca, R. O., Laurenz, V., Mallmann, G., Luguet, A., Hoehne, N., and Jochum, K. P., 2012, New constraints on the genesis and long-term stability of Os-

rich alloys in the Earth's mantle: Geochimica et Cosmochimica Acta, v. 87, p. 227-242, https://doi.org/10.1016/j.gca.2012.04.002.

Gaetani, G. A., and Grove, T. L., 1998, The influence of water on melting of mantle peridotite: Contributions to Mineralogy and Petrology, v. 131, p. 323-346, https://doi.org/10.1007/s004100050396.

Gehrels, G., and Pecha, M. , 2014, Detrital zircon U-Pb geochronology and Hf isotope geochemistry of Paleozoic and Triassic passive margin strata of western North America: Geosphere, v. 10, p. 49-65, https://doi.org/10.1130/GES00889.1.

Gervilla, F., Proenza, J. A., Frei, R., Gonzalez-Jimenez, J. M., Garrido, C. J., Melgarejo, J. C., Meibom, A., Díaz-Martínez, R., and Lavaut, W., 2005, Distribution of platinum-group elements and Os isotopes in chromite ores from Mayarí-Baracoa Ophiolitic Belt (eastern Cuba): Contributions to Mineralogy and Petrology, v. 150, p. 589-607, https://doi.org/10.1007/s00410-005-0039-2.

Giordano, D., Russell, J. K., and Dingwell, D. B., 2008, Viscosity of magmatic liquids: a model: Earth and Planetary Science Letters, v. 271, p. 123-134, https://doi.org/10.1016/j.epsl.2008.03.038.

Godel, B., Barnes, S. J., and Maier, W. D., 2007, Platinum-group elements in sulphide minerals, platinum-group minerals, and whole-rocks of the Merensky Reef (Bushveld Complex, South Africa): implications for the formation of the reef: Journal of Petrology, v. 48, p. 1569-1604, https://doi.org/10.1093/petrology/egm030.

Gómez-Pugnaire, M. T., Sánchez-Vizcaíno, V. L., Fernández-Soler, J. M., and Acosta-Vigil, A., 2019, Mesozoic and Cenozoic Magmatism in the Betics, in Quesada C., Oliveira J., eds., The Geology of Iberia: A Geodynamic Approach: Springer, Cham, p. 545-566.

Gómez-Tuena, A., Orozco-Esquivel, M.T., and Ferrari, L., 2005, Magmatismo y tectónica en la Sierra Madre Occidental y su relación con la evolución de la margen occidental de Norteamérica: Boletín de la Sociedad Geológica Mexicana, v. 57, p. 343-378, doi: 10.18268/BSGM2005v57n3a5.

Gómez-Tuena, A., Orozco-Esquivel, M.T., and Ferrari, L., 2007, Igneous petrogenesis of the Trans-Mexican Volcanic Belt, in Alaniz-Álvarez, S.A., Nieto-Samaniego, Á.F., eds., Geology of México: Celebrating the centenary of the Geological Society of México: Boulder, Colorado, USA, The Geological Society of America. Geological Society of America Special Paper, 422, 129-182, doi: 10.1130/2007.2422(05).

González-Jiménez, J. M., Villaseca, C., Griffin, W. L., Belousova, E., Konc, Z., Ancochea, E., O'Reilly, S. Y., Pearson, N. J., Garrido, C. J., and Gervilla, F., 2013, The architecture of the European-Mediterranean lithosphere: A synthesis of the Re-Os evidence: Geology, v. 41, p. 547-550, https://doi.org/10.1130/G34003.1.

González-Jiménez, J. M., Villaseca, C., Griffin, W. L., O'Reilly, S. Y., Belousova, E., Ancochea, E., and Pearson, N. J., 2014, Significance of ancient sulfide PGE and Re–Os signatures in the mantle beneath Calatrava, Central Spain: Contributions to Mineralogy and Petrology, v. 168, p. 1047, https://doi.org/10.1007/s00410-014-1047-x.

González-Jiménez, J. M., Camprubí, A., Colás, V., Griffin, W. L., Proenza, J. A., O'Reilly, S. Y., Centeno-García, E., García-Casco, A., Belousova, E., Talavera, C., Farré-de-Pablo, J., and Satsukawa, T., 2017, The recycling of chromitites in ophiolites from southwestern North America: Lithos, v. 294-295, p. 53-72.

González-Jiménez, J. M., Proenza, J. A., Martini, M., Camprubí, A., Griffin, W. L., O'Reilly, S. Y., and Pearson, N. J., 2017, Deposits associated with ultramafic–mafic complexes in Mexico: the Loma Baya case: Ore Geology Reviews, v. 81, p. 1053-1065, https://doi.org/10.1016/j.oregeorev.2015.05.014.

González-Jiménez, J. M., Roqué-Rosell, J., Jiménez-Franco, A., Tassara, S., Nieto, F., Gervilla, F., Baurier, S., Proenza, J. A., Saunders, E., Deditius, A. P., Schilling, M., and Corgne, A., 2019, Magmatic platinum nanoparticles in metasomatic silicate glasses and sulfides from Patagonian mantle xenoliths: Contributions to Mineralogy and Petrology, v. 174, p. 47, https://doi.org/10.1007/s00410-019-1583-5.

González-Jiménez, J. M., Tassara, S., Schettino, E., Roqué-Rosell, J., Farré-de-Pablo, J., Saunders, J. E., Deditius, A. P., Colás, V., Rovira-Medina, J. J., Guadalupe-Dávalos, M., Schilling, M., Jimenez-Franco, A., Marchesi, C., Nieto, F., Proenza, J. A., and Gervilla, F., 2020, Mineralogy of the HSE in the subcontinental lithospheric mantle—an interpretive review: Lithos, v. 372, 105681, https://doi.org/10.1016/j.lithos.2020.105681.

González-Jiménez, J. M., Piña, R., Kerestedjian, T. N., Gervilla, F., Borrajo, I., Farré-de Pablo, J., Proenza, J. A., Tornos, F., Roqué, J., & Nieto, F., 2021, Mechanisms for PdAu enrichment in porphyry-epithermal ores of the Elatsite deposit, Bulgaria: Journal of Geochemical Exploration, v. 220, 106664, https://doi.org/10.1016/j.gexplo.2020.106664.

Greaney, A. T., Rudnick, R. L., Helz, R. T., Gaschnig, R. M., Piccoli, P. M., and Ash, R. D., 2017, The behavior of chalcophile elements during magmatic differentiation as observed in Kilauea Iki lava lake, Hawaii: Geochimica et Cosmochimica Acta, v. 210, p. 71-96, https://doi.org/10.1016/j.gca.2017.04.033.

Grégoire, M., Bell, D., and Le Roex, A., 2002, Trace element geochemistry of phlogopite-rich mafic mantle xenoliths: their classification and their relationship to phlogopite-bearing peridotites and kimberlites revisited: Contributions to Mineralogy and Petrology, v. 142, p. 603-625, https://doi.org/10.1007/s00410-001-0315-8.

Griffin, W. L., Doyle, B. J., Ryan, C. G., Pearson, N. J., Suzanne, Y. O. R., Davies, R., Kivi, K., Van Achterbergh, E., and Natapov, L. M., 1999, Layered mantle lithosphere in the Lac de Gras area, Slave craton: composition, structure and origin: Journal of Petrology, v. 40, p. 705-727, https://doi.org/10.1093/petroj/40.5.705.

Griffin, W. L., Spetsius, Z. V., Pearson, N. J., and O'Reilly, S. Y., 2002, In situ Re-Os analysis of sulfide inclusions in kimberlitic olivine: New constraints on depletion events in the Siberian lithospheric mantle: Geochemistry, Geophysics, Geosystems, v. 3, p. 1-25, https://doi.org/10.1029/2001GC000287.

Griffin, W. L., Graham, S., O'Reilly, S. Y., and Pearson, N. J., 2004, Lithosphere evolution beneath the Kaapvaal Craton: Re–Os systematics of sulfides in mantle-derived peridotites: Chemical Geology, v. 208, p. 89-118, https://doi.org/10.1016/j.chemgeo.2004.04.007.

Griffin, W. L., 2008, GLITTER: data reduction software for laser ablation ICP-MS. Laser Ablation ICP-MS in the Earth Sciences: Current practices and outstanding issues, p. 308-311.

Griffin, W. L., O'Reilly, S. Y., Afonso, J. C., and Begg, G. C., 2009, The composition and evolution of lithospheric mantle: a re-evaluation and its tectonic implications: Journal of Petrology, v. 50, p. 1185-1204, https://doi.org/10.1093/petrology/egn033.

Griffin, W. L., Begg, G. C., Dunn, D., O'Reilly, S. Y., Natapov, L. M., and Karlstrom, K., 2011, Archean lithospheric mantle beneath Arkansas: Continental growth by microcontinent accretion: Geological Society of America Bulletin, v. 123, p. 1763-1775, doi: 10.1130/B30253.1.

Griffin, W. L., Begg, G. C., and O'Reilly, S. Y., 2013, Continental-root control on the genesis of magmatic ore deposits: Nature Geoscience, v. 6, p. 905-910, https://doi.org/10.1038/ngeo1954.

Groves, D. I., Zhang, L., and Santosh, M., 2019, Subduction, mantle metasomatism, and gold: A dynamic and genetic conjunction: Geological Society of America Bulletin, v. 132, p. 1419-1426, https://doi.org/10.1130/B35379.1.

Groves, D. I., Santosh, M., Zhang, L., Deng, J., Yang, L. Q., and Wang, Q. F., 2021, Subduction: The recycling engine room for global metallogeny: Ore Geology Reviews, v. 134, 104130, https://doi.org/10.1016/j.oregeorev.2021.104130.

Groves, D. I., and Santosh, M., 2021, Craton and thick lithosphere margins: The sites of giant mineral deposits and mineral provinces: Gondwana Research, v. 100, p. 195-222, https://doi.org/10.1016/j.gr.2020.06.008.

Groves, D. I., Santosh, M., Müller, D., Zhang, L., Deng, J., Yang, L. Q., and Wang, Q. F., 2022, Mineral systems: Their advantages in terms of

developing holistic genetic models and for target generation in global mineral exploration: Geosystems and Geoenvironment, v. 1, 100001, https://doi.org/10.1016/j.geogeo.2021.09.001.

Hagemann, S. G., Lisitsin, V. A., and Huston, D. L., 2016, Mineral system analysis: Quo vadis: Ore Geology Reviews, v. 76, p. 504-522, https://doi.org/10.1016/j.oregeorev.2015.12.012.

Harvey, J., Dale, C. W., Gannoun, A., and Burton, K. W., 2011, Osmium mass balance in peridotite and the effects of mantle-derived sulphides on basalt petrogenesis: Geochimica et Cosmochimica Acta, v. 75, p. 5574-5596, https://doi.org/10.1016/j.gca.2011.07.001.

Harvey, J., Warren, J. M., and Shirey, S. B., 2016, Mantle sulfides and their role in Re–Os and Pb isotope geochronology: Reviews in Mineralogy and Geochemistry, v. 81, p. 579-649, https://doi.org/10.2138/rmg.2016.81.10.

Hastie, E. C. G., Schindler, M., Kontak, D. J., and Lafrance, B., 2021, Transport and coarsening of gold nanoparticles in an orogenic deposit by dissolution–reprecipitation and Ostwald ripening: Communications Earth & Environment, v. 2, p. 1-9, https://doi.org/10.1038/s43247-021-00126-6.

Hauri, E. H., Wagner, T. P., and Grove, T. L., 1994, Experimental and natural partitioning of Th, U, Pb and other trace elements between garnet, clinopyroxene and basaltic melts: Chemical Geology, v. 117, p. 149-166, https://doi.org/10.1016/0009-2541(94)90126-0.

Hedenquist, J. W., and Lowenstern, J. B., 1994, The role of magmas in the formation of hydrothermal ore deposits: Nature, v. 370, p. 519-527, https://doi.org/10.1038/370519a0.

Heinrich, W., and Besch, T., 1992, Thermal history of the upper mantle beneath a young back-arc extensional zone: ultramafic xenoliths from San Luis Potosi, Central Mexico: Contributions to Mineralogy and Petrology, v. 111, p. 126-142.

Heinrich, C. A., Gunther, D., Audétat, A., Ulrich, T., and Frischknecht, R., 1999, Metal fractionation between magmatic brine and vapor, determined by

microanalysis of fluid inclusions: Geology, v. 27, p. 755-758, https://doi.org/10.1130/0091-7613(1999)027<0755:MFBMBA>2.3.CO;2.

Heinrich, C. A., and Connolly, J. A., 2022, Physical transport of magmatic sulfides promotes copper enrichment in hydrothermal ore fluids: Geology, v. 50, p. 1101-1105, https://doi.org/10.1130/G50138.1.

Helmy, H. M., Ballhaus, C., Berndt, J., Bockrath, C., and Wohlgemuth-Ueberwasser, C., 2007, Formation of Pt, Pd and Ni tellurides: experiments in sulfide–telluride systems: Contributions to Mineralogy and Petrology, v. 153, p. 577-591, https://doi.org/10.1007/s00410-006-0163-7.

Helmy, H. M., Ballhaus, C., Fonseca, R. O., Wirth, R., Nagel, T., and Tredoux, M., 2013, Noble metal nanoclusters and nanoparticles precede mineral formation in magmatic sulphide melts: Nature communications, v. 4, p. 2405, https://doi.org/10.1038/ncomms3405.

Helmy, H. M., and Botcharnikov, R., 2020, Experimental determination of the phase relations of Pt and Pd antimonides and bismuthinides in the Fe-Ni-Cu sulfide systems between 1100 and 700° C: American Mineralogist, v. 105, p. 344-352, https://doi.org/10.2138/am-2020-7154.

Helmy, H. M., and Bragagni, A., 2017, Platinum-group elements fractionation by selective complexing, the Os, Ir, Ru, Rh-arsenide-sulfide systems above 1020° C: Geochimica et Cosmochimica Acta, v. 216, p. 169-183, https://doi.org/10.1016/j.gca.2017.01.040.

Helmy, H. M., Botcharnikov, R., Ballhaus, C., Deutsch-Zemlitskaya, A., Wirth, R., Schreiber, A., Buhre, S., and Häger, T., 2021, Evolution of magmatic sulfide liquids: how and when base metal sulfides crystallize?: Contributions to Mineralogy and Petrology, v. 176, p. 1-15, https://doi.org/10.1007/s00410-021-01868-4.

Hidas, K., Konc, Z., Garrido, C. J., Tommasi, A., Vauchez, A., Padrón-Navarta, J. A., Marchesi, C., Booth-Rea, G., Acosta-Vigil, A., Szabó, C., Varas-Reus, M. I., and Gervilla, F., 2016, Flow in the western Mediterranean shallow mantle: Insights from xenoliths in Pliocene alkali basalts from SE Iberia (eastern Betics, Spain): Tectonics, v. 35, p. 2657-2676, https://doi.org/10.1002/2016TC004165.

Holwell, D. A., and McDonald, I., 2007, Distribution of platinum-group elements in the Platreef at Overysel, northern Bushveld Complex: a combined PGM and LA-ICP-MS study: Contributions to Mineralogy and Petrology, v. 154, p. 171-190, https://doi.org/10.1007/s00410-007-0185-9.

Holwell, D. A., Keays, R. R., McDonald, I., and Williams, M. R., 2015, Extreme enrichment of Se, Te, PGE and Au in Cu sulfide microdroplets: evidence from LA-ICP-MS analysis of sulfides in the Skaergaard Intrusion, east Greenland: Contributions to Mineralogy and Petrology, v. 170, p. 53, https://doi.org/10.1007/s00410-015-1203-y.

Holwell, D. A., Fiorentini, M., McDonald, I., Lu, Y., Giuliani, A., Smith, D. J., Keith, M., and Locmelis, M., 2019, A metasomatized lithospheric mantle control on the metallogenic signature of post-subduction magmatism: Nature Communications, v. 10, p. 1-10, https://doi.org/10.1038/s41467-019-11065-4.

Holwell, D. A., Fiorentini, M. L., Knott, T. R., McDonald, I., Blanks, D. E., Campbell McCuaig, T., and Gorczyk, W., 2022, Mobilisation of deep crustal sulfide melts as a first order control on upper lithospheric metallogeny: Nature Communications, v. 13, p. 1-12, https://doi.org/10.1038/s41467-022-28275-y.

Holzheid, A., 2010, Separation of sulfide melt droplets in sulfur saturated silicate liquids: Chemical Geology, v. 274, p. 127-135, https://doi.org/10.1016/j.chemgeo.2010.03.005.

Hou, Z., Duan, L., Lu, Y., Zheng, Y., Zhu, D., Yang, Z., Wang, B., Pei, Y., Zhao, Z., and McCuaig, T. C., 2015, Lithospheric architecture of the Lhasa terrane and its control on ore deposits in the Himalayan-Tibetan orogen: Economic Geology, v. 110, p. 1541-1575, https://doi.org/10.2113/econgeo.110.6.1541.

Hou, Z., Zhou, Y., Wang, R., Zheng, Y., He, W., Zhao, M., Evans, N. J., and Weinberg, R. F., 2017, Recycling of metal-fertilized lower continental crust: Origin of non-arc Au-rich porphyry deposits at cratonic edges: Geology, v. 45, p. 563-566, https://doi.org/10.1130/G38619.1.

Hronsky, J. M., Groves, D. I., Loucks, R. R., and Begg, G. C., 2012, A unified model for gold mineralisation in accretionary orogens and implications for regional-scale exploration targeting methods: Mineralium Deposita, v. 47, p. 339-358, https://doi.org/10.1007/s00126-012-0402-y.

Huang, M. L., Gao, J. F., Bi, X. W., Xu, L. L., Zhu, J. J., and Wang, D. P., 2020, The role of early sulfide saturation in the formation of the Yulong porphyry Cu-Mo deposit: Evidence from mineralogy of sulfide melt inclusions and platinum-group element geochemistry: Ore Geology Reviews, v. 124, 103644, https://doi.org/10.1016/j.oregeorev.2020.103644.

Hughes, H. S., McDonald, I., Loocke, M., Butler, I. B., Upton, B. G., and Faithfull, J. W., 2017, Paradoxical co-existing base metal sulphides in the mantle: the multi-event record preserved in Loch Roag peridotite xenoliths, North Atlantic Craton: Lithos, v. 276, p. 103-121, https://doi.org/10.1016/j.lithos.2016.09.035.

Iacono-Marziano, G., Le Vaillant, M., Godel, B. M., Barnes, S. J., and Arbaret, L., 2022, The critical role of magma degassing in sulphide melt mobility and metal enrichment: Nature Communications, v. 13, p. 1-10, https://doi.org/10.1038/s41467-022-30107-y.

Ionov, D. A., Hofmann, A. W., and Shimizu, N., 1994, Metasomatism-induced melting in mantle xenoliths from Mongolia: Journal of Petrology, v. 35, p. 753-785, https://doi.org/10.1093/petrology/35.3.753.

Ionov, D. A., Bodinier, J. L., Mukasa, S. B., and Zanetti, A., 2002, Mechanisms and sources of mantle metasomatism: major and trace element compositions of peridotite xenoliths from Spitsbergen in the context of numerical modelling: Journal of Petrology, v. 43, p. 2219-2259, https://doi.org/10.1093/petrology/35.3.753.

Jarosewich, E., Nelen, J. A., and Norberg, J. A., 1980, Reference samples for electron microprobe analysis: Geostandards Newsletter, v. 4, p. 43-47.

Jenner, F. E., O'Neill, H. S. C., Arculus, R. J., and Mavrogenes, J. A., 2010, The magnetite crisis in the evolution of arc-related magmas and the initial

concentration of Au, Ag and Cu: Journal of Petrology, v. 51, p. 2445-2464, https://doi.org/10.1093/petrology/egq063.

Jenner, F. E., 2017, Cumulate causes for the low contents of sulfide-loving elements in the continental crust: Nature Geoscience, v. 10, p. 524-529, https://doi.org/10.1038/ngeo2965.

Jin, Z. M., Green, H. W., and Zhou, Y., 1994, Melt topology in partially molten mantle peridotite during ductile deformation: Nature, v. 372, p. 164-167, https://doi.org/10.1038/372164a0.

Johnson, K. T., Dick, H. J., and Shimizu, N., 1990, Melting in the oceanic upper mantle: an ion microprobe study of diopsides in abyssal peridotites: Journal of Geophysical Research: Solid Earth, v. 95, p. 2661-2678, https://doi.org/10.1029/JB095iB03p02661.

Johto, H., and Taskinen, P., 2013, Phase stabilities and thermodynamic assessment of the system Cu–Pb–S: Minerals Engineering, v. 42, p. 68-75, . https://doi.org/10.1016/j.mineng.2012.11.009.

Jordan, T. H., 1975, The continental tectosphere: Reviews of Geophysics, v. 13, p. 1-12, https://doi.org/10.1029/RG013i003p00001.

Jordan, T. H., 1978, Composition and development of the continental tectosphere: Nature, v. 274, p. 544-548, https://doi.org/10.1038/274544a0.

Jugo, P. J., Wilke, M., and Botcharnikov, R. E., 2010, Sulfur K-edge XANES analysis of natural and synthetic basaltic glasses: Implications for S speciation and S content as function of oxygen fugacity: Geochimica et Cosmochimica Acta, v. 74, p. 5926-5938, https://doi.org/10.1016/j.gca.2010.07.022.

Junge, M., Wirth, R., Oberthür, T., Melcher, F., and Schreiber, A., 2015, Mineralogical siting of platinum-group elements in pentlandite from the Bushveld Complex, South Africa: Mineralium Deposita, v. 50, p. 41-54, https://doi.org/10.1007/s00126-014-0561-0.

Kamenetsky, V. S., Park, J. W., Mungall, J. E., Pushkarev, E. V., Ivanov, A. V., Kamenetsky, M. B., and Yaxley, G. M., 2015, Crystallization of platinum-group minerals from silicate melts: Evidence from Cr-spinel–hosted

inclusions in volcanic rocks: Geology, v. 43, p. 903-906, https://doi.org/10.1130/G37052.1.

Kamenetsky, V. S., and Zelenski, M., 2020, Origin of noble-metal nuggets in sulfide-saturated arc magmas: A case study of olivine-hosted sulfide melt inclusions from the Tolbachik volcano (Kamchatka, Russia): Geology, v. 48, p. 620-624, https://doi.org/10.1130/G47086.1.

Karlstrom, K. E., Harlan, S. S., Williams, M. L., McLelland, J., Geissman, J. W., and Ahall, K. I., 1999, Refining Rodinia: Geologic evidence for the Australia–western US connection in the Proterozoic: GSA Today, v. 9, p. 1-7.

Keays, R. R., Sewell, D. K., and Mitchell, R. H., 1981, Platinum and palladium minerals in upper mantle-derived lherzolites: Nature, v. 294, p. 646-648, https://doi.org/10.1038/294646a0.

Keays, R. R., 1995, The role of komatiitic and picritic magmatism and S-saturation in the formation of ore deposits: Lithos, v. 34, p. 1-18, https://doi.org/10.1016/0024-4937(95)90003-9.

Kepezhinskas, P., Defant, M. J., and Widom, E., 2002, Abundance and distribution of PGE and Au in the island-arc mantle: implications for sub-arc metasomatism: Lithos, v. 60, p. 113-128, https://doi.org/10.1016/S0024-4937(01)00073-1.

Kepezhinskas, P., Berdnikov, N., Kepezhinskas, N., and Konovalova, N., 2022, Metals in Avachinsky peridotite xenoliths with implications for redox heterogeneity and metal enrichment in the Kamchatka mantle wedge: Lithos, v. 412, 106610, https://doi.org/10.1016/j.lithos.2022.106610.

Keppie, J. D., 2004, Terranes of Mexico revisited: A 1.3 billion year odyssey: International Geology Review, v. 46, p. 765-794, https://doi.org/10.2747/0020-6814.46.9.765.

Kerrich, R., Goldfarb, R. J., and Richards, J. P., 2005, Metallogenic provinces in an evolving geodynamic framework, in Jeffrey W. Hedenquist, John F. H. Thompson, Richard J. Goldfarb, Jeremy P. Richards (eds.), One

Hundredth Anniversary Volume, Society of Economic Geologist, https://doi.org/10.5382/AV100.33.

Kirsch, M., Keppie, J. D., Murphy, J. B., and Solari, L. A., 2012, Permian-Carboniferous arc magmatism and basin evolution along the western margin of Pangea: Geochemical and geochronological evidence from the eastern Acatlán Complex, southern Mexico: Geological Society of America Bulletin, v. 124, p. 1607-1628, doi:10.1130/B30649.1.

Kiseeva, E. S., and Wood, B. J., 2013, A simple model for chalcophile element partitioning between sulphide and silicate liquids with geochemical applications: Earth and Planetary Science Letters, v. 383, p. 68-81, https://doi.org/10.1016/j.epsl.2013.09.034.

Kitakaze, A., 2018, Phase relation of some sulfide system-(4) especially Cu–Fe–S system: Memories of the Faculty of Engineering, Yamaguchi University, v. 68, p. 55-76.

Kovács, I., Hidas, K., Hermann, J., Sharygin, V., Szabo, C., and Ntaflos, T., 2007, Fluid induced melting in mantle xenoliths and some implications for the continental lithospheric mantle from the Minusinsk Region (Khakasia, southern Siberia): Geologica Carpathica, v. 58, p. 211.

Kullerud, G., Yund, R. A., Moh, G. H., 1969, Phase relations in the Cu-Fe-S, Cu-Ni-S and Fe-Ni-S system, in Wilson, H. D. B., Ed., Magmatic ore deposits. Economic Geology Publishing Co.: Lancaster, Pennsylvania, p. 323-343.

Lambart, S., Laporte, D., Provost, A., and Schiano, P., 2012, Fate of pyroxenite-derived melts in the peridotitic mantle: thermodynamic and experimental constraints: Journal of Petrology, v. 53, p. 451-476, https://doi.org/10.1093/petrology/egr068.

Larocque, A. C., Stimac, J. A., Keith, J. D., and Huminicki, M. A., 2000, Evidence for open-system behavior in immiscible Fe–S–O liquids in silicate magmas: implications for contributions of metals and sulfur to ore-forming fluids: The Canadian Mineralogist, v. 38, p. 1233-1249, https://doi.org/10.2113/gscanmin.38.5.1233.

Lee, C. T., Yin, Q., Rudnick, R. L., and Jacobsen, S. B., 2001, Preservation of ancient and fertile lithospheric mantle beneath the southwestern United States: Nature, v. 411, p. 69-73, https://doi.org/10.1038/35075048.

Le Roux, V., Bodinier, J. L., Tommasi, A., Alard, O., Dautria, J. M., Vauchez, A., and Riches, A. J. V., 2007, The Lherz spinel lherzolite: refertilized rather than pristine mantle: Earth and Planetary Science Letters, v. 259, p. 599-612, https://doi.org/10.1016/j.epsl.2007.05.026.

Levresse, G., Cervantes-de la Cruz, K. E., Aranda-Gómez, J. J., Dávalos-Elizondo, M. G., Jimenez-Sandoval, S., Rodriguez-Melgarejo, F., and Alba-Aldave, L. A. 2016, CO2 fluid inclusion barometry in mantle xenoliths from central Mexico: A detailed record of magma ascent: Journal of Volcanology and Geothermal Research, v. 310, p. 72-88, https://doi.org/10.1016/j.chemgeo.2021.120270.

Li, Y., and Audétat, A., 2012, Partitioning of V, Mn, Co, Ni, Cu, Zn, As, Mo, Ag, Sn, Sb, W, Au, Pb, and Bi between sulfide phases and hydrous basanite melt at upper mantle conditions: Earth and Planetary Science Letters, v. 355, p. 327-340, https://doi.org/10.1016/j.epsl.2012.08.008.

Li, Y., and Audétat, A., 2013, Gold solubility and partitioning between sulfide liquid, monosulfide solid solution and hydrous mantle melts: Implications for the formation of Au-rich magmas and crust–mantle differentiation: Geochimica et Cosmochimica Acta, v. 118, p. 247-262, https://doi.org/10.1016/j.gca.2013.05.014.

Li, Y., Feng, L., Kiseeva, E. S., Gao, Z., Guo, H., Du, Z., Wang, F., and Shi, L., 2019, An essential role for sulfur in sulfide-silicate melt partitioning of gold and magmatic gold transport at subduction settings: Earth and Planetary Science Letters, v. 528, p. 115850, https://doi.org/10.1016/j.epsl.2019.115850.

Li, Y., Audétat, A., Liu, Z., and Wang, F., 2021, Chalcophile element partitioning between Cu-rich sulfide phases and silicate melt and implications for the formation of Earth's continental crust: Geochimica et Cosmochimica Acta, v. 302, p. 61-82, https://doi.org/10.1016/j.gca.2021.03.020.

Liang, Y., and Elthon, D., 1990, Geochemistry and petrology of spinel lherzolite xenoliths from Xalapasco de La Joya, San Luis Potosi, Mexico: partial melting and mantle metasomatism: Journal of Geophysical Research: Solid Earth, v. 95, p. 15859-15877.

Lonergan, L., and White, N., 1997, Origin of the Betic-Rif mountain belt: Tectonics, v. 16, p. 504-522, https://doi.org/10.1029/96TC03937.

Lorand, J. P., and Alard, O., 2001, Platinum-group element abundances in the upper mantle: new constraints from in situ and whole-rock analyses of Massif Central xenoliths (France): Geochimica et Cosmochimica Acta, v. 65, p. 2789-2806, https://doi.org/10.1016/S0016-7037(01)00627-5.

Lorand, J. P., Delpech, G., Grégoire, M., Moine, B., O'Reilly, S. Y., and Cottin, J. Y., 2004, Platinum-group elements and the multistage metasomatic history of Kerguelen lithospheric mantle (South Indian Ocean): Chemical Geology, v. 208, p. 195-215, https://doi.org/10.1016/j.chemgeo.2004.04.012.

Lorand, J. P., and Gregoire, M., 2006, Petrogenesis of base metal sulphide assemblages of some peridotites from the Kaapvaal craton (South Africa): Contributions to Mineralogy and Petrology, v. 151, p. 521-538, https://doi.org/10.1007/s00410-006-0074-7.

Lorand, J. P., Luguet, A., Alard, O., Bezos, A., and Meisel, T., 2008, Abundance and distribution of platinum-group elements in orogenic lherzolites; a case study in a Fontete Rouge lherzolite (French Pyrénées): Chemical Geology, v. 248, p. 174-194, https://doi.org/10.1016/j.chemgeo.2007.06.030.

Lorand, J. P., Alard, O., and Luguet, A., 2010, Platinum-group element micronuggets and refertilization process in Lherz orogenic peridotite (northeastern Pyrenees, France): Earth and Planetary Science Letters, v. 289, p. 298-310, https://doi.org/10.1016/j.epsl.2009.11.017.

Lorand, J. P., Luguet, A., and Alard, O., 2013, Platinum-group element systematics and petrogenetic processing of the continental upper mantle: A review: Lithos, v. 164, p. 2-21, https://doi.org/10.1016/j.lithos.2012.08.017.

Lorand, J. P., and Luguet, A., 2016, Chalcophile and siderophile elements in mantle rocks: Trace elements controlled by trace minerals: Reviews in Mineralogy and Geochemistry, v. 81, p. 441-488, https://doi.org/10.2138/rmg.2016.81.08.

Loucks, R. R., and Mavrogenes, J. A., 1999, Gold solubility in supercritical hydrothermal brines measured in synthetic fluid inclusions: Science, v. 284, p. 2159-2163, DOI: 10.1126/science.284.5423.2159.

Loucks, R. R., 2014, Distinctive composition of copper-ore-forming arcmagmas: Australian Journal of Earth Sciences, v. 61, p. 5-16, https://doi.org/10.1080/08120099.2013.865676..

Luguet, A., Alard, O., Lorand, J. P., Pearson, N. J., Ryan, C., and O'Reilly, S. Y., 2001, Laser-ablation microprobe (LAM)-ICPMS unravels the highly siderophile element geochemistry of the oceanic mantle: Earth and Planetary Science Letters, v. 189, p. 285-294, https://doi.org/10.1016/S0012-821X(01)00357-0.

Luguet, A., Lorand, J. P., and Seyler, M., 2003, Sulfide petrology and highly siderophile element geochemistry of abyssal peridotites: A coupled study of samples from the Kane Fracture Zone (45 W 23 20N, MARK area, Atlantic Ocean): Geochimica et Cosmochimica Acta, v. 67, p. 1553-1570, https://doi.org/10.1016/S0016-7037(02)01133-X.

Luguet, A., Shirey, S. B., Lorand, J. P., Horan, M. F., and Carlson, R. W., 2007, Residual platinum-group minerals from highly depleted harzburgites of the Lherz massif (France) and their role in HSE fractionation of the mantle: Geochimica et Cosmochimica Acta, v. 71, p. 3082-3097, https://doi.org/10.1016/j.gca.2007.04.011.

Luguet, A., and Reisberg, L., 2016, Highly siderophile element and 187Os signatures in non-cratonic basalt-hosted peridotite xenoliths: Unravelling the origin and evolution of the post-Archean lithospheric mantle: Reviews in Mineralogy and Geochemistry, v. 81, p. 305-367, https://doi.org/10.2138/rmg.2016.81.06.

Luguet, A., and Pearson, G., 2019, Dating mantle peridotites using Re-Os isotopes: The complex message from whole rocks, base metal sulfides, and

platinum group minerals: American Mineralogist, v. 104, p. 165-189, https://doi.org/10.2138/am-2019-6557.

Luhr, J. F., and Aranda-Gómez, J. J., 1997, Mexican peridotite xenoliths and tectonic terranes: correlations among vent location, texture, temperature, pressure, and oxygen fugacity: Journal of Petrology, v. 38, p. 1075-1112, https://doi.org/10.1093/petroj/38.8.1075.

Luhr, J. F., Henry, C. D., Housh, T. B., Aranda-Gómez, J. J., and McIntosh, W. C., 2001, Early extension and associated mafic alkalic volcanism from the southern Basin and Range Province: Geology and petrology of the Rodeo and Nazas volcanic fields, Durango, México: Geological Society of America Bulletin, v. 113, p. 760-773, https://doi.org/10.1130/0016-7606(2001)113<0760:EEAAMA>2.0.CO;2.

McLeish, D. F., Williams-Jones, A. E., Vasyukova, O. V., Clark, J. R., and Board, W. S., 2021, Colloidal transport and flocculation are the cause of the hyperenrichment of gold in nature: Proceedings of the National Academy of Sciences, v. 118, e2100689118, https://doi.org/10.1073/pnas.2100689118.

Mancilla, F. de Lis, Booth-Rea, G., Stich, D., Pérez-Peña, J. V., Morales, J., Azañón, J. M., Martín, R., and Giaconia, F., 2015, Slab rupture and delamination under the Betics and Rif constrained from receiver functions: Tectonophysics, v. 663, p. 225-237, https://doi.org/10.1016/j.tecto.2015.06.028.

Mancilla, F. de Lis, Heit, B., Morales, J., Yuan, X., Stich, D., Molina-Aguilera, A., Azañon, J. M., and Martín, R., 2018, A STEP fault in Central Betics, associated with lateral lithospheric tearing at the northern edge of the Gibraltar arc subduction system: Earth and Planetary Science Letters, v. 486, p. 32-40, https://doi.org/10.1016/j.epsl.2018.01.008.

Mansur, E. T., Barnes, S. J., and Duran, C. J., 2019, Textural and compositional evidence for the formation of pentlandite via peritectic reaction: Implications for the distribution of highly siderophile elements: Geology, v. 47, p. 351-354, https://doi.org/10.1130/G45779.1.

Marchesi, C., Dale, C. W., Garrido, C. J., Pearson, D. G., Bosch, D., Bodinier, J. L., Gervilla, F., and Hidas, K., 2014, Fractionation of highly siderophile elements in refertilized mantle: Implications for the Os isotope composition of basalts: Earth and Planetary Science Letters, v. 400, p. 33-44, https://doi.org/10.1016/j.epsl.2014.05.025.

Marchesi, C., Konc, Z., Garrido, C. J., Bosch, D., Hidas, K., Varas-Reus, M. I., and Acosta-Vigil, A., 2017, Multi-stage evolution of the lithospheric mantle beneath the westernmost Mediterranean: Geochemical constraints from peridotite xenoliths in the eastern Betic Cordillera (SE Spain): Lithos, v. 276, p. 75-89, https://doi.org/10.1016/j.lithos.2016.12.011.

Mathur, R., Ruiz, J., and Munizaga, F., 2000, Relationship between copper tonnage of Chilean base-metal porphyry deposits and Os isotope ratios: Geology, v. 28, p. 555-558, https://doi.org/10.1130/0091-7613(2000)28<555:RBCTOC>2.0.CO;2.

Mavrogenes, J. A., and O'Neill, H. S. C., 1999, The relative effects of pressure, temperature and oxygen fugacity on the solubility of sulfide in mafic magmas: Geochimica et Cosmochimica Acta, v. 63, p. 1173-1180, https://doi.org/10.1016/S0016-7037(98)00289-0.

McCoy-West, A. J., Bennett, V. C., Puchtel, I. S., and Walker, R. J., 2013, Extreme persistence of cratonic lithosphere in the southwest Pacific: Paleoproterozoic Os isotopic signatures in Zealandia: Geology, v. 41, p. 231-234, https://doi.org/10.1130/G33626.1.

McCuaig, T. C., Beresford, S., and Hronsky, J., 2010, Translating the mineral systems approach into an effective exploration targeting system: Ore Geology Reviews, v. 38, p. 128-138, https://doi.org/10.1016/j.oregeorev.2010.05.008.

McCuaig, T. C., and Hronsky, J. M., 2014, The mineral system concept: the key to exploration targeting: in Kelley, K. D., Golden, H. C., eds., Special Publications of the Society of Economic Geologists, v. 18, p. 153-175, https://doi.org/10.5382/SP.18.08.

McDonough, W. F., and Sun, S. S., 1995, The composition of the Earth: Chemical Geology, v. 120, p. 223-253, https://doi.org/10.1016/0009-2541(94)00140-4.

McInnes, B. I., McBride, J. S., Evans, N. J., Lambert, D. D., and Andrew, A. S., 1999, Osmium isotope constraints on ore metal recycling in subduction zones: Science, v. 286, p. 512-516, DOI: 10.1126/science.286.5439.512.

McKenzie, D. P., 1969, Speculations on the consequences and causes of plate motions: Geophysical Journal International, v. 18, p. 1-32, https://doi.org/10.1111/j.1365-246X.1969.tb00259.x.

McKenzie, D. A. N., and O'Nions, R. K., 1991, Partial melt distributions from inversion of rare earth element concentrations: Journal of Petrology, v. 32, p. 1021-1091, https://doi.org/10.1093/petrology/32.5.1021.

McKenzie, D., Jackson, J., and Priestley, K., 2005, Thermal structure of oceanic and continental lithosphere: Earth and Planetary Science Letters, v. 233, p. 337-349, https://doi.org/10.1016/j.epsl.2005.02.005.

Mercier, J. C. C., and Nicolas, A., 1975, Textures and Fabrics of Upper-Mantle Peridotites as Illustrated by Xenoliths from Basalts: Journal of Petrrology, v. 16, no. 2, p. 454-487.

Milot, J., Blichert-Toft, J., Sanz, M. A., Malod-Dognin, C., Télouk, P., and Albarède, F., 2022, Silver isotope and volatile trace element systematics in galena samples from the Iberian Peninsula and the quest for silver sources of Roman coinage: Geology, v. 50, p. 422-426, https://doi.org/10.1130/G49690.1.

Misra, K., 2012, Understanding mineral deposits: Springer Science & Business Media.

Mitchell, R. H., and Keays, R. R., 1981, Abundance and distribution of gold, palladium and iridium in some spinel and garnet lherzolites: implications for the nature and origin of precious metal-rich intergranular components in the upper mantle: Geochimica et Cosmochimica Acta, v. 45, p. 2425-2442, https://doi.org/10.1016/0016-7037(81)90096-X.

Mole, D. R., Fiorentini, M. L., Cassidy, K. F., Kirkland, C. L., Thebaud, N., McCuaig, T. C., Doublier, M. P., Duuring, P., Romano, S. S., Maas, R., Belousova, E. A., Barnes, S. J., and Miller, J., 2015, Crustal evolution, intra-cratonic architecture and the metallogeny of an Archaean craton: Geological Society, London, Special Publications, v. 393, p. 23-80, https://doi.org/10.1144/SP393.8.

Morales-Ruano, S. M., Rosúa, F. J. C., Hach-Alí, P. F., De La Fuente Chacón, F., and López, E. C., 2000, Epithermal Cu–Au mineralization in the Palai–Islica deposit, Almeria, Southeastern Spain: fluid-inclusion evidence for mixing of fluids as a guide to gold mineralization: The Canadian Mineralogist, v. 38, p. 553-565, https://doi.org/10.2113/gscanmin.38.3.553.

Mungall, J. E., 2002, Roasting the mantle: Slab melting and the genesis of major Au and Au-rich Cu deposits: Geology, v. 30, p. 915-918, https://doi.org/10.1130/0091-7613(2002)030<0915:RTMSMA>2.0.CO;2.

Mungall, J. E., 2003, Magmatic Ore Deposits: Treatise on Geochemistry, v. 3, p. 759-792.

Mungall, J. E., and Brenan, J. M., 2014, Partitioning of platinum-group elements and Au between sulfide liquid and basalt and the origins of mantle-crust fractionation of the chalcophile elements: Geochimica et Cosmochimica Acta, v. 125, p. 265-289, https://doi.org/10.1016/j.gca.2013.10.002.

Mungall, J. E., Brenan, J. M., Godel, B., Barnes, S. J., and Gaillard, F., 2015, Transport of metals and sulphur in magmas by flotation of sulphide melt on vapour bubbles: Nature Geoscience, v. 8, p. 216-219, https://doi.org/10.1038/ngeo2373.

Naldrett, A. J., 1969, A portion of the system Fe–S–O between 900 and 1080 C and its application to sulfide ore magmas: Journal of Petrology, v. 10, p. 171-201, https://doi.org/10.1093/petrology/10.2.171.

Naldrett, A. J., Wilson, A., Kinnaird, J., and Chunnett, G., 2009, PGE tenor and metal ratios within and below the Merensky Reef, Bushveld Complex: implications for its genesis: Journal of Petrology, v. 50, p. 625-659, https://doi.org/10.1093/petrology/egp015.

Nance, R. D., Fernández-Suárez, J., Keppie, J. D., Storey, C., and Jeffries, T. E., ,2007, Provenance of the Granjeno Schist, Ciudad Victoria, México: Detrital zircon U-Pb age constraints and implications for the Paleozoic paleogeography of the Rheic Ocean: in Linnemann, U., Nance, R. D., Kraft, P., Zulauf, G., eds., The Evolution of the Rheic Ocean: From Avalonian-Cadomian Active Margin to Alleghenian-Variscan Collision: Special Papers of the Geological Society of America, v. 423, p. 453-464.

Nance, R. D., Keppie, J. D., Miller, B. V., Murphy, J. B., and Dostal, J., 2009, Palaeozoic palaeogeography of Mexico: constraints from detrital zircon age data: Geological Society of London Special Publications, v. 327, p. 239-269.

Navon, O., and Stolper, E., 1987, Geochemical consequences of melt percolation: the upper mantle as a chromatographic column: The Journal of Geology, v. 95, p. 285-307.

Neumann, E. R., and Wulff-Pedersen, E., 1997, The origin of highly silicic glass in mantle xenoliths from the Canary Islands: Journal of Petrology, v. 38, p. 1513-1539, https://doi.org/10.1093/petroj/38.11.1513.

Nieto-Samaniego, Á. F., Ferrari, L., Alaniz-Álvarez, S. A., Labarthe-Hernández, G. L., and Rosas-Elguera, J., 1999, Variation of Cenozoic extension and volcanism across the southern Sierra Madre Occidental volcanic province, Mexico: Geological Society of America Bulletin, v. 111, p. 347-363.

Nieto-Samaniego, Á. F., Alaniz-Álvarez, S. A., and Camprubí , A., 2005, La Mesa Central de México: estratigrafía, estructura y evolución tectónica cenozoica: Boletín de la Sociedad Geológica Mexicana, v. 57, p. 285-318, doi: 10.18268/BSGM2005v57n3a3.

Nieto-Samaniego, Á. F., Alaniz-Álvarez, S. A., and Camprubí , A., 2007, Mesa Central of México: Stratigraphy, structure, and Cenozoic tectonic evolution: in Alaniz-Álvarez, S. A., Nieto-Samaniego, Á. F., eds., Geology of México: Celebrating the Centenary of the Geological Society of México: Boulder, Colorado, USA, The Geological Society of America. Geological Society of America Special Paper, v. 442, p. 41-70, doi: 10.1130/2007.2422(02).

Niu, Y., 1997, Mantle melting and melt extraction processes beneath ocean ridges: evidence from abyssal peridotites: Journal of Petrology, v. 38, p. 1047-1074.

Norman, M. D., Pearson, N. J., Sharma, A., and Griffin, W. L., 1996, Quantitative analysis of trace elements in geological materials by laser ablation ICPMS: instrumental operating conditions and calibration values of NIST glasses: Geostandards Newsletter, v. 20, p. 247-261.

O'Driscoll, B., and González-Jiménez, J. M., 2016, Petrogenesis of the platinum-group minerals: Reviews in Mineralogy and Geochemistry, v. 81, p. 489-578, https://doi.org/10.2138/rmg.2016.81.09.

O'Driscoll, B., and VanTongeren, J. A., 2017, Layered intrusions: from petrological paradigms to precious metal repositories: Elements, v. 13, p. 383-389, https://doi.org/10.2138/gselements.13.6.383.

Ortega-Gutiérrez, F., Ruiz, J., and Centeno-García, E., 1995, Oaxaquia, a Proterozoic microcontinent accreted to North America during the late Paleozoic: Geology, v. 23, p. 1127–1130.

Ortega-Gutiérrez, F., Elías-Herrera, M., Morán-Zenteno, D. J., Solari, L., Weber, B., and Luna-González, L., 2018, The pre-Mesozoic metamorphic basement of Mexico, 1.5 billion years of crustal evolution: Earth-Science Reviews, v. 183, p. 2-37, https://doi.org/10.1016/j.earscirev.2018.03.006.

Pan, S., Zheng, J., Yin, Z., Griffin, W. L., Xia, M., Lin, A., and Zhang, H., 2018, Spongy texture in mantle clinopyroxene recordsdecompression-induced melting. Lithos, 320, 144-154, https://doi.org/10.1016/j.lithos.2018.08.035.

Park, J. W., Campbell, I. H., Malaviarachchi, S. P., Cocker, H., Hao, H., and Kay, S. M., 2019, Chalcophile element fertility and the formation of porphyry Cu±Au deposits: Mineralium Deposita, v. 54, p. 657-670, https://doi.org/10.1007/s00126-018-0834-0.

Paton, C., Hellstrom, J., Paul, B., Woodhead, J., and Hergt, J., 2011, Iolite: Freeware for the visualisation and processing of mass spectrometric data: Journal of Analytical Atomic Spectrometry, v. 26, p. 2508-2518.

Patten, C., Barnes, S. J., and Mathez, E. A., 2012, Textural variations in MORB sulfide droplets due to differences in crystallization history: The Canadian Mineralogist, v. 50, p. 675-692, https://doi.org/10.3749/canmin.50.3.675.

Patten, C., Barnes, S. J., Mathez, E. A., and Jenner, F. E., 2013, Partition coefficients of chalcophile elements between sulfide and silicate melts and the early crystallization history of sulfide liquid: LA-ICP-MS analysis of MORB sulfide droplets: Chemical Geology, v. 358, p. 170-188, https://doi.org/10.1016/j.chemgeo.2013.08.040.

Pearson, N. J., Alard, O., Griffin, W. L., Jackson, S. E., and O'Reilly, S. Y, 2002, In situ measurement of Re-Os isotopes in mantle sulfides by laser ablation multicollector-inductively coupled plasma mass spectrometry: Analytical methods and preliminary results: Geochimica et Cosmochimica Acta, v. 66, p. 1037-1050, https://doi.org/10.1016/S0016-7037(01)00823-7.

Pearson, D. G., Canil, D., and Shirey, S. B., 2003, Mantle samples included in volcanic rocks: xenoliths and diamonds: Treatise on geochemistry, 2, 568.

Pearson, D. G., Parman, S. W., and Nowell, G. M., 2007, A link between large mantle melting events and continent growth seen in osmium isotopes: Nature, v. 449, p. 202-205, https://doi.org/10.1038/nature06122.

Pearson, D.G., and Wittig, N., 2014, The formation and evolution of cratonic mantle lithosphere—Evidence from mantle xenoliths, in Holland, H.D., and Turekian, K.K., eds., The Mantle and the Core (2nd ed.): Treatise on Geochemistry, v 3, p. 255–292, https://doi .org /10 .1016 /B978-0-08-095975-7 .00205-9.

Pearson, D. G., Scott, J. M., Liu, J., Schaeffer, A., Wang, L. H., van Hunen, J., Szilas, K., Chacko, T., and Kelemen, P. B., 2021, Deep continental roots and cratons: Nature, v. 596, p. 199-210, https://doi.org/10.1038/s41586-021-03600-5.

Peredo, C. R., Yutsis, V., Martin, A. J., and Aranda-Gómez, J. J., 2021, Crustal structure and Curie point depth in central Mexico inferred from the spectral analysis and forward modeling of potential fiel data: Journal of South American Earth Sciences, v. 112, no. 103565, p. 1-28.

Peregoedova, A., and Ohnenstetter, M., 2002, Collectors of Pt, Pd and Rh in a S-poor Fe–Ni–Cu sulfide system at 760 C: experimental data and application to ore deposits: The Canadian Mineralogist, v. 40, p. 527-561, https://doi.org/10.2113/gscanmin.40.2.527.

Peregoedova, A., Barnes, S. J., and Baker, D. R., 2004, The formation of Pt–Ir alloys and Cu–Pd-rich sulfide melts by partial desulfurization of Fe–Ni–Cu sulfides: results of experiments and implications for natural systems: Chemical Geology, v. 208, p. 247-264, https://doi.org/10.1016/j.chemgeo.2004.04.015.

Pérez-Valera, L. A., Rosenbaum, G., Sánchez-Gómez, M., Azor, A., Fernández-Soler, J. M., Pérez-Valera, F., and Vasconcelos, P. M., 2013, Age distribution of lamproites along the Socovos Fault (southern Spain) and lithospheric scale tearing: Lithos, v. 180, p. 252-263, https://doi.org/10.1016/j.lithos.2013.08.016.

Petrella, L., Thébaud, N., Fougerouse, D., Evans, K., Quadir, Z., and Laflamme, C., 2020, Colloidal gold transport: A key to high-grade gold mineralization?: Mineralium Deposita, v. 55, p. 1247-1254, https://doi.org/10.1007/s00126-020-00965-x.

Petrella, L., Thébaud, N., Fougerouse, D., Tattitch, B., Martin, L., Turner, S., Suvorova, A., and Gain, S., 2022, Nanoparticle suspensions from carbon-rich fluid make high-grade gold deposits: Nature Communications, v. 13, p. 1-9, https://doi.org/10.1038/s41467-022-31447-5.

Pettke, T., Oberli, F., and Heinrich, C. A., 2010, The magma and metal source of giant porphyry-type ore deposits, based on lead isotope microanalysis of individual fluid inclusions: Earth and Planetary Science Letters, v. 296, p. 267-277, https://doi.org/10.1016/j.epsl.2010.05.007.

Pier, J. G., Luhr, J. F., Podosek, F. A., and Aranda-Gómez, J. J., 1992, The La Breña-El Jaguey maar complex, Durango, Mexico: II. Petrology and geochemistry: Bull. Volcanol., v. 54, p. 405-428.

Piña, R., Gervilla, F., Barnes, S. J., Ortega, L., and Lunar, R., 2012, Distribution of platinum-group and chalcophile elements in the Aguablanca Ni–Cu

sulfide deposit (SW Spain): evidence from a LA-ICP-MS study: Chemical Geology, v. 302, p. 61-75, https://doi.org/10.1016/j.chemgeo.2011.02.010.

Platt, J. P., Behr, W. M., Johanesen, K., and Williams, J. R., 2013, The Betic-Rif arc and its orogenic hinterland: a review: Annual Review of Earth and Planetary Sciences, v. 41, p. 313-357, https://doi.org/10.1146/annurev-earth-050212-123951.

Prichard, H. M., Barnes, S. J., Maier, W. D., and Fisher, P. C., 2004, Variations in the nature of the platinum-group minerals in a cross-section through the Merensky Reef at Impala Platinum: Implications for the mode of formation of the reef: The Canadian Mineralogist, v. 42, p. 423-437, https://doi.org/10.2113/gscanmin.42.2.423.

Rabayrol, F., and Hart, C. J., 2020, Petrogenetic and tectonic controls on magma fertility and the formation of post-subduction porphyry and epithermal mineralization along the late Cenozoic Anatolian Metallogenic Trend, Turkey: Mineralium Deposita, p. 1-28, https://doi.org/10.1007/s00126-020-00967-9.

Rabayrol, F., and Hart, C. J. R., 2021, Petrogenetic and tectonic controls on magma fertility and the formation of post-subduction porphyry and epithermal mineralization along the late Cenozoic Anatolian Metallogenic Trend, Turkey: Mineralium Deposita, v. 56, p. 279-306, https://doi.org/10.1007/s00126-020-00967-9.

Raffone, N., Chazot, G., Pin, C., Vannucci, R., and Zanetti, A., 2009, Metasomatism in the lithospheric mantle beneath Middle Atlas (Morocco) and the origin of Fe-and Mg-rich wehrlites: Journal of Petrology, v. 50, p. 197-249, https://doi.org/10.1093/petrology/egn069.

Rämö, O. T., and Calzia, J. P., 1998, Nd isotopic composition of cratonic rocks in the southern Death Valley region: Evidence for a substantial Archean source component in Mojavia: Geology, v. 26, p. 891-894.

Rampone, E., Piccardo, G. B., Vannucci, R., and Bottazzi, P., 1997, Chemistry and origin of trapped melts in ophioiitic peridotites: Geochimica et Cosmochimica Acta, v. 61, p. 4557-4569, https://doi.org/10.1016/S0016-7037(97)00260-3.

Rampone, E., Vissers, R. L. M., Poggio, M., Scambelluri, M., and Zanetti, A., 2010, Melt migration and intrusion during exhumation of the Alboran lithosphere: the Tallante mantle xenolith record (Betic Cordillera, SE Spain): Journal of Petrology, v. 51, p. 295-325, https://doi.org/10.1093/petrology/egp061.

Rao, N. C., Kamde, G. D., Kale, H. S., and Dongre, A., 2008, Geological setting and petrographic diversity of the lamproite dykes at the Northern and North eastern margin of the Cuddapah basin, southern India, in Indian Dykes: Geochemistry, Geophysics and Geochronology (pp. 281-290). Narosa Publishing House Pvt. Ltd. New Delhi.

Rehkämper, M., Halliday, A. N., Alt, J., Fitton, J. G., Zipfel, J., and Takazawa, E., 1999, Non-chondritic platinum-group element ratios in oceanic mantle lithosphere: petrogenetic signature of melt percolation?: Earth and Planetary Science Letters, v. 172, p. 65-81, https://doi.org/10.1016/S0012-821X(99)00193-4.

Richards, J. P., 2009, Postsubduction porphyry Cu-Au and epithermal Au deposits: Products of remelting of subduction-modified lithosphere: Geology, v. 37, p. 247-250, https://doi.org/10.1130/G25451A.1.

Richards, J. P., 2013, Giant ore deposits formed by optimal alignments and combinations of geological processes: Nature Geoscience, v. 6, p. 911-916, https://doi.org/10.1038/ngeo1920.

Richardson, S. H., and Shirey, S. B., 2008, Continental mantle signature of Bushveld magmas and coeval diamonds: Nature, v. 453, p. 910-913, https://doi.org/10.1038/nature07073.

Ringwood, A. E., 1962, A model for the upper mantle. Journal of Geophysical Research, v. 67, p. 857-867, https://doi.org/10.1029/JZ067i002p00857.

Ripley, E. M., and Li, C., 2013, Sulfide saturation in mafic magmas: Is external sulfur required for magmatic Ni-Cu-(PGE) ore genesis?: Economic Geology, v. 108, p. 45-58, https://doi.org/10.2113/econgeo.108.1.45.

Rudnick, R. L., and Lee, C. T., 2002, Osmium isotope constraints on tectonic evolution of the lithosphere in the southwestern United States: International Geology Review, v. 44, p. 501-511, https://doi.org/10.2747/0020-6814.44.6.501.

Rudnick, R. L., and Walker, R. J., 2009, Interpreting ages from Re–Os isotopes in peridotites: Lithos, v. 112, p. 1083-1095, https://doi.org/10.1016/j.lithos.2009.04.042.

Ruiz, J., Patchett, P. J., and Ortega-Gutiérrez, F., 1988, Proterozoic and Phanerozoic basement terranes of Mexico from Nd isotopic studies: Geological Society of America Bulletin, v. 100, p. 274-281.

Sambridge, M., and Lambert, D. D., 1997, Propagating errors in decay equations: Examples from the Re-Os isotopic system: Geochimica et Cosmochimica Acta, v. 61, p. 3019-3024.

Sänger-von Oepen, P., Friedrich, G., and Vogt, J. H., 1989, Fluid evolution, wallrock alteration, and ore mineralization associated with the Rodalquilar epithermal gold-deposit in southeast Spain: Mineralium Deposita, v. 24, p. 235-243, https://doi.org/10.1007/BF00206385.

Saunders, J. E., Pearson, N. J., O'Reilly, S. Y., and Griffin, W. L., 2015, Sulfide metasomatism and the mobility of gold in the lithospheric mantle: Chemical Geology, v. 410, p. 149-161, https://doi.org/10.1016/j.chemgeo.2015.06.016.

Saunders, J. E., Pearson, N. J., O'Reilly, S. Y., and Griffin, W. L., 2016, Gold in the mantle: the role of pyroxenites: Lithos, v. 244, p. 205-217, https://doi.org/10.1016/j.lithos.2015.12.008.

Saunders, J. E., Pearson, N. J., O'Reilly, S. Y., and Griffin, W. L., 2018, Gold in the mantle: A global assessment of abundance and redistribution processes: Lithos, v. 322, p. 376-391, https://doi.org/10.1016/j.lithos.2018.10.022.

Scott, J. M., Pearson, D. G., Liu, J., Auer, A., Cooper, A. F., Li, D., Palmer, M. C., Read, S. E., Reid, M. R., and Woodland, S. J., 2021, Osmium isotopes in peridotite xenoliths reveal major mid-Proterozoic lithosphere formation

under the Transantarctic Mountains: Geochimica et Cosmochimica Acta, v. 312, p. 25-43, https://doi.org/10.1016/j.gca.2021.08.009.

Sedlock, R. L., Ortega-Gutiérrez, F., and Speed, R. C., 1993, Tectonostratigraphic terranes and tectonic evolution of Mexico: Geological Society of America Special Paper, v. 278, p. 153.

Sen, I. S., Bizimis, M., and Sen, G., 2010, Geochemistry of sulfides in Hawaiian garnet pyroxenite xenoliths: implications for highly siderophile elements in the oceanic mantle: Chemical Geology, v. 273, p. 180-192, https://doi.org/10.1016/j.chemgeo.2010.02.021.

Shimizu, Y., Arai, S., Morishita, T., Yurimoto, H., and Gervilla, F., 2004, Petrochemical characteristics of felsic veins in mantle xenoliths from Tallante (SE Spain): an insight into activity of silicic melt within the mantle wedge: Earth and Environmental Science Transactions of The Royal Society of Edinburgh, v. 95, p. 265-276.

Shimizu, Y., Arai, S., Morishita, T., and Ishida, Y., 2008, Origin and significance of spinel–pyroxene symplectite in lherzolite xenoliths from Tallante, SE Spain: Mineralogy and Petrology, v. 94, p. 27-43.

Shirey, S. B., and Walker, R. J., 1998, The Re-Os isotope system in cosmochemistry and high-temperature geochemistry: Annual Review of Earth and Planetary Sciences, v. 26, p. 423-500.

Shishin, D., Chen, J., and Jak, E., 2020, Thermodynamic modeling of the Pb-S and Cu-Pb-S systems with focus on lead refining conditions: Journal of Phase Equilibria and Diffusion, v. 41, p. 218-233, https://doi.org/10.1007/s11669-020-00811-7.

Siegrist, M., Yogodzinski, G. M., and Bizimis, M., 2021, Origins of Os-isotope and platinum-group element compositions of metasomatized peridotite and cumulate pyroxenite xenoliths from Kharchinsky Volcano, Kamchatka: Geochimica et Cosmochimica Acta, v. 299, p. 130-150, https://doi.org/10.1016/j.gca.2021.01.045.

Sillitoe, H. R., 2012, Copper provinces, in Jeffrey W. Hedenquist, Michael Harris, Francisco Camus (eds), Geology and Genesis of Major Copper Deposits

and Districts of the World: A Tribute to Richard H. Sillitoe, Special Publications of the Society of Economic Geologist, https://doi.org/10.5382/SP.16.01.

Silver, L.T., and Anderson, T.H., 1974, Possible left-lateral early to middle Mesozoic disruption of the southwestern North American craton margin: Geological Society of America Abstracts with Programs, v. 6, p. 955–956.

Simmons, S. F., and Brown, K. L., 2006, Gold in magmatic hydrothermal solutions and the rapid formation of a giant ore deposit: Science, v. 314, p. 288-291, DOI: 10.1126/science.1132866.

Sinyakova, E., Kosyakov, V., Distler, V., and Karmanov, N., 2016, Behavior of Pt, Pd, and Au during crystallization of Cu-rich magmatic sulfide minerals: The Canadian Mineralogist, v. 54, p. 491-509, https://doi.org/10.3749/canmin.1500015.

Sinyakova, E., Kosyakov, V., Palyanova, G., and Karmanov, N., 2019, Experimental modeling of noble and chalcophile elements fractionation during solidification of Cu-Fe-Ni-S melt: Minerals, v. 9, p. 531, https://doi.org/10.3390/min9090531.

Solari, L. A., Aranda Gómez, J. J., Maldonado-Rivera, R., and Moreno-Arredondo, A., 2022, U-Pb age of a Late Cenozoic ultra-high temperature metamorphic event under Central Mexico, as inferred from granulite xenoliths from Cerro El Toro, Mexico: International Geolgoy Review.

Steltenpohl, M. G., Heatherington, A., and Mueller, P., 2004, Pre-Appalachian tectonic evolution of the Pine Mountsin window in the southernmost Appalachians, Alabama end Georgia: in Tollo, R. P., McLelland, J., Corriveau, L., Bartholomew, M. J., eds., Proterozoic Tectonic Evolution of the Grenville Orogen in North America: Geological Society of America Memoir, v. 197, p. 633-646.

Stern, R. J., 1994, Arc assembly and continental collision in the Neoproterozoic East African Orogen: implications for the consolidation of Gondwanaland: Annual Review of Earth and Planetary Sciences, v. 22, p. 319-351.

Su, Y., and Langmuir, C. H., 2003, Global MORB chemistry compilation at the segment scale: PhD thesis, Department of Earth and Environmental Sciences, Columbia University, New York.

Sugaki, A., and Kitakaze, A., 1998, High form of pentlandite and its thermal stability: American Mineralogist, v. 83, p. 133-140, https://doi.org/10.2138/am-1998-0113.

Takazawa, E., Frey, F. A., Shimizu, N., Obata, M., and Bodinier, J. L., 1992, Geochemical evidence for melt migration and reaction in the upper mantle: Nature, v. 359, p. 55-58.

Tassara, S., González-Jiménez, J. M., Reich, M., Schilling, M. E., Morata, D., Begg, G., Saunders, E., Griffin, W. L., O'Reilly, S. Y., Grégoire, M., Barra, F., and Corgne, A., 2017, Plume-subduction interaction forms large auriferous provinces: Nature Communications, v. 8, p. 1-7, https://doi.org/10.1038/s41467-017-00821-z.

Tassara, S., González-Jiménez, J. M., Reich, M., Saunders, E., Luguet, A., Morata, D., Grégoire, M., van Acken, D., Schilling, M. E., Barra, F., Nowell, G., and Corgne, A., 2018, Highly siderophile elements mobility in the subcontinental lithospheric mantle beneath southern Patagonia: Lithos, v. 314, p. 579-596, https://doi.org/10.1016/j.lithos.2018.06.022.

Tassara, S., Reich, M., Konecke, B. A., González-Jiménez, J. M., Simon, A. C., Morata, D., Barra, F., Fiege, A., Schilling, M. E., and Corgne, A., 2020, Unraveling the Effects of Melt–Mantle Interactions on the Gold Fertility of Magmas: Frontiers in Earth Science, v. 8, p. 29, https://doi.org/10.3389/feart.2020.00029.

Tassara, S., Rooney, A. D., Ague, J. J., Guido, D., Reich, M., Barra, F., and Navarrete, C., 2022, Osmium isotopes fingerprint mantle controls on the genesis of an epithermal gold province: Geology, v. 50, p. 1291-1295, https://doi.org/10.1130/G50045.1.

The MELT SEISMIC Team, 1998, Imaging the deep seismic structure beneath a mid-ocean ridge: The MELT experiment: Science, v. 280, p. 1215-1218.

Tian, H., Fan, M., Valencia, V. A., Chamberlain, K., Stern, R. J., and Waite, L., 2021, Mississippian southern Laurentia tuffs came from a northern Gondwana arc: Geology, https://doi.org/10.1130/G49502.1.

Tiepolo, M., Vannucci, R., Oberti, R., Foley, S., Bottazzi, P., and Zanetti, A., 2000, Nb and Ta incorporation and fractionation in titanian pargasite and kaersutite: crystal–chemical constraints and implications for natural systems: Earth and Planetary Science Letters, v. 176, p. 185-201, https://doi.org/10.1016/S0012-821X(00)00004-2.

Toscani, L., 1999, Magmatic gold grains in the El Tale lamproite, Fortuna, SE Spain: Mineralogical Magazine, v. 63, p. 595-602, doi:10.1180/minmag.1999.063.4.12.

Tredoux, M., Davies, G., McDonald, I., and Lindsay, N. M., 1995, The fractionation of platinum-group elements in magmatic systems, with the suggestion of a novel causal mechanism: South African Journal of Geology, v. 98, p. 157-167.

Turner, S., and Costa, F., 2007, Measuring timescales of magmatic evolution: Elements, v. 3, p. 267-272, https://doi.org/10.2113/gselements.3.4.267.

Ulrich, T., Günther, D., and Heinrich, C. A., 1999, Gold concentrations of magmatic brines and the metal budget of porphyry copper deposits: Nature, v. 399, p. 676-679, https://doi.org/10.1038/21406.

van Acken, D., Becker, H., Hammerschmidt, K., Walker, R. J., and Wombacher, F., 2010, Highly siderophile elements and Sr–Nd isotopes in refertilized mantle peridotites—a case study from the Totalp ultramafic body, Swiss Alps: Chemical Geology, v. 276, p. 257-268, https://doi.org/10.1016/j.chemgeo.2010.06.011.

Varas-Reus, M. I., Garrido, C. J., Marchesi, C., Bosch, D., Acosta-Vigil, A., Hidas, K., Barich, A., and Booth-Rea, G., 2017, Sr-Nd-Pb isotopic systematics of crustal rocks from the western Betics (S. Spain): Implications for crustal recycling in the lithospheric mantle beneath the westernmost Mediterranean: Lithos, v. 276, p. 45-61, https://doi.org/10.1016/j.lithos.2016.10.003.

Vidal, O., Goffé, B., and Arndt, N., 2013, Metals for a low-carbon society: Nature Geoscience, v. 6, p. 894-896, https://doi.org/10.1038/ngeo1993.

von Bargen, N., and Waff, H. S., 1986, Permeabilities, interfacial areas and curvatures of partially molten systems: results of numerical computations of equilibrium microstructures: Journal of Geophysical Research: Solid Earth, v. 91, p. 9261-9276, https://doi.org/10.1029/JB091iB09p09261.

Walker, R. J., Horan, M. F., Morgan, J. W., Becker, H., Grossman, J. N., Rubin, A. E., 2002, Comparative ^{187}Re-^{187}Os systematics of chondrites: Implications regarding early solar system processes: Geochimica et Cosmochimica Acta, v. 66, p. 4187-4201, https://doi.org/10.1016/S0016-7037(02)01003-7.

Walter, M. J., 1998, Melting of garnet peridotite and the origin of komatiite and depleted lithosphere: Journal of Petrology, v. 39, p. 29-60.

Wang, K. L., O'Reilly, S. Y., Griffin, W. L., Pearson, N. J., and Zhang, M., 2009, Sulfides in mantle peridotites from Penghu Islands, Taiwan: melt percolation, PGE fractionation, and the lithospheric evolution of the South China block: Geochimica et Cosmochimica Acta, v. 73, p. 4531-4557, https://doi.org/10.1016/j.gca.2009.04.030.

Wang, Z., Cheng, H., Zong, K., Geng, X., Liu, Y., Yang, J., Wu, F., Becker, H., Foley, S., and Wang, C. Y., 2020, Metasomatized lithospheric mantle for Mesozoic giant gold deposits in the North China craton: Geology, v. 48, p. 169-173, https://doi.org/10.1130/G46662.1.

Wang, Z., Jin, Z., Mungall, J. E., and Xiao, X., 2020, Transport of coexisting Ni-Cu sulfide liquid and silicate melt in partially molten peridotite: Earth and Planetary Science Letters, v. 536, 116162, https://doi.org/10.1016/j.epsl.2020.116162.

Wasylenki, L. E., Baker, M. B., Kent, A. J., and Stolper, E. M., 2003, Near-solidus melting of the shallow upper mantle: partial melting experiments on depleted peridotite: Journal of Petrology, v. 44, p. 1163-1191, https://doi.org/10.1093/petrology/44.7.1163.

Weber, B., Scherer, E. E., Schulze, C., Valencia, V. A., Montecinos, P., Mezger, K., and Ruiz, J., 2010, U–Pb and Lu–Hf isotope systematics of lower crust from central-southern Mexico–Geodynamic significance of Oaxaquia in a Rodinia Realm: Precambrian Research, v. 182, p. 149-162, https://doi.org/10.1016/j.precamres.2010.07.007.

Wedepohl, K. H., 1995, The composition of the continental crust: Geochimica et cosmochimica Acta, v. 59, p. 1217-1232, https://doi.org/10.1016/0016-7037(95)00038-2.

Whitmeyer, S. J., and Karlstrom, K. E., 2007, Tectonic model for the Proterozoic growth of North America: Geosphere, v. 3, p. 220-259.

Wiemer, D., Hagemann, S. G., Hronsky, J., Kemp, A. I. S., Thébaud, N., Ireland, T., and Villanes, C., 2022, Ancient structural inheritance explains gold deposit clustering in northern Perú: Geology, doi.org/10.1130/G50208.1.

Wilkinson, J. J., 2013, Triggers for the formation of porphyry ore deposits in magmatic arcs: Nature Geoscience, v. 6, p. 917-925, https://doi.org/10.1038/ngeo1940.

Wirth, R., 2009, Focused Ion Beam (FIB) combined with SEM and TEM: Advanced analytical tools for studies of chemical composition, microstructure and crystal structure in geomaterials on a nanometre scale: Chemical Geology, v. 261, p. 217-229, https://doi.org/10.1016/j.chemgeo.2008.05.019.

Wirth, R., Reid, D., and Schreiber, A., 2013, Nanometer-sized platinum-group minerals (PGM) in base metal sulfides: New evidence for an orthomagmatic origin of the Merensky Reef PGE ore deposit, Bushveld Complex, South Africa: The Canadian Mineralogist, v. 51, p. 143-155, https://doi.org/10.3749/canmin.51.1.143.

Wyborn, L. A. I., Heinrich, C. A., and Jaques, A. L., 1994, Australian Proterozoic Mineral Systems: Essential ingredients and mappable criteria: Australian Institute of Mining and Metallurgy Annual Conference, Melbourne, p. 109-115.

Xu, B., Hou, Z. Q., Griffin, W. L., Zheng, Y. C., Wang, T., Guo, Z., Hou, J., Santosh, M., and O'Reilly, S. Y., 2021, Cenozoic lithospheric architecture and metallogenesis in Southeastern Tibet: Earth-Science Reviews, v. 214, 103472, https://doi.org/10.1016/j.earscirev.2020.103472.

Yaxley, G. M., Kamenetsky, V., Green, D. H., and Falloon, T. J., 1997, Glasses in mantle xenoliths from western Victoria, Australia, and their relevance to mantle processes: Earth and Planetary Science Letters, v. 148, p. 433-446, https://doi.org/10.1016/S0012-821X(97)00058-7.

Zelenski, M., Kamenetsky, V. S., Mavrogenes, J. A., Danyushevsky, L. V., Matveev, D., and Gurenko, A. A., 2017, Platinum-group elements and gold in sulfide melts from modern arc basalt (Tolbachik volcano, Kamchatka): Lithos, v. 290, p. 172-188, https://doi.org/10.1016/j.lithos.2017.08.012.

Zelenski, M., Kamenetsky, V. S., Mavrogenes, J. A., Gurenko, A. A., and Danyushevsky, L. V., 2018, Silicate-sulfide liquid immiscibility in modern arc basalt (Tolbachik volcano, Kamchatka): Part I. Occurrence and compositions of sulfide melts: Chemical Geology, v. 478, p. 102-111, https://doi.org/10.1016/j.chemgeo.2017.09.013.

Zhang, M., O'Reilly, S. Y., Wang, K. L., Hronsky, J., and Griffin, W. L., 2008, Flood basalts and metallogeny: the lithospheric mantle connection: Earth-Science Reviews, v. 86, p. 145-174, https://doi.org/10.1016/j.earscirev.2007.08.007.

Zhang, Y., 2015, Toward a quantitative model for the formation of gravitational magmatic sulfide deposits: Chemical Geology, v. 391, p. 56-73, https://doi.org/10.1016/j.chemgeo.2014.10.025.

Zheng, J., Griffin, W. L., O'Reilly, S. Y., Lu, F., Wang, C., Zhang, M., Wang, F., and Li, H., 2004, 3.6 Ga lower crust in central China: new evidence on the assembly of the North China Craton: Geology, v. 32, p. 229-232, https://doi.org/10.1130/G20133.1.

Zheng, J., Griffin, W. L., O'Reilly, S. Y., Zhang, M., Pearson, N., and Pan, Y., 2006, Widespread Archean basement beneath the Yangtze craton: Geology, v. 34, p. 417-420, https://doi.org/10.1130/G22282.1.

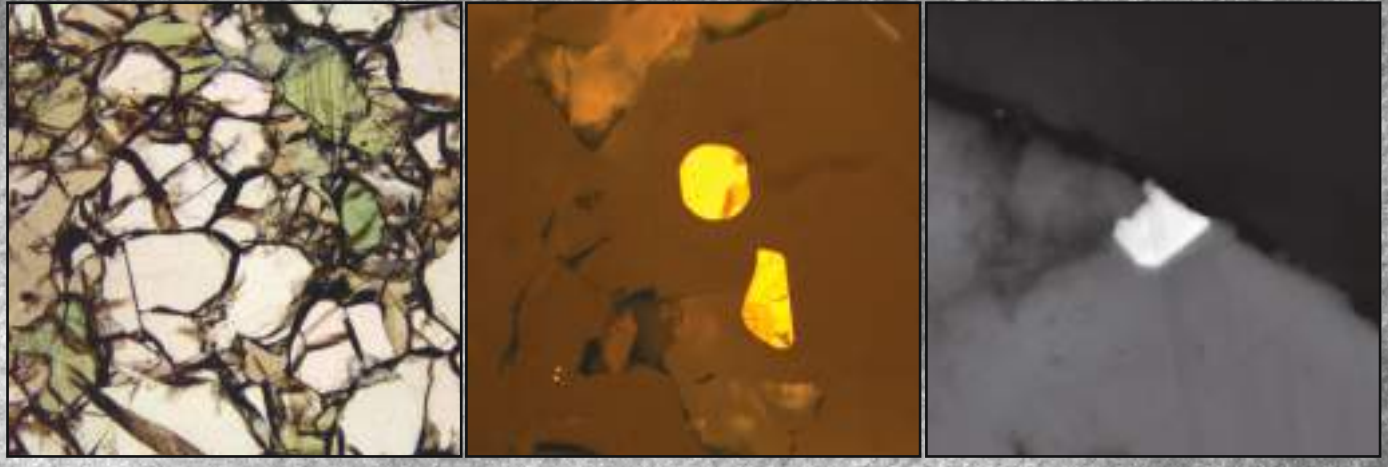

Ore deposits are rock volumes that contain specific elements with concentrations that are anomalously higher than their normal abundaces in the continental crust. The extreme concentration of metallic elements in magmatic-hydrothermal ores requires the combination of several geological factors that contribute to transfer metals from background levels in a source region to exploitable amounts in the accessible crust. The main purpose of this thesis is to provide a stepforward in our understanding of the processes and repositories that control the mobility and storage of metals in the subcontinental lithospheric mantle (SCLM) and in mantle-derived magmas, which may ultimately feed the metallogenic endowment of the continental crust.

To fulfil this general goal, this Ph.D thesis presents the mineralogical, petrological and geochemical characterization of two suites of peridotite mantle xenoliths and associated volcanic rocks from mineralized areas in off-craton regions of the continental lithosphere, such as Mesa Central (Central Mexico) and the southern Iberian margin (Southeast Spain). The combination of mineralogical and microstructural observations from the rock texture to the nanoscale structure with advanced techniques for the in-situ chemical characterization of minerals provided key constraints to: 1) define how the regional architecture and evolution of the SCLM may determine the distribution of magmatic-hydrothermal ore deposits in the continental crust; 2) assess the petrological mechanisms and mineral repositories that enhance the metallogenic fertility of the SCLM; 3) track the mechanisms that control the transfer of metals within ore-productive magmas ascending from the mantle to the crust.

IACT
INSTITUTO ANDALUZ DE CIENCIAS DE LA TIERRA

Research Group on
Petrology, Geochemistry and Geochronology
Thesis Memoir